A STOCHASTIC WAVELET FINITE ELEMENT METHOD USING B-SPLINE WAVELET ON THE INTERVAL FOR PROBLEMS IN STRUCTURAL MECHANICS

A thesis submitted

in partial fulfillment for the award of the degree of

Doctor of Philosophy

by

SHASHANK VADLAMANI

Department of Aerospace Engineering

Indian Institute of Space Science and Technology

Thiruvananthapuram, India

November 2019

Certificate

This is to certify that the thesis titled ***A STOCHASTIC WAVELET FINITE ELEMENT METHOD USING B-SPLINE WAVELET ON THE INTERVAL FOR PROBLEMS IN STRUCTURAL MECHANICS*** submitted by **SHASHANK VADLAMANI**, to the Indian Institute of Space Science and Technology, Thiruvananthapuram, in partial fulfillment for the award of the degree of **Doctor of Philosophy** is a bona fide record of the original work carried out by him under my supervision. The contents of this thesis, in full or in parts, have not been submitted to any other Institute or University for the award of any degree or diploma.

Dr. Arun C.O.
Assistant Professor
Department of Aerospace Engineering

Dr. Manoj T. Nair
Head of the Department
Department of Aerospace Engineering

Place: Thiruvananthapuram
Date: November 2019

Declaration

I declare that this thesis titled ***A STOCHASTIC WAVELET FINITE ELEMENT METHOD USING B-SPLINE WAVELET ON THE INTERVAL FOR PROBLEMS IN STRUCTURAL MECHANICS*** submitted in partial fulfillment for the award of the degree of **Doctor of Philosophy** is a record of the original work carried out by me under the supervision of **Dr. Arun C.O.**, and has not formed the basis for the award of any degree, diploma, associateship, fellowship, or other titles in this or any other Institution or University of higher learning. In keeping with the ethical practice in reporting scientific information, due acknowledgments have been made wherever the findings of others have been cited.

Place: Thiruvananthapuram
Date: November 2019

SHASHANK VADLAMANI
(SC15D002)

Dedicated to my family and friends

Acknowledgements

Firstly, I would like to sincerely thank my research adviser Dr. Arun C.O. from IIST for his continuous support throughout the tenure of my doctoral research. His experience and guidance has been instrumental and has proved to be of immense help at every stage of my work. I am also grateful to my Doctoral committee members (Dr. Praveen Krishna, IIST; Dr. Bijudas C.R., IIST; Dr. Deepak T.G., IIST; Dr. Rajib Chowdhury, IIT Roorkee; Dr. Mira Mitra, IIT Kharagpur) for their time and patience. Their feedback on certain aspects of my work has been invaluable.

I would also like to express my gratitude towards my colleagues and the entire staff of Department of Aerospace engineering at IIST. Finally, I would like to acknowledge the warm support and care of my family and friends, without whose encouragement this journey would not have been possible.

SHASHANK VADLAMANI

Abstract

A stochastic modelling approach takes into account the inherent uncertainties during the design of engineering systems. The additional statistical information that a stochastic model provides when compared with a deterministic model, leads to a comprehensive description and optimum design of the system; thereby improving its reliability. On the other hand, a stochastic approach also increases the model complexity and requires a higher computational effort to obtain the system response when compared with a deterministic approach. Numerical method such as B-spline wavelet on the interval (BSWI) based wavelet finite element method (WFEM) has shown to be efficient in dealing with the issues of low convergence as encountered in a conventional finite element method (FEM). At the same time, the underlying properties of wavelets could also be used to develop algorithms in the stochastic framework which could alleviate the issues related to accuracy and mapping of random field mesh that are encountered in FEM.

Based on the preceding notion, the current thesis at first proposes a background cell based Gauss quadrature numerical integration approach for BSWI WFEM. In the proposed approach, background cells are placed over each BSWI element and Gauss quadrature rule is defined for each of these cells. During the analysis, background cells of various lengths are used for evaluating the integrals for various combination of order and resolution of BSWI scaling functions. The dimensions of the background cells are varied and its effect on the condition number and sparseness of the element stiffness matrix is studied for one dimensional (1D) (bar, beams) and two dimensional (2D) plane stress problems. Further, a detailed analysis to understand the effect of number of Gauss points within each background cell on the accuracy of the results is done.

The development of stochastic BSWI WFEM algorithms for linear static problems in 1D (bar), beams (based on Euler-Bernoulli and Timoshenko beam theory) and 2D plane elasto-statics (plane stress) is shown in the thesis wherein, the spatial variation of modulus of elasticity is modelled as a homogeneous random field. BSWI scaling functions are used for the discretization of the random field. The response statistics are obtained using the perturbation approach. Numerical examples are solved based on the proposed background cell integration scheme. The results from perturbation approach are compared with that obtained from Monte Carlo simulation (MCS). A parametric study is also done

to understand the effect of coefficient of variation values and correlation length parameters on the response statistics. For 1D problem in particular, results from proposed stochastic WFEM method are compared with those found using stochastic FEM wherein random field discretization is done using Lagrange shape functions. Furthermore, normalized computational times for the execution of perturbation approach and MCS based on WFEM are evaluated and compared with those obtained for FEM.

In addition to the aforementioned formulations, the thesis shows the construction of beam elements by incorporating von Kármán nonlinear strains using BSWI WFEM. The mathematical model is developed in both the deterministic as well as the stochastic framework. An algorithm for evaluating the derivatives of response quantities from nonlinear equilibrium equations is derived. The results are analyzed accordingly for different boundary conditions. Results show that BSWI WFEM can be used as an alternate numerical tool for developing an efficient and rigorous stochastic based algorithms.

Contents

List of Figures

List of Tables

Abbreviations

FEM	Finite element method
SFEM	Stochastic finite element method
WFEM	Wavelet finite element method
MRA	Multiresolution analysis
BSWI	B-spline wavelet on the interval
1D	One dimensional
2D	Two dimensional
EBT	Euler-Bernoulli beam theory
TBT	Timoshenko beam theory
MCS	Monte Carlo simulation
WGM	Wavelet Galerkin method
3D	Three dimensional
MF	Mesh-free
FE	Finite element
MLPG	Meshless local Petrov-Galerkin
EFGM	Element free Galerkin method
KL	Karhunen-Loéve
PC	Polynomial Chaos
WSFE	Wavelet based spectral finite element
FFT	Fast Fourier transform
HCSWI	Hermite cubic spline wavelets on the interval
SGW	Second generation wavelets
PDE	Partial differential equations
C1BKP	C_1 type B-spline Kirchhoff plate
MWFEM	Multivariable wavelet finite element method
WEM	Wavelet element method
SEM	Spectral element method

SIFs	Stress intensity factors
2DPCs	2D phononic crystals
DOF	Degrees of freedom
UDL	Uniformly distributed load
FOP	First order perturbation
SOP	Second order perturbation
CV	Coefficient of variation
CPU	Central Processing Unit
TL	Total Lagrangian

Nomenclature

$\mathbb{R}$	Real numbers
$\mathbf{Z}$	Integers
j	Scale/resolution parameter
k	Translation parameter
$\boldsymbol{\sigma}$	Stress vector
$\boldsymbol{D}$	Material property matrix
$\boldsymbol{\epsilon}$	Strain vector
$\boldsymbol{u}$	Displacement vector
$\boldsymbol{b}$	Body force vector
$\overline{\boldsymbol{t}}$	Surface traction vector
$\overline{\boldsymbol{u}}$	Surface displacement vector
$\boldsymbol{n}$	Unit normal
Ω	Global problem domain
Γ_t	Traction portion of the boundary
Γ_u	Displacement portion of the boundary
ϕ	Scaling function
ψ	Wavelet function
Ω_e	Local element solving domain
m	Order of scaling function
ξ, η	Local co-ordinates in element solving domain
$f(x)$	Distributed axial load per unit length
Q_i	Generalized lumped nodal forces
n_d	Total number of nodes per BSWI WFEM bar element
u_0	Axial displacement field
$\boldsymbol{a^e}, \boldsymbol{b^e}, \boldsymbol{c^e}, \boldsymbol{d^e}$	Column vector of wavelet coefficients
$\boldsymbol{\varphi}$	Row vector of BSWI scaling functions
$\boldsymbol{T^e}$	Transformation matrix

$\boldsymbol{R^e}$	Inverse of transformation matrix
$\boldsymbol{N^e}$	Wavelet shape functions
$\boldsymbol{K^e}$	BSWI WFEM element stiffness matrix
$\boldsymbol{u^e}$	Column vector of elemental axial DOF
$\boldsymbol{w^e}$	Column vector of elemental transverse DOF
$\boldsymbol{F^e}$	Element force vector
l_{ex}	Length of BSWI element in x direction
l_{ey}	Length of BSWI element in y direction
w_0	Transverse deflection field
I	Second moment of area
$q(x)$	Uniformly distributed transverse load per unit length
Q_i	Generalized lumped transverse nodal forces
M_k	Bending moments
n_e	Total number of nodes per BSWI WFEM beam element based on EBT
θ	Slope in a BSWI WFEM beam element based on EBT
θ_x	Slope in a BSWI WFEM beam element based on TBT
K_s	Shear correction coefficient
G	Shear modulus
n_f	Total number of nodes per BSWI WFEM beam element based on TBT
t	Uniform thickness in a 2D plane stress problem
$\boldsymbol{W^e}$	Column vector of elemental DOF for BSWI WFEM TBT beam element
$\boldsymbol{\theta^e}$	Column vector of elemental rotational DOF
$\boldsymbol{p}$	Column vector of surface tractions in x and y directions respectively
$\boldsymbol{F_i}$	Column vector of point forces
$\boldsymbol{u_i}$	Column vector of point displacements at the point of application of forces
n_{ep}	Total number of nodes per 2D BSWI plane elasto-statics element
v_0	Displacement field in y direction in 2D plane stress problem
$\boldsymbol{v^e}$	Column vector of elemental DOF in y direction
ν	Poisson's ratio
E	Young's modulus
L	Length/span
δ	Axial displacements
σ_{xx}	Axial stresses
b, h	Breadth and depth of beam
r_u	Relative error in displacement norm

a	Radius of hole
r	Distance in radial direction
F	Distributed tensile load
θ_s	Angle associated with polar co-ordinate system in the plate with a hole problem
K_t	Stress concentration factor
$E(\mathbf{x})$	Young's modulus expressed as a homogeneous random field
μ_E	Mean value of Young's modulus for Gaussian random field
σ_E	Standard deviation of Young's modulus for Gaussian random field
$\alpha(\mathbf{x})$	Zero mean Gaussian field
Γ_α	Auto-covariance kernel of $\alpha(\mathbf{x})$
c_i	Correlation length parameter
σ_α	Standard deviation of zero mean Gaussian field
μ_{E_l}	Mean value of Young's modulus for lognormal random field
σ_{E_l}	Standard deviation of Young's modulus for lognormal random field
$(.)_{\boldsymbol{R}}, (.)_r$	Subscript denotes function or variable associated with random field
$G(\mathbf{x})$	Rigidity modulus expressed as a homogeneous random field
μ_G	Mean value of Rigidity modulus for Gaussian random field
$\boldsymbol{\mu}_U$	Mean value of displacement vector
$\boldsymbol{\gamma}_U$	Variance of displacement vector
$\boldsymbol{K}$	Global BSWI WFEM stiffness matrix
$\boldsymbol{U}$	Global column vector of all the axial DOF
$\boldsymbol{F}$	Global force vector
$\boldsymbol{K_0}$	Global deterministic BSWI WFEM stiffness matrix at K(0)
$\boldsymbol{U_0}$	Global deterministic column vector of all the axial DOF at U(0)
$\boldsymbol{F_0}$	Global deterministic force vector at F(0)
$\boldsymbol{\Lambda}$	Vector of zero mean random variables
$\boldsymbol{\mu}_u$	Mean value of axial displacement field
$\boldsymbol{\sigma}_u$	Standard deviation of axial displacement field
$\boldsymbol{\mu}_v$	Mean value of displacement field in y direction in 2D plane stress problem
$\boldsymbol{\sigma}_v$	Standard deviation of displacement field in y direction in 2D plane stress problem
$\boldsymbol{\mu}_w$	Mean value of transverse displacement field in BSWI beam element
$\boldsymbol{\sigma}_w$	Standard deviation of transverse displacement field in BSWI beam element
E_{IJ}	Green-Lagrange strain tensor
S_{IJ}	Piola-Kirchoff stress tensor
C_{IJKL}	Material elasticity tensor

δW_I^i	Internal virtual work done
δW_E^i	External virtual work done
σ_{ij}	Cauchy stress tensor
$\delta\epsilon_{ij}$	Virtual strains
Q_i^a, Q_i^t	Generalized nodal forces for axial, transverse DOF
Q_1^r, Q_2^r	Generalized nodal forces for rotational DOF
z	parameter along depth of beam
E_{XX}	Axial strain tensor
γ_{XZ}	Shear strain tensor
$\boldsymbol{R}_s$	Residual of Newton-Raphson method
$\boldsymbol{T}_s$	Tangent stiffness matrix
q	Number of iterations
E_{XX}^0	Membrane strain tensor
P_c	Axial compressive load

Chapter 1

Introduction

1.1 Motivation

During the design of engineering structural systems, maximizing the safety levels and minimizing the cost incurred, becomes one of the key objectives. A deterministic approach with a factor of safety does not provide adequate information to maximize the safety of the system. On the other hand, a stochastic approach takes into account the inherent uncertainties that exist in its material properties, loads, geometry, operating environments, etc., during the design and analysis stage of the system. It provides additional statistical information about the system which leads to a more comprehensive description and optimum design of the system, thereby improving its reliability [1] [2]. On the downside, a stochastic approach increases the model complexity and requires a higher computational effort to obtain the solution of the system response as compared to a deterministic approach. However, the advent of powerful computational resources during the past few decades has led to an extensive research in the field of stochastic mechanics [3]. Nonetheless, due to the growing complexity in the system design, there is a need for the development of more efficient and elegant stochastic based numerical methods.

The randomness that exists in the input parameters varies not only for different samples but also at different points in the domain of its respective sample. Hence, mathematical models which consider a random field by incorporating correlation properties of input random parameters are needed for the calculation of response statistics in the analysis. Over the years, due to the versatility of finite element method (FEM) [4] for solving stochastic partial differential equations, extensive research has gone into the development of stochastic finite element methods (SFEM) [3], wherein a stochastic mesh is generated to discretize the input random field and calculate the response statistics [5–14]. However, the high mesh dependency of FEM creates difficulties in mapping the random field

discretization to response discretization [15] [16]. Moreover, the accuracy and reliability of the method is a cause for concern. The rate of convergence decreases significantly in FEM by the presence of singularities due to stress concentration and crack. Convergence issues in FEM are usually addressed by h, p and h-p refinements. Babuska and Guoś [17] pioneering work gives a theoretical understanding of these refinements. However, low convergence rate, higher computational effort and re-meshing are some of the limitations that are associated with h, p and h-p refinements respectively. Hence, there is a need for the development of stochastic based numerical methods, which can address these limitations of FEM.

Meshless methods have been used in the stochastic analysis [18–21] to alleviate the mesh dependency of FEM. Wavelet finite element method (WFEM) is another alternate numerical tool which has gained the interest of the research community in recent times, and has shown to reduce the issues related to FEM considerably. Over the past few decades, there has been a widespread research into the development of wavelet based numerical methods in many areas of scientific importance [22]. Wavelets are mathematical functions that can be used to approximate other functions at different levels of resolution. The multiresolution analysis (MRA) [23–25] property that wavelets possess leads to the development of a hierarchy of solutions during the approximation process. Wavelets have a compact support and are localized in space, which leads to a refinement of solution locally in the regions of high gradient [26]. Therefore, issues such as slow convergence in the vicinity of high gradients and re-meshing in adaptive mesh sensitive problems, that are encountered in conventional FEM can be avoided using wavelet based numerical methods. There exist different wavelet based numerical methods in the literature [22]. Among these B-spline wavelet on the interval (BSWI) based WFEM has gained wide prominence. This can be attributed to the underlying properties of BSWI [24] [27] that make it more efficient as compared to other wavelet based numerical methods in dealing with boundary value problems elegantly. The aforementioned properties of wavelets can make it an efficient and a reliable mathematical tool, which can be used for nonlinear analysis in structural mechanics problems. Moreover, it can have wide applications in the field of stochastic mechanics, where material properties and loads appear to be random fields or variables. The next section presents a brief outline of the thesis.

1.2 Outline of the thesis

The thesis is divided into six chapters. Chapter 1 presents the motivation for pursuing the current thesis. Chapter 2 presents a detailed literature review on wavelets. The review focuses on wavelet based Galerkin methods used for solid mechanics problems. Research works leading up to the current state of research are discussed. Literature review is followed by a brief introduction to wavelets and its properties. Further, a description of BSWI and its construction is also provided. The research objectives of the thesis are set and the scope of the study is defined in this chapter. Chapter 3 presents a methodology for evaluating the integrals involved in BSWI WFEM. In line with element free Galerkin method [18], multiple background cells are proposed to use over each element for numerical integration using Gauss quadrature. Numerical examples, based on one dimensional (1D) and two dimensional (2D) plane elasto-statics and beams based on Euler-Bernoulli beam theory (EBT) and Timoshenko beam theory (TBT) are solved. Suggestions on selection of background cells and Gauss quadrature points along with order and resolution of B-spline scaling functions for different class of problems, to obtain a well-conditioned stiffness matrix are given. Chapter 4 proposes the formulation of stochastic BSWI WFEM for 1D and 2D problems in elasto-statics and beams wherein, the spatial variation of modulus of elasticity is modelled as a homogeneous random field. Random field discretization is done using BSWI scaling functions. Perturbation approach is used to calculate the response statistics and the results are validated using Monte Carlo simulation (MCS). For 1D problem in particular, results from proposed stochastic WFEM method are compared with those found using SFEM. Chapter 5 presents the formulation of stochastic BSWI based WFEM for beams by incorporating von Kármán nonlinear strains. In both Chapter 4 and Chapter 5, numerical examples of beams based on EBT and TBT are solved during the study. BSWI scaling functions are used for the discretization of the random field and the response statistics that are obtained using the perturbation approach, are compared with that obtained from MCS and SFEM. Chapter 6 is the concluding chapter which provides with an overview to the current thesis, highlights the major contribution of the thesis and suggestions for future work.

Chapter 2

Literature review

The current chapter gives an introduction to wavelets and its properties. This is followed by a comprehensive literature review on wavelet based Galerkin methods used for solid mechanics problems. A brief introduction to the properties of semi-orthogonal BSWI is given and the reasons that make BSWI more efficient as compared to other wavelets are also discussed.

2.1 Wavelets and multiresolution analysis

Wavelets are a class of functions that can be used in data representation and approximation of other functions by satisfying certain mathematical requirements [28]. There are two ways to understand the concept of wavelets; Mallat [29, 30] approached wavelets and its properties from a signal processing perspective; whereas Morlet [31–33], Meyer [34], and Daubechies [23, 25] approached it from a functional space perspective. In a signal processing perspective, wavelet transform works as a filter which acts upon an input signal to give an output signal [35]. Here, data can be represented by components of different frequency and each component can be studied with the desired resolution matched to its scale. Thus, local representation of functions in both frequency (space) and time is possible. However, from a functional space point of view, wavelet basis can be constructed by the realization of a multiresolution analysis (MRA) [23]. In MRA, concept of basis functions and scale varying basis functions are the keys [36]. The idea behind MRA is to approximate a function as a limit of successive approximations; as shown in Figure 2.1, each having a different resolution till a smoothed version of it is obtained [23].

Thus, MRA is a nested sequence $\{V_j\}_{j\in\mathbf{Z}}$ of closed subspaces of $L^2(\mathbb{R})$. If a function $\phi \in V_0$ known as the scaling function generates MRA $\{V_j\}_{j\in\mathbf{Z}}$ of $L^2(\mathbb{R})$ then $\{\phi(.-k)\}_{k\in\mathbf{Z}}$

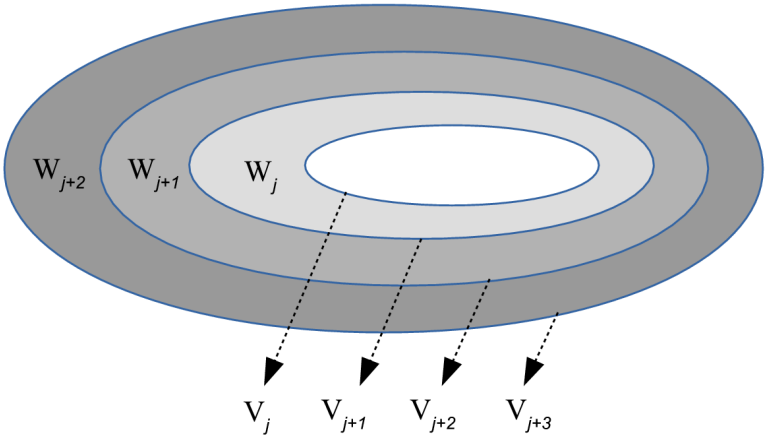

Figure 2.1: Multiresolution analysis showing nested sequence of closed subspaces

forms a Riesz basis of V_0. By setting,

$$\phi_{j,k}(x) = 2^{j/2}\phi(2^j x - k), j, k \in \mathbf{Z} \tag{2.1}$$

it follows that, for each integer value of j the family $\{\phi_{j,k}\}_{k\in\mathbf{Z}}$ is also a basis of $\{V_j\}_{j\in\mathbf{Z}}$ [24]. Additionally, a complementary subspace $\{W_j\}_{j\in\mathbf{Z}}$ of subspace $\{V_j\}_{j\in\mathbf{Z}}$ also exists. Moreover, the Hilbert space $L^2(\mathbb{R})$ can be decomposed into a direct sum of closed subspaces $\{W_j\}_{j\in\mathbf{Z}}$, using a function ψ known as the wavelet function. Here, each subspace W_j is the closure in $L^2(\mathbb{R})$ of the linear span of collection of functions, by taking ψ as,

$$\psi_{j,k}(x) = 2^{j/2}\psi(2^j x - k), j, k \in \mathbf{Z} \tag{2.2}$$

Thus, $L^2(\mathbb{R})$ can be decomposed as a direct sum of the spaces W_j in the sense that every function $f \in L^2(\mathbb{R})$ has a unique decomposition;

$$f(x) = ... + g_{-2}(x) + g_{-1}(x) + g_0(x) + ..., \tag{2.3}$$

where, $g_j \in \{W_j\}_{j\in\mathbf{Z}}$ [24]. Moreover, if ψ is an orthogonal wavelet, then the subspace W_j of $L^2(\mathbb{R})$ are mutually orthogonal, which implies $< g_j, g_l >$ = 0, $j \neq l$, where, $g_j \in W_j$ & $g_l \in W_l$. Then the corresponding subspace can be written as,

$$V_j := .... \oplus W_{j-2} \oplus W_{j-1} \oplus ...., j \in \mathbf{Z} \tag{2.4}$$

Based on the above discussions, the properties of MRA can be summarized as follows:

$$.... \subset V_{-1} \subset V_0 \subset V_1 \subset .... \tag{2.5}$$

$$clos_{L^2}(\bigcup_{j \in \mathbf{Z}} V_j) = L^2(\mathbb{R}) \tag{2.6}$$

$$\bigcap_{j \in \mathbf{Z}} V_j = 0 \tag{2.7}$$

$$V_{j+1} = V_j \oplus W_j \tag{2.8}$$

$$f(x) \in V_j \iff f(2x) \in V_{j+1}, j \in \mathbf{Z} \tag{2.9}$$

and

$$f(x) \in V_j \iff f(x-k) \in V_j, j \in \mathbf{Z} \tag{2.10}$$

Equation 2.5 shows that the subspace $\{V_j\}_{j \in \mathbf{Z}}$ is completely nested within the next subspace $\{V_{j+1}\}_{j \in \mathbf{Z}}$. Equation 2.6 shows that a function $f \in L^2(\mathbb{R})$ can be approximated as a series of successive approximations by a nested sequence $\{V_j\}_{j \in \mathbf{Z}}$ of closed subspaces of $L^2(\mathbb{R})$. When the resolution is decreased, the details of the approximating function f are reduced. Eventually, when the resolution goes to 0, all the details are lost; which is deduced from Equation 2.7. More importantly, Equation 2.8 indicates that the orthogonal sum (provided the wavelet function leads to an orthogonal decomposition of $\{W_j\}_{j \in \mathbf{Z}}$) of complementary subspace $\{W_j\}_{j \in \mathbf{Z}}$ with $\{V_j\}_{j \in \mathbf{Z}}$ form the next higher subspace $\{V_{j+1}\}_{j \in \mathbf{Z}}$. It can also be concluded that the complementary subspaces $\{W_j\}_{j \in \mathbf{Z}}$ capture the finer details of $\{V_{j+1}\}_{j \in \mathbf{Z}}$, whereas the coarse details are obtained by $\{V_j\}_{j \in \mathbf{Z}}$. Equation 2.9 and Equation 2.10 represent the scale invariant and shift invariant conditions respectively. Equation 2.9 indicates that if a function $f(x) \in V_j$ then a scaled version of the same function $f(2x) \in V_{j+1}$. Consequently, as the scale is increased, the approximation of the function gets better due to MRA. Finally, Equation 2.10 shows that, translates of a function remain in the same subspace $\{V_j\}_{j \in \mathbf{Z}}$. Several factors like desired order of numerical accuracy, computational speed and scale decoupling govern the choice for choosing an ideal wavelet basis function. However, some of the most desirable features for any wavelet include [35, 37];

Compact support: ideal for resolving high gradients, implementation of adaptive refinement schemes and faster computation.
Vanishing moments: Vanishing moments measure the local regularity (indicates the number of its continuous derivatives) of a function. A wavelet function is said to have n vanishing moments if it satisfies,

$$\int_{-\infty}^{\infty} x^k \psi(x) dx = 0,\ k = 0, 1...n-1 \tag{2.11}$$

Most often, classification of wavelets takes place by the number of vanishing moments. All wavelets must satisfy Equation 2.11 for $k = 0$.
Orthnormality: The wavelets $\psi_{j,k}(x)$ form an orthonormal basis if

$$\langle \psi_{j,k}(x), \psi_{p,q}(x) \rangle = \delta_{j,p}\delta_{k,q} \tag{2.12}$$

for all $j, k, p, q \in \mathbf{Z}$ and $\delta_{j,p}, \delta_{k,q}$ are the kronecker delta.
Semi-orthnormality: The wavelets $\psi_{j,k}(x)$ form a semi-orthonormal basis if

$$\langle \psi_{j,k}(x), \psi_{p,q}(x) \rangle = 0 \tag{2.13}$$

$j \neq p$ for all $j, k, p, q \in \mathbf{Z}$.
Polynomial degree: A polynomial can be matched exactly up to a certain degree by choosing the appropriate wavelet basis. Moreover, the accuracy of the polynomial expansion that the wavelet basis can match is reflected in the number of vanishing moments of the wavelet.

In conclusion, the properties of wavelets make it a viable mathematical tool for many engineering applications such as in the study of earthquake, wind and ocean engineering [38], turbulence studies, data compression algorithms, study of galaxies [39], for statistical applications and data analysis [40, 41], in image compression and modulation channel coding [42, 43], etc. Moreover, these properties also make wavelets a feasible tool for numerical solution of differential equations and so find its wide applications in the development of wavelet based Galerkin methods which will be discussed in detail in the next section.

2.2 Wavelet Galerkin method

Wavelets have an advantage over the standard polynomial or trigonometric basis while using with the Galerkin method since they form MRA, which facilitates fast switching of resolution levels and functional bases. In wavelet based Galerkin methods the trial function and weighting function are approximated using either scaling functions or both scaling and wavelet functions. Owing to these desirable properties of wavelets, wavelet Galerkin method (WGM) has been widely used since the early 1990's. However, it is difficult to incorporate boundary conditions for a wavelet series expansion on a bounded domain [44, 45]. The difficulty arises because wavelet bases are defined on the real line, which is unbounded and when these bases are used for solving boundary value problem on the interval by restricting them to the bounded interval; it gives rise to an instability problem [46]. As a result, several researchers have proposed novel methods for treating the boundary conditions in an elegant way. Anderson et al. [47], Monasse and Perrier [48] and Cohen and Masson [49] suggested methods by which wavelets were modified at the boundaries of the domain. However, these methods were not able to satisfactorily handle general boundary conditions in 2D or three dimensional (3D) domains [50].

1D counterpart of Helmholtz's partial differential equation was solved using Daubechies wavelets by Amaratunga et al. [26], in which Dirichlet boundary conditions were implemented using the capacitance matrix method, which was proposed by Proskurowski and Widlund [51]. Qian and Weiss [52] used WGM for the numerical solution of the Helmholtz equation in non-separable 2D geometry and defined a wavelet-capacitance matrix method for treating boundary conditions which overcomes the limitations of the capacitance matrix method. WGM was extended to solve general boundary value problems by Amaratunga and Williams [35], wherein wavelets were adapted to an interval using an extrapolation method called wavelet extrapolation. Boundary conditions were enforced in partial differential equations when wavelets were defined on an interval. WGM was applied to two point boundary value problems of second order elliptical equations by Xu and Shann [53]. A new approach was suggested in this paper wherein, instead of using Daubechies wavelets directly as trial functions, their anti-derivatives were chosen. The suggested advantages were that the singularity is smoothed in wavelets, boundary condition can be easily handled and the underlying orthogonality of wavelets can be used to construct efficient algorithms.

Bertoluzza et al. [46] suggested two separate techniques for treating dirichlet boundary conditions with WGM and wavelet collocation method for solving differential equation

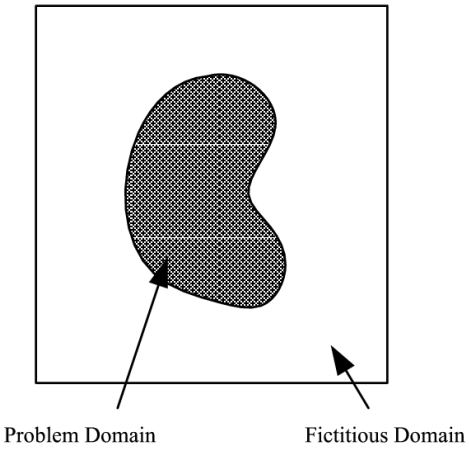

Figure 2.2: Problem domain of interest is embedded into a larger simple domain known as fictitious domain

on the interval [0, 1]. In the first technique as proposed by Bertoluzza et al. [46], MRA on the interval using Daubechies scaling functions were used to impose dirichlet boundary conditions without instabilites; and in the second technique proposed by the same authors, autocorrelation function of the Daubechies scaling functions were used to impose the boundary conditions. Another approach that was widely used, to deal with general boundary conditions was the fictitious domain method. In this method, an original domain of interest was embedded into a larger simple domain as shown in Figure 2.2, and then boundary conditions were imposed via penalty parameters or Lagrange multipliers using the WGM approach.

Diaz [54], proposed a fictitious domain approach to address large scale boundary value problems defined on domains of simple geometry. Boundary conditions were imposed via Lagrange multipliers. This approach was extended to topology optimization examples in 3D elasticity by DeRose Jr and Diaz [55]. However, it was pointed out by Jang et al. [50] that the imposition of boundary conditions via penalty parameters or Lagrange multipliers becomes difficult in the framework of adaptive multi-scale WGM. Hence, a fictitious domain based formulation was proposed by them, in which no penalty term or Lagrange multiplier was used for the adaptive multi-scale WGM. One may refer to Glowinski et al. [56, 57], Wells Jr and Zhou [58] and DeRose Jr G. [59] for more information on the fictitious domain approach. Implementation of WGM for 2D elastoplasticity problems using Daubechies wavelets was discussed in a series of papers by Liu et al. [60–62]. It was

noted that the approximation by Daubechies wavelet was non-interpolatory in nature [60], and lacked Kronecker delta properties in scaling functions and wavelet functions [61]. A new method for evaluation of integrals was proposed to deal with general boundaries and improve the efficiency and accuracy of solution. Additionally, analogous to meshless methods, essential boundary conditions were implemented using Lagrange multipliers. Numerical examples illustrated that the method was effective and stable and could be used for solving complicated deformation problems. B-spline wavelets based WGM was also used for large deformation problems [63] and boundary value problems [64]. It was noticed that unlike Daubechies wavelet that does not have an explicit functional form and has a relatively low computational efficiency; B-spline functions were simple and easy to work with. Spline wavelet bases have a closed form expression in both the time and frequency domain, which easily facilitates their manipulation. They have a compact support and optimal time-frequency localization can be achieved. B-spline scaling functions are also the most regular scaling functions and have the best approximation properties as compared to all the other known wavelets of a given order [37, 65].

B-spline basis functions were used in WGM for elasto-statics problems based on a voxel approach in a series of papers by Tanaka et al. [66–68]. Voxel approach [69–71] is a virtual meshless approach in which element connectivity information is not needed in the input data but elements are used in the computation. This is because the problem domain is discretized by using elements having identical configurations and properties. As a result, voxel elements have a common element stiffness matrix and it is not necessary to store a global stiffness matrix as it can be easily assembled from the common element stiffness matrix of voxel elements when the body is homogeneous. Tanaka et al. [68] also noted that when penalty formulation was adopted in the fictitious domain framework to enforce essential boundary conditions the global stiffness matrix became ill conditioned which subsequently lead to convergence issues. Hence, an alternative method to fictitious domain approach was suggested in which basis functions were eliminated selectively so that the ones remaining were linearly independent. This approach was combined with X-FEM to solve fracture mechanics problems in the papers by Tanaka et al. [72, 73]. In other study, WGM was also used for 1D structural problem in the presence of elastic-plastic damage behaviour [74, 75]. Venini and Morana [74] used linear shape functions of finite element framework as the scaling functions and the wavelet functions were chosen as given by Goubet [76], whereas biorthogonal spline wavelet and Daubechies wavelet were used by Navarro et al. [75] in their study. In the literature, 2D Hat interpolation wavelets have also been used as the trial functions in WGM formulation. Kim et al. [77] proposed

adaptive multi-scale WGM using 2D Hat interpolation wavelets to solve plane elasticity problems and multi-scale topology design optimization, Jang et al. [50,78] used it for shape optimization based on wavelet adaptive analysis and extended it to 2D elliptic problems in general domains. 2D Hat interpolation wavelets were also used for thin-walled box beam analysis by Kim and Jang [79].

A combined wavelet based mesh-free (MF) method was proposed by Yang et al. [80] for solving electromagnetic field problems and later, to solve the forward problem in electrical impedance tomography by Yousefi et al. [81]. Here, the solution domain was divided into three sub-domains as finite element (FE) sub-domain, MF sub-domain and FE-MF sub-domain having mutual influences. Daubechies wavelet scaling functions were used as the trial functions to approximate the unknown function in MF domain. The scaling functions of B-spline wavelet were also used as the basis of the moving least square method to construct the meshless interpolation function in [82], wherein h-adaptive meshless local Petrov-Galerkin (MLPG) method for solving Mindlin plate and shell problems was presented. Additionally, Afsari and Movahhedi [83] used wavelet based meshless method (radial point interpolation method) for simulation of conducting materials and Xia and Ren [84] used element free Galerkin method (EFGM) with a wavelet basis. Xu et al. [85] used cubic B-spline wavelet as the weight function in meshless method and employed it to study 1D and 2D structures whereas Chen et al. [86] presented MLPG method employing B-spline wavelet basis functions for the displacement field variable of membrane structures.

Traditional wavelet based numerical methods rely on uniform grids for analysis. However, more recently, Liu and Din [87] proposed a WGM in which the analysis was carried out on non-uniform grids as well. An isoparametric analysis approach was adapted wherein, the function approximation based on Daubechies wavelet scaling functions were implemented on B-spline patches that were used to describe the problem domain. Another interesting study was done by Kamiński [88], who modelled interface defects and structural non-homogeneities in uni-directional periodic composites. Here, an algebraic combination of the Haar wavelet, Mexican hat and harmonic wavelets was proposed to describe analytically the material properties (heat conductivity and capacity, Young modulus, mass density). Computational studies were carried out that highlighted the crucial role of the interface in the macro-scale behaviour of even unidirectional composites.

The usage of wavelets in the framework of stochastic processes can be traced back to Wornell [89], who used orthonormal wavelet bases to construct for scaling processes from a set of uncorrelated random variables. Two main aspects of numerical methods for problems wherein parameters are observed to be random fields are random field approximation and

response approximation. Zeldin and Spanos [90] have shown that Daubechies wavelet bases can be used effectively to model random fields. Karhunen-Loéve (KL) expansion technique is known to be an efficient technique for random field discretization. Phoon et al. [91] and Proppe [92,93] implemented a wavelet Galerkin approach using basis functions of Haar wavelets to solve the Fredholm integral equation involved in KL expansion technique. Further, Phoon et al. [94] showed that use of a wavelet-Galerkin scheme for determination of Eigen-solutions in KL expansion is computationally equivalent to using wavelets directly for stochastic expansion of a Gaussian process. However, the drawback of using KL expansion is that the values of true variance are underpredicted [95]. Angulo and Ruiz-Medina [96] addressed an inverse problem wherein an input random field is derived from the observation of an output random field using the orthogonal expansion of second-order random fields in terms of a wavelet basis. Le Maitre et al. [97] constructed an uncertainty quantification scheme based on Polynomial Chaos (PC) representations, in which a Haar or a Legendre basis was used for the orthogonal projection of uncertain data and solution variables. Kamiński [98] showed a stochastic perturbation approach to the wavelet based analysis. Later, Spanos et al. [99] estimated the power spectrum of non-stationary stochastic processes using dyadic, generalized, and filtered harmonic wavelets. Andreev [100], investigated the numerical aspects of the stochastic Galerkin method when applied to linear stochastic PDEs. A discretization procedure was developed based on a spectral expansion of the solution into orthogonal polynomials induced by the KL expansion. The spatial variable was discretized using the piecewise linear and quadratic spline wavelet-Galerkin bases which lead to well-conditioned system matrices.

It can be concluded that WGM has found widespread application in many engineering problems. Several researchers have proposed novel methods to treat wavelets at the boundaries. When WGM is used for geometry with non-uniform boundary or with non-homogeneous boundary conditions, the implementation may become cumbersome and rigorous [22]. Computational effort also increases when wavelets, which have no explicit expression, are used in the analysis because a separate algorithm is needed for the evaluation of integrals of products of wavelet basis functions, with or without derivatives, known as connection coefficients; which will be discussed next.

2.2.1 Connection coefficients

When wavelets are used in the numerical analysis, a scenario that is encountered is the evaluation of connection coefficients, which are integrals of products of wavelet basis

functions, with or without derivatives [101]. When there is no explicit expression for the scaling and wavelet functions (as in the case of Daubechies wavelet), then accurate evaluation of the connection coefficients becomes a priority. One of the first papers on this was by Latto et al. [102], who developed the procedure for the evaluation of these integrals on $(-\infty, \infty)$. This method uses the scaling relation, normalization condition and moment conditions of the wavelets. Beylkin [103] found exact and explicit representations for basic operators like derivatives, Hilbert transform, shifts, etc. in orthonormal bases of compactly supported wavelets.

However, in order to deal with bounded intervals, Romine and Peyton [101] and Lu et al. [45] provided two different methods. According to Romine and Peyton [101], the method developed by Latto et al. [102] does not provide the correct inner product near the end points of a bounded interval, making the implementation of boundary conditions difficult. Therefore, a procedure for calculating the correct inner product was suggested wherein, the connection coefficients obtained by Latto et al. [102] were modified at the boundaries. On the other hand, Lu et al. [45] modified the interval and used the connection coefficients as obtained by Latto et al. [102] directly by considering a fictitious boundary approach.

Several papers have been published [104–107] involving the development of algorithms for the exact evaluations of connection coefficients on a bounded interval. Chen et al. [108], presented a method to calculate connection coefficients at different scales (multiscale connection coefficients) for stiffness matrices and load vectors. Based on it, an algorithm of multiscale lifting computation was developed and its validity and effectiveness via multiscale lifting scheme were demonstrated via numerical examples. Jones et al. [109], presented an algorithm for the computation of triple product integrals involving Daubechies scaling functions. When WGM was used to solve differential equations involving non-linearity or parameters with field variable dependence, then triple product integrals were encountered. An alternative way to compute the connection coefficients was suggested more recently by Bulut [110]. The algorithm relies on the scaling and translation relation of the functions; whereas the existing algorithms involve scaling relation, normalization condition and moment conditions.

It can be concluded that when there is no explicit expression for the scaling and wavelet functions (as in the case of Daubechies wavelet), then accurate evaluation of the connection coefficients becomes a priority. Thus, the evaluation of connection coefficients further adds to the computational effort. However, the computational effort can be reduced if wavelets that have an explicit expression are used in the numerical analysis. This way, numerical

integration techniques such as Gauss quadrature method can be used for approximating the integrals [68, 111]. In addition, few researchers [112–114] have also noted that derivation of connection coefficients can only be obtained for integration in global coordinates and it tends to fail when the integrand involves a variant Jacobian.

Besides, the development of numerical methods based on WGM, widespread research has also gone into the development of WFEM, which will be reviewed in detail, in the next section.

2.3 Wavelet finite element method

Over the years, several researchers have worked on the development of WFEM elements and their application to structural problems. WFEM is one such numerical technique in which instead of using the traditional polynomial interpolation, scaling and wavelet functions of wavelets are used to form the shape functions over the elements. Different wavelet scaling and wavelet functions (B-spline, Trigonometric, Hermitian and Daubechies, etc.) have been used to form the FEM shape functions, some of which have been discussed here.

2.3.1 Daubechies WFEM

One of the first works that employed Daubechies wavelet basis functions to construct a class of finite elements was by Ko et al. [115]. The constructed elements could be used to represent a class of irregular domains in higher dimensions via tensor products. Youhe et al. [116], proposed a method for calculating higher order differentials of Daubechies scaling functions and applied it to the numerical analysis of boundary-value problems with order higher than 2, eventually demonstrating on beam bending and plate structures. A weak form formulation was developed by Ho et al. [117], wherein a jump function approach for dealing with discontinuous derivatives was suggested. In this approach additional shape functions were introduced in the sub-regions where discontinuities occurred. Daubechies wavelet based Euler-beam element, thin plate and Mindlin Reissner plate element were constructed in a series of papers by Ma et al. [118], Chen et al. [119], Martin and Vampa [120] and Diaz et al. [121].

Daubechies wavelet was also used for the formulation of wavelet based spectral finite element (WSFE). WSFE was developed by Mitra and Gopalakrishnan [122] for studying elastic wave propagation in 1D connected waveguides. The advantages of the proposed

method over FFT (fast Fourier transform)-based spectral element methods (SEM) were highlighted. Longitudinal and flexural wave propagation in a rod, beam and frame structures were studied; along with impact force identification. It was also used to extract the wave characteristics (spectrum and dispersion relation for these waveguides) in [123]. Studies of wave propagation in higher order composite beams [124], isotropic plates [125], damage detection in a composite beam with embedded de-lamination [126] and more recently, 2D and 3D anisotropic and non-homogeneous structures [127] were carried out using WSFE.

2.3.2 Trignometric WFEM

Trigonometric wavelets have also found their place in the construction of WFEM. Trigonometric wavelets have approximating capabilities of a trigonometric function along with desirable features of wavelets. Moreover, the Hermite interpolation characteristic of the trigonometric wavelet helps in dealing with boundary conditions. One of the first papers on this was by Quak [128]. Later, He and Ren formulated Trigonometric WFEM for beams in [129] and for thin elastic plates in [130]. One may refer to the papers by Shan and Du [131] and Gao and Jiang [132] for more information on the application of Trigonometric wavelets for elliptical boundary value problems and Fredholm integral equations respectively.

2.3.3 Hermitian WFEM

Hermite cubic splines were also used to construct wavelets on the interval [0, 1] by Jia and Liu [133]. Hermite cubic spline wavelets on the interval (HCSWI) were used for the analysis of shafts [134] and bending of thin plates [135]. Xue et al. [136] constructed 2D Hermitian plane wavelet element and applied it in wave propagation and load identification in rod and Timoshenko beam problems. Moreover, Hermitian Mindlin plate wavelet element was proposed by Xue et al. in [137]. However, a major drawback of this approach is that HCSWI scaling functions and wavelets need truncation at the boundaries, except for the homogeneous boundary conditions [22]. Hence, Xue et al. [138] suggested a modified Hermitian wavelet finite element. Due to the restrictions at the boundaries, existing Hermite interpolation wavelet base do not have a transformation matrix, but with the modified method a transformation can be obtained and modified Hermitian scaling function can be used to interpolate the field functions in wavelet finite element which otherwise, would not have been possible.

Hermite WFEM based on second generation cubic Hermite multi-wavelets was also proposed for damage detection via adaptive-scaling in frame structures using beam type finite element [139], for spatially and dynamically varying structural modelling scales [140] and for thin plates [141]. The traditional (first generation) wavelets are the dyadic translates and dilates of a single function called the mother wavelet. However, second generation wavelets (SGW) are not necessarily translates and dilates of each other but do possess all the desirable properties of first generation wavelets [142]. They can be custom designed depending on application. Traditional wavelets cannot be constructed on complicated, irregularly spaced meshes as they are the dyadic translates and dilates of a single function on a regularly spaced grid over a theoretically infinite or periodic domain. Hence, to deal with the deficiencies of the traditional wavelets, SGW are needed. SGW were used for solving elliptic partial differential equations (PDE's) over irregularly spaced meshes on bounded domains by D'Heedene et al. [143]. Furthermore, Wang et al. [144] proposed SGW based finite element method for solving PDEs with high gradients and singularity.

In addition to the class of wavelets mentioned so far, scale-orthogonal wavelets from general finite element interpolation functions were presented in the papers by Amaratunga and Sudarshan [145] and Sudarshan et al. [146]. These wavelets, unlike classical hierarchical bases, are scale-orthogonal with respect to a given inner-product which results in block diagonal stiffness matrices and computation of solution in an efficient manner.

2.3.4 B-spline WFEM

One of the earliest papers which discusses about employing the spline wavelets expansions as the shape function for finite element analysis with a fixed mesh was by Chen and Wu [112]. It was proposed for vibration analysis of frame structures and later extended to membrane vibration analysis [113]. Han et al. [147], adopted the B-spline wavelet scaling functions for the construction of the element displacement interpolation functions. The detailed formulation of typical spline wavelet elements such as plane beam element, in-plane triangular element, in-plane rectangular element, tetrahedral solid element, and hexahedral solid element was presented. In addition, spline wavelet formulation for thin plate bending was also developed [148].

The theory of spline wavelets for whole square integrable real space $L^2(\mathbb{R})$ was developed in papers by Chui and Wang [149–151]. Spline wavelets are semi-orthogonal. These wavelets retain inter-scale orthogonality and there is no necessity for the basis functions to be orthogonal to its translates within the same resolution level. As a result,

this allows for symmetry and antisymmetry and for deriving explicit formulae for the spline wavelets. If the spline wavelets defined on $L^2(\mathbb{R})$ are used as interpolating functions, it would lead to numerical instability [46]. Moreover, it is difficult to apply boundary conditions explicitly when these bases are used for solving boundary value problem [44, 45]. Therefore, to incorporate boundary conditions, spline wavelet bases were constructed for the bounded interval [0, 1] which came to be known as BSWI [27]. The algorithm for fast decomposition and reconstruction of BSWI was given by Quak and Weyrich [152] and BSWI scaling and wavelet functions were used by Goswami et al. [37] for solving first kind integral equations. The construction of BSWI over [0, 1] is predominantly based on classical spline theory. The advantage of spline approach is that it readily adapts to the case of the bounded interval [0, 1] by introducing multiple knots at the endpoints. Therefore, no truncation is needed when the function on $L^2(\mathbb{R})$ is restricted to [0, 1]. With suitable adaptation at the endpoints, most of the concepts of the B-spline MRA of $L^2(\mathbb{R})$ can be carried over to [0, 1] [27, 37].

B-splines used in BSWI are the basis functions for the splines, which are constructed by taking piecewise polynomial segments and joining these segments together at points known as knots. For a given knot sequence that is used in the construction of B-splines, if there are no multiple knots in the sequence, the smoothness of the curve remains same at all the knots. However, if multiple knots exist in the knot sequence, the smoothness decreases at the points with multiple knots where knot coalescence takes place, and elsewhere it remains unaffected. During the construction of BSWI a certain order of overall smoothness is obtained. The continuity of B-splines depends on its order in such a way that B-splines with order m are in C_{m-2} continuity [111]. The dependency of the knot sequence on order m and resolution j used in BSWI were shown in the papers by [37, 111], wherein $\{\xi_k^j\}_{k=-m+1}^{2^j+m-1}$ is a knot sequence with ξ being the local co-ordinate used for mapping the domain $[a, b]$ onto [0, 1]. The local co-ordinate ξ can be defined as $\xi = (x-a)/(b-a)$. The knot sequence on the interval [0, 1] is given by [27],

$$\{\xi_k^j\} = \begin{cases} 0, & -m+1 \leq k < 1 \\ 2^{-j}k, & 1 \leq k < 2^j \\ 1, & 2^j \leq k \leq 2^j + m - 1 \end{cases} \tag{2.14}$$

The knot sequence defined in 2.14 can be used to obtain the explicit expression for the basis functions in subspace V_j for B-splines of order m and scale $j > 0$ given by the

recursive relation [27, 153, 154] as,

$$B^j_{m,k}(\xi) = \frac{\xi - \xi^j_k}{\xi^j_{k+m-1} - \xi^j_k} B^j_{m-1,k}(\xi) + \frac{\xi^j_{k+m} - \xi}{\xi^j_{k+m} - \xi^j_{k+1}} B^j_{m-1,k+1}(\xi) \tag{2.15}$$

such that,

$$B^j_{1,k}(\xi) = \begin{cases} 1, & k \leq \xi \leq k+1 \\ 0, & \text{otherwise} \end{cases} \tag{2.16}$$

$$\text{supp} B^j_{m,k}(\xi) = [\xi^j_k, \xi^j_{k+m}] \tag{2.17}$$

The basis functions $B^j_{m,k}(\xi)$ contain multiple knots at 0 and 1 and correspond to cardinal B-splines at m^{th} order and j scale from the inner knots. The cardinal B-splines are used as the inner scaling functions $\phi^j_{m,k}(\xi)$ for j scale, m^{th} order BSWI. Chui and Quak [27] categorized BSWI scaling functions as the boundary scaling functions that exist at boundary points 0 and 1 on the domain and inner scaling functions that are just dilation and translations of cardinal B-spline. The corresponding wavelets can be constructed by utilizing the scaling functions eventually. In the scenario when $2^j < 2m - 1$ no inner wavelets are inherited from the MRA of $L^2(\mathbb{R})$ and so, the effects of endpoints 0 and 1 cannot be separated. However, if $2^j \geq 2m - 1$, there exists at least one inner wavelet whose support lies completely in [0, 1]. With suitable adaptation at the endpoints, MRA generated by the B-splines in BSWI on $L^2(\mathbb{R})$ is carried over to [0, 1] elegantly without loss of accuracy. The explicit expressions for scaling and wavelet functions for j scale, m^{th} order BSWI are given as [111],

$$\phi^j_{m,k}(\xi) = \begin{cases} \phi^l_{m,k}(2^{j-l}\xi), & k = -m+1, ..., -1 \\ (0 \quad \text{boundary} \quad \text{scaling} \quad \text{function}) \\ \phi^l_{m,2^j-m-k}(1 - 2^{j-l}\xi), & k = 2^j - m + 1, ..., 2^j - 1 \\ (1 \quad \text{boundary} \quad \text{scaling} \quad \text{function}) \\ \phi^l_{m,0}(2^{j-l}\xi - 2^{-l}k), & k = 0, ..., 2^j - m \\ (\text{inner} \quad \text{scaling} \quad \text{function}) \end{cases} \tag{2.18}$$

$$\psi^j_{m,k}(\xi) = \begin{cases} \psi^l_{m,k}(2^{j-l}\xi), \quad k = -m+1, ..., -1 \\ (0 \quad \text{boundary} \quad \text{wavelet} \quad \text{function}) \\ \psi^l_{m,2^j-2m-k+1}(1-2^{j-l}\xi), \quad k = 2^j-2m+2, ..., 2^j-m \\ (1 \quad \text{boundary} \quad \text{wavelet} \quad \text{function}) \\ \psi^l_{m,0}(2^{j-l}\xi - 2^{-l}k), \quad k = 0, ..., 2^j-2m+1 \\ (\text{inner} \quad \text{wavelet} \quad \text{function}) \end{cases} \tag{2.19}$$

where,

$$\text{supp } \psi^j_{m,k}(\xi) = \begin{cases} [0, \ (2m-1+k)2^{-j}] \\ (0 \quad \text{boundary} \quad \text{wavelets}) \\ [k2^{-j}, \ 1] \\ (1 \quad \text{boundary} \quad \text{wavelets}) \\ [k2^{-j}, \ (2m-1+k)2^{-j}] \\ (\text{inner} \quad \text{wavelets}) \end{cases} \tag{2.20}$$

If j_0 is the scale for which $2^j \geq 2m-1$ is satisfied, then for each $j > j_0$ the corresponding wavelets can be obtained by substituting $l = 0$ in the Equations 2.18-2.20.

Xiang et al. [111], constructed 1D C_0 and C_1 type BSWI elements for structural analysis. To solve plane elastomechanics and moderately thick plate problems, a class of C_0 type plate elements were also constructed [114] based on 2D tensor product of BSWI. Several papers have been published which have shown the construction of different BSWI based elements. Wavelet based truncated conical shell element was developed by Xiang et al. [155] using compactly supported semi-orthogonal BSWI to solve axisymmetric problems. In their papers, Xiang et al. [156] also constructed BSWI thin plate element and BSWI flat shell element by the assembly of BSWI plane elastomechanics and Mindlin plate elements [157]. Further, it has been shown in the preceding papers that, due to the MRA and two scale relation property of wavelets, (1 or 2 BSWI elements) are sufficient to discretize the physical domain, control (increase or decrease) the nodal refinement without changing the order and solve the problem accurately.

Chen et al. [158] presented a wavelet based multiscale element using BSWI for the adaptive finite element analysis by constructing 2D C_0 type multiscale BSWI elements by

means of lifting scheme. Zhong and Xiang [159], formulated BSWI elements to study the stability of plates and shells and the static displacement of 3D elastic problems. Xu et al. [160] constructed BSWI transition elements with 7 and 10 nodes for multi-scale analysis of foundations. Meanwhile, BSWI have also been used in the formulation of curved beam element [161], construction of Rayleigh Euler rotating beam element to analyze rotor bearing system [162] and curved shell elements (cylindrical shells, doubly-curved shallow shells and hyperbolic paraboloidal shells) [163]. Shen et al. [164] suggested an adaptive strategy by moving the nodes, which was based on the principle that number of nodes in certain region is proportional to the error in that region. Analysis of buckling of plates based on Reissner-Mindlin theory was carried out by Yang et al. [165] using a BSWI Mindlin element. Geng et al. [166] proposed a high frequency vibration analysis of thin plate based on wavelet multi-elements method using C_1 type B-spline Kirchhoff plate (C1BKP) element. Oke and Khulief [167] studied the vibration analysis of composite pipes with internal wall defects due to erosion-induced surface degradation. Moreover, static, free vibration and buckling analysis of functionally graded beam (based on TBT) and functionally graded plates was also done by Zuo et al. in their papers [168, 169].

A multivariable wavelet finite element method (MWFEM) for 1D structural problem was proposed by Zhang et al. [170]. It is based on a multivariable generalized variational principle wherein, generalized displacement, strain and stress are considered as independent variables and interpolated separately. MWFEM is obtained when wavelets are used in the multivariable finite element method framework. One may refer to the series of papers by Shen et al. [171–174] for more information on the development of multivariable finite elements for beam, plate and shell. Based on multivariable generalized variational principle, multivariable BSWI-based elements for thin plates [175], for Reissner-Mindlin plates [176], for hyperboloid shell and open cylindrical shell [177], for flexible skew thin plate analysis [178] and for shallow hyperbolic shell [179] were constructed. Furthermore, Han et al. [180] formulated MWFEM to resolve the bending problems of thick plates based on the Hellinger Reissner generalized variational principle wherein, interpolating wavelets were used to represent the generalized field functions of thick plates.

In other study, the construction of a wavelet element method (WEM) for 1D, 2D and 3D cases was given by Canuto et al. [181, 182]. In WEM, biorthogonal wavelet systems on a general bounded domain were obtained by combining SEM's philosophy with biorthogonal wavelet system. In this, a general domain is split into sub-domains. Each sub-domain is mapped onto a single reference hypercube. Then, tensor product of scaling functions and wavelet functions is defined on the unit interval, to be used on the reference domain.

BSWI based WFEM has also been popular in the structural crack identification [183–186] analysis of stress intensity factors in a cracked plane plate [187] and analysis of laminated plates and shells [188, 189]. Moreover, BSWI elements were used for elastic wave propagation in 1D structures [190] in which cracked axial rod and Timoshenko beam BSWI elements were constructed. It was also used for elastic wave propagation in intact membranes and notched membranes [191] and for the analysis of elastic wave propagation in arches [192] to understand wave motion in curved structures. Xiang et al. [187] using BSWI WFEM, proposed a new approach for the analysis of stress intensity factors (SIFs) for cracked plane plate. BSWI plane elastomechanical plate element was used to develop a numerical method to calculate the elastic band structures of 2D phononic crystals (2DPCs), composed of square lattices of solid cuboids in a solid matrix [193]. Spline wavelet-based FEM along with MCS was also used for bending analysis of plates by Han et al. [194] when parameters are random variables. Further, Zhang et al. [195] used BSWI based finite element method by combining with MCS for structural analysis.

From the review of literature on WGM and WFEM, it can be concluded that WFEM is an accurate and an efficient methodology for solving boundary value problems. Further, among all the different wavelets, BSWI have been popular and widely used because of its underlying properties which make it more efficient and user friendly. It can be also be concluded that the MRA and two scale relation property of wavelets facilitates fast switching of resolution levels and functional bases. As a result, the physical problem can be discretized using less number of WFEM elements (1 or 2 elements) and by varying the scale/resolution, the nodal refinement within an element can be controlled without changing the order. From an industrial application point of view, the usage of fewer elements vastly reduces the burden of mesh assembly and also the programming effort needed in the pre-processing stage of the analysis. Further, controlling the nodal discretization without changing the order within an element can also ease the computational effort needed in certain cases as opposed to conventional FEM. In addition, in the stochastic framework, due to the high mesh dependency of FEM, the mapping of the random field discretization to response discretization becomes cumbersome and wavelets could provide an alternative via alleviating the mesh dependency to an extent.

The existing literature does not discuss about mathematical modelling of beams and plate elements incorporating von Kármán nonlinear strains or any other geometric nonlinearity using BSWI WFEM. Further, it is found that works on random field modelling using BSWI WFEM, when the formulation is done in a stochastic framework do not exist. Even though BSWI WFEM has been used with MCS for structural analysis

(process involves random variables and not random fields); MCS makes the whole process computationally expensive and is not a viable option. Moreover, it is noted that no guidelines are provided for the numerical integration in the framework of BSWI WFEM. On account of the preceding discussion and extensive literature study that has been done, the objective and scope of the current thesis is formulated and presented in the forthcoming sections.

2.4 Objective of the work

The main research objective of the current thesis is the development of a stochastic WFEM for solving problems in structural mechanics wherein material properties are modelled as a random field.

2.5 Scope of the thesis

The scope of the work encompasses;

- Proposing a numerical integration scheme based on Gauss quadrature and guidelines for the same to be used for BSWI WFEM.
- A stochastic BSWI WFEM formulation for problems in elasto-statics in which random field discretization is done using wavelet based shape function method.
  - Problems involving C_0 continuity elements (1D bar, 2D plane stress/strain).
  - Problems involving beam elements based on Euler-Bernoulli and Timoshenko beam theories.
- A deterministic BSWI FEM formulation for beam analysis by incorporating von Kármán nonlinear strains.
- A stochastic BSWI WFEM formulation for beam analysis by incorporating von Kármán nonlinear strains in which random field discretization is done using wavelet based shape function method.

2.6 Conclusion

In the current chapter, an extensive literature review has been done; based on which, the main research objective and scope of the work has been established. In the next chapter, a methodology is proposed for the evaluation of integrals in BSWI WFEM using Gauss quadrature.

Chapter 3

Numerical integration for BSWI WFEM using a background cell approach

The current chapter discusses about evaluating the integrals involving BSWI, in wavelet finite element formulations, using Gauss quadrature. It is essential to be noted that the existing literature does not discuss about the methodology used for the implementation of Gauss quadrature and its effect on the accuracy of results in the context of BSWI WFEM. Moreover, to the best of author's knowledge, use of background cell based integration scheme for BSWI WFEM has not been reported in the literature. Hence, it demands an in-depth discussion on the quantitative aspects of numerical integration for BSWI WFEM for different class of problems, which does not exist in the literature. Therefore, a numerical integration scheme is proposed wherein, background cells are placed over each BSWI element and Gauss quadrature rule is defined for each of these cells. The nodal discretization used for BSWI WFEM element is independent to the selection of number of background cells used for the integration process. During the analysis, background cells of various lengths are used for evaluating the integrals for various combination of order and resolution of BSWI scaling functions. Numerical examples based on 1D and 2D plane elasto-statics are solved. Problems on beams based on EBT and TBT under different boundary conditions are also examined. Furthermore, the condition number and sparseness of the formulated stiffness matrices are analyzed.

3.1 Formulation of 1D and 2D BSWI elements

The equilibrium equations and boundary conditions for small displacements in linear elastic solids are,

$$\boldsymbol{\nabla} \cdot \boldsymbol{\sigma} + b = 0 \ \text{ in } \ \Omega \tag{3.1}$$

$$\boldsymbol{\sigma} \cdot \boldsymbol{n} = \bar{\boldsymbol{t}} \ \text{ on } \ \Gamma_t \ \text{ (natural boundary conditions)} \tag{3.2}$$

$$\boldsymbol{u} = \overline{\boldsymbol{u}} \ \text{ on } \ \Gamma_u \ \text{ (essential boundary conditions)} \tag{3.3}$$

Here, $\boldsymbol{\sigma} = \boldsymbol{D\epsilon}$ is the stress vector, $\boldsymbol{D}$ is the material property matrix, $\boldsymbol{\epsilon} = \boldsymbol{\nabla}_s \boldsymbol{u}$ is the strain vector, $\boldsymbol{u}$ is the displacement vector, $\boldsymbol{b}$ is the body force vector, $\bar{\boldsymbol{t}}$ and $\overline{\boldsymbol{u}}$ are the vectors of prescribed surface tractions and displacements respectively, $\boldsymbol{n}$ is a unit normal to the domain Ω, Γ_t and Γ_u are the portions of boundary Γ, where tractions and displacements are prescribed respectively. $\boldsymbol{\nabla} = \{\frac{\partial}{\partial x_1}, \frac{\partial}{\partial x_2}, ...\}$ is the vector of gradient operators and $\boldsymbol{\nabla}_s \boldsymbol{u}$ is the symmetric part of $\boldsymbol{\nabla u}$.

3.1.1 Bar and beam elements

In BSWI WFEM, the problem domain Ω is divided into sub-domains $\Omega_i\{i = 1, 2, 3...\}$. Each Ω_i is mapped onto element solving domain $\Omega_e = \xi, \xi \in [0, 1]$, where instead of using the traditional polynomial interpolation, scaling or scaling and wavelet functions of BSWI are used to form the shape functions over the elements Ω_e. Here, ξ is the local co-ordinate used for solving 1D BSWI on [0, 1] along x axis as shown in Figure 3.1.

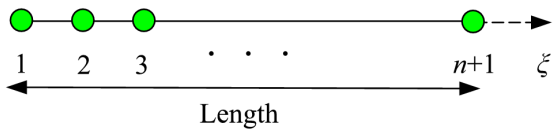

Figure 3.1: Distribution of nodes in 1D BSWI WFEM element

3.1.1.1 1D BSWI WFEM bar element

The generalized functional of potential energy for a bar element with Young's modulus E is:

$$\Pi = \int_{x_a}^{x_b} \frac{1}{2} EA \left(\frac{du_0}{dx} \right)^2 dx - \int_{x_a}^{x_b} f(x) u_0 dx - \sum_{i=1}^{n_d} Q_i u_0(x_i) \tag{3.4}$$

Here, $f(x)$ is the distributed load, Q_i are the generalized lumped nodal forces, n_d is the total number of nodes per BSWI wavelet finite bar element, and u_0 is the axial displacement. The formulation of a BSWI WFEM bar element was given by Xiang et al. [111]. One BSWI bar element with C_0 continuity is divided into $n = 2^j + m - 2$ segments and $n + 1$ nodes as shown in Figure 3.2, where m, j are the order and resolution of BSWI scaling functions respectively.

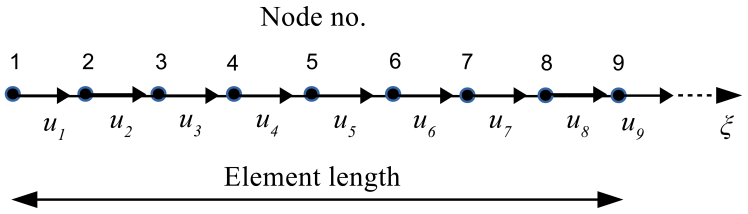

Figure 3.2: Distribution of nodes and DOF for one bar element with C_0 continuity using $m = 2, j = 3$

The unknown axial displacement field of a bar element in the element solving domain ξ is approximated in terms of wavelet scaling functions as [111],

$$u_0(\xi) = \sum_{k=-m+1}^{2^j-1} a_{m,k}^j \phi_{m,k}^j(\xi) = \boldsymbol{\varphi} \boldsymbol{a}^{\boldsymbol{e}} \tag{3.5}$$

where, $\boldsymbol{\varphi} = \left\{ \phi_{m,-m+1}^j(\xi) ..... \phi_{m,2^j-1}^j(\xi) \right\}$ is row vector of BSWI scaling functions, $\boldsymbol{a}^{\boldsymbol{e}} = \{a_1, a_2 ..... a_{n+1}\}^T$ is column vector of wavelet coefficients that needs to be determined.
The unknown axial displacement field function is expressed in terms of C_0 element type transformation matrix and physical degrees of freedom (DOF) as,

$$u_0(\xi) = \boldsymbol{\varphi} \left(\boldsymbol{R}^{\boldsymbol{e}} \right)^{-1} \boldsymbol{u}^{\boldsymbol{e}} = \boldsymbol{\varphi} \boldsymbol{T}^{\boldsymbol{e}} \boldsymbol{u}^{\boldsymbol{e}} = \boldsymbol{N}^{\boldsymbol{e}} \boldsymbol{u}^{\boldsymbol{e}} \tag{3.6}$$

where,

$$\left.\begin{aligned} \boldsymbol{u^e} &= \boldsymbol{R^e a^e} \\ \boldsymbol{R^e} &= \left\{\boldsymbol{\varphi^T}(\xi_1)\ \boldsymbol{\varphi^T}(\xi_2)....\boldsymbol{\varphi^T}(\xi_{n+1})\right\}^T \\ \boldsymbol{u^e} &= \left\{u_1\ u_2.....u_{n+1}\right\}^T \\ \boldsymbol{T^e} &= \left(\boldsymbol{R^e}\right)^{-1} \\ \boldsymbol{N^e} &= \boldsymbol{\varphi T^e} \end{aligned}\right\} \tag{3.7}$$

Substituting Equation 3.6 into the weak form and invoking the stationary condition for variation of admissible displacements, element solving equations are obtained as,

$$\boldsymbol{K^e u^e} = \boldsymbol{F^e} \tag{3.8}$$

where,

$$\left.\begin{aligned} \boldsymbol{K^e} &= \frac{EA}{l_{ex}} \int_0^1 \left(\boldsymbol{T^e}\right)^T \left(\frac{d\boldsymbol{\varphi}}{d\xi}\right)^T \left(\frac{d\boldsymbol{\varphi}}{d\xi}\right) \left(\boldsymbol{T^e}\right) d\xi \\ \boldsymbol{F^e} &= l_{ex} \int_0^1 f(\xi) \left(\boldsymbol{T^e}\right)^T \left(\boldsymbol{\varphi}\right)^T d\xi + \sum_{i=1}^{n_d} Q_i^e \left(\boldsymbol{T^e}\right)^T \left(\boldsymbol{\varphi}\right)^T (\xi_i) \end{aligned}\right\} \tag{3.9}$$

3.1.1.2 1D BSWI WFEM Euler-Bernoulli beam element

The generalized functional of potential energy for an Euler-Bernoulli beam element is:

$$\begin{aligned} \Pi = \int_{x_a}^{x_b} \frac{1}{2} EI \left(-\frac{d^2 w_0}{dx^2}\right)^2 dx - \int_{x_a}^{x_b} q(x) w_0 dx - \sum_{i=1}^{n_e} Q_i^e w_0 \left(x_i\right) \\ - \sum_{k=1,n_e} M_k^e \frac{dw_0}{dx} \left(x_k\right) \end{aligned} \tag{3.10}$$

Here, w_0 is the transverse deflection, I is the second moment of area, $q(x)$ is the distributed transverse load per unit length, Q_i are the generalized lumped transverse nodal forces, M_k are the bending moments and n_e is the total number of nodes per BSWI wavelet finite Euler-Bernoulli beam element. The formulation of a BSWI WFEM Euler-Bernoulli beam element can be found in the paper by Xiang et al. [111]. One BSWI EBT beam element with C_1 continuity is divided into $n = 2^j + m - 4$ segments and $n+1$ nodes with end nodes having both transverse and rotational DOF and internal nodes having only transverse DOF as shown in Figure 3.3, where m, j are the order and resolution of BSWI scaling functions respectively.

The unknown transverse displacement field function of Euler-Bernoulli beam element is

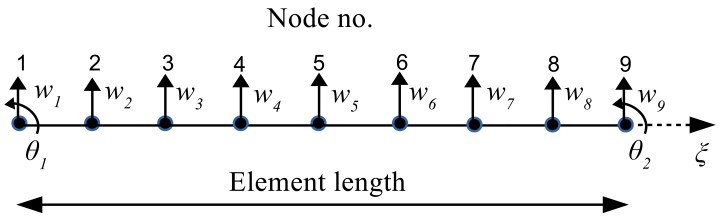

Figure 3.3: Distribution of nodes and DOF for one BSWI EBT based beam element with C_1 continuity using $m = 4, j = 3$

approximated in terms of wavelet scaling functions as,

$$w_0(\xi) = \sum_{k=-m+1}^{2^j-1} b^j_{m,k}\phi^j_{m,k}(\xi) = \boldsymbol{\varphi}\boldsymbol{b^e} \tag{3.11}$$

Here, $\boldsymbol{\varphi} = \left\{\phi^j_{m,-m+1}(\xi).....\phi^j_{m,2^j-1}(\xi)\right\}$ is row vector of BSWI scaling functions, $\boldsymbol{b^e} = \{b_1, b_2.....b_{n+1}\}^T$ is column vector of wavelet coefficients that needs to be determined. The unknown transverse displacement field function can be expressed in terms of C_1 element type transformation matrix and physical DOF as,

$$w_0(\xi) = \boldsymbol{\varphi}\left(\boldsymbol{R^e}\right)^{-1}\boldsymbol{w^e} = \boldsymbol{\varphi}\boldsymbol{T^e}\boldsymbol{w^e} = \boldsymbol{N^e}\boldsymbol{w^e} \tag{3.12}$$

where,

$$\left.\begin{aligned} \boldsymbol{w^e} &= \{w_1, \theta_1, w_2.....w_{n+1}, \theta_{n+1}\}^T \\ \theta = \frac{1}{l_e}\left(\frac{dw_0\left(\xi_1\right)}{d\xi}\right), \theta_{n+1} &= \frac{1}{l_e}\left(\frac{dw_0\left(\xi_{n+1}\right)}{d\xi}\right) \\ \boldsymbol{T^e} &= \left(\boldsymbol{R^e}\right)^{-1} \\ \boldsymbol{R^e} = \left\{\boldsymbol{\varphi^T}(\xi_1)\frac{1}{l_e}\left(\frac{d\boldsymbol{\varphi^T}\left(\xi_1\right)}{d\xi}\right)\boldsymbol{\varphi^T}(\xi_2).....\boldsymbol{\varphi^T}(\xi_{n+1})\frac{1}{l_e}\left(\frac{d\boldsymbol{\varphi^T}\left(\xi_{n+1}\right)}{d\xi}\right)\right\}^T & \\ \boldsymbol{N^e} &= \boldsymbol{\varphi}\boldsymbol{T^e} \end{aligned}\right\} \tag{3.13}$$

Upon substituting the displacement field of Equation 3.12 into the weak form and invoking the stationary condition for variation of admissible displacements, the element solving

equations for BSWI WFEM Euler-Bernoulli beam element can be obtained as,

$$\boldsymbol{K^e w^e} = \boldsymbol{F^e} \tag{3.14}$$

where,

$$\left.\begin{aligned} \boldsymbol{K^e} &= \frac{EI}{l_{ex}^3}\int_0^1 (\boldsymbol{T^e})^T \left(\frac{d^2\boldsymbol{\varphi}}{d\xi^2}\right)^T \left(\frac{d^2\boldsymbol{\varphi}}{d\xi^2}\right)(\boldsymbol{T^e})\, d\xi \\ \boldsymbol{F^e} &= l_{ex}\int_0^1 q(\xi)(\boldsymbol{T^e})^T(\boldsymbol{\varphi})^T d\xi - \sum_{i=1}^{n_e} Q_i^e (\boldsymbol{T^e})^T(\boldsymbol{\varphi})^T(\xi_i) - \\ &\qquad \sum_{k=1,n_e} M_k^e (\boldsymbol{T^e})^T(\boldsymbol{\varphi})^T(\xi_i) \end{aligned}\right\} \tag{3.15}$$

3.1.1.3 1D BSWI WFEM Timoshenko beam element

The generalized functional of potential energy for a Timoshenko beam element is:

$$\begin{aligned} \Pi = \int_{x_a}^{x_b} \frac{1}{2} EI \left(-\frac{d\theta_x}{dx}\right)^2 dx + \int_{x_a}^{x_b} \frac{K_s GA}{2}\left(\frac{dw_0}{dx} - \theta_x\right)^2 dx - \\ \int_{x_a}^{x_b} q(x) w_0 dx - \sum_{i=1}^{n_f} Q_i^e w_0(x_i) - \sum_{i=1,n_f} M_i^e \theta_x(x_i) \end{aligned} \tag{3.16}$$

Here, θ_x is the slope; however, it is not equal to θ defined in Equation 3.13 as θ_x is not equal to $\frac{dw_0}{dx}$ in TBT. K_s is the shear correction coefficient, G is the shear modulus and n_f is the total number of nodes per BSWI wavelet finite Timoshenko beam element. Rest of the variables discussed in the context of Euler-Bernoulli beam element are applicable for Timoshenko beam element as well. The formulation of a BSWI WFEM Timoshenko beam element can also be found in the paper by Xiang et al. [111]. One BSWI TBT beam element with C_0 continuity is divided into $n = 2^j + m - 2$ segments and $n + 1$ nodes with each node having both transverse and rotational DOF as shown in Figure 3.4, where m, j are the order and resolution of BSWI scaling functions respectively.

Here, the unknown transverse and rotational displacement field functions are approximated independently in the element solving domain ξ in terms of linear or quadratic wavelet

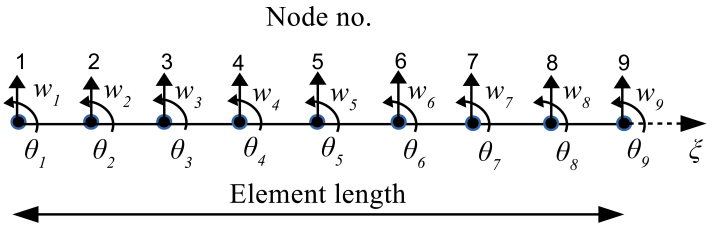

Figure 3.4: Distribution of nodes and DOF for one BSWI TBT based beam element with C_0 continuity using $m = 2, j = 3$

scaling functions as,

$$\left.\begin{aligned} w_0(\xi) &= \sum_{k=-m+1}^{2^j-1} a^j_{m,k}\phi^j_{m,k}(\xi) = \boldsymbol{\varphi a^e} \\ \theta_x(\xi) &= \sum_{k=-m+1}^{2^j-1} b^j_{m,k}\phi^j_{m,k}(\xi) = \boldsymbol{\varphi b^e} \end{aligned}\right\} \tag{3.17}$$

where, $\boldsymbol{\varphi} = \left\{\phi^j_{m,-m+1}(\xi).....\phi^j_{m,2^j-1}(\xi)\right\}$ is row vector of BSWI scaling functions, $\boldsymbol{a^e}, \boldsymbol{b^e}$ are column vector of wavelet coefficients that needs to be determined. The unknown displacement field function is expressed in terms of C_0 element type transformation matrix and physical DOF as,

$$\left.\begin{aligned} w_0(\xi) &= \boldsymbol{\varphi}\left(\boldsymbol{R^e}\right)^{-1}\boldsymbol{w^e} = \boldsymbol{\varphi T^e w^e} = \boldsymbol{N^e w^e} \\ \theta_x(\xi) &= \boldsymbol{\varphi}\left(\boldsymbol{R^e}\right)^{-1}\boldsymbol{\theta^e_x} = \boldsymbol{\varphi T^e \theta^e_x} = \boldsymbol{N^e \theta^e_x} \end{aligned}\right\} \tag{3.18}$$

where,

$$\left.\begin{aligned} \boldsymbol{w^e} = \boldsymbol{R^e a^e},\ \boldsymbol{\theta^e_x} &= \boldsymbol{R^e b^e} \\ \boldsymbol{R^e} = \left\{\boldsymbol{\varphi^T}(\xi_1)\ \boldsymbol{\varphi^T}(\xi_2)....\boldsymbol{\varphi^T}(\xi_{n+1})\right\}^T & \\ \boldsymbol{T^e} = \left(\boldsymbol{R^e}\right)^{-1},\ \boldsymbol{N^e} &= \boldsymbol{\varphi T^e} \end{aligned}\right\} \tag{3.19}$$

Upon substituting Equation 3.18 into the weak form and invoking the stationary condition, the element solving equations for BSWI WFEM Timoshenko beam element can be obtained as,

$$\boldsymbol{K^e W^e} = \boldsymbol{F^e} \tag{3.20}$$

where,

$$\left.\begin{aligned} \boldsymbol{K^e} &= \begin{bmatrix} \boldsymbol{K_1^e} \boldsymbol{K_2^e} \\ \boldsymbol{K_3^e} \boldsymbol{K_4^e} \end{bmatrix} \\ \boldsymbol{W^e} = \begin{Bmatrix} \boldsymbol{w^e} \\ \boldsymbol{\theta_T^e} \end{Bmatrix}, \boldsymbol{F^e} &= \begin{Bmatrix} \boldsymbol{F_d^e} \\ 0 \end{Bmatrix} + \begin{Bmatrix} \boldsymbol{F_l^e} \\ \boldsymbol{M_l^e} \end{Bmatrix} \end{aligned}\right\} \tag{3.21}$$

such that,

$$\left.\begin{aligned} \boldsymbol{K_1^e} &= \frac{K_s G A}{l_{ex}} \left(\boldsymbol{T^e}\right)^T \left(\int_0^1 \left(\frac{d\boldsymbol{\varphi}}{d\xi} \right)^T \left(\frac{d\boldsymbol{\varphi}}{d\xi} \right) d\xi \right) \left(\boldsymbol{T^e}\right) \\ \boldsymbol{K_2^e} &= -K_s G A \left(\boldsymbol{T^e}\right)^T \left(\int_0^1 \left(\frac{d\boldsymbol{\varphi}}{d\xi} \right)^T (\boldsymbol{\varphi}) \, d\xi \right) \left(\boldsymbol{T^e}\right) \\ \boldsymbol{K_3^e} &= \left(\boldsymbol{K_2^e}\right)^T \\ \boldsymbol{K_4^e} &= \frac{EI}{l_{ex}} \left(\boldsymbol{T^e}\right)^T \left(\int_0^1 \left(\frac{d\boldsymbol{\varphi}}{d\xi} \right)^T \left(\frac{d\boldsymbol{\varphi}}{d\xi} \right) d\xi \right) \left(\boldsymbol{T^e}\right) + \\ & \quad K_s G A l_{ex} \left(\boldsymbol{T^e}\right)^T \left(\int_0^1 (\boldsymbol{\varphi})^T (\boldsymbol{\varphi}) \, d\xi \right) \left(\boldsymbol{T^e}\right) \\ \boldsymbol{F_d^e} &= \int_0^1 l_{ex} q\left(\xi\right) \left(\boldsymbol{T^e}\right)^T (\boldsymbol{\varphi})^T \, d\xi \\ \boldsymbol{F_l^e} &= \sum_{i=1}^{n_f} Q_i^e \left(\boldsymbol{T^e}\right)^T (\boldsymbol{\varphi})^T \left(\xi_i\right) \\ \boldsymbol{M_l^e} &= \sum_{i=1,n_f} M_i^e \left(\boldsymbol{T^e}\right)^T (\boldsymbol{\varphi})^T \left(\xi_i\right) \end{aligned}\right\} \tag{3.22}$$

3.1.2 2D BSWI plane stress element

In BSWI WFEM, the problem in 2D domain Ω is divided into sub-domains $\Omega_i (i = 1, 2...)$ where, each Ω_i is then mapped into the standard 2D element solving domain $\Omega_e = \xi, \eta$ such that, $\xi, \eta \in [0, 1]$ as shown in Figure 3.5. Here, ξ, η are the local co-ordinates used for solving 2D BSWI on [0, 1]. For a BSWI scaling function of order m and resolution j , the 2D element solving domain Ω_e is discretized into $(n + 1)^2$ nodes where, $n = 2^j + m - 2$ segments on each side. Instead of using the traditional polynomial interpolation, 2D tensor product of scaling or scaling and wavelet functions of BSWI are used to form the shape functions over the elements Ω_e in 2D domain.

The generalized functional of potential energy for a sub-domain Ω_i in a 2D plane stress

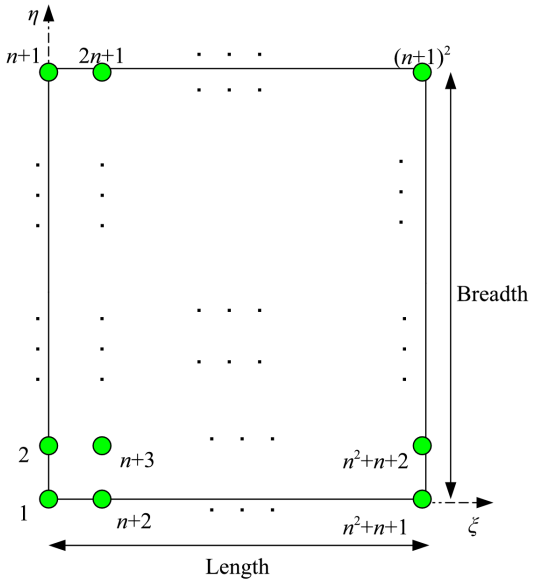

Figure 3.5: Distribution of nodes in 2D plane stress element

problem can be written as,

$$\Pi = \int_{\Omega_i} \frac{1}{2} \boldsymbol{\epsilon}^{\boldsymbol{T}} \boldsymbol{D} \boldsymbol{\epsilon} t dx dy - \int_{\Omega_i} \boldsymbol{u}^{\boldsymbol{T}} \boldsymbol{b} t dx dy - \int_{\Gamma_i} \boldsymbol{u}^{\boldsymbol{T}} \boldsymbol{p} t d\Gamma - \sum_{i=1}^{n_{ep}} \boldsymbol{u}_{\boldsymbol{i}}^{\boldsymbol{T}} \boldsymbol{F}_{\boldsymbol{i}} \tag{3.23}$$

such that, $\boldsymbol{b}$ is the body force column vector, $\boldsymbol{u}$ is the displacement vector, t is the uniform thickness and $\boldsymbol{p}$ is the column vector of surface traction in x and y directions respectively. $\boldsymbol{F_i}$ is column vector of point forces, $\boldsymbol{u_i}$ is the column vector of point displacements at the point of application of forces and n_{ep} is the total number of nodes per 2D BSWI plane elasto-statics element. The formulation of a BSWI WFEM plane elasto-statics element was given by Xiang et al. [114].

The displacement field function in the local co-ordinate system can be approximated as,

$$\left.\begin{aligned} u_0(\xi, \eta) &= \boldsymbol{\varphi} \boldsymbol{c}^{\boldsymbol{e}} \\ v_0(\xi, \eta) &= \boldsymbol{\varphi} \boldsymbol{d}^{\boldsymbol{e}} \end{aligned}\right\} \tag{3.24}$$

where, $\boldsymbol{\varphi}$ is obtained by taking 2D tensor product of BSWI scaling functions in the element

solving domain Ω_e as,

$$\left.\begin{aligned} \boldsymbol{\varphi} &= \boldsymbol{\varphi_1} \otimes \boldsymbol{\varphi_2} \\ \boldsymbol{\varphi_1} &= \left\{\phi^j_{m,-m+1}(\xi).....\phi^j_{m,2^j-1}(\xi)\right\} \\ \boldsymbol{\varphi_2} &= \left\{\phi^j_{m,-m+1}(\eta).....\phi^j_{m,2^j-1}(\eta)\right\} \\ \boldsymbol{c^e} &= \{c_1, c_2.....c_{n+1^2}\}^T \\ \boldsymbol{d^e} &= \{d_1, d_2.....d_{n+1^2}\}^T \end{aligned}\right\} \tag{3.25}$$

Here, $\boldsymbol{\varphi_1}, \boldsymbol{\varphi_2}$ are the rows vectors combined by the scaling functions for order m and resolution j and $\boldsymbol{c^e}, \boldsymbol{d^e}$, are the column vector of wavelet coefficients to be determined. By making appropriate substitutions, the 2D elemental transformation matrix can be obtained as,

$$\left.\begin{aligned} \boldsymbol{u^e} &= \boldsymbol{R^e c^e} \\ \boldsymbol{v^e} &= \boldsymbol{R^e d^e} \\ \boldsymbol{R^e} &= \boldsymbol{T^e_1} \otimes \boldsymbol{T^e_2} \\ \boldsymbol{T^e_1} &= \left\{\boldsymbol{\varphi^T_1}(\xi_1)\ \boldsymbol{\varphi^T_1}(\xi_2)....\boldsymbol{\varphi^T_1}(\xi_{n+1})\right\}^T \\ \boldsymbol{T^e_2} &= \left\{\boldsymbol{\varphi^T_2}(\eta_1)\ \boldsymbol{\varphi^T_2}(\eta_2)....\boldsymbol{\varphi^T_2}(\eta_{n+1})\right\}^T \end{aligned}\right\} \tag{3.26}$$

Upon simplification, the equations for displacement field in the standard element solving domain can be replaced as,

$$\left.\begin{aligned} u_0(\xi,\eta) &= \boldsymbol{\varphi}^T \left(\boldsymbol{R^e}\right)^{-1} \boldsymbol{u^e} = \boldsymbol{N u^e} \\ v_0(\xi,\eta) &= \boldsymbol{\varphi}^T \left(\boldsymbol{R^e}\right)^{-1} \boldsymbol{v^e} = \boldsymbol{N v^e} \end{aligned}\right\} \tag{3.27}$$

By using the principle of minimum potential, the element stiffness matrix and force vector (for a unit thickness) can be obtained as,

$$\boldsymbol{K^e U^e} = \boldsymbol{F^e} \tag{3.28}$$

where,

$$\left.\begin{aligned} \boldsymbol{K^e} &= \begin{bmatrix} \boldsymbol{K_1^e K_2^e} \\ \boldsymbol{K_3^e K_4^e} \end{bmatrix} \\ \boldsymbol{U^e} = \begin{Bmatrix} \boldsymbol{u^e} \\ \boldsymbol{v^e} \end{Bmatrix}, \boldsymbol{F^e} &= \begin{Bmatrix} \boldsymbol{P_a}^e \\ \boldsymbol{P_b}^e \end{Bmatrix} \end{aligned}\right\} \tag{3.29}$$

such that,

$$\left.\begin{aligned} \boldsymbol{P_a}^e &= (\boldsymbol{R}^e)^{-1} \left(\int_S p_x \boldsymbol{\varphi}^T dS + \int_\Omega b_x \boldsymbol{\varphi}^T d\Omega + \sum_{i=1}^{n} (\boldsymbol{R}^e)^{-1} \boldsymbol{\varphi}(\boldsymbol{\xi_i}, \boldsymbol{\eta_i})^T F_{ix} \right) \\ \boldsymbol{P_b}^e &= (\boldsymbol{R}^e)^{-1} \left(\int_S p_y \boldsymbol{\varphi}^T dS + \int_\Omega b_y \boldsymbol{\varphi}^T d\Omega + \sum_{i=1}^{n} (\boldsymbol{R}^e)^{-1} \boldsymbol{\varphi}(\boldsymbol{\xi_i}, \boldsymbol{\eta_i})^T F_{iy} \right) \end{aligned}\right\} \tag{3.30}$$

and,

$$\left.\begin{aligned} \boldsymbol{K_1^e} &= \frac{E}{1-\nu^2} \left(\boldsymbol{A_1^{11}} \otimes \boldsymbol{A_2^{00}} + \frac{1-\nu}{2} \boldsymbol{A_1^{00}} \otimes \boldsymbol{A_2^{11}} \right) \\ \boldsymbol{K_2^e} &= \frac{E}{1-\nu^2} \left(\nu \boldsymbol{A_1^{10}} \otimes \boldsymbol{A_2^{01}} + \frac{1-\nu}{2} \boldsymbol{A_1^{01}} \otimes \boldsymbol{A_2^{10}} \right) \\ \boldsymbol{K_3^e} &= (\boldsymbol{K_2^e})^T \\ \boldsymbol{K_4^e} &= \frac{E}{1-\nu^2} \left(\boldsymbol{A_1^{00}} \otimes \boldsymbol{A_2^{11}} + \frac{1-\nu}{2} \boldsymbol{A_1^{11}} \otimes \boldsymbol{A_2^{00}} \right) \end{aligned}\right\} \tag{3.31}$$

with,

$$\left.\begin{aligned} \boldsymbol{A_1^{00}} &= \left(\left(\boldsymbol{T_1^e} \right)^{-1} \right)^T \left(l_{ex} \int_0^1 (\boldsymbol{\varphi_1})^T (\boldsymbol{\varphi_1}) \, d\xi \right) \left(\left(\boldsymbol{T_1^e} \right)^{-1} \right) \\ \boldsymbol{A_1^{01}} &= \left(\left(\boldsymbol{T_1^e} \right)^{-1} \right)^T \left(\int_0^1 (\boldsymbol{\varphi_1})^T \left(\frac{d\boldsymbol{\varphi_1}}{d\xi} \right) d\xi \right) \left(\left(\boldsymbol{T_1^e} \right)^{-1} \right) \\ \boldsymbol{A_1^{10}} &= \left(\left(\boldsymbol{T_1^e} \right)^{-1} \right)^T \left(\int_0^1 \left(\frac{d\boldsymbol{\varphi_1}}{d\xi} \right)^T (\boldsymbol{\varphi_1}) \, d\xi \right) \left(\left(\boldsymbol{T_1^e} \right)^{-1} \right) \\ \boldsymbol{A_1^{11}} &= \left(\left(\boldsymbol{T_1^e} \right)^{-1} \right)^T \left(\frac{1}{l_{ex}} \int_0^1 \left(\frac{d\boldsymbol{\varphi_1}}{d\xi} \right)^T \left(\frac{d\boldsymbol{\varphi_1}}{d\xi} \right) d\xi \right) \left(\left(\boldsymbol{T_1^e} \right)^{-1} \right) \end{aligned}\right\} \tag{3.32}$$

Analogous to $\boldsymbol{A_1^{ij}}(i,j=0,1)$, $\boldsymbol{A_2^{ij}}(i,j=0,1)$ can be found out using $l_{ey}, d\eta, \boldsymbol{T_2^e}, \boldsymbol{\varphi_2}$. The essential boundary conditions are implemented by setting the corresponding DOF to the respective value and eliminating them from the system of equations.

The element stiffness matrices formulated for respective element types as given in Equations 3.8,3.14,3.20 and 3.28 for all the sub-domains can be assembled to form the

corresponding algebraic set of global equilibrium equations. To evaluate the integrals defined in these equations, numerical integration needs to be employed. In the next section, a detailed discussion on the proposed background cell based Gauss quadrature numerical integration in the context of BSWI WFEM is given.

3.2 Background cell-based numerical integration for Gauss quadrature

Gauss quadrature numerical integration scheme is used for evaluating the integrals in BSWI WFEM. In a BSWI WFEM element, the total number of internal nodes and their position within an element changes when the resolution is varied. Concurrently, the support domain of the scaling function associated with the nodes also moves. Hence, implementation of Gauss quadrature rules invites additional troubles. In EFGM, where only nodes exist in the problem domain for modelling field quantity, a background cell based approach is implemented to carry out the numerical integrations involved [18]. In the current section, a similar approach is proposed to use for every element in BSWI WFEM. In this methodology, background cells are placed over every BSWI WFEM element. The length of the background cell can be independent of the position and number of nodes in a BSWI WFEM element as shown in Figure 3.6.

The element shown in Figure 3.6 is constructed using quadratic order scaling functions $m = 3$ and resolution $j = 3$. Figures 3.6a-3.6c show the placement of 1, 2 and 4 background cells respectively, over a 1D BSWI C_0 element with Gauss points within each cell. Likewise, Figure 3.6d shows a background cell whose dimensions are selected such that the length of each cell is equal to the distance between adjacent WFEM element nodes.

In the present study, both two-point integration and one-point integration is attempted, in which, two Gauss points per background cell and one Gauss point per background cell are considered respectively, for solving the numerical examples. The arrangement of Gauss points, nodes and background cells for a two-point integration and one-point integration schemes over a 1D BSWI element for quadratic order scaling functions with $m = 3$ and resolution $j = 3$ is shown in Figure 3.7. The distribution of nodes and Gauss points in a single C_0 2D element domain for two-point and one-point integration using a background cell whose vertices coincide with the BSWI WFEM element nodes with $m = 2$ and resolution $j = 2$ is shown in Figure 3.8. It is to be noted that, in contrast with FEM where every single element is mapped to a single cell and Gauss points are also placed within the

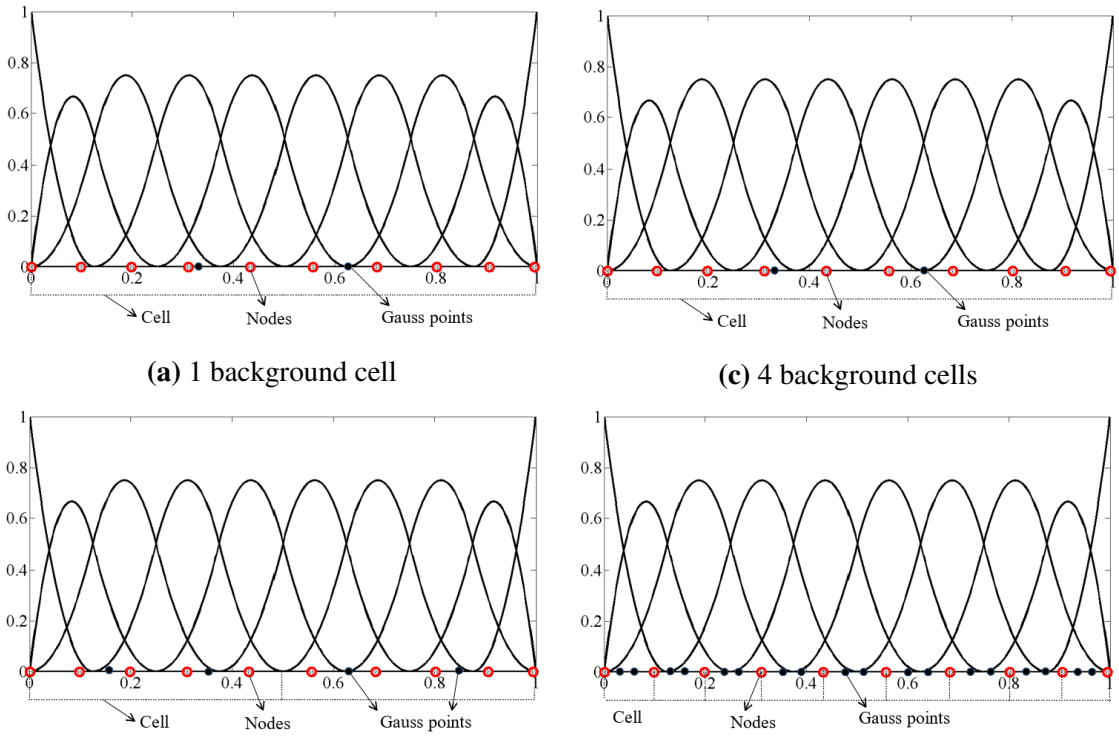

(a) 1 background cell

(c) 4 background cells

(b) 2 background cells

(d) cells coincide with nodes

Figure 3.6: Distribution of background cell with Gauss points for a 1D C_0 continuity element with $m = 3$, $j = 3$

same element, in the proposed approach for BSWI WFEM, every element takes multiple cells and the quadrature rule is stated for the cell. When BSWI WFEM elements have irregular geometry, they need to be mapped on to a regular parent element in the element solving domain. Following which, a background cell is used over the regular element in the element solving domain for integration. A few numerical examples are solved in the next section and the accuracy of results is studied by varying the dimension of the background cell and also using one-point and two-point integration schemes in the process.

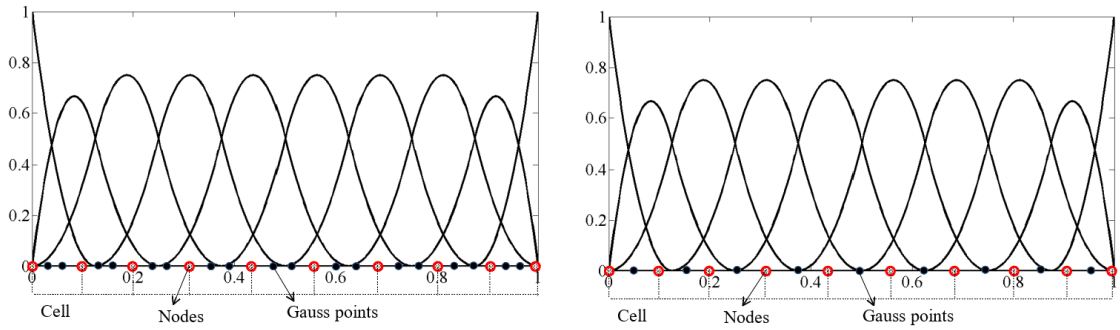

(a) Two Gauss points per background cell

(b) One Gauss points per background cell

Figure 3.7: Distribution of Gauss points for two- and one-point integration in a 1D C_0 continuity element for $m = 3$, $j = 3$

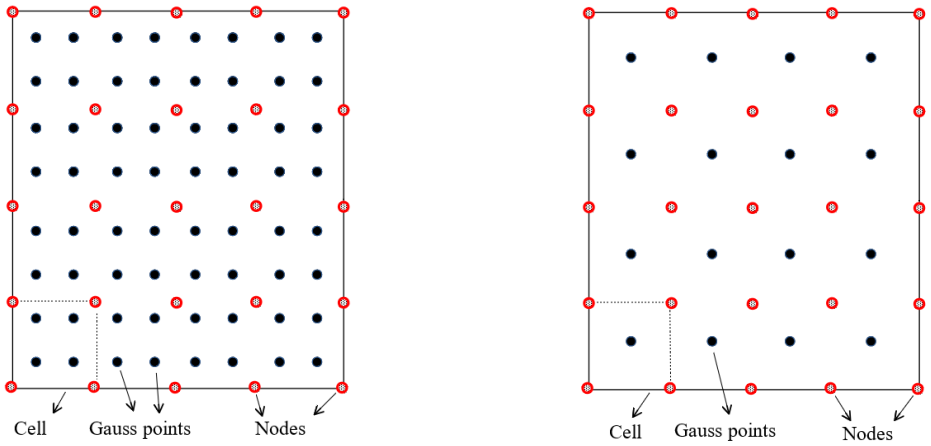

(a) Two-point integration

(b) One-point integration

Figure 3.8: Distribution of Gauss points for two-point and one-point integration in a 2D C_0 continuity element for $m = 2$, $j = 2$

3.3 Numerical examples

Three numerical examples are solved to understand the merits and demerits of background cell-based numerical integration. Results from WFEM are compared with the available analytical solutions for different order of scaling functions and resolutions.

3.3.1 1D Bar with a linear body force

In this example, a 1D bar with a linear body force $b(x) = x$ as shown in Figure 3.9 is considered. The bar with $Length(L) = 100$mm and $Area = 1\text{mm}^2$ is fixed at one end. The material of the bar is considered to be isotropic with Young's modulus $E = 1 \times 10^5$MPa. The entire domain of the bar is modelled using one BSWI C_0 element. The resulting system of integral equations, as given in Equation 3.9, is solved by selecting different background cell dimensions as detailed in Figure 3.6. Both two-point and one-point integration schemes as shown in Figure 3.7 are attempted. Table 3.1 show the condition number of the stiffness matrix obtained by two-point Gauss integration scheme, when background cells of different dimensions are used with scaling functions of various order and resolutions.

As observed from Table 3.1, when 1 and 2 background cells are used; it results in a badly scaled and ill-conditioned stiffness matrix, thereby giving erroneous results for different order of scaling functions and resolutions except for $m = 2, j = 2$ with 2 background cells. The erroneous results can be attributed to the reason that when a fewer background cells are used, there will be fewer Gauss points used for integration and the positioning of these Gauss points makes them lie outside the local support of scaling function. Hence, it will have less or no contribution to the corresponding stiffness coefficient. The sparseness of the corresponding stiffness matrices using two-point integration for different dimension of background cell are shown in Figures 3.10-3.13. It can be seen from Figures 3.10a-3.10c that because of insufficient number of Gauss points when 1 background cell is used, stiffness matrix with linear scaling functions have few non-zero values. However, with quadratic scaling functions, the stiffness matrix is fully populated as shown in Figures 3.10d-3.10f, but ill-conditioned as given in Table 3.1. The sparseness of stiffness matrices obtained by using linear scaling function, when 2 and 4 background cells are used for integration is shown in Figures 3.11 and 3.12, respectively.

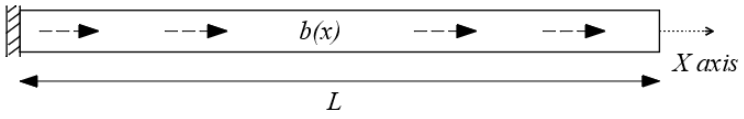

Figure 3.9: One end fixed bar subjected to linear body force $b(x)$

It can be observed from these figures and Table 3.1 that for $m = 2, j = 2$ with two background cells and for $m = 2, j = \{2, 3\}$ with four background cells, the stiffness matrices become banded and well-conditioned. In all these three cases, it is found that at

Table 3.1: Condition number of stiffness matrix for 1D bar with linear body force, obtained using two-point integration

m, j	**1 cell**	**2 cell**	**4 cell**	**cell coincide**
2,2	∞	29.28	29.28	29.28
2,3	∞	∞	113.49	113.50
2,4	∞	∞	∞	437.69
3,2	7.69×10^{16}	3.11×10^{16}	80.05	81.90
3,3	1.53×10^{20}	1.99×10^{18}	2.28×10^{16}	330.20
3,4	4.77×10^{27}	3.92×10^{21}	2.43×10^{17}	1887.44

least one Gauss point lies inside the local support of scaling functions. However, when quadratic scaling functions with two and four background cells are used, the stiffness matrices are found to be fully populated and ill-conditioned. The sparseness pattern obtained in this case is same as that of single background cell as shown in Figure 3.10. Meanwhile, for $m = 3, j = 2$ with four background cells, where every support of scaling function is found to possess at least one Gauss Point, stiffness matrix is found to be well-conditioned. The last case considered for the dimension of the background cell is wherein, the vertices of the background cells coincide with the nodes of a BSWI WFEM element and Gauss points are placed within each of the background cell. In this case, using two-point integration, it is observed that because of sufficient number of Gauss points, the stiffness matrices are well conditioned as observed from the values in Table 3.1. Figure 3.13 also shows the sparseness of the stiffness matrices for the present case using linear scaling functions. The stiffness matrices are found to be fully populated when quadratic scaling functions are used with different dimensions of the background cell. This can be reasoned to the fact that because of the extended local support of the quadratic scaling functions, they overlap each other. Hence, there are always Gauss points which contribute to the local stiffness coefficient. However, when the contribution from some of the Gauss points is less, it results in a badly scaled stiffness matrix as seen with one, two and four background cells.

The condition number of the stiffness matrices when background cell of different dimension are used with different order and resolution, using one-point integration scheme is shown in Table 3.2. It can be observed from Table 3.2 that when one, two and four background cells are used, the stiffness matrix is badly scaled and ill-conditioned for different order and resolutions except at $m = 2, j = 2$ using four background cells. However, when background cell coinciding with the nodes is used, the stiffness matrix

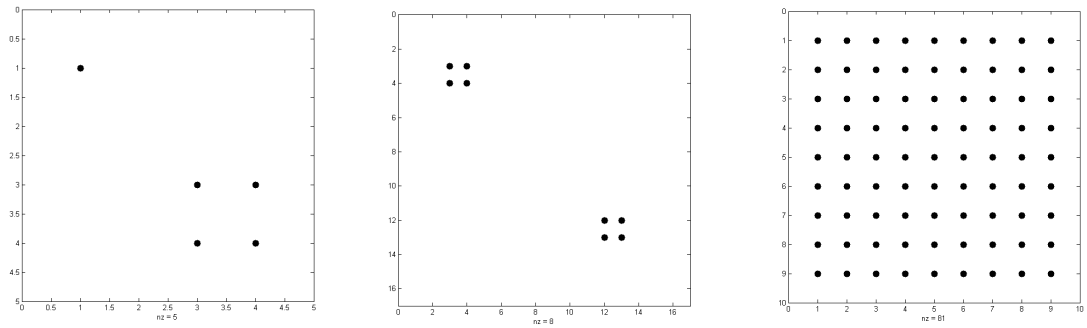

(a) $m = 2, j = 2$ **(c)** $m = 2, j = 4$ **(e)** $m = 3, j = 3$

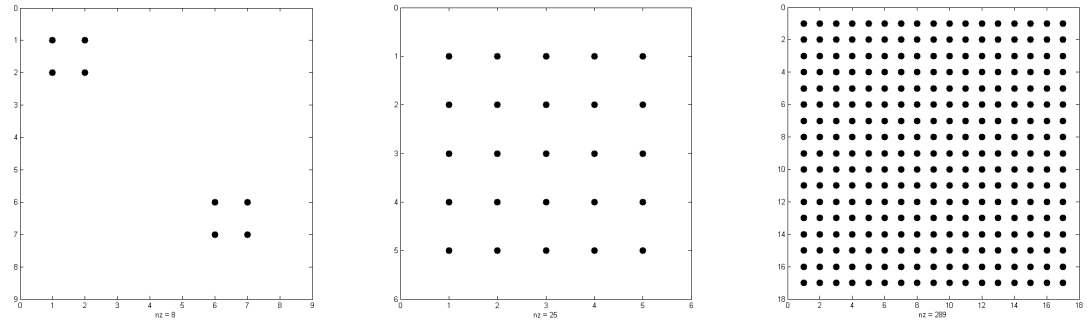

(b) $m = 2, j = 3$ **(d)** $m = 3, j = 2$ **(f)** $m = 3, j = 4$

Figure 3.10: Sparseness of stiffness matrix for linear and quadratic scaling functions at different resolutions using one background cell with two-point integration

obtained for all the order and resolution are well-conditioned. From the analysis done so far, it can be concluded that a background cell whose vertices coincide with the element nodes leads to a well-conditioned stiffness matrix and, hence, selected to further analyze the displacement and stresses. One- and two-point integration schemes are used for numerical integration. Linear (order $m = 2$) and quadratic (order $m = 3$) scaling functions are used with resolutions $j = \{2, 3, 4\}$ to calculate axial displacement, axial stress and relative error in displacement norm. The axial displacements (δ) obtained by using two-point integration and one-point integration is shown in Figure 3.14a and Figure 3.14b, respectively. They are in good agreement with the analytical solution, which is given by:

$$\delta(x) = \frac{1}{E}\{\frac{-x^3}{6} + 5000x\} \tag{3.33}$$

The axial stresses (σ_{xx}) obtained, when two-point integration is used, are shown in Figure 3.15a. Here, erroneous results are produced by all the resolutions when linear BSWI scaling functions are used. However, accurate results are obtained, even at lower resolutions, with quadratic BSWI scaling functions. The axial stresses (σ_{xx}) calculated,

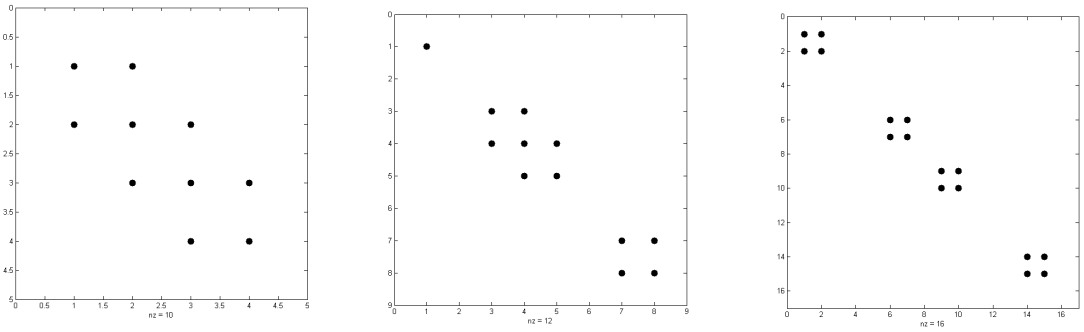

(a) $m = 2, j = 2$ **(b)** $m = 2, j = 3$ **(c)** $m = 2, j = 4$

Figure 3.11: Sparseness of stiffness matrix for linear scaling functions at different resolutions using two background cells with two-point integration

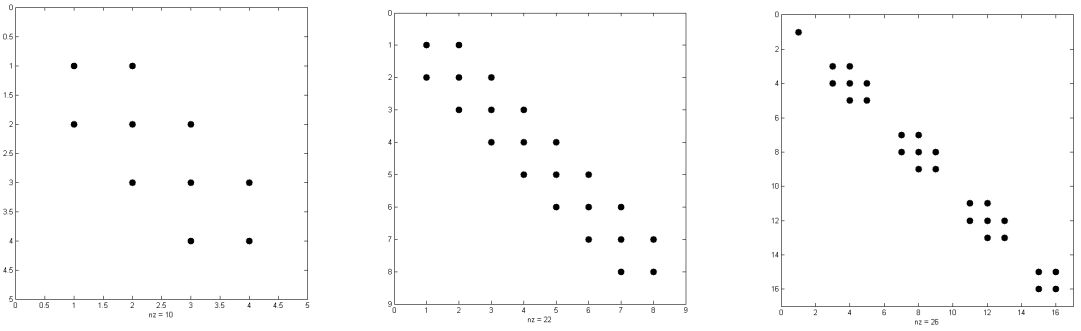

(a) $m = 2, j = 2$ **(b)** $m = 2, j = 3$ **(c)** $m = 2, j = 4$

Figure 3.12: Sparseness of stiffness matrix for linear scaling functions at different resolutions using four background cells with two-point integration

Table 3.2: Condition number of stiffness matrix for 1D bar with linear body force, obtained using one-point integration

m, j	**1 cell**	**2 cell**	**4 cell**	**cell coincide**
2,2	∞	∞	29.28	29.28
2,3	∞	∞	∞	113.50
2,4	∞	∞	∞	437.69
3,2	∞	8.13×10^{19}	1.68×10^{17}	88.08
3,3	3.28×10^{37}	3.06×10^{22}	2.70×10^{19}	329.21
3,4	2.70×10^{38}	4.56×10^{30}	1.25×10^{25}	1350.10

with one-point Gauss quadrature for integration, are shown in Figure 3.15b. In this case also, linear BSWI scaling functions gives an error and accurate results are obtained only when quadratic BSWI scaling functions at higher resolutions are used. A convergence

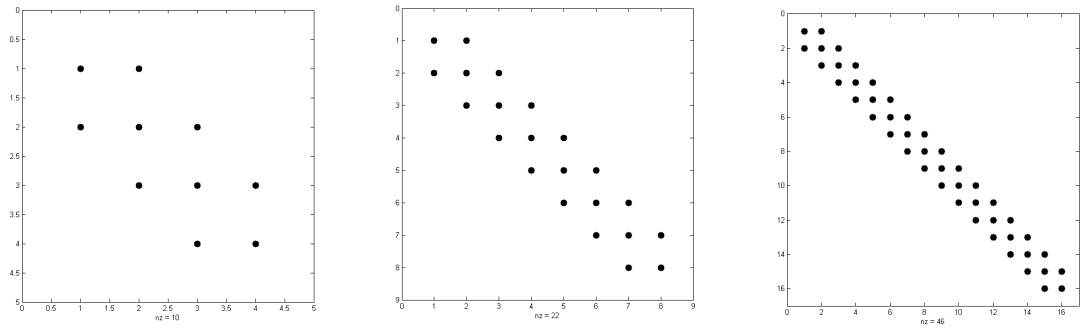

(a) $m = 2, j = 2$ **(b)** $m = 2, j = 3$ **(c)** $m = 2, j = 4$

Figure 3.13: Sparseness of stiffness matrix for linear scaling functions at different resolutions when vertices of background cells coincide with nodes and two-point quadrature rule is used for integration

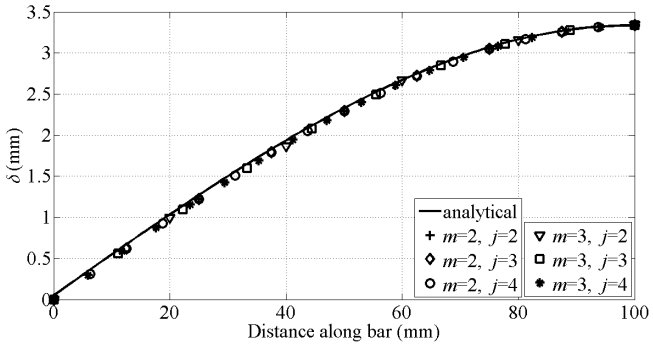

(a) Using 2 point integration

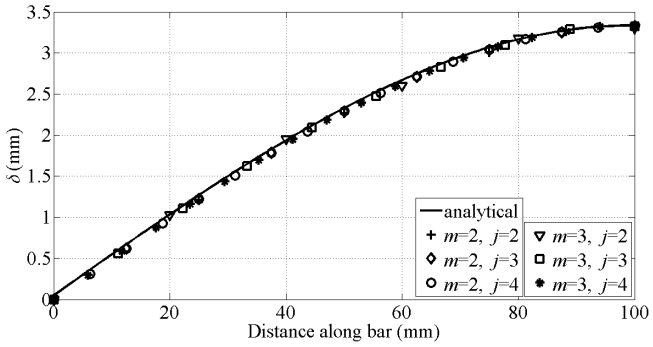

(b) Using 1 point integration

Figure 3.14: Displacement δ of bar along x axis using linear and quadratic BSWI scaling functions

study based on relative error in the displacement norm using linear and quadratic BSWI scaling functions with different resolutions for one- and two-point integrations is shown in

Figure 3.16. The relative error in displacement norm is given as,

$$r_u = \frac{\|\boldsymbol{u}_{num} - \boldsymbol{u}_{exact}\|}{\|\boldsymbol{u}_{exact}\|} \tag{3.34}$$

where, $\|\boldsymbol{u}\| = \left(\int_\Omega \boldsymbol{u}^T \boldsymbol{u} d\Omega\right)^{\frac{1}{2}}$.

It is observed from Figure 3.16 that when one-point integration is used, the error is around 3 % for $m = 2, j = 2$ and it decreases to 0.2 % at higher resolution $j = 4$. But with a higher order $m = 3, j = 2$, the error is reduced to 1.5 %. When two-point integration is used, the error is found to be less than 1 % even at lower order and resolution. Hence, it can be reasoned from this example that the user needs to find a balance between the increasing computational effort and accuracy of the solution when choosing between one- and two-point integration schemes.

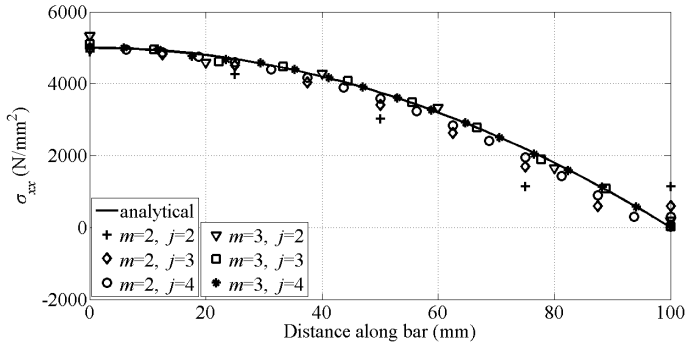

(a) Using 2 point integration

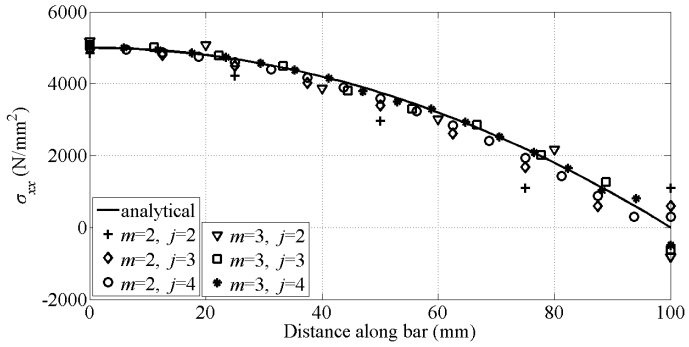

(b) Using 1 point integration

Figure 3.15: Axial stress (σ_{xx}) along x axis using linear and quadratic BSWI scaling functions

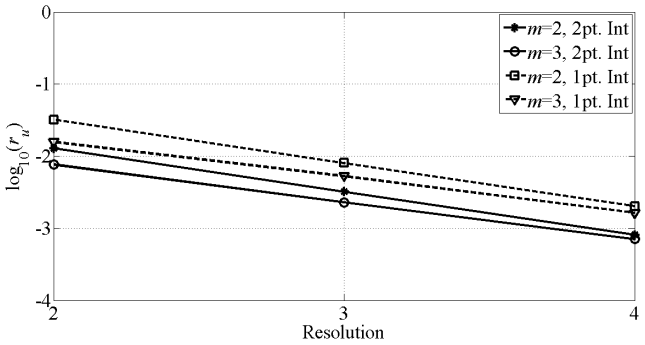

Figure 3.16: Relative error in the displacement norm for one- and two-point integration scheme

3.3.2 Thin beam under different boundary conditions

3.3.2.1 Based on Euler-Bernoulli beam theory

In this example, a cantilever and a simply supported beam with a uniformly distributed load (UDL) $q(x) = 1$N/mm as shown in Figures 3.17 and 3.18 is considered for analysis. In both the cases, the Young's modulus is considered to be $E = 2 \times 10^5$MPa. The geometric dimensions of the beam are taken as, span $L = 100$mm; and cross-sectional dimensions, $b, h = 1$mm. The entire domain of the beam is modelled using one BSWI WFEM Euler-Bernoulli beam element. The length of the background cell is varied as explained in Figure 3.6 and analysis is carried out. The condition number of stiffness matrices, after removing the rows and columns corresponding to essential boundary conditions, obtained for these background cells with different order and resolution of BSWI scaling function is tabulated in Tables 3.3 and 3.4 for cantilever and simply supported beam under uniformly distributed load (UDL) respectively.

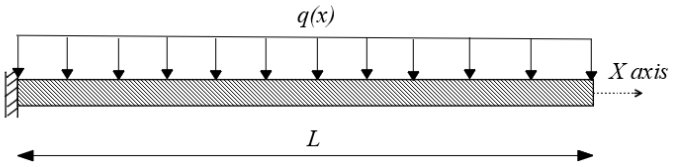

Figure 3.17: A cantilever beam with a uniformly distributed load

The numerical integration is performed using a two-point integration scheme. It is observed from both Tables 3.3 and 3.4 that the stiffness matrix becomes ill-conditioned when one, two and four background cells are used for solving the integrals of Equation 3.15

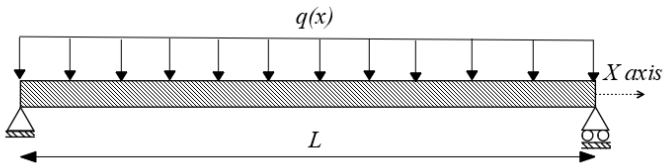

Figure 3.18: A simply supported beam with a uniformly distributed load

Table 3.3: Condition number of stiffness matrix constructed using two-point integration, for cantilever beam based on EBT

m, j	**1 cell**	**2 cell**	**4 cell**	**cell coincide**
3,2	5.08×10^{18}	5.88×10^{04}	5.88×10^{04}	5.88×10^{04}
3,3	1.96×10^{20}	1.64×10^{18}	3.05×10^{05}	3.30×10^{05}
3,4	9.18×10^{23}	1.48×10^{19}	6.78×10^{17}	2.16×10^{06}
4,2	4.70×10^{17}	2.52×10^{18}	7.06×10^{04}	7.06×10^{04}
4,3	6.47×10^{17}	1.03×10^{17}	5.32×10^{18}	2.33×10^{05}
4,4	1.99×10^{20}	1.09×10^{18}	6.10×10^{17}	9.11×10^{05}

Table 3.4: Condition number of stiffness matrix constructed using two-point integration for simply supported beam based on EBT

m, j	**1 cell**	**2 cell**	**4 cell**	**cell coincide**
3,2	8.35×10^{18}	4.47×10^{03}	4.47×10^{03}	3.21×10^{03}
3,3	8.65×10^{20}	1.00×10^{18}	2.92×10^{04}	2.87×10^{04}
3,4	5.29×10^{23}	1.63×10^{19}	7.78×10^{17}	2.25×10^{05}
4,2	1.60×10^{17}	9.62×10^{16}	5.78×10^{03}	5.78×10^{03}
4,3	5.25×10^{17}	2.13×10^{17}	4.93×10^{17}	2.31×10^{04}
4,4	2.59×10^{20}	1.11×10^{18}	6.01×10^{18}	9.83×10^{04}

except for the cases $m = 3, j = 2$ with two background cells and $m = 3, j = \{2, 3\}, m = 4, j = 2$ with four background cells. The reason that is given for the ill-conditioning of the stiffness matrix in the previous example is applicable for the current example as well. When a background cell whose vertices coincide with the element nodes is used, it can be observed from Tables 3.3 and 3.4 that the stiffness matrices are well-conditioned. The condition number of the element stiffness matrix calculated using one-point integration for cantilever and simply supported case is shown in Tables 3.5 and 3.6. It is observed from Tables 3.5 and 3.6 that the stiffness matrices are ill-conditioned for all the dimensions of the background cells using different order and resolutions except for $m = 3, j = 2$ when

four background cells are used. Hence, for further analysis to study the deflection and slope, a background cell whose vertices coincide with the element nodes is considered with two-point integration. Here, it is also noted that the element stiffness matrix remains fully populated at all the dimensions of the background cells whose figures are not shown here.

Table 3.5: Condition number of stiffness matrix constructed using one-point integration, for cantilever beam based on EBT

m, j	**1 cell**	**2 cell**	**4 cell**	**cell coincide**
3,2	9.14×10^{17}	1.48×10^{19}	5.88×10^{04}	4.73×10^{17}
3,3	1.57×10^{19}	5.36×10^{18}	2.82×10^{18}	4.11×10^{17}
3,4	1.17×10^{22}	2.62×10^{23}	6.93×10^{18}	1.41×10^{18}
4,2	6.74×10^{33}	2.42×10^{18}	6.64×10^{17}	6.64×10^{17}
4,3	2.72×10^{49}	5.34×10^{18}	2.06×10^{17}	2.95×10^{17}
4,4	8.05×10^{39}	2.42×10^{35}	3.44×10^{33}	5.47×10^{17}

Table 3.6: Condition number of stiffness matrix constructed using one-point integration, for simply supported beam based on EBT

m, j	**1 cell**	**2 cell**	**4 cell**	**cell coincide**
3,2	8.29×10^{17}	1.32×10^{18}	4.47×10^{03}	1.59×10^{17}
3,3	1.66×10^{18}	1.14×10^{19}	1.68×10^{18}	1.25×10^{17}
3,4	6.09×10^{21}	3.34×10^{22}	1.26×10^{19}	9.08×10^{16}
4,2	1.65×10^{33}	2.63×10^{17}	5.69×10^{17}	5.69×10^{17}
4,3	1.52×10^{34}	6.74×10^{17}	2.97×10^{17}	1.49×10^{17}
4,4	2.60×10^{23}	2.96×10^{20}	1.27×10^{18}	1.67×10^{17}

Quadratic and cubic BSWI scaling functions with resolution $j = \{2, 3, 4\}$ are used to plot transverse deflection, slope and relative error in displacement norm for a cantilever and a simply supported beam under UDL. The deflection plots using two-point integration for cantilever and simply supported beams are shown in Figures 3.19 and 3.20. The analytical solution for the deflections of a cantilever and simply supported beams under UDL is given as [196],

Cantilever:

$$\delta(x) = \frac{q}{24EI}\{x^4 - 4Lx^3 + 6L^2x^2\} \tag{3.35}$$

Simply supported:

$$\delta(x) = \frac{q}{24EI}\{L^3x - 2Lx^3 + x^4\} \tag{3.36}$$

It is observed from Figures 3.19 and 3.20 that WFEM results are in good agreement with the analytical solution. Further, even at lower resolutions, accurate results are obtained when cubic BSWI scaling functions are used. The variation of slope along x axis for cantilever and simply supported beams are shown in Figures 3.21 and 3.22. It is observed that the slope is captured accurately when cubic BSWI scaling functions are used for the analysis of a cantilever beam. But, in the case of a simply supported beam, the error is low when quadratic scaling functions at lower resolutions are used.

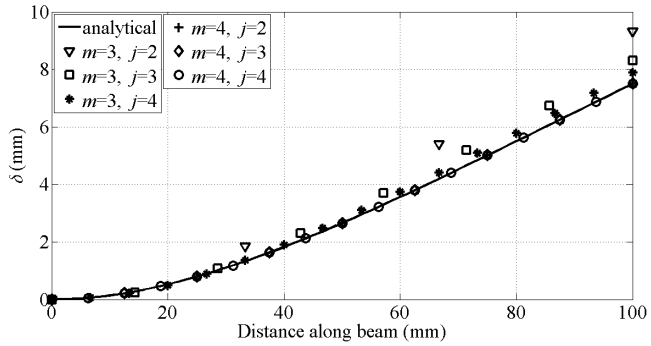

Figure 3.19: Variation of deflection (δ) along x axis using quadratic and cubic BSWI scaling functions for cantilever beam

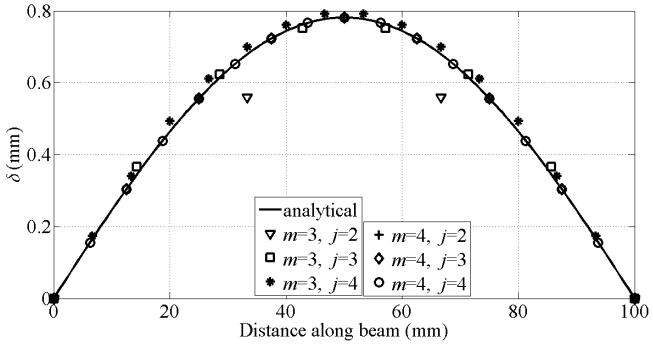

Figure 3.20: Variation of deflection (δ) along x axis using quadratic and cubic BSWI scaling functions for simply supported beam

The relative error in displacement norm is shown in Figure 3.23. From Figure 3.23, it can be concluded that, for quadratic BSWI scaling functions, as the resolution is increased, the error reduces from 27 % to 5 % for a cantilever beam and 17 % to 3.5 % for a simply

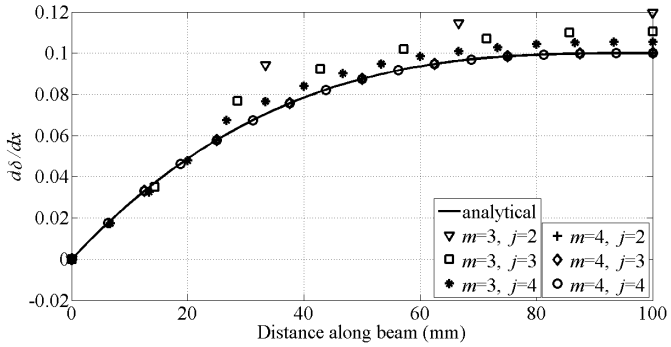

Figure 3.21: Variation of slope ($d\delta/dx$) along x axis using quadratic and cubic BSWI scaling functions for cantilever beam

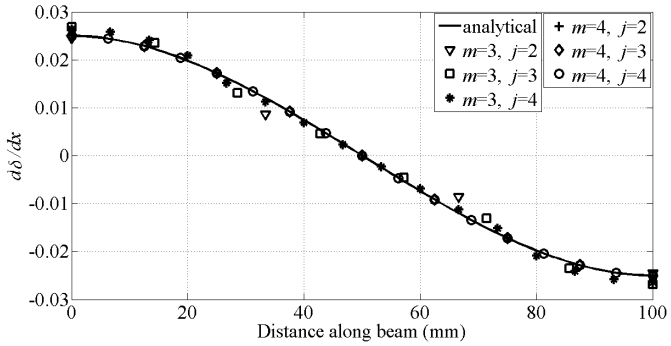

Figure 3.22: Variation of slope ($d\delta/dx$) along x axis using quadratic and cubic BSWI scaling functions for simply supported beam

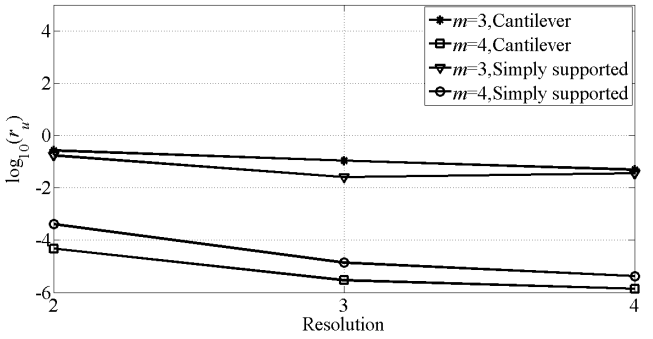

Figure 3.23: Relative error in the displacement norm obtained using two-point integration scheme

supported beam. However, when cubic BSWI scaling functions are used, the maximum error encountered is less than 0.48×10^{-2} % for a cantilever beam and 0.04 % for a simply supported beam among all the resolutions $j = \{2, 3, 4\}$.

3.3.2.2 Based on Timoshenko beam theory

When thin beams are analyzed based on TBT, in FEM a numerical issue known as shear locking is encountered. To overcome this issue, reduced integration of shear terms in stiffness matrix is suggested [4]. Here, BSWI WFEM beam element formulated on TBT is investigated for the effect of the integration scheme on the accuracy of results and on shear locking. The material and geometric properties considered here are same as those were in the case of an Euler-Bernoulli beam. Only the depth h is varied to obtain L/h ratio of 100 (thin beam limit) [197]. Two different cases of integration schemes are considered. In one of the cases, namely 2pt, all the terms of Equation 3.22 are integrated using two-point integration, while in the other case namely 1pt, only the shear terms are integrated using one-point integration and the rest of the terms with two-point integration. Also, for this study, only one configuration of background cells whose vertices coincide with element nodes as shown in Figure 3.6d is selected for analysis as usage of other configuration of background cells led to ill-conditioning of stiffness matrices because of the reasons already discussed in the context of Euler-Bernoulli beam. It can be seen from Table 3.7 that the stiffness matrices are well-conditioned at all the orders and resolutions using the selected background cell configuration for both two- and one-point integration schemes.

Table 3.8 shows the relative error in displacement norm using two- and one-point integration for cantilever and simply supported boundary conditions. It is observed from Table 3.8 that when linear BSWI scaling functions are used with two-point integration, the error is high for all the resolutions because of the existence of shear locking. However, when quadratic BSWI scaling functions are used at higher resolution, the error is reduced to less than 1 % for both the boundary conditions as observed from Table 3.8. When one-point integration is used it is observed from Table 3.8 that for both the beams and for all the orders and resolutions of scaling functions, the error is reduced to a large extent. For linear BSWI scaling function, the error is reduced to 2 % at $j = 2$ and 0.13 % for $j = 4$, for a cantilever beam. For a simply supported beam, the error reduces to 1.09 % using linear scaling function for $j = 4$. It is observed from Table 3.8 that when quadratic scaling functions are used with 1 point integration, the error is 0.84% and 5.28 % at $j = 2$ for the cantilever and simply supported cases; and at $j = 4$ it is only 0.06 % and 0.4 % for the same. Hence, the error can be significantly reduced and shear locking effects can be tackled easily when one-point Gauss quadrature is used in the background cells for integrating shear terms, while modelling slender beams using a TBT element.

Table 3.7: Condition number of stiffness matrix constructed using two- and one-point integration based on TBT for cantilever (C) and simply supported (SS)

$L/h = 100$	m=2,$j = 2$	m=2,$j = 3$	m=2,$j = 4$	m=3,$j = 2$	m=3,$j = 3$	m=3,$j = 4$
C, 2 pt	2.22×10^{05}	7.55×10^{05}	2.59×10^{06}	3.78×10^{07}	4.60×10^{07}	6.19×10^{07}
SS, 2 pt	1.82×10^{04}	7.59×10^{04}	2.91×10^{05}	3.50×10^{06}	4.53×10^{06}	6.93×10^{06}
C, 1 pt	4.22×10^{07}	3.79×10^{07}	3.48×10^{07}	5.07×10^{07}	5.77×10^{07}	9.16×10^{07}
SS, 1 pt	3.38×10^{06}	3.78×10^{06}	3.91×10^{06}	4.61×10^{06}	5.97×10^{06}	1.03×10^{07}

Table 3.8: Relative % error in displacement norm obtained from two- and one-point integration based on TBT for cantilever (C) and simply supported (SS)

$L/h = 100$	m=2,$j = 2$	m=2,$j = 3$	m=2,$j = 4$	m=3,$j = 2$	m=3,$j = 3$	m=3,$j = 4$
C, 2 pt.	99.49	98.02	92.85	27.90	4.58	0.375
SS, 2 pt.	99.55	98.09	92.64	16.77	6.98	0.68
C, 1 pt.	2.11	0.54	0.136	0.84	0.23	0.06
SS, 1 pt.	17.08	4.42	1.09	5.28	1.51	0.412

3.3.3 A plate with a hole under uniaxial tension

In this example, a plate with a hole under uniaxial far field tensile loading is considered for analysis. Only a quarter portion of the plate is modelled because of symmetry as shown in Figure 3.24 having dimensions $L = 5$mm, $b = 6$mm and radius of hole ($a = 0.1$mm). The plate is considered as isotropic with $E = 2 \times 10^5$MPa, $\nu = 0.3$, and pulled with a uniformly distributed tensile load on top edge $F = 1000\mathrm{N/mm}^2$. The analytical solution is given as [198]:

$$\left.\begin{aligned} \sigma_r &= \frac{F}{2}(1-\frac{a^2}{r^2}) + \frac{F}{2}(1+\frac{3a^4}{r^4}-\frac{4a^2}{r^2})\cos(2\theta_s) \\ \sigma_{\theta_s} &= \frac{F}{2}(1+\frac{a^2}{r^2}) - \frac{F}{2}(1+\frac{3a^4}{r^4})\cos(2\theta_s) \\ \tau_{r\theta_s} &= -\frac{F}{2}(1-\frac{3a^4}{r^4}+\frac{2a^2}{r^2})\sin(2\theta_s) \end{aligned}\right\} \tag{3.37}$$

The domain of the quarter plate is discretized using two 2D BSWI C_0 elements as seen in Figure 3.24. Background cells are used over each of the two BSWI elements in the element solving domain for integration of Equations 3.29-3.32. Analogous to the 1D case, the condition numbers of the stiffness matrices are calculated for the current 2D problem

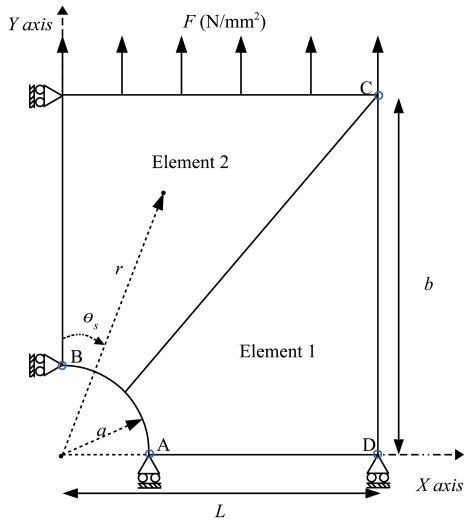

Figure 3.24: Plate with a hole under uniaxial far field tensile loading

and are shown in Tables 3.9 and 3.10 for different dimensions of the background cell with two- and one-point integration rule, respectively. It should be noted that background cells are used over each of the two BSWI WFEM elements used in the present problem.

It is observed from Table 3.9 that when one, two and four background cells per element are used with two-point integration, the condition number obtained is observed to be very high, especially for higher resolutions. However, when the length of the background cell is reduced further, by equating to the distance between adjacent nodes of the BSWI element, the stiffness matrices obtained are well-conditioned. The aforementioned observation can be attributed to the reason that as the length of background cell is reduced, the support of scaling functions possesses sufficient number of Gauss points, thereby resulting in a well-conditioned matrix. The condition number of stiffness matrices when one-point integration is used is shown in Table 3.10. It is noted that the condition number from one-point integration is higher when compared with the same obtained using two-point integration at different dimensions of the background cell except for $m = 2, j = 1$ with four background cells. Hence, two-point integration is considered for further analysis in the current example.

The sparseness of the stiffness matrices constructed with one, two and four background cells per elements using two-point integration is shown in Figures 3.25, 3.26 and 3.27. It can be noted that for linear scaling functions, as the resolution is increased the Gauss points lying outside the support of scaling functions have no contribution to the element

Table 3.9: Condition number of stiffness matrix for 2D plate with a hole, obtained using two-point integration

m, j	**1 cell**	**2 cell**	**4 cell**	**cell coincide**
2,2	8.24×10^{04}	1.18×10^{02}	1.40×10^{02}	1.18×10^{02}
2,3	1.08×10^{67}	3.86×10^{05}	7.36×10^{02}	7.36×10^{02}
2,4	∞	2.12×10^{86}	2.15×10^{06}	4.58×10^{03}
3,2	1.89×10^{19}	6.01×10^{02}	6.45×10^{02}	6.00×10^{02}
3,3	7.72×10^{22}	9.46×10^{18}	2.97×10^{03}	3.11×10^{03}
3,4	1.18×10^{28}	4.84×10^{23}	1.56×10^{19}	2.43×10^{04}

Table 3.10: Condition number of stiffness matrix for 2D plate with a hole, obtained using one-point integration

m, j	**1 cell**	**2 cell**	**4 cell**	**cell coincide**
2,2	∞	4.64×10^{04}	1.10×10^{02}	4.64×10^{04}
2,3	∞	∞	2.56×10^{05}	2.56×10^{05}
2,4	∞	∞	∞	1.60×10^{06}
3,2	2.55×10^{34}	5.78×10^{18}	5.71×10^{02}	1.18×10^{05}
3,3	1.47×10^{70}	6.00×10^{33}	1.14×10^{19}	1.58×10^{06}
3,4	8.68×10^{45}	1.86×10^{31}	6.71×10^{33}	3.10×10^{08}

stiffness coefficient. However, when quadratic scaling functions are used with single background cell, stiffness matrices are found to be fully populated for all resolutions as shown in Figure 3.25. Moreover, for all other cases of background cell considered, the sparseness of stiffness matrix formulated with quadratic scaling function, is found to be same as that of single background cell and hence not shown here. It can be concluded from the results obtained so far that background cells with their vertices coinciding with the element nodes results in well-conditioned stiffness matrices by means of two-point Gauss quadrature, and hence, is selected for further analysis of current numerical example. The stress concentration factor (K_t) based on hoop stress along the edge $\theta_s = pi/2$ (i.e. $y = 0$) is studied and compared with the analytical solution given by Sadd [198]. Figure 3.28 shows the distribution of nodes over the plate using $m = 3, j = 3$ and Figure 3.29 shows the variation of K_t plotted along bottom edge $y = 0$ for the current example. It is observed that, the stress concentration factor $K_t = 3$ is accurately captured using quadratic BSWI scaling functions. On the contrary, with linear BSWI scaling functions results are underestimated even at higher resolutions. The computational effort will be high when two-point integration is used at high resolutions in a 2D domain as number of Gauss points

becomes two times that in one 1D cell. Nonetheless, because of their localized functions in space and multiresolution properties, wavelets offer a solution to the problems related to slow convergence in the vicinity of high gradients and re-meshing, which otherwise would have required an even higher computational effort at pre-processing stage with FEM.

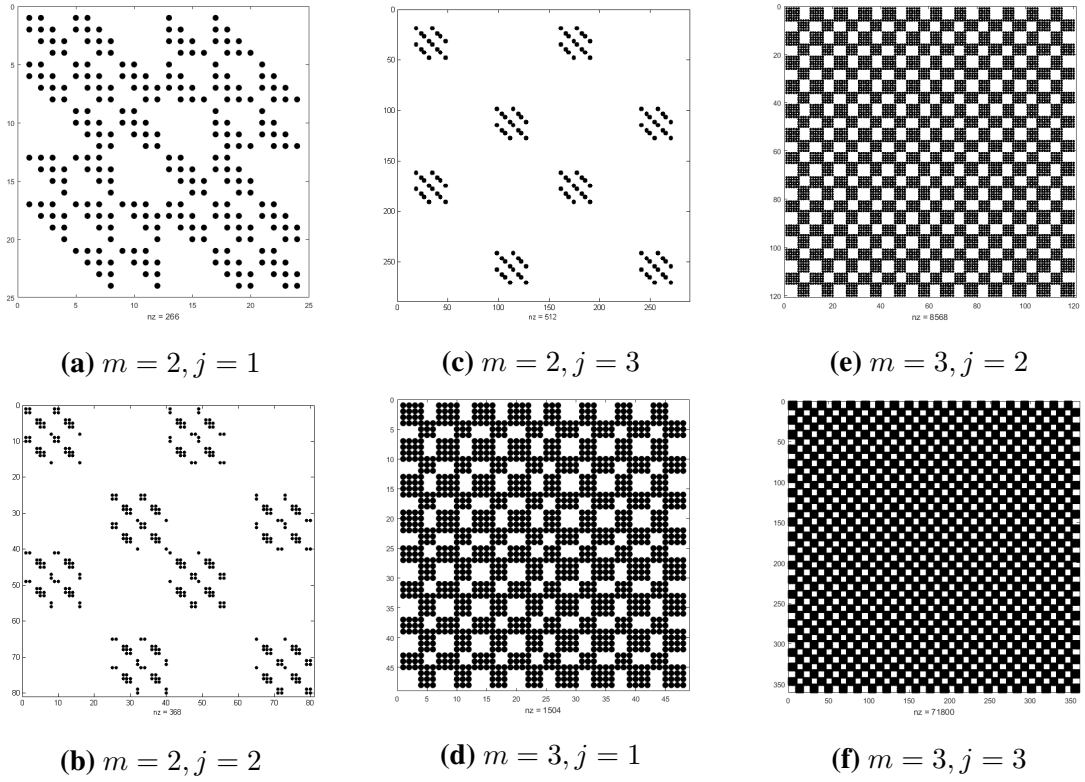

(a) $m = 2, j = 1$ **(c)** $m = 2, j = 3$ **(e)** $m = 3, j = 2$

(b) $m = 2, j = 2$ **(d)** $m = 3, j = 1$ **(f)** $m = 3, j = 3$

Figure 3.25: Sparseness of stiffness matrix for linear and quadratic scaling functions at different resolutions when one background cell per element is used for integration

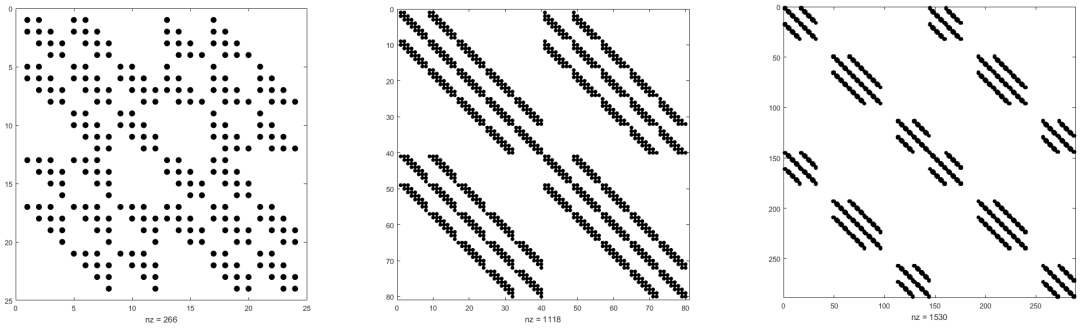

(a) $m = 2, j = 1$ **(b)** $m = 2, j = 2$ **(c)** $m = 2, j = 3$

Figure 3.26: Sparseness of stiffness matrix for linear scaling functions at different resolutions when two background cells per element is used for integration

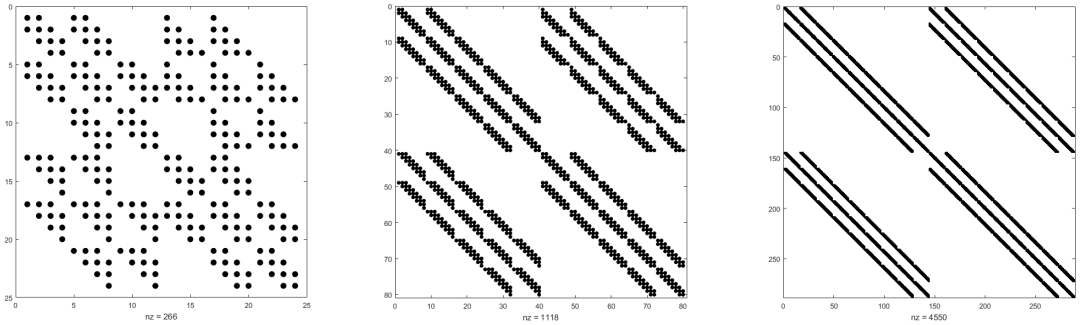

(a) $m = 2, j = 1$ **(b)** $m = 2, j = 2$ **(c)** $m = 2, j = 3$

Figure 3.27: Sparseness of stiffness matrix for linear scaling functions at different resolutions when four background cells per element is used for integration

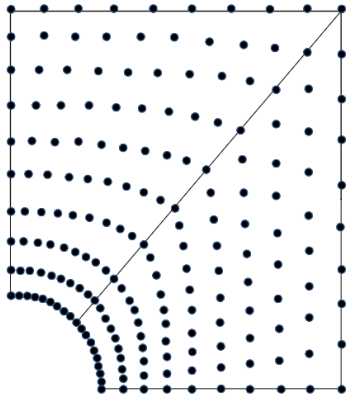

Figure 3.28: Distribution of nodes over the plate with a hole using $m = 3, j = 3$

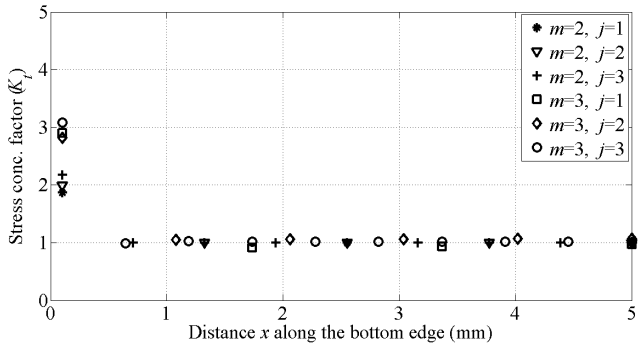

Figure 3.29: Stress concentration factor (K_t) plotted along $y = 0$ with linear and quadratic BSWI scaling functions using two-point integration

3.4 Conclusion

In the current chapter, a background cell-based Gauss point integration approach is proposed for BSWI WFEM. Background cells are placed over the BSWI WFEM element solving domain and Gauss points are positioned inside each background cell. The dimensions of the background cells are varied and its effect on the condition number and sparseness of the element stiffness matrix is studied for 1D and 2D problems. Further, the detailed analysis of effect of number of Gauss points within each background cell on the accuracy of the results is also done. Upon analyzing the results of the background cell approach on various numerical examples, it is observed that for both 1D and 2D problems background cell whose vertices coincide with the element nodes with an appropriate selection of quadrature points always results in a well-conditioned stiffness matrix for all the order and resolutions. The present study suggest to have sufficient number of Gauss points in the support domain of scaling functions for constructing a well-conditioned stiffness matrix.

For 1D problem with C_0 continuity, both two- and one-point integration schemes performed well when background cells whose vertices coincide with the element nodes are used. But, in the case of an Euler-Bernoulli beam, one-point integration results in an ill-conditioned stiffness matrix because of insufficient number of Gauss points and only two-point integration is able to give a well-conditioned stiffness matrix and accurate results. Further in the case of a TBT used for thin beams, it is observed that relative error in displacement norm is less when one-point quadrature is used for integrating the shear terms alone in comparison with the error encountered when two-point integration is used for all the terms at a given order and resolution. Finally, a 2D plate with a hole subjected

to far field stress is considered for analysis. Here, with background cell coinciding with element nodes, two-point integration gives accurate results in comparison with one-point integration. In all other cases, it is found that support domain of scaling functions does not possess sufficient number of Gauss points and, hence, leads to ill-conditioned matrices.

To conclude, the current chapter shows that the accuracy of the solution for the given order and resolution of BSWI scaling function is improved when the size of the background cells is decreased and more number of Gauss points, as encountered in two-point integration approach is used. This invariably leads to a more computational effort at higher resolutions, but this disadvantage is overcome by the MRA properties of the wavelets which aid in reducing its computational effort in highly mesh sensitive problems as seen in plate with a hole problem.

Hence, the proposed background cell based numerical integration scheme for BSWI WFEM, in which a background cell whose vertices coincide with the element nodes is used to evaluate the integrals in the forthcoming formulations. The stochastic BSWI WFEM formulation for problems in elasto-statics and beams is shown in the next chapter.

Chapter 4

Stochastic BSWI WFEM formulation for linear problems in elasto-statics

The current chapter presents the formulation of stochastic BSWI based WFEM for 1D and 2D problems in elasto-statics and beams wherein, the spatial variation of modulus of elasticity is modelled as a homogeneous random field. Numerical examples of beams based on EBT and TBT are solved during the study. BSWI scaling functions are used for the discretization of the random field and the response statistics are obtained using the perturbation approach. The results from perturbation approach are compared with that obtained from MCS. A parametric study is also done to understand the effect of different coefficient of variation (CV) values and correlation length parameters on the response statistics. For 1D problem in particular, results from proposed stochastic WFEM method are compared with those found using SFEM wherein random field discretization is done using Lagrange shape functions. Furthermore, normalized computational times for the execution of perturbation approach and MCS based on WFEM are evaluated and compared with those obtained for FEM.

4.1 Formulation of stochastic BSWI element for elasto-statics and beams

In the current work, the Young's modulus is considered as a spatially varying homogeneous random field. Consequently, the equilibrium equations given in Equation 3.1, and the generalized functional of total potential for 1D and 2D problems as given in Equation 3.4 and Equation 3.23 will also become stochastic in nature and hence the response too. This necessitates for modelling of random fields present in the physical system. In

order to simplify the algebraic equations required to estimate the statistics, it is a general practice to transform the field to a Gaussian field before modelling [20]. In the current study $E(\mathbf{x})$ is modelled using a homogeneous Gaussian field. However, to demonstrate that the proposed method also works for non-Gaussian fields, $E(\mathbf{x})$ is modelled using a homogeneous lognormal field for 1D numerical examples (bar and beam). If $E(\mathbf{x})$ is a Gaussian random field with mean μ_E, it can be written as [20],

$$E(\mathbf{x}) = \mu_E \left(1 + \alpha(\mathbf{x})\right) \tag{4.1}$$

where, $\alpha(\mathbf{x})$ is the zero mean Gaussian field with exponential auto-covariance kernel given as,

$$\Gamma_\alpha = \sigma_\alpha^2 exp\left[-\left(\sum_i^n \frac{|\Delta_i|}{c_i}\right)\right] \tag{4.2}$$

Here, $n \in \Re^n$, Δ_i is the distance between 2 points x_a, x_b along i, c_i is the correlation length parameter which determines the statistical correlation of field variable in the domain and σ_α is the standard deviation of zero mean random field, which can be expressed in terms of σ_E of $E(\mathbf{x})$ as,

$$\sigma_\alpha = \sigma_E / \mu_E \tag{4.3}$$

However, when $E(\mathbf{x})$ is a homogeneous lognormal field with mean μ_{E_l} and standard deviation σ_{E_l}, it is expressed in terms of $\alpha(\mathbf{x})$ as,

$$E(\mathbf{x}) = C_l exp\left(\alpha(\mathbf{x})\right) \tag{4.4}$$

with,

$$C_l = \frac{\mu_{E_l}^2}{\sqrt{\mu_{E_l}^2 + \sigma_{E_l}^2}} \tag{4.5}$$

The auto-covariance kernel for $\alpha(\mathbf{x})$ is written as [199],

$$\Gamma_\alpha = ln\left(1 + \frac{\sigma_{E_l}^2}{\mu_{E_l}^2}\right) exp\left[-\left(\sum_i^n \frac{|\Delta_i|}{c_i}\right)\right] \tag{4.6}$$

A transformation to Gaussian field from other distributions can be done using suitable transformation models [200]. To evaluate the integrals defined in Equation 3.9 and

Equation 3.32, an explicit expression for $E(\mathbf{x})$, and hence $\alpha(\mathbf{x})$ as a function of spatial coordinates is necessary. But $\alpha(\mathbf{x})$ being a random field does not possess an explicit expression and hence requires an approximation. Generally, this is done by approximating a function over a set of random variables distributed in the domain obtained by discretization of the field and is known as random field discretization [8, 90, 201, 202]. In the current work, it is proposed to use a shape function method for random field modelling. Shape function method is found to give better approximation when compared to KL expansion technique [95]. Shape function method using Lagrange interpolation and moving least square shape functions has been employed in SFEM [3] and stochastic meshless methods [20] respectively. In the present study, it is proposed to use wavelet functions to model both the random field and response.

4.1.1 Stochastic BSWI WFEM bar element

On similar lines, as the displacement field is approximated in Equation 3.5, the unknown Gaussian random field can be approximated in the element solving domain ξ in terms of wavelet scaling functions as,

$$\alpha(\xi) = \sum_{k=-m_r+1}^{2_r^j-1} b_{m_r,k}^{j_r} \phi_{m_r,k}^{j_r}(\xi) = \boldsymbol{\varphi_R} \boldsymbol{b^e} \tag{4.7}$$

where, $\boldsymbol{\varphi_R} = \left\{ \phi_{m_r,-m_r+1}^{j_r}(\xi) ..... \phi_{m_r,2^{j_r}-1}^{j_r}(\xi) \right\}$ is row vector of BSWI scaling functions, $\boldsymbol{b^e} = \left\{ b_{m_r,-m_r+1}^{j_r}, b_{m_r,-m_r+2}^{j_r} ..... b_{m_r,2^{j_r}-1}^{j_r} \right\}^T$ is column vector of wavelet coefficients that needs to be determined and m_r, j_r are the order and resolution of BSWI scaling functions selected for modelling the random field. The subscripts $\boldsymbol{R}, r$ used here denote that the function or variable used is associated with random field. It can be noted from Equation 3.5 and Equation 4.7 that the order and resolution that is used for the discretization of the displacement field and random field can be different from each other. The unknown random field function can be expressed in terms of C_0 element type transformation matrix as,

$$\alpha(\xi) = \boldsymbol{\varphi_R} \left(\boldsymbol{R_R^e} \right)^{-1} \boldsymbol{\alpha_R^e} = \boldsymbol{\varphi_R} \boldsymbol{T_R^e} \boldsymbol{\alpha_R^e} \tag{4.8}$$

where, $\boldsymbol{\alpha_R^e} = \left\{ \alpha_{1R}, \alpha_{2R}, ... \alpha_{(n+1)R} \right\}^T$ is the set of random variables distributed over the domain of the element. Thus, element stiffness coefficients and hence the element displacements will become functions of random variables $\boldsymbol{\alpha_R^e}$ and in general Equation 3.8

can be written as,

$$\boldsymbol{K^e}(\boldsymbol{\alpha_R^e})\boldsymbol{u^e}(\boldsymbol{\alpha_R^e}) = \boldsymbol{F^e} \tag{4.9}$$

Here, $\boldsymbol{K^e}$ is the elemental stochastic stiffness matrix. When $E(\mathbf{x})$ is modelled as homogeneous Gaussian field as given in Equation 4.1, the $\boldsymbol{K^e}$ in Equation 3.9 can be written as,

$$\left.\begin{aligned}\boldsymbol{K^e} = \frac{\mu_E A}{l_{ex}} \int_0^1 (\boldsymbol{T^e})^T \left(\frac{d\boldsymbol{\varphi}}{d\xi}\right)^T \left(\frac{d\boldsymbol{\varphi}}{d\xi}\right) (\boldsymbol{T^e})\, d\xi + \\ \frac{\mu_E A}{l_{ex}} \int_0^1 \left(\boldsymbol{\varphi_R T_R^e \alpha_R^e}\right) (\boldsymbol{T^e})^T \left(\frac{d\boldsymbol{\varphi}}{d\xi}\right)^T \left(\frac{d\boldsymbol{\varphi}}{d\xi}\right) (\boldsymbol{T^e})\, d\xi\end{aligned}\right\} \tag{4.10}$$

When $E(\mathbf{x})$ is modelled as a homogeneous lognormal field as given in Equation 4.4, the $\boldsymbol{K^e}$ in Equation 3.9 can be written as,

$$\left.\begin{aligned}\boldsymbol{K^e} = \frac{\mu_{E_l} A}{l_{ex}\sqrt{1+\frac{\sigma_{E_l}^2}{\mu_{E_l}^2}}} \int_0^1 exp^{(\boldsymbol{\varphi_R T_R^e \alpha_R^e})} \\ (\boldsymbol{T^e})^T \left(\frac{d\boldsymbol{\varphi}}{d\xi}\right)^T \left(\frac{d\boldsymbol{\varphi}}{d\xi}\right) (\boldsymbol{T^e})\, d\xi\end{aligned}\right\} \tag{4.11}$$

The element stochastic stiffness matrices as given in Equations 4.9 for all the sub-domains can be assembled to form the algebraic set of respective global stochastic equilibrium equations as,

$$\boldsymbol{K}(\boldsymbol{\alpha_R})\boldsymbol{U}(\boldsymbol{\alpha_R}) = \boldsymbol{F} \tag{4.12}$$

Next, the formulation of stochastic BSWI WFEM plane elasto-statics element is shown.

4.1.2 Stochastic BSWI WFEM plane elasto-statics element

The unknown Gaussian random field can be approximated by taking 2D tensor product of BSWI scaling functions on the same lines as the displacement field is approximated in Equation 3.24 as,

$$\alpha(\xi,\eta) = \boldsymbol{\varphi_R g^e} \tag{4.13}$$

where,

$$\left.\begin{aligned} \boldsymbol{\varphi_R} &= \boldsymbol{\varphi_{1R}} \otimes \boldsymbol{\varphi_{2R}} \\ \boldsymbol{\varphi_{1R}} &= \left\{\phi^{j_r}_{m_r,-m_r+1}(\xi).....\phi^{j_r}_{m_r,2^{j_r}-1}(\xi)\right\} \\ \boldsymbol{\varphi_{2R}} &= \left\{\phi^{j_r}_{m_r,-m_r+1}(\eta).....\phi^{j_r}_{m_r,2^{j_r}-1}(\eta)\right\} \\ \boldsymbol{g^e} &= \left\{g_1, g_2.....g_{(n+1)^2}\right\}^T \end{aligned}\right\} \tag{4.14}$$

The unknown random field function can be expressed in terms of C_0 element type 2D transformation matrix as,

$$\alpha(\xi,\eta) = \boldsymbol{\varphi_R}\left(\boldsymbol{R^e_R}\right)^{-1}\boldsymbol{\alpha^e_R} = \boldsymbol{N_2}\boldsymbol{\alpha^e_R} \tag{4.15}$$

such that,

$$\left.\begin{aligned} \boldsymbol{R^e_R} &= \boldsymbol{T^e_{1R}} \otimes \boldsymbol{T^e_{2R}} \\ \boldsymbol{T^e_{1R}} &= \left\{\boldsymbol{\varphi^T_{1R}}(\xi_1)\ \boldsymbol{\varphi^T_{1R}}(\xi_2)....\boldsymbol{\varphi^T_{1R}}(\xi_{n+1})\right\}^T \\ \boldsymbol{T^e_{2R}} &= \left\{\boldsymbol{\varphi^T_{2R}}(\eta_1)\ \boldsymbol{\varphi^T_{2R}}(\eta_2)....\boldsymbol{\varphi^T_{2R}}(\eta_{n+1})\right\}^T \end{aligned}\right\} \tag{4.16}$$

Thus, element stiffness coefficients and hence the element displacements will become functions of random variables $\boldsymbol{\alpha^e_R}$. When $E(\mathbf{x})$ is modelled as a homogeneous Gaussian field, the $\boldsymbol{K^e}$ in Equation 3.28 can be written as,

$$\boldsymbol{K^e}(\boldsymbol{\alpha^e_R})\boldsymbol{U^e}(\boldsymbol{\alpha^e_R}) = \boldsymbol{F^e} \tag{4.17}$$

where,

$$\boldsymbol{K^e} = \begin{bmatrix} \boldsymbol{K^e_1} & \boldsymbol{K^e_2} \\ \boldsymbol{K^e_3} & \boldsymbol{K^e_4} \end{bmatrix} + \frac{\mu_E}{1-\nu^2}\int_0^1\int_0^1 \left(\boldsymbol{N_2}\boldsymbol{\alpha^e_R}\right)\boldsymbol{K^e_\beta} d\xi d\eta \tag{4.18}$$

Here, $\boldsymbol{K^e_1}$, $\boldsymbol{K^e_2}$, $\boldsymbol{K^e_3}$ and $\boldsymbol{K^e_4}$ are the components of deterministic matrix as given in Equation 3.31-3.32. Futher, $\boldsymbol{K^e_\beta}$ can be simplified as,

$$\boldsymbol{K^e_\beta} = \begin{bmatrix} \boldsymbol{K^e_{\beta 1}} & \boldsymbol{K^e_{\beta 2}} \\ \boldsymbol{K^e_{\beta 3}} & \boldsymbol{K^e_{\beta 4}} \end{bmatrix} \tag{4.19}$$

such that,

$$\left.\begin{aligned}
\boldsymbol{K}^{\boldsymbol{e}}_{\boldsymbol{\beta 1}} &= \frac{l_{ey}}{l_{ex}}\left(\frac{d\boldsymbol{N_1}}{d\xi}\right)^T\left(\frac{d\boldsymbol{N_1}}{d\xi}\right) + \frac{l_{ex}}{l_{ey}}\left(\frac{1-\nu}{2}\right)\left(\frac{d\boldsymbol{N_1}}{d\eta}\right)^T\left(\frac{d\boldsymbol{N_1}}{d\eta}\right)\\
\boldsymbol{K}^{\boldsymbol{e}}_{\boldsymbol{\beta 2}} &= \nu\left(\frac{d\boldsymbol{N_1}}{d\xi}\right)^T\left(\frac{d\boldsymbol{N_1}}{d\eta}\right) + \left(\frac{1-\nu}{2}\right)\left(\frac{d\boldsymbol{N_1}}{d\eta}\right)^T\left(\frac{d\boldsymbol{N_1}}{d\xi}\right)\\
\boldsymbol{K}^{\boldsymbol{e}}_{\boldsymbol{\beta 3}} &= \nu\left(\frac{d\boldsymbol{N_1}}{d\eta}\right)^T\left(\frac{d\boldsymbol{N_1}}{d\xi}\right) + \left(\frac{1-\nu}{2}\right)\left(\frac{d\boldsymbol{N_1}}{d\xi}\right)^T\left(\frac{d\boldsymbol{N_1}}{d\eta}\right)\\
\boldsymbol{K}^{\boldsymbol{e}}_{\boldsymbol{\beta 4}} &= \frac{l_{ex}}{l_{ey}}\left(\frac{d\boldsymbol{N_1}}{d\eta}\right)^T\left(\frac{d\boldsymbol{N_1}}{d\eta}\right) + \frac{l_{ey}}{l_{ex}}\left(\frac{1-\nu}{2}\right)\left(\frac{d\boldsymbol{N_1}}{d\xi}\right)^T\left(\frac{d\boldsymbol{N_1}}{d\xi}\right)
\end{aligned}\right\} \tag{4.20}$$

The element stochastic stiffness matrices as given in Equations 4.17 for all the sub-domains can be assembled to form the algebraic set of respective global stochastic equilibrium equations on the same lines as shown in Equation 4.12.

4.1.3 Stochastic BSWI WFEM EBT based beam element

In the formulation of stochastic BSWI WFEM EBT based beam element, $E(\mathbf{x})$ is modelled as a homogeneous random field, $w_0(\xi)$ is expressed in terms of C_1 type element transformation matrix and $\alpha(\xi)$ is expressed in terms of C_0 type element transformation matrix. On similar lines, as the deflection field is approximated in Equation 3.11, the unknown random field can be approximated in the element solving domain in terms of BSWI wavelet scaling functions and expressed in terms of elemental transformation matrix. The element stiffness coefficients and hence the element deflections will become functions of random variables $\boldsymbol{\alpha_R}$ and 3.14 can be written as,

$$\boldsymbol{K^e}(\boldsymbol{\alpha^e_R})\boldsymbol{w^e}(\boldsymbol{\alpha^e_R}) = \boldsymbol{F^e} \tag{4.21}$$

When $E(\mathbf{x})$ is modelled as a homogeneous Gaussian field as given in Equation 4.1, $\boldsymbol{K^e}$ in Equation 3.15 can be written as,

$$\left.\begin{aligned}
\boldsymbol{K^e} &= \frac{\mu_E I}{l_{ex}^3}\int_0^1 (\boldsymbol{T^e})^T\left(\frac{d^2\boldsymbol{\varphi}}{d\xi^2}\right)^T\left(\frac{d^2\boldsymbol{\varphi}}{d\xi^2}\right)(\boldsymbol{T^e})\,d\xi\\
&+\frac{\mu_E I}{l_{ex}^3}\int_0^1 \left(\boldsymbol{\varphi_R}\boldsymbol{T^e_R}\boldsymbol{\alpha^e_R}\right)(\boldsymbol{T^e})^T\left(\frac{d^2\boldsymbol{\varphi}}{d\xi^2}\right)^T\left(\frac{d^2\boldsymbol{\varphi}}{d\xi^2}\right)(\boldsymbol{T^e})\,d\xi
\end{aligned}\right\} \tag{4.22}$$

and when $E(\mathbf{x})$ is modelled as a homogeneous lognormal field as given in Equation 4.4,

$\boldsymbol{K^e}$ in Equation 3.15 can be written as,

$$\left.\begin{aligned}\boldsymbol{K^e} = \frac{\mu_{E_l} I}{l_{ex}^3 \sqrt{1+\frac{\sigma_{E_l}^2}{\mu_{E_l}^2}}} \int_0^1 exp^{(\boldsymbol{\varphi_R T_R^e \alpha_R^e})} \\ (\boldsymbol{T^e})^T \left(\frac{d^2\boldsymbol{\varphi}}{d\xi^2}\right)^T \left(\frac{d^2\boldsymbol{\varphi}}{d\xi^2}\right) (\boldsymbol{T^e})\, d\xi\end{aligned}\right\} \tag{4.23}$$

The element stochastic stiffness matrices as given in Equations 4.21 for all the sub-domains can be assembled to form the algebraic set of respective global stochastic equilibrium equations on the same lines as Equation 4.12.

4.1.4 Stochastic BSWI WFEM TBT based beam element

In the formulation of stochastic BSWI WFEM TBT based beam element, $E(\mathbf{x})$ is modelled as homogeneous random field and both $w_0(\xi)$ as well as $\alpha(\xi)$ are expressed in terms of C_0 type element transformation matrix. On similar lines, as the unknown transverse and rotational displacement field functions are approximated in Equation 3.17, the unknown random field can also be approximated in the element solving domain in terms of BSWI wavelet scaling functions and expressed in terms of elemental transformation matrix. The element stiffness coefficients and hence the element deflections will become functions of random variables $\boldsymbol{\alpha_R}$ and Equation 3.20 can be written as,

$$\boldsymbol{K^e}(\boldsymbol{\alpha_R^e})\boldsymbol{W^e}(\boldsymbol{\alpha_R^e}) = \boldsymbol{F^e} \tag{4.24}$$

Further, when $E(\mathbf{x})$ is modelled as a homogeneous random field, $G(\mathbf{x})$ is also modelled as a homogeneous random field from the relation $G(\mathbf{x}) = E(\mathbf{x})/2(1+\nu)$ where, ν is the deterministic Poisson's ratio. When $E(\mathbf{x})$ is modelled as a homogeneous Gaussian field as

given in Equation 4.1, the components of $\boldsymbol{K^e}$ in Equation 3.21 and 3.22 can be written as,

$$\left.\begin{aligned}
\boldsymbol{K_1^e} &= \frac{K_s\mu_G A}{l_{ex}}\left(\boldsymbol{T^e}\right)^T\left(\int_0^1\left(\frac{d\boldsymbol{\varphi}}{d\xi}\right)^T\left(\frac{d\boldsymbol{\varphi}}{d\xi}\right)d\xi\right)\left(\boldsymbol{T^e}\right)\\
&+\frac{K_s\mu_G A}{l_{ex}}\left(\boldsymbol{T^e}\right)^T\left(\int_0^1\left(\boldsymbol{\varphi_R T_R^e \alpha_R^e}\right)\left(\frac{d\boldsymbol{\varphi}}{d\xi}\right)^T\left(\frac{d\boldsymbol{\varphi}}{d\xi}\right)d\xi\right)\left(\boldsymbol{T^e}\right)\\
\boldsymbol{K_2^e} &= -K_s\mu_G A\left(\boldsymbol{T^e}\right)^T\left(\int_0^1\left(\frac{d\boldsymbol{\varphi}}{d\xi}\right)^T\left(\boldsymbol{\varphi}\right)d\xi\right)\left(\boldsymbol{T^e}\right)\\
&-K_s\mu_G A\left(\boldsymbol{T^e}\right)^T\left(\int_0^1\left(\boldsymbol{\varphi_R T_R^e \alpha_R^e}\right)\left(\frac{d\boldsymbol{\varphi}}{d\xi}\right)^T\left(\boldsymbol{\varphi}\right)d\xi\right)\left(\boldsymbol{T^e}\right)\\
\boldsymbol{K_3^e} &= \left(\boldsymbol{K_2^e}\right)^T\\
\boldsymbol{K_4^e} &= \frac{\mu_E I}{l_{ex}}\left(\boldsymbol{T^e}\right)^T\left(\int_0^1\left(\frac{d\boldsymbol{\varphi}}{d\xi}\right)^T\left(\frac{d\boldsymbol{\varphi}}{d\xi}\right)d\xi\right)\left(\boldsymbol{T^e}\right)+\\
&K_s\mu_G A l_{ex}\left(\boldsymbol{T^e}\right)^T\left(\int_0^1\left(\boldsymbol{\varphi}\right)^T\left(\boldsymbol{\varphi}\right)d\xi\right)\left(\boldsymbol{T^e}\right)\\
&+\frac{\mu_E I}{l_{ex}}\left(\boldsymbol{T^e}\right)^T\left(\int_0^1\left(\boldsymbol{\varphi_R T_R^e \alpha_R^e}\right)\left(\frac{d\boldsymbol{\varphi}}{d\xi}\right)^T\left(\frac{d\boldsymbol{\varphi}}{d\xi}\right)d\xi\right)\left(\boldsymbol{T^e}\right)+\\
&K_s\mu_G A l_{ex}\left(\boldsymbol{T^e}\right)^T\left(\int_0^1\left(\boldsymbol{\varphi_R T_R^e \alpha_R^e}\right)\left(\boldsymbol{\varphi}\right)^T\left(\boldsymbol{\varphi}\right)d\xi\right)\left(\boldsymbol{T^e}\right)
\end{aligned}\right\} \tag{4.25}$$

When $E(\mathbf{x})$ is modelled as a homogeneous lognormal field as given in Equation 4.4, the components of $\boldsymbol{K^e}$ in Equation 3.21 and 3.22 can be written as,

$$\left.\begin{aligned}
\boldsymbol{K_1^e} &= \frac{K_s C_l A}{2(1+\nu)l_{ex}}\left(\boldsymbol{T^e}\right)^T\left(\int_0^1 exp^{\left(\boldsymbol{\varphi_R T_R^e \alpha_R^e}\right)}\left(\frac{d\boldsymbol{\varphi}}{d\xi}\right)^T\left(\frac{d\boldsymbol{\varphi}}{d\xi}\right)d\xi\right)\left(\boldsymbol{T^e}\right)\\
\boldsymbol{K_2^e} &= -\frac{K_s C_l A}{2(1+\nu)}\left(\boldsymbol{T^e}\right)^T\left(\int_0^1 exp^{\left(\boldsymbol{\varphi_R T_R^e \alpha_R^e}\right)}\left(\frac{d\boldsymbol{\varphi}}{d\xi}\right)^T\left(\boldsymbol{\varphi}\right)d\xi\right)\left(\boldsymbol{T^e}\right)\\
\boldsymbol{K_3^e} &= \left(\boldsymbol{K_2^e}\right)^T\\
\boldsymbol{K_4^e} &= \frac{C_l I}{l_{ex}}\left(\boldsymbol{T^e}\right)^T\left(\int_0^1 exp^{\left(\boldsymbol{\varphi_R T_R^e \alpha_R^e}\right)}\left(\frac{d\boldsymbol{\varphi}}{d\xi}\right)^T\left(\frac{d\boldsymbol{\varphi}}{d\xi}\right)d\xi\right)\left(\boldsymbol{T^e}\right)+\\
&\frac{K_s C_l A l_{ex}}{2(1+\nu)}\left(\boldsymbol{T^e}\right)^T\left(\int_0^1 exp^{\left(\boldsymbol{\varphi_R T_R^e \alpha_R^e}\right)}\left(\boldsymbol{\varphi}\right)^T\left(\boldsymbol{\varphi}\right)d\xi\right)\left(\boldsymbol{T^e}\right)
\end{aligned}\right\} \tag{4.26}$$

where, C_l is obtained from Equation 4.5. The element stochastic stiffness matrices as

given in Equations 4.24 for all the sub-domains can be assembled to form the algebraic set of respective global stochastic equilibrium equations on the same lines as Equation 4.12.

4.1.5 Stochastic BSWI WFEM for elastic buckling of columns

The generalized functional of potential energy governing static buckling of columns is given as,

$$\Pi = \int_0^L \frac{1}{2} EI \left(\frac{d^2 w_0}{dx^2} \right)^2 dx - \int_0^L \frac{P_c}{2} \left(\frac{dw_0}{dx} \right)^2 dx \tag{4.27}$$

where, P_c is the axial compressive load and rest of the parameters are same as considered in Equation 3.10. Here, one BSWI WFEM beam element based on EBT, as given in 3.1.1.2 is used for modelling the deflection field. Upon substituting the deflection field of Equation 3.12 into the weak form and invoking the stationary condition for variation of admissible deflections, the solution of static buckling of columns is obtained in the form of an Eigen value problem as,

$$\left[\boldsymbol{K^e} - P_c \boldsymbol{G^e} \right] \boldsymbol{w^e} = 0 \tag{4.28}$$

where, $\boldsymbol{K^e}$ is the elemental stiffness matrix as given in Equation 3.14 and $\boldsymbol{G^e}$ is the elemental geometric stiffness matrix given as,

$$\boldsymbol{G^e} = \frac{1}{l_{ex}} \int_0^1 (\boldsymbol{T^e})^T \left(\frac{d\boldsymbol{\varphi}}{d\xi} \right)^T \left(\frac{d\boldsymbol{\varphi}}{d\xi} \right) (\boldsymbol{T^e}) \, d\xi \tag{4.29}$$

The Eigen values P_c from Equation 4.28 correspond to the buckling loads and the Eigen vectors $\boldsymbol{w^e}$ correspond to the mode shapes.

When the Young's modulus $E(\mathbf{x})$ is modelled as a spatially varying homogeneous random field, the generalized functional of total potential as given in Equation 4.27 along with response, will also become stochastic in nature. Thus, element stiffness coefficients, Eigen values and Eigen vectors will become functions of random variables $\boldsymbol{\alpha_R^e}$ and Equation 4.28 becomes a stochastic Eigen value problem that can be written as,

$$\left[\boldsymbol{K^e}(\boldsymbol{\alpha_R^e}) - P_c(\boldsymbol{\alpha_R^e}) \boldsymbol{G^e} \right] \boldsymbol{w^e}(\boldsymbol{\alpha_R^e}) = 0 \tag{4.30}$$

Here, $\boldsymbol{K^e}$ is the elemental stochastic stiffness matrix for beams based on EBT formulation as given in Equations 4.22 and 4.23. The element stiffness matrices $\boldsymbol{K^e}$ and $\boldsymbol{G^e}$ are obtained for all the sub-domains and assembled together to obtain a global stochastic

Eigen value problem. From the global stochastic equilibrium equations, the second moment characteristics of deflections are calculated using the perturbation method which is discussed in the next section.

4.2 Perturbation method

A Gaussian random field can be completely described by the mean, variance and auto-correlation function of its random variables. The response statistics aids to understand how the uncertainties in the input are propagating through the mechanical system. Several methods (perturbation method, weighted integral method, quadrature method) exist for the calculation of the second moment response statistics. However, from among these perturbation method has been selected due to its simplicity, good accuracy and low computational cost when compared with other methods used for calculating second moment statistics [95].

On the contrary, it is well known that the second order perturbation approach based on Taylor series expansion provides accurate results in comparison with MCS only when the CV is kept around 15-20%. Kamiński proposed the generalized stochastic perturbation approach [203] for any order of Taylor series expansion wherein, higher order moments and coefficients are calculated to recognize the resulting distributions of structural response and allow for larger input coefficient of variation (20-25%). A method based on an ad hoc expansion of the displacement response with respect to random variables, which claim to maintain good accuracy even at high degree of uncertainty was proposed by Falsone and Impollonia [204, 205]. However, the issue with the higher order methods is that it also increases the computational effort. Further, in cases wherein, the deviation between the results obtained from second order perturbation method and MCS is around 5%, there is no substantial gain in accuracy with higher order methods. Moreover, since uncertainty in most of the engineering materials can be accounted with a CV of up to 20%, second order perturbation methods are sufficient to calculate the statistics with acceptable accuracy. Hence, in the present thesis classical perturbation approach based on Taylor series expansion, only first and second order truncation, is considered to investigate the performance of the proposed method.

Perturbation method uses the expansion of the global stiffness matrix and the displacement vector via Taylor series [3, 20, 206]. It is based on the assumption that the variance of the random field should be small. Let $\mathbf{\Lambda} = \{\alpha_i\}_{i=1}^{N}$ is a vector of zero mean random variables representing the random field in the global domain Ω. The Taylor

series expansion of global stiffness matrix $\boldsymbol{K}$ and displacement vector $\boldsymbol{U}$ (in case of beams/columns it is $\boldsymbol{W}$) can be obtained as,

$$\boldsymbol{K} = \boldsymbol{K_0} + \sum_{i=1}^{N} \boldsymbol{K_i^I}\alpha_i + \frac{1}{2}\sum_{i=1}^{N}\sum_{j=1}^{N} \boldsymbol{K_{ij}^{II}}\alpha_i\alpha_j + ..., \tag{4.31}$$

$$\boldsymbol{U} = \boldsymbol{U_0} + \sum_{i=1}^{N} \boldsymbol{U_i^I}\alpha_i + \frac{1}{2}\sum_{i=1}^{N}\sum_{j=1}^{N} \boldsymbol{U_{ij}^{II}}\alpha_i\alpha_j + ..., \tag{4.32}$$

Upon substitution into equilibrium equations and equating the terms with the same order the following equations are obtained,

$$\left.\begin{aligned} \boldsymbol{U_0} &= \boldsymbol{K_0^{-1}}\boldsymbol{F_0}, \\ \boldsymbol{U_i^I} &= -\boldsymbol{K_0^{-1}}\left(\boldsymbol{K_i^I}\boldsymbol{U_0}\right), \\ \boldsymbol{U_{ij}^{II}} &= -\boldsymbol{K_0^{-1}}\left(\boldsymbol{K_i^I}\boldsymbol{U_j^I} + \boldsymbol{K_j^I}\boldsymbol{U_i^I} + \boldsymbol{K_{ij}^{II}}\boldsymbol{U_0}\right) \end{aligned}\right\} \tag{4.33}$$

where, $\boldsymbol{K_0}$, $\boldsymbol{U_0}$ and $\boldsymbol{F_0}$ are evaluated at $\boldsymbol{K}(0)$, $\boldsymbol{U}(0)$ and $\boldsymbol{F}(0)$ respectively; and $(.)_i^I = \left.\frac{\partial(.)}{\partial\alpha_i}\right|_{\boldsymbol{\Lambda}=0}$ and $(.)_{ij}^{II} = \left.\frac{\partial^2(.)}{\partial\alpha_i\partial\alpha_j}\right|_{\boldsymbol{\Lambda}=0}$. By applying expectation and variance operators on Eq.4.32, first and second order perturbation approximations can be obtained as,

First order approximation

$$\left.\begin{aligned} \boldsymbol{\mu}_U &= \boldsymbol{U_0}, \\ \boldsymbol{\gamma}_U &= \sum_{i=1}^{N}\sum_{j=1}^{N} \boldsymbol{U_i^I}\left(\boldsymbol{U_j^I}\right)^T \boldsymbol{\Gamma_\alpha}\left(\alpha_i, \alpha_j\right) \end{aligned}\right\} \tag{4.34}$$

Second order approximation

$$\left.\begin{aligned} \boldsymbol{\mu}_U &= \boldsymbol{U_0} + \frac{1}{2}\sum_{i=1}^{N}\sum_{j=1}^{N} \boldsymbol{U_{ij}^{II}}\boldsymbol{\Gamma_\alpha}\left(\alpha_i, \alpha_j\right), \\ \boldsymbol{\gamma}_U &= \sum_{i=1}^{N}\sum_{j=1}^{N} \boldsymbol{U_i^I}\left(\boldsymbol{U_j^I}\right)^T \boldsymbol{\Gamma_\alpha}\left(\alpha_i, \alpha_j\right) + \\ &\frac{1}{4}\sum_{i=1}^{N}\sum_{j=1}^{N}\sum_{k=1}^{N}\sum_{l=1}^{N} \boldsymbol{U_{ij}^{II}}\left(\boldsymbol{U_{kl}^{II}}\right)^T \{\boldsymbol{\Gamma_\alpha}\left(\alpha_i, \alpha_l\right)\boldsymbol{\Gamma_\alpha}\left(\alpha_j, \alpha_k\right) + \\ &\boldsymbol{\Gamma_\alpha}\left(\alpha_i, \alpha_k\right)\boldsymbol{\Gamma_\alpha}\left(\alpha_j, \alpha_l\right)\} \end{aligned}\right\} \tag{4.35}$$

Similarly, statistics of other response functions of interest, like stresses and strains can also be found out. Further, the study can also be extended to a reliability analysis on the same

lines as shown in Rahman and Rao [207].

4.2.1 Perturbation approximation for buckling of columns

In addition to the Taylor series expansion of the global stiffness matrix and displacement vector (Eigen vector) as shown in Equations 4.31 and 4.32, the perturbation method for buckling of columns uses the expansion of the axial compressive load (Eigen values), which is also a function of random variables. The Taylor series expansion of the Eigen values is given as,

$$P_c = P_{c0} + \sum_{i=1}^{N} P_{ci}^{I} \alpha_i + \frac{1}{2} \sum_{i=1}^{N} \sum_{j=1}^{N} P_{cij}^{II} \alpha_i \alpha_j + ..., \tag{4.36}$$

where, P_{c0} is the deterministic value evaluated at $P_c(0)$. The partial derivatives of Eigen values P_{ci}^{I} and P_{cij}^{II} with respect to the random variables can be obtained as follows. Upon substituting the Taylor series expansion of the global stiffness matrix, Eigen values and Eigen vectors as given in Equations 4.31, 4.32 and 4.36 respectively into the global stochastic Eigen value problem and rearranging the terms of the same order, the following equations are obtained,

$$\left[\boldsymbol{K_0} - P_{c0}\boldsymbol{G}\right] \boldsymbol{W_0} = 0 \tag{4.37}$$

$$\left[\boldsymbol{K_0} - P_{c0}\boldsymbol{G}\right] \boldsymbol{W_i^I} + \left[\boldsymbol{K_i^I} - P_{ci}^{I}\boldsymbol{G}\right] \boldsymbol{W_0} = 0 \tag{4.38}$$

$$\left.\begin{aligned}\left[\boldsymbol{K_0} - P_{c0}\boldsymbol{G}\right] \boldsymbol{W_{ij}^{II}} + \left[\boldsymbol{K_i^I} - P_{ci}^{I}\boldsymbol{G}\right] \boldsymbol{W_j^I} + \left[\boldsymbol{K_j^I} - P_{cj}^{I}\boldsymbol{G}\right] \boldsymbol{W_i^I} + \\ \left[\boldsymbol{K_{ij}^{II}} - P_{cij}^{II}\boldsymbol{G}\right] \boldsymbol{W_0} = 0\end{aligned}\right\} \tag{4.39}$$

Here, $[\boldsymbol{K_0} - P_{c0}\boldsymbol{G}]$ is symmetric, which leads to,

$$\left[\boldsymbol{K_0} - P_{c0}\boldsymbol{G}\right] = \left[\boldsymbol{K_0} - P_{c0}\boldsymbol{G}\right]^T \tag{4.40}$$

By pre-multiplying Equations 4.38 and 4.39 with $\boldsymbol{W_0}^T$ and using 4.40 leads to,

$$\left[\left(\boldsymbol{K_0} - P_{c0}\boldsymbol{G}\right)\boldsymbol{W_0}\right]^T \boldsymbol{W_i^I} + \boldsymbol{W_0}^T \left[\boldsymbol{K_i^I} - P_{ci}^{I}\boldsymbol{G}\right] \boldsymbol{W_0} = 0 \tag{4.41}$$

$$\left.\begin{aligned}\left[\left(\boldsymbol{K_0}-P_{c0}\boldsymbol{G}\right)\boldsymbol{W_0}\right]^T\boldsymbol{W_{ij}^{II}}+\boldsymbol{W_0}^T\left[\boldsymbol{K_i^I}-P_{ci}^I\boldsymbol{G}\right]\boldsymbol{W_j^I}+\boldsymbol{W_0}^T\left[\boldsymbol{K_j^I}-P_{cj}^I\boldsymbol{G}\right]\boldsymbol{W_i^I}+\\ \boldsymbol{W_0}^T\left[\boldsymbol{K_{ij}^{II}}-P_{cij}^{II}\boldsymbol{G}\right]\boldsymbol{W_0}=0\end{aligned}\right\} \tag{4.42}$$

Equation 4.41 can be simplified as,

$$P_{ci}^{\ I}=\left[\boldsymbol{W_0}^T\boldsymbol{G}\boldsymbol{W_0}\right]^{-1}\left[\boldsymbol{W_0}^T\boldsymbol{K_i^I}\boldsymbol{W_0}\right] \tag{4.43}$$

Upon substituting Equation 4.43 into 4.41, $\boldsymbol{W_i^I}$ can be obtained, which can be further substituted into Equation 4.42 to obtain,

$$\left.\begin{aligned}P_{cij}^{II}=\left[\boldsymbol{W_0}^T\boldsymbol{G}\boldsymbol{W_0}\right]^{-1}\Big(\boldsymbol{W_0}^T\left[\boldsymbol{K_i^I}-P_{ci}^I\boldsymbol{G}\right]\boldsymbol{W_j^I}+\boldsymbol{W_0}^T\left[\boldsymbol{K_j^I}-P_{cj}^I\boldsymbol{G}\right]\boldsymbol{W_i^I}+\\ \boldsymbol{W_0}^T\boldsymbol{K_{ij}^{II}}\boldsymbol{W_0}\Big)\end{aligned}\right\} \tag{4.44}$$

By substituting Equation 4.44 into 4.42, $\boldsymbol{W_{ij}^{II}}$ can be obtained. Further, by applying the expectation and variance operators on the first order or second order approximation of Equation 4.36 and by substituting $P_{ci}^{\ I}$ and P_{cij}^{II} from Equation 4.43 and 4.44 respectively, the first and second order statistics of critical buckling load ($\mu_{P_{cr}}$, $\gamma_{P_{cr}}$) can be obtained on the same lines as given in Equations 4.34 and 4.35. Similarly, statistics of other response functions of interest, like $\boldsymbol{W}$ can also be found out. In the next section, a few 1D and 2D numerical examples are solved based on the preceding formulations and the results are analyzed.

4.3 Numerical examples

4.3.1 Numerical examples for 1D bar and 2D plane elasto-statics

Three numerical examples are solved based on the proposed stochastic BSWI WFEM formulations for 1D and 2D problems in elasto-statics. Once the response statistics are calculated via perturbation method, the results are compared with the statistics obtained from MCS.

4.3.1.1 One-dimensional bar with a linear body force

In this example, a 1D bar with a linear body force $b(x) = x$ as shown in Figure 3.9 in chapter 3 is considered for analysis. Two cases are studied in which the modulus of elasticity is modelled as a homogeneous random field with a Gaussian distribution as given by Equation 4.1; and with a lognormal distribution as given in Equation 4.4. For both the cases, the results from stochastic WFEM wherein both the input random field and response are discretized using BSWI scaling functions are compared with those obtained from SFEM wherein both random field and response are discretized using Lagrange shape functions. The mean value of Young's modulus is taken as $\mu_E = 1 \times 10^5$MPa for both the distributions, with $Length(L) = 100$mm and $area = 1\text{mm}^2$. The entire domain of the bar is modelled using one BSWI C_0 type element.

Initially, a convergence study is done to determine the order and resolution of scaling functions used for displacement approximation. Figure 4.1 and 4.2 shows the displacement and stress obtained from deterministic WFEM analysis for different order and resolution. It is observed that converged results in displacement and axial stress can be obtained when linear order $m = 2$ and quadratic order $m = 3$ BSWI wavelet scaling functions with resolution $j = 3$ are used. Hence, for further analysis the displacement field is approximated using the order $m = \{2, 3\}$ and resolution $j = 3$. The minimum resolution needed to accurately capture the spatially varying Young's modulus while approximating with the wavelet based shape functions is established by examining the mean and standard deviation of generated sample values along the bar from a MCS. From a convergence study, based on the calculation of relative percentage variation in L^2 norm of mean and standard deviation values of Young's modulus for various MCS sample size; it is noted that a variation of less than 1% is obtained when the MCS sample size is 5000. Hence, a sample size of 5000 is selected to be used during the process. Further, this study is extended to Lagrange shape functions also to identify the number of nodes required for random field discretization. The process is repeated for both Gaussian and non-Gaussian approximations and is explained in the following discussions.

Case 1: Random field $E(\boldsymbol{x})$ follows Gaussian distribution

The mean values and standard deviation of a Young's modulus with a Gaussian approximation as defined in Equation 4.1 is reproduced from the MCS samples when random field α is modelled using Equation 4.7. The same has been calculated when α is modelled with the help of linear and quadratic Lagrange shape functions too. Variation of mean values and standard deviation of Young's modulus at $x = 100$mm for the discretization of the random field using different number of random variables is shown

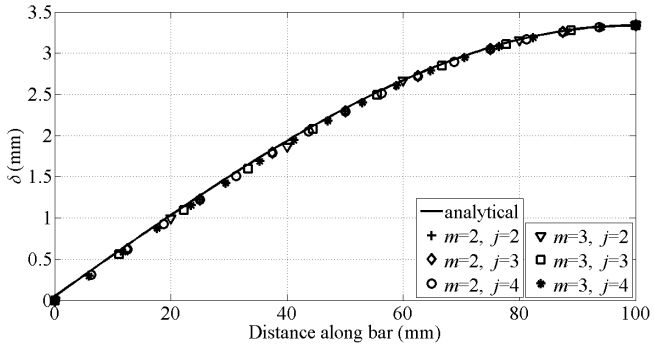

Figure 4.1: Variation of axial displacement (δ) along the length of the rod obtained from a deterministic study while linear and quadratic BSWI scaling functions are used to model displacement

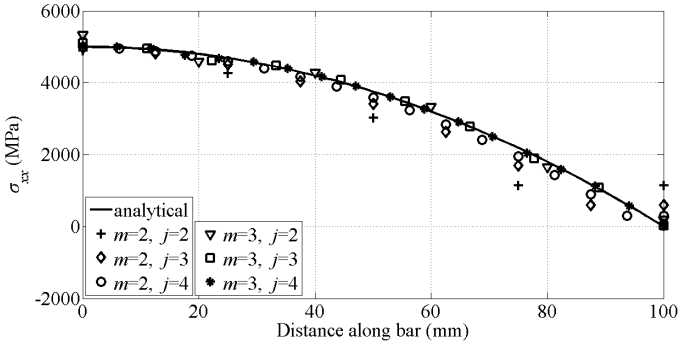

Figure 4.2: Variation of axial stress (σ_{xx}) along the length of the rod obtained from a deterministic study while linear and quadratic BSWI scaling functions are used to model displacement

in Figure 4.3 and 4.4 respectively. It can be observed that a resolution of $j = 1$ with linear and quadratic scaling functions resulting in 3 and 4 nodes respectively captures the mean and standard deviation values of Young's modulus accurately. Further, in the case of FEM based shape function, 2 linear elements and 2 quadratic elements resulting in 3 and 5 nodes respectively is sufficient to capture the first moment statistics of the field accurately.

Using MCS, the values of the first row of covariance matrix are found out for various correlation length parameters using linear and quadratic WFEM and FEM based shape functions and compared with the exact values as shown in Figure 4.5. A CV of 10% is considered for the study. A resolution of $j = 1$ is used for the discretization of a random field using WFEM. It can be observed that the covariance matrix values calculated using WFEM and FEM are in good agreement with the exact values for all the correlation length parameters. This also proves that the shape function methods can accurately reproduce the

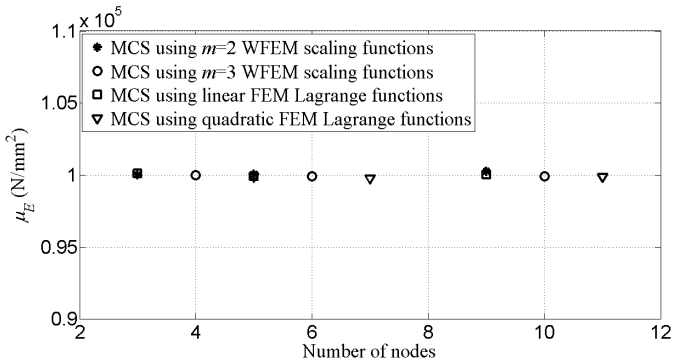

Figure 4.3: Variation of mean values of Young's modulus at $x = 100$mm with number of nodes (random variables) while linear and quadratic BSWI scaling functions and FEM based shape functions are used to model Gaussian field

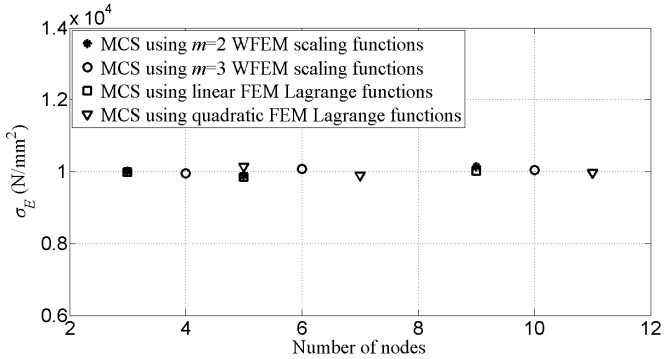

Figure 4.4: Variation of standard deviation values of Young's modulus at $x = 100$mm with number of nodes (random variables) while linear and quadratic BSWI scaling functions and FEM based shape functions are used to model Gaussian field

second order statistics of a random field regardless of the correlation length parameter.

Based on the above studies, for further analysis to solve the stochastic boundary value problem as described in *Case 1*, the displacement field and random field are approximated by BSWI scaling function having resolution $j = 3$ and $j = 1$ respectively. In the same way, for discretization of displacement field and random field using FEM, 8 and 2 linear elements respectively and 5 and 2 quadratic elements respectively are used. The mean values of displacement field at $x = 100$mm obtained by using the first order perturbation (FOP) approximation as in Equation 4.34 and second order perturbation approximation (SOP) as given in Equation 4.35 respectively are shown in Figure 4.6 and 4.7. The values are compared with the same obtained from MCS. The values are calculated and plotted for different values of CV, obtained by varying the standard deviation of Young's modulus $E(\mathbf{x})$. The correlation length parameter considered during the process is equal to 50. It

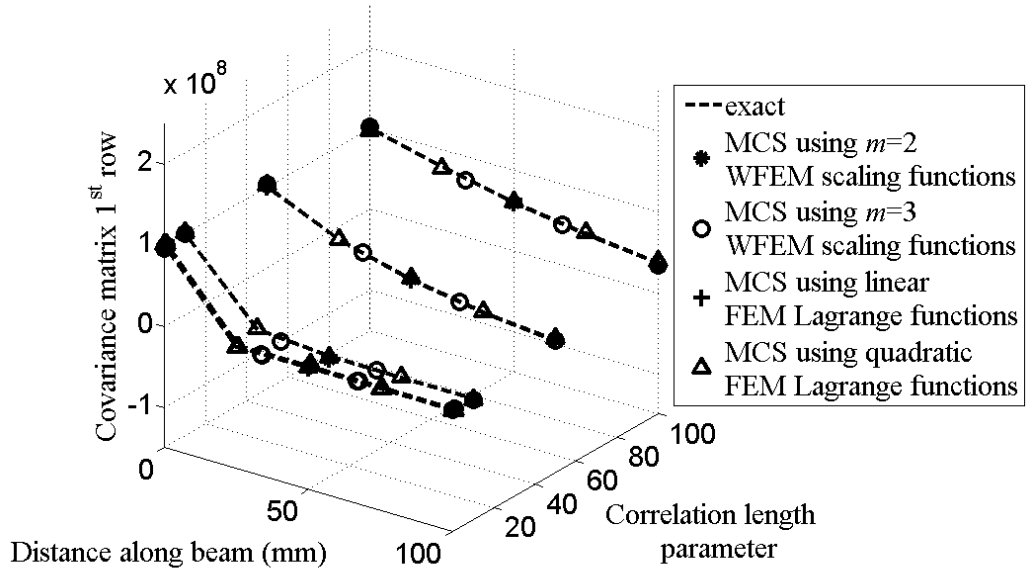

Figure 4.5: Comparison of values of first row of covariance matrix obtained using linear and quadratic BSWI WFEM and FEM based shape functions for Gaussian field, with exact values for various correlation length parameters

can be observed that when linear shape functions are used, at a CV of 20%, FOP results underestimate the mean values of displacement when compared with SOP and MCS results by around 11%. When quadratic shape functions are used, the deviation between FOP and the rest increases to 15% at a CV of 20%. Further, it can be seen from Figure 4.8 and 4.9 that at a CV of 20%, the standard deviation of displacements obtained from FOP and SOP deviates by around 6% in comparison with the MCS results. Hence, this observation reiterates the assumption that the perturbation approach used in Equation 4.34 and Equation 4.35 is suitable for small variances of $E(\mathbf{x})$ for which CV is kept under 20%.

For a CV of 10%, Figure 4.10 and 4.11 shows variation of the mean values calculated at $x = 100$mm for different correlation length parameters by employing linear and quadratic shape functions for both response and random field modelling. It is observed from Figure 4.10 and 4.11 that regardless of correlation length parameters, the mean values of displacement evaluated using FOP and SOP accord well with the MCS values for both WFEM and FEM using linear or quadratic shape functions. Figure 4.12 and 4.13 shows the variation of the standard deviation of displacement evaluated using linear and quadratic shape functions against correlation length parameter. When the correlation length parameter is decreased to a small value of 0.1, it is observed that the deviation between the

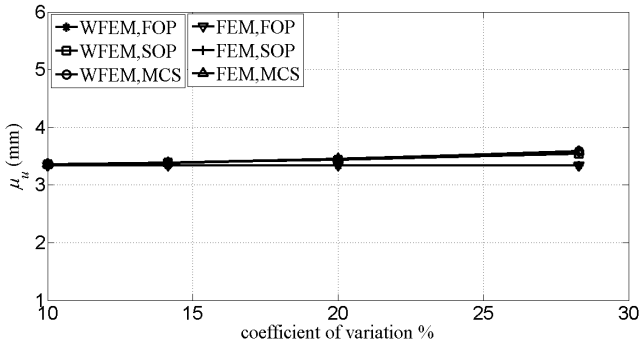

Figure 4.6: Mean value of displacement at $x = 100$mm on the bar for different values of CV by varying standard deviation of $E(\mathbf{x})$ with Gaussian random field approximation, obtained by using linear BSWI WFEM and FEM based shape functions for both response and random field modelling

results obtained from WFEM and FEM is less than 1% when linear shape functions are used for modelling. However, the deviation between WFEM and FEM values increase to 3% when quadratic shape functions are used in the analysis. It is also observed that when the correlation length parameter is increased to 100, the deviation between the results obtained from the perturbation method and MCS (for both WFEM and FEM) increases to 1% - 2%.

The dependency of size of the stochastic mesh on correlation length parameter for FEM shape functions is well documented in the literature [9, 95, 208, 209]. In the present study, the deviation that is observed while using SFEM, though it is small can be attributed to improper mapping between response mesh and random field mesh due to non-selection of appropriate mesh size for the given correlation length parameters. This reinstates the fact that using FEM shape functions will put a limitation on the selection of the random field mesh size. On the contrary, no such limitation exists when BSWI scaling functions are used and a coarse random field discretization can also be used to accurately capture the results irrespective of the correlation length parameter.

Besides the evaluation of mean and standard deviation of displacement as discussed so far, the normalized computational time required for implementing the perturbation method (FOP and SOP combined) and MCS using WFEM and FEM based shape functions is also calculated and shown in Table 4.1. The configuration of CPU (Central Processing Unit) is kept the same throughout the computational process. While evaluating the computational time, the correlation length parameter is kept equal to 50 and CV of 10% is assumed. The sample size used for MCS is equal to 5000.

It can be observed from Table 4.1 that perturbation approach requires less

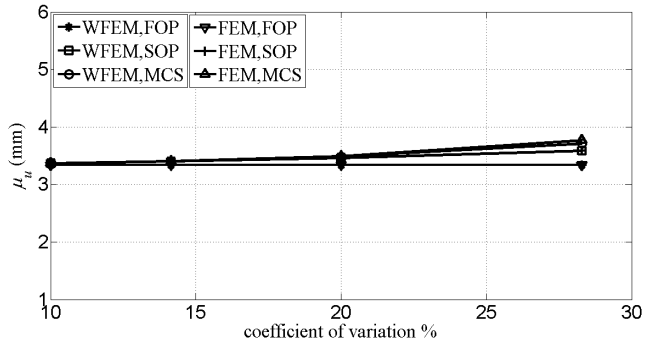

Figure 4.7: Mean value of displacement at $x = 100$mm on the bar for different values of CV by varying standard deviation of $E(\mathbf{x})$ with Gaussian random field approximation, obtained by using quadratic BSWI WFEM and FEM based shape functions for both response and random field modelling

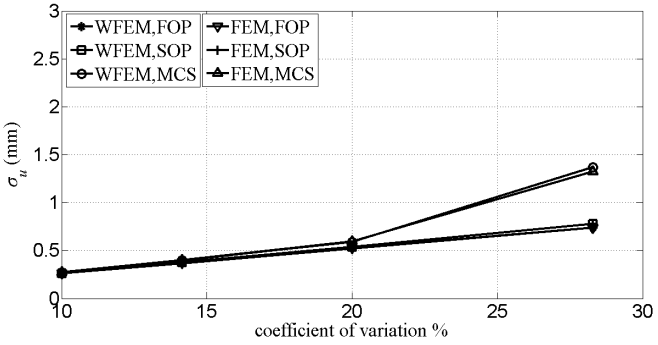

Figure 4.8: Standard deviation of displacement at $x = 100$mm on the bar for different values of CV by varying standard deviation of $E(\mathbf{x})$ with Gaussian random field approximation, obtained by using linear BSWI WFEM and FEM based shape functions for both response and random field modelling

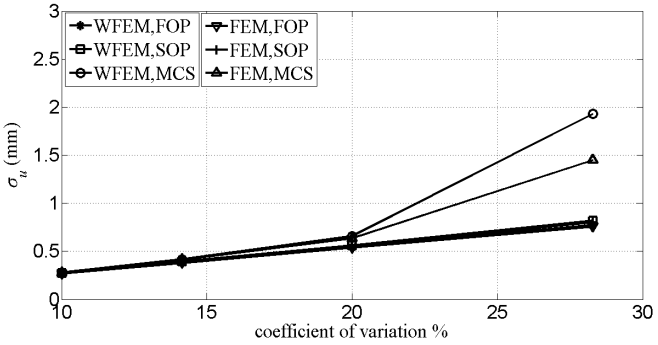

Figure 4.9: Standard deviation of displacement at $x = 100$mm on the bar for different values of CV by varying standard deviation of $E(\mathbf{x})$ with Gaussian random field approximation, obtained by using quadratic BSWI WFEM and FEM based shape functions for both response and random field modelling

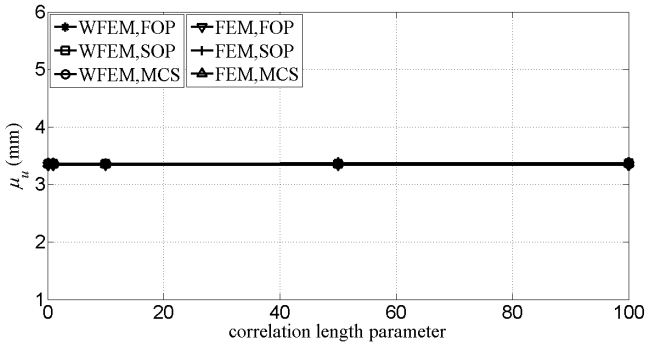

Figure 4.10: Mean value of displacement at $x = 100$mm on the bar for varying correlation length parameter of $E(\mathbf{x})$ with Gaussian random field approximation, obtained by using linear BSWI WFEM and FEM based shape functions for both response and random field modelling

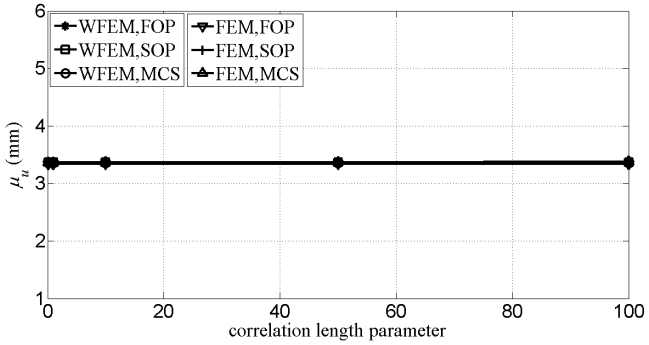

Figure 4.11: Mean value of displacement at $x = 100$mm on the bar for varying correlation length parameter of $E(\mathbf{x})$ with Gaussian random field approximation, obtained by using quadratic BSWI WFEM and FEM based shape functions for both response and random field modelling

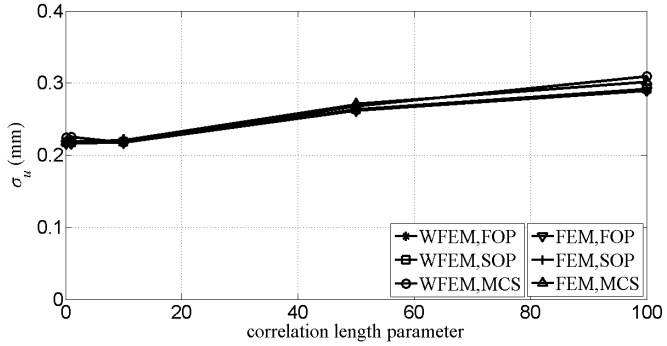

Figure 4.12: Standard deviation of displacement at $x = 100$mm on the bar for varying correlation length parameter of $E(\mathbf{x})$ with Gaussian random field approximation, obtained by using linear BSWI WFEM and FEM based shape functions for both response and random field modelling

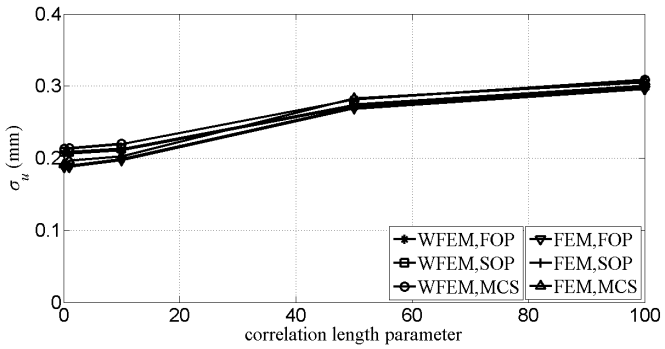

Figure 4.13: Standard deviation of displacement at $x = 100$mm on the bar for varying correlation length parameter of $E(\mathbf{x})$ with Gaussian random field approximation, obtained by using quadratic BSWI WFEM and FEM based shape functions for both response and random field modelling

Table 4.1: Normalized computational times for perturbation method and MCS using linear and quadratic WFEM and FEM shape functions, for Gaussian distribution of $E(\mathbf{x})$

Order of shape functions	**WFEM**		**FEM**	
	Perturbation	MCS	Perturbation	MCS
Linear	4.57	53.65	1	51.46
Quadratic	11.47	129.77	2.46	75.58

computational effort when compared with MCS (5000 samples). It is also noted that FEM based perturbation approach takes less time when compared with WFEM. The higher computational times needed by WFEM could be attributed to the fact that the scaling functions of WFEM are formed using B-splines, which are piecewise polynomials and its explicit expression are obtained at Gauss points during the evaluation of system of equations. As a result, when the number of Gauss points increases, the number of function calls for obtaining the explicit expression of B-splines and thereby evaluating the scaling functions also increases. This increases the computational overhead resulting in a higher computational time. On the contrary, FEM shape functions are not piecewise polynomials due to which, this issue is not encountered. The issue of higher computational overhead as encountered in the case of WFEM can be possibly addressed and the computational times can be further reduced by way of better programming practices and optimized implementation of algorithms.

Case 2: Random field $E(\boldsymbol{x})$ follows lognormal distribution

Here, the modulus of elasticity is modelled as a homogeneous random field with a lognormal distribution as given in Equation 4.4. A similar procedure analogous to the one discussed in the context of a Gaussian distribution is followed and convergence is established for the discretization of random field. A MCS sample size of 5000 is selected. A resolution of $j = 1$ using linear and quadratic wavelet scaling functions resulting in 3 and 4 nodes respectively and with FEM shape functions 2 linear elements and 2 quadratic elements resulting in 3 and 5 nodes respectively lead to converged solutions. Hence, these parameters are used in further calculations. The mean values of displacement field obtained using FOP, SOP and MCS is shown in Figure 4.14 and 4.15. The values are calculated at $x = 100$mm, for different values of CV obtained by varying the standard deviation of Young's modulus $E(\mathbf{x})$. It can be observed from Figure 4.14 and 4.15 that at a CV of 20%, the mean values of displacement field using FOP deviate away from SOP and MCS values by more than 4.5%. Moreover, there is a difference of 13%-15% between the MCS values and the SOP values for CV beyond 20% when WFEM (linear and quadratic shape functions) and FEM (linear shape functions) are used. Hence, the perturbation approach that is used here is suitable for CV of less than 20%. The standard deviation of displacement field obtained for different values of CV is shown in Figure 4.16 and 4.17. It can be observed that at a CV of 20%, SOP values deviate away from MCS values by 2.5% - 3.5%. When the CV is increased beyond 20%, the deviation also increases to 7.5% - 9%.

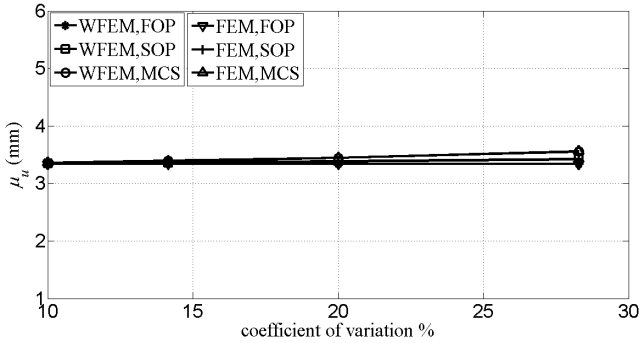

Figure 4.14: Mean value of displacement at $x = 100$mm on the bar for different values of CV by varying standard deviation of $E(\mathbf{x})$ with lognormal random field approximation, obtained by using linear BSWI WFEM and FEM based shape functions for both response and random field modelling

The mean values of displacement field calculated for varying correlation length parameter is shown in Figure 4.18 and 4.19. It can be seen that the values obtained from SOP deviate away from MCS values by at the most 1.5% - 2% for different correlation

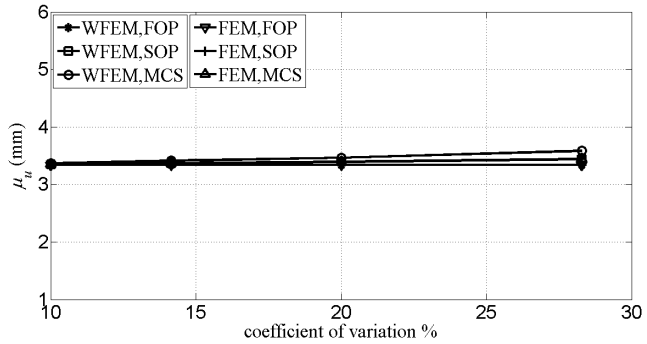

Figure 4.15: Mean value of displacement at $x = 100$mm on the bar for different values of CV by varying standard deviation of $E(\mathbf{x})$ with lognormal random field approximation, obtained by using quadratic BSWI WFEM and FEM based shape functions for both response and random field modelling

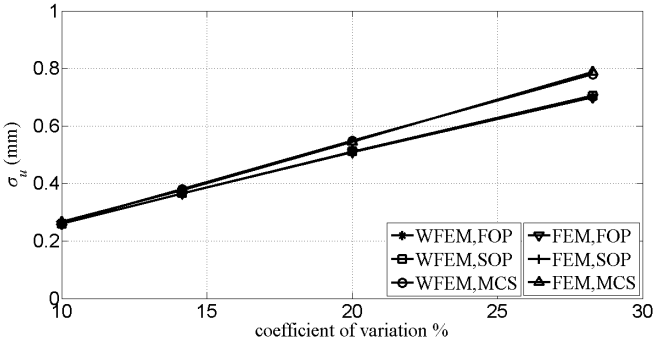

Figure 4.16: Standard deviation of displacement at $x = 100$mm on the bar for different values of CV by varying standard deviation of $E(\mathbf{x})$ with lognormal random field approximation, obtained by using linear BSWI WFEM and FEM based shape functions for both response and random field modelling

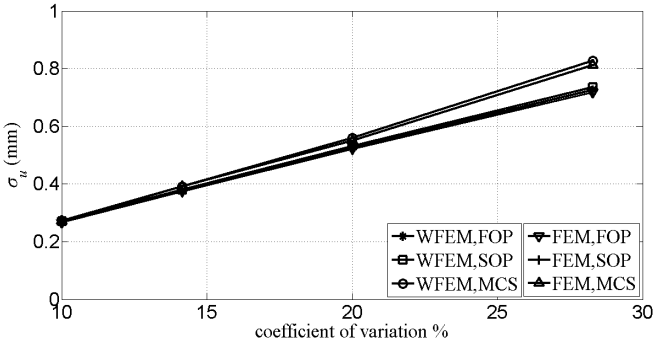

Figure 4.17: Standard deviation of displacement at $x = 100$mm on the bar for different values of CV by varying standard deviation of $E(\mathbf{x})$ with lognormal random field approximation, obtained by using quadratic BSWI WFEM and FEM based shape functions for both response and random field modelling

length parameters. The variation of standard deviation of displacement against correlation length parameters for linear and quadratic shape functions is shown in Figure 4.20 and 4.21. When linear shape functions are used for modelling the random field, the values obtained from WFEM and FEM concur well with each other. In the case of quadratic shape functions, it can be observed that there is a deviation of 2% - 3% between WFEM and FEM values at small correlation length parameters.

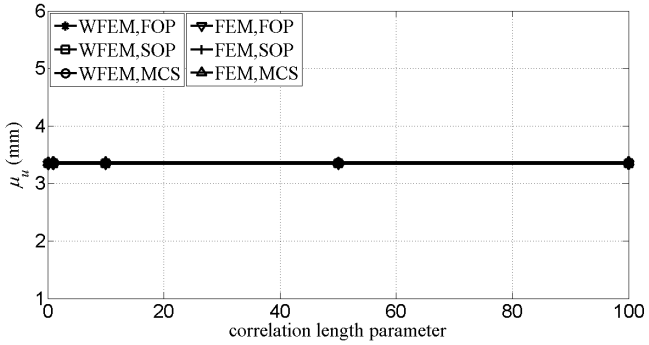

Figure 4.18: Mean value of displacement at $x = 100$mm on the bar for varying correlation length parameter of $E(\mathbf{x})$ with lognormal random field approximation, obtained by using linear BSWI WFEM and FEM based shape functions for both response and random field modelling

Analogous to Gaussian distribution, the normalized computational time required for implementing the perturbation method and MCS based on WFEM and FEM shape functions is also calculated for lognormal distribution and given in Table 4.2. The parameters such as correlation length parameter, CV of $E(\mathbf{x})$ and MCS sample size are all kept the same as, in the case of Gaussian distribution. From Table 4.2 it can be noted that MCS (5000 samples) takes more computational effort when compared to a perturbation approach. The perturbation method based on FEM shape functions has the least computational time when compared with other methods, which could be attributed to the reasons already discussed in the case of Gaussian distribution.

In conclusion, perturbation approach using wavelet scaling functions is found to be accurate for both Gaussian and non-Gaussian fields, when compared with MCS and FEM based evaluations. The computational times obtained from WFEM based perturbation approach are on a higher side in comparison with FEM. However, it is important to note that if randomness associated with geometric parameters are involved, re-meshing and convergence studies needs to be done; in which case WFEM due to its inherent properties like MRA could become more attractive with respect to computational time too. Further, the effect of small correlation length on convergence associated with FEM discretization

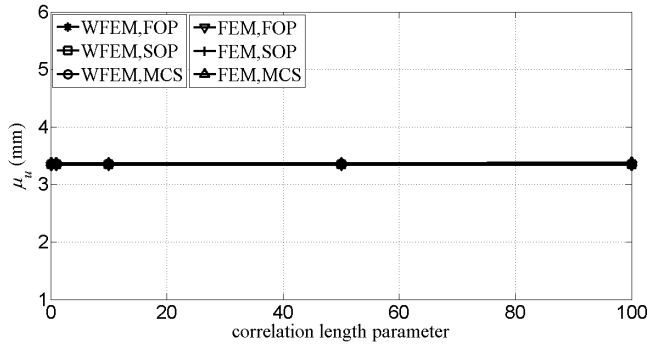

Figure 4.19: Mean value of displacement at $x = 100$mm on the bar for varying correlation length parameter of $E(\mathbf{x})$ with lognormal random field approximation, obtained by using quadratic BSWI WFEM and FEM based shape functions for both response and random field modelling

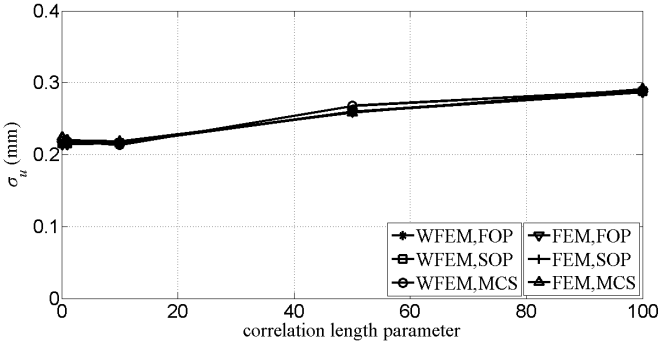

Figure 4.20: Standard deviation of displacement at $x = 100$mm on the bar for varying correlation length parameter of $E(\mathbf{x})$ with lognormal random field approximation, obtained by using linear BSWI WFEM and FEM based shape functions for both response and random field modelling

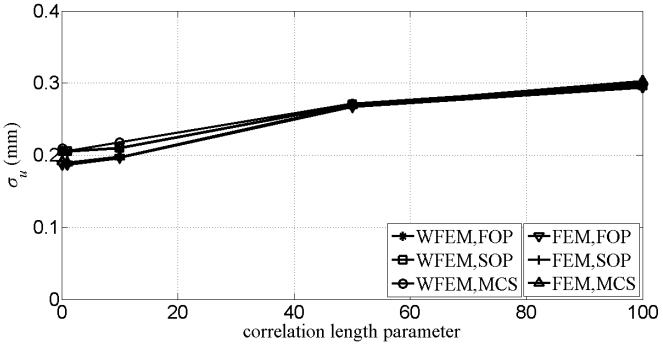

Figure 4.21: Standard deviation of displacement at $x = 100$mm on the bar for varying correlation length parameter of $E(\mathbf{x})$ with lognormal random field approximation, obtained by using quadratic BSWI WFEM and FEM based shape functions for both response and random field modelling

Table 4.2: Normalized computational times for perturbation method and MCS using linear and quadratic WFEM and FEM shape functions, for lognormal distribution of $E(\mathbf{x})$

Order of shape functions	WFEM		FEM	
	Perturbation	MCS	Perturbation	MCS
Linear	4.87	51.76	1	44.19
Quadratic	10.32	115.51	2.08	62.52

also needs to be accounted for in the overall computational time. Thus, it is clear from this example that BSWI WFEM results are comparable in different aspects to FEM, for both Gaussian and non-Gaussian input fields. Hence, for further numerical examples only Gaussian input field and WFEM is used.

4.3.1.2 Two-dimensional plane stress problem

In this example, a plane stress problem under uni-axial loading is studied to understand the efficiency of the proposed method in problems having large stress gradients. Due to symmetry, only a quarter portion of the plate is considered for analysis. Roller supports are employed at the left edge and bottom edge as shown in Figure 4.22. The modulus of elasticity is modelled as a homogeneous Gaussian random field as given by Equation 4.1. The mean value of Young's modulus is taken as $\mu_E = 2 \times 10^5$MPa , with $\nu = 0.3$, $L = 5$mm, $b = 6$mm and $F = 1000\mathrm{N/mm}^2$. The analytical solution obtained from deterministic analysis is given in Sadd [198]. The entire domain is modelled using one 2D BSWI C_0 type element. In this problem, the displacement and random field are approximated using linear and quadratic shape functions and the results are studied for each case separately. For the current study to approximate the displacement field, scaling functions with $m = 2$ and $m = 3$ with a resolution $j = 3$ is considered. Further, random field is approximated with scaling function of same order that is used for displacement approximation but having a coarse resolution of $j = 1$ to reduce the computational effort. For illustration, the nodal distribution used for displacement and random field approximation using linear wavelet scaling functions is shown in Figure 4.23a and 4.23b respectively.

The mean and standard deviation values of displacement in y direction (μ_v and σ_v), along the path A to B ($x = 2.5$mm, $y = [0 : 6]$mm) as seen in Figure 4.22, is calculated using FOP, SOP and MCS for both linear and quadratic WFEM scaling functions. During this analysis, the spatially varying Young's modulus $E(\mathbf{x})$ is considered having a variance

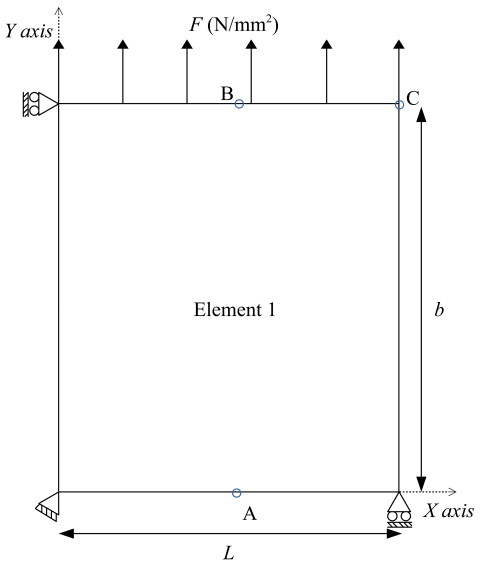

Figure 4.22: Uni-axial loading of a plate under plane stress

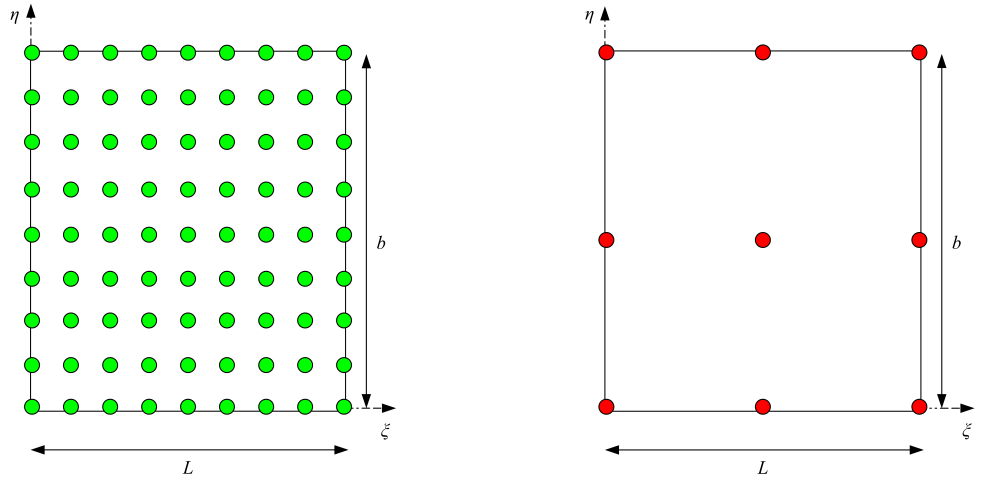

(a) Displacement field under $m = 2, j = 3$

(b) Random field under $m = 2, j = 1$

Figure 4.23: Nodal distribution used for displacement and random field approximation when the domain is discretized using single 2D BSWI C_0 type element constructed using linear WFEM scaling functions

of magnitude 2×10^8 which leads to a CV of 7.07%. The correlation length parameters c_1, c_2, in x and y directions are considered equal to 2.5 and 3 respectively. Table 4.3 shows the mean and standard deviation values of displacement obtained when linear scaling

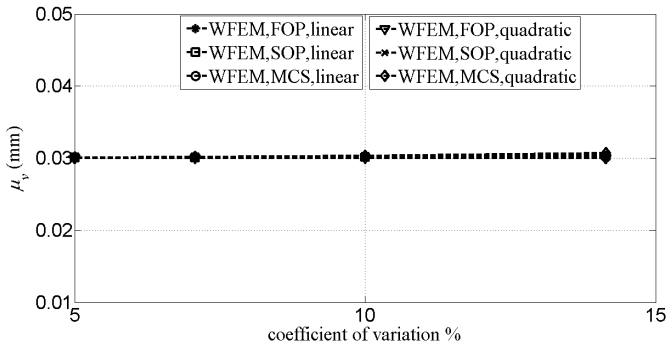

Figure 4.24: Mean value of displacement in y direction at position C, for different values of CV by varying standard deviation of $E(\mathbf{x})$, obtained using linear and quadratic BSWI WFEM based scaling functions

functions and quadratic scaling functions are employed. It can be observed from Table 4.3 that the mean and standard deviation values obtained using FOP and SOP concur well with the MCS values for linear as well as quadratic shape functions.

Table 4.3: Mean and standard deviation values of displacement in y direction (μ_v and σ_v) along path A to B obtained by using linear and quadratic WFEM scaling functions

Linear/Quadratic	Distance (mm)	$\boldsymbol{\mu_v}$			$\boldsymbol{\sigma_v}$		
		FOP	SOP	MCS	FOP	SOP	MCS
$m = 2$	0	0	0	0	0	0	0
	1.5	0.00750	0.00751	0.00752	0.000365	0.000365	0.000365
	3.0	0.01500	0.01503	0.01503	0.000682	0.000683	0.000690
	4.5	0.02250	0.02255	0.02254	0.001000	0.001002	0.001010
	6.0	0.03000	0.03008	0.03006	0.001286	0.001289	0.001310
$m = 3$	0	0	0	0	0	0	0
	1.33	0.00665	0.00671	0.00672	0.00060	0.00061	0.00062
	2.00	0.00992	0.00999	0.01000	0.00072	0.00072	0.00073
	3.33	0.01668	0.01675	0.01675	0.00088	0.00088	0.00089
	4.66	0.02335	0.02343	0.02343	0.00106	0.00106	0.00106
	6.00	0.03000	0.03016	0.03015	0.00153	0.00154	0.00149

The variation of mean values of displacement in y direction at position C($x = 5$mm, $y = 6$mm) for different CV is shown in Figure 4.24. It can be observed that mean values obtained from perturbation approach are in good agreement with MCS values, for the range of CV considered. The variation of the standard deviation values of displacement in y direction at position C are shown in Figure 4.25. The difference in the standard deviation of perturbation results from MCS is within 5% as observed for different values of CV. Thus, it can be concluded that the mean values can be accurately captured using the WFEM based

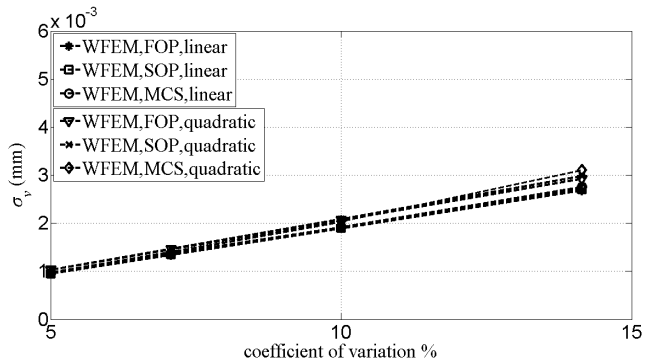

Figure 4.25: Standard deviation of displacement in y direction at position C, for different values of CV by varying standard deviation of $E(\mathbf{x})$, obtained using linear and quadratic BSWI WFEM based scaling functions

perturbation approach for a 2D plane stress problem. It is also observed that when the CV is increased beyond 12%, the standard deviation values obtained from WFEM deviate by not more than 5% in comparison with MCS values. In conclusion, perturbation results obtained from WFEM concur well with the results of MCS for a 2D plane stress problem with only a small margin of variation at higher CV values.

4.3.1.3 Plate with a hole under uni-axial far field tension

In this example, a plate with a hole under uni-axial far field tensile loading is studied. Due to symmetry, a quarter portion of the plate with dimensions, ($L = 5$mm, $b = 6$mm) , and radius of the hole, $a = 0.1$mm having symmetry boundary conditions at the left edge and bottom edge as shown in Figure 3.24 is considered for analysis. The modulus of elasticity is modelled as a homogeneous Gaussian random field. The mean value of Young's modulus is taken as $\mu_E = 2 \times 10^5$MPa, Poisson's ratio is considered to be deterministic with a value, $\nu = 0.3$ and a far-field stress of $F = 1000\mathrm{N}/\mathrm{mm}^2$ is applied. The 2D irregular domain of this problem is modelled using two 2D BSWI C_0 type elements as it is the minimum number of quadrilateral elements needed to discretize the geometry. The analytical solution of the deterministic analysis is given in Sadd [198]. The results of convergence study using a deterministic approach showing the stress concentration factor along $y = 0$ for various order and resolutions of wavelet scaling functions are shown in the previous chapter 3 and it is observed that $m = 3, j = 3$ leads to a converged solution. Hence, in the current stochastic approach, the displacement field is approximated using $m = 3, j = 3$; but random field is approximated using a coarser discretization of $m = 2, j = 1$ for both the elements to reduce the computational effort. For illustration, the nodal distribution used for

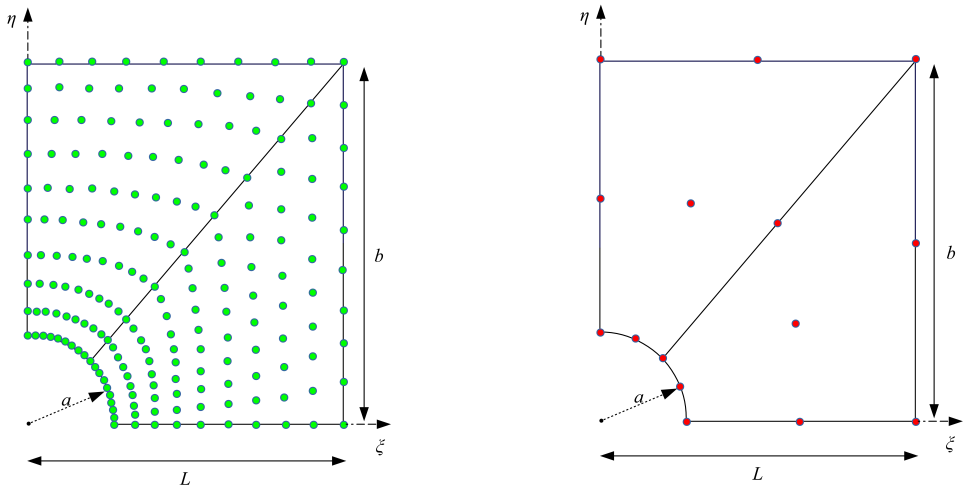

(a) Displacement field under $m = 3, j = 3$ **(b)** Random field under $m = 2, j = 1$

Figure 4.26: Nodal distribution used for displacement and random field approximation when the domain is discretized using two 2D BSWI C_0 type elements

displacement and random field approximation is shown in Figure 4.26a and Figure 4.26b respectively.

A variance of magnitude 2×10^8 which leads to a CV of 7.07% is considered. Further, in the present study the correlation length parameters c_1, c_2, in x and y directions are considered equal to 2.5 and 3 respectively. The mean and standard deviation values of displacement in x direction, μ_u and σ_u respectively, along $y = 0$ are plotted in Figure 4.27 and 4.28. It can be seen that the values obtained from perturbation approach are in good agreement with MCS values. Further, for different values of CV (5% to 14.14%), mean and standard deviation of displacement are calculated at various positions A and B on the problem domain. Table 4.4 shows the perturbation and MCS results of the mean and standard deviation of displacement at position A ($x = 0.1$mm, $y = 0$mm). It can be observed that the perturbation and MCS results match well even for the highest CV considered in the study. The difference between perturbation and MCS is observed to be less than 2%. A similar observation can be made for the mean and standard deviation of displacement at position B ($x = 0$mm, $y = 0.1$mm) which is also tabulated in Table 4.4.

In conclusion, it can be observed that accurate results are obtained when BSWI scaling functions at lower order and resolution, resulting in less number of random variables, are used for modelling the random field. Hence, with the proposed stochastic WFEM for C_0 type problems, a good accuracy can be achieved. The accuracy of the proposed stochastic

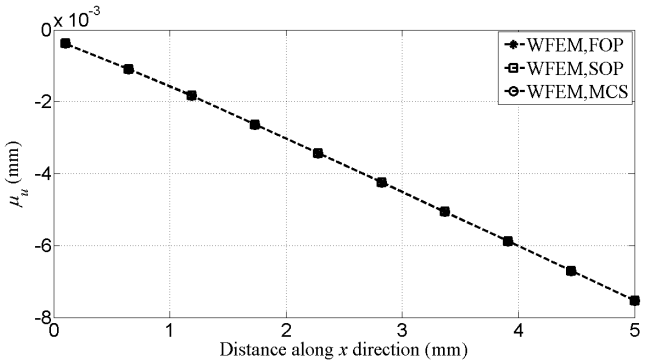

Figure 4.27: Mean (μ) of displacement in x direction, along path A to D

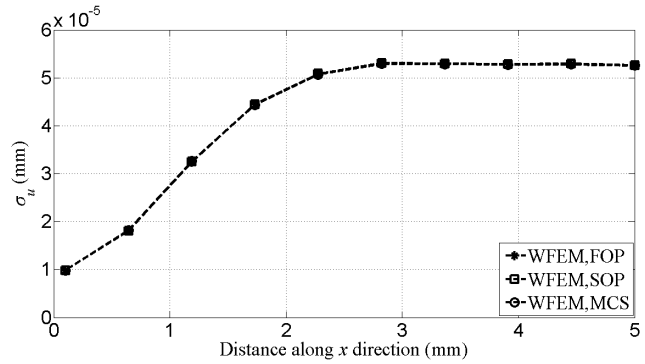

Figure 4.28: Standard deviation (σ) of displacement in x direction, along path A to D

Table 4.4: Mean and standard deviation values of displacement in x direction (μ_u and σ_u) at position A and in y direction (μ_v and σ_v) at position B, for different values of CV obtained by varying the standard deviation of $E(\mathbf{x})$

Position	**CV%**	$\boldsymbol{\mu_u}$			$\boldsymbol{\sigma_u}$		
		FOP	SOP	MCS	FOP	SOP	MCS
A	5.00	-3.822×10^{-4}	-3.822×10^{-4}	-3.822×10^{-4}	6.93×10^{-6}	6.94×10^{-6}	6.94×10^{-6}
	7.07	-3.822×10^{-4}	-3.822×10^{-4}	-3.821×10^{-4}	9.81×10^{-6}	9.83×10^{-6}	9.83×10^{-6}
	10.00	-3.822×10^{-4}	-3.821×10^{-4}	-3.820×10^{-4}	1.38×10^{-5}	1.39×10^{-5}	1.40×10^{-5}
	14.14	-3.822×10^{-4}	-3.821×10^{-4}	-3.818×10^{-4}	1.96×10^{-5}	1.97×10^{-5}	2.01×10^{-5}
		$\boldsymbol{\mu_v}$			$\boldsymbol{\sigma_v}$		
B	5.00	1.195×10^{-3}	1.195×10^{-3}	1.195×10^{-3}	1.12×10^{-5}	1.12×10^{-5}	1.12×10^{-5}
	7.07	1.195×10^{-3}	1.196×10^{-3}	1.196×10^{-3}	1.58×10^{-5}	1.58×10^{-5}	1.58×10^{-5}
	10.00	1.195×10^{-3}	1.196×10^{-3}	1.197×10^{-3}	2.24×10^{-5}	2.25×10^{-5}	2.26×10^{-5}
	14.14	1.195×10^{-3}	1.198×10^{-3}	1.199×10^{-3}	3.17×10^{-5}	3.19×10^{-5}	3.26×10^{-5}

WFEM is also demonstrated for the numerical examples based on C_1 type problems (beams), which is shown next.

4.3.2 Numerical examples for beams based on Euler-Bernoulli and Timoshenko beam theories

4.3.2.1 Cantilever beam based on Euler-Bernoulli beam theory

In this example, a cantilever beam as shown in Figure 3.17 is considered for analysis. The modulus of elasticity is modelled as a homogeneous random field with a Gaussian distribution, as given by Equation 4.1. The results from stochastic WFEM wherein both the input random field and response are discretized using BSWI scaling functions are compared with those obtained from SFEM wherein both random field and response are discretized using Lagrange shape functions. The mean value of Young's modulus is taken as $\mu_E = 2 \times 10^5$MPa with $L = 100$mm, $b = 1$mm, $h = 1$mm and $q(x) = 0.01\mathrm{N/mm}$. The entire domain of the beam is modelled using one BSWI C_1 continuity element. The order and resolution of BSWI scaling functions that are selected to be used for the deflection approximation are obtained via a convergence study as shown in Figure 3.23 in chapter 3. Figure 3.23 shows the relative variation in deflection norm obtained from deterministic WFEM analysis using different order (quadratic and cubic) and resolution for various boundary conditions. It is observed that for $m = 4$ (cubic order) with $j = 3$ (resolution), the relative variation is less than 0.1%. Hence, the deflection field is approximated using cubic BSWI WFEM scaling functions with $m = 4$, $j = 3$ and the random field is discretized using linear or quadratic scaling functions with resolution $j = 1$. For analysis using SFEM, 8 beam elements based on Hermite cubic interpolation are used for discretization of the deflection field and 2 linear and quadratic elements based on Lagrange shape functions are used for the discretization of the random field.

The mean values of deflection field at $x = 100$mm obtained by using the perturbation approach is shown in Figure 4.29 and Figure 4.30. These values are compared with the values obtained from MCS and the results are plotted for different values of CV, obtained by varying the standard deviation of Young's modulus $E(\mathbf{x})$. The correlation length parameter considered is 50. It can be observed from that in the case of both WFEM and FEM when linear and quadratic shape functions are used to model the random field respectively, at a CV of 10% and beyond, FOP results underestimate the mean values of deflection when compared with SOP and MCS results. The standard deviation values of deflection field obtained by using the perturbation approach are shown in Figure 4.31 and Figure 4.32. It

can be seen in Figure 4.31 and Figure 4.32 that for a CV of less than 20%, the standard deviation values of deflection obtained from FOP and SOP deviate by 10% at the most in comparison with the MCS results. However, at a CV of 25%, the deflections are observed to deviate by around 25% and 32% when the random field is modelled using linear and quadratic shape functions respectively.

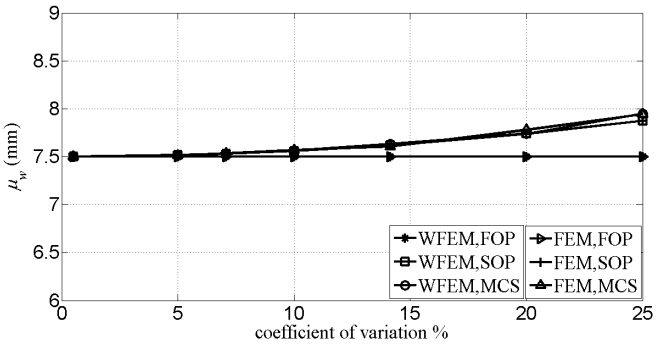

Figure 4.29: Variation of mean value of deflection at $x = 100$mm for the EBT based cantilever beam against CV, when linear BSWI WFEM and FEM based shape functions are used for random field modelling

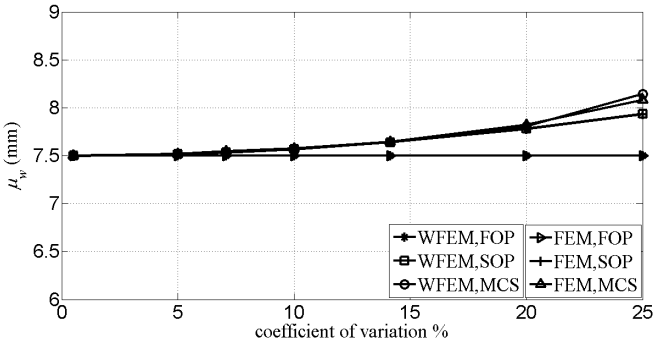

Figure 4.30: Variation of mean value of deflection at $x = 100$mm for the EBT based cantilever beam against CV, when quadratic BSWI WFEM and FEM based shape functions are used for random field modelling

Figure 4.33 and Figure 4.34 shows the variation of mean values of deflection calculated at $x = 100$mm for different correlation length parameters by using linear and quadratic shape functions for random field modelling respectively. A CV of 5% is considered during the process. It can be observed from Figure 4.33 and Figure 4.34 that the mean values of deflection evaluated using FOP and SOP concur well with the MCS values in the case of both WFEM and FEM using linear or quadratic shape functions for different values

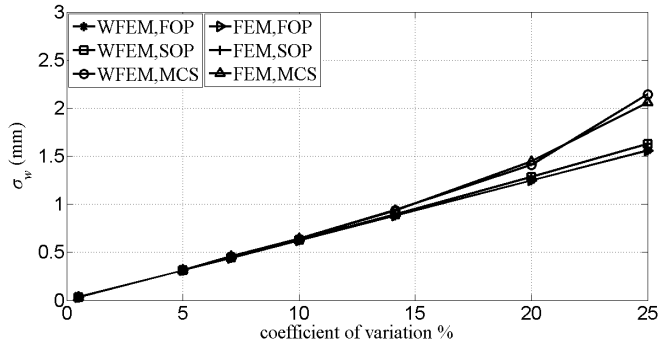

Figure 4.31: Variation of standard deviation of deflection at $x = 100$mm for the EBT based cantilever beam against CV, when linear BSWI WFEM and FEM based shape functions are used for random field modelling

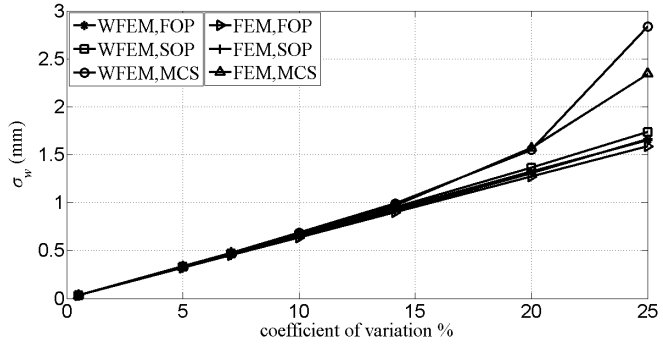

Figure 4.32: Variation of standard deviation of deflection at $x = 100$mm for the EBT based cantilever beam against CV, when quadratic BSWI WFEM and FEM based shape functions are used for random field modelling

of correlation length parameters. The variation of standard deviation values of deflection against correlation length parameter in which the random field is modelled using linear or quadratic shape functions are shown in Figure 4.35 and Figure 4.36 respectively. It can be observed from Figure 4.35 that the deviation between FOP and SOP values from MCS is less than 5% for different correlation length parameters when the random field is discretized using linear shape functions. When the standard deviation of deflection is evaluated by utilizing quadratic shape functions for random field discretization, it is observed from Figure 4.36 that the FOP and SOP values obtained by using FEM Lagrange shape functions underestimate the standard deviation of deflection by around 10% in comparison with WFEM for a correlation length parameter less than 10. However, when the correlation length parameter is greater than 10, the standard deviation values obtained with FEM Lagrange shape functions deviate away from its own MCS values by around

5%-10%. Further, it can be observed from both Figure 4.35 and Figure 4.36 that the standard deviation values obtained from perturbation approach using BSWI WFEM shape functions closely match with its own MCS results.

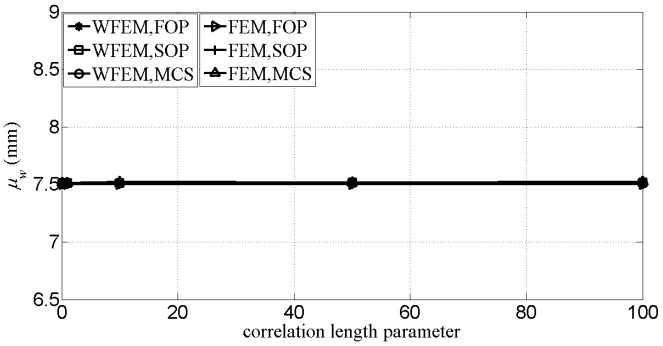

Figure 4.33: Variation of mean value of deflection at $x = 100$mm for the EBT based cantilever beam against correlation length parameter, when linear BSWI WFEM and FEM based shape functions are used for random field modelling

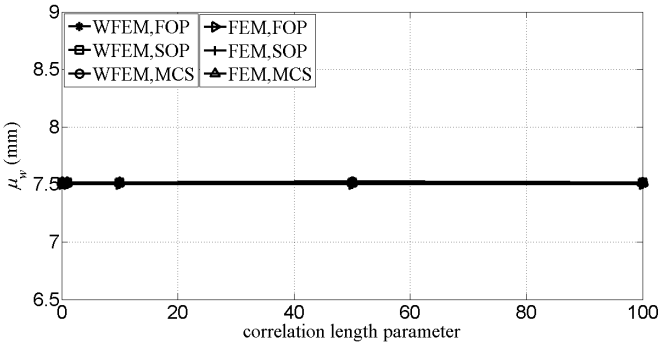

Figure 4.34: Variation of mean value of deflection at $x = 100$mm for the EBT based cantilever beam against correlation length parameter, when quadratic BSWI WFEM and FEM based shape functions are used for random field modelling

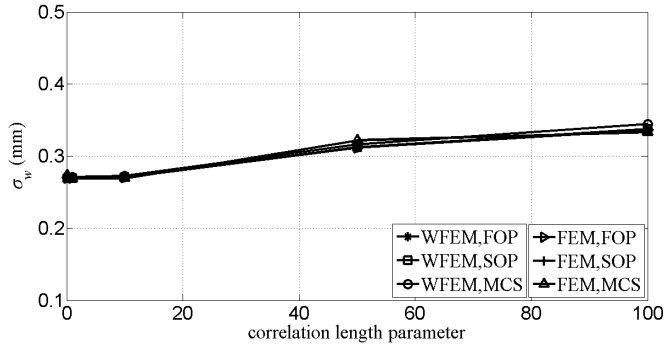

Figure 4.35: Variation of standard deviation of deflection at $x = 100$mm for the EBT based cantilever beam against correlation length parameter, when linear BSWI WFEM and FEM based shape functions are used for random field modelling

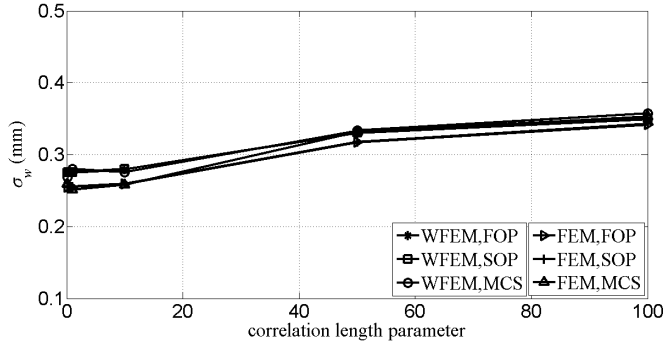

Figure 4.36: Variation of standard deviation of deflection at $x = 100$mm for the EBT based cantilever beam against correlation length parameter, when quadratic BSWI WFEM and FEM based shape functions are used for random field modelling

4.3.2.2 Simply supported beam based on Euler-Bernoulli beam theory

In this example, a simply supported beam as shown in Figure 3.18 is considered for analysis. The material and geometric properties along with discretization that were considered in the case of a cantilever beam are used in the current study as well. The mean values of deflection field at $x = 50$mm obtained by using the perturbation approach is shown in Figure 4.37 and Figure 4.38. The values obtained from the perturbation approach are compared with the MCS values and the results are plotted for different values of CV, obtained by varying the standard deviation of Young's modulus $E(\mathbf{x})$. The correlation length parameter considered during the process is 50. It can be observed from Figure 4.37 and Figure 4.38 that analogous to the case of a cantilever beam, when linear and quadratic shape functions are used to model the random field respectively, at a CV of 10% and beyond, FOP results obtained from WFEM and FEM underestimate the mean values

of deflection when compared with SOP and MCS results. The standard deviation values of deflection field obtained by using the perturbation approach are shown in Figure 4.39 and Figure 4.40. It can be noted that the deviation between the standard deviation values obtained from perturbation approach and MCS is around 12% at a CV of 20% and it is increased to 30% when the CV is increased to 25%.

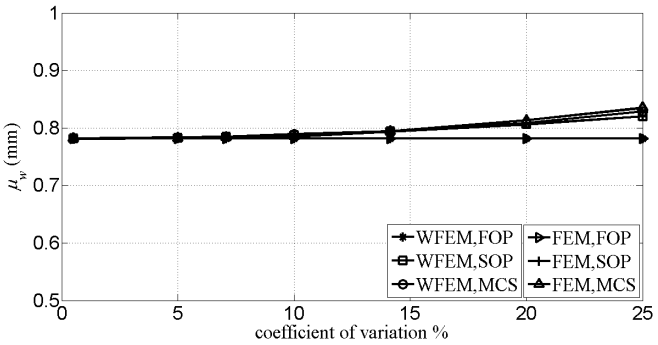

Figure 4.37: Variation of mean value of deflection at $x = 50$mm for the EBT based simply supported beam against CV, when linear BSWI WFEM and FEM based shape functions are used for random field modelling

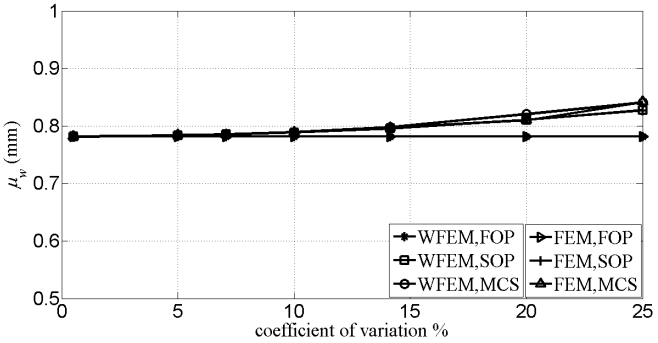

Figure 4.38: Variation of mean value of deflection at $x = 50$mm for the EBT based simply supported beam against CV, when quadratic BSWI WFEM and FEM based shape functions are used for random field modelling

The variation of mean values of deflection calculated at $x = 50$mm for different correlation length parameters at a CV of 5% while linear and quadratic shape functions are used for random field modelling is shown in Figure 4.41 and Figure 4.42 respectively. It can be observed from Figure 4.41 and Figure 4.42 that the mean values of deflection evaluated using FOP and SOP concur well with the MCS values using linear or quadratic shape functions for different values of correlation length parameters. On the same lines, the

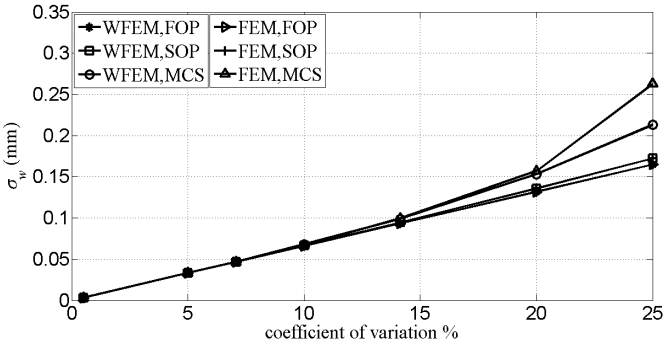

Figure 4.39: Variation of standard deviation of deflection at $x = 50$mm for the EBT based simply supported beam against CV, when linear BSWI WFEM and FEM based shape functions are used for random field modelling

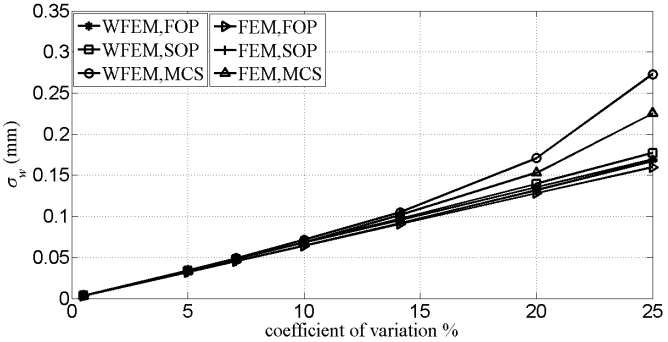

Figure 4.40: Variation of standard deviation of deflection at $x = 50$mm for the EBT based simply supported beam against CV, when quadratic BSWI WFEM and FEM based shape functions are used for random field modelling

variation of standard deviation values of deflection against correlation length parameter in which the random field is discretized using linear and quadratic shape functions are shown in Figure 4.43 and Figure 4.44 respectively. It can be observed from Figure 4.43 that the values obtained from perturbation approach are in good agreement with the values of MCS for different correlation length parameters when the random field is discretized using linear shape functions. Even when the correlation length parameter is small, the deviation is observed to be less than 5%. However, when quadratic shape functions are used for random field discretization, it is observed from Figure 4.44 that for correlation length parameter less than 10, the FOP and SOP values obtained by using FEM Lagrange shape functions underestimate the standard deviation values of deflection by around 15% in comparison with WFEM. Also it is found that, for correlation length parameter greater than 10, the standard deviation values obtained with the help of FEM Lagrange shape functions shows

a 5% deviation from its own MCS values, while FEM MCS results are approaching the values obtained from WFEM. It is also observed that unlike FEM, the standard deviation values obtained from perturbation approach using BSWI WFEM shape functions remain in good agreement with its own MCS results for different correlation length parameters

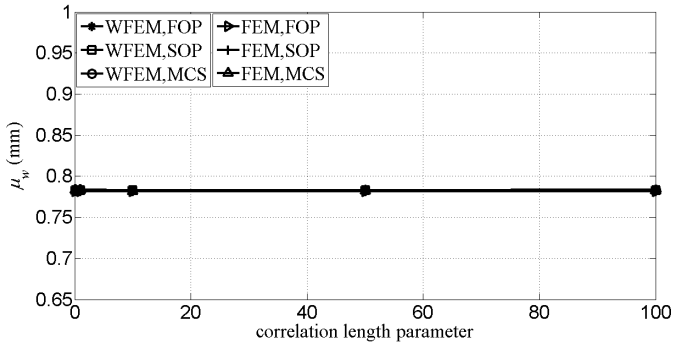

Figure 4.41: Variation of mean value of deflection at $x = 50$mm for the EBT based simply supported beam against correlation length parameter, when linear BSWI WFEM and FEM based shape functions are used for random field modelling

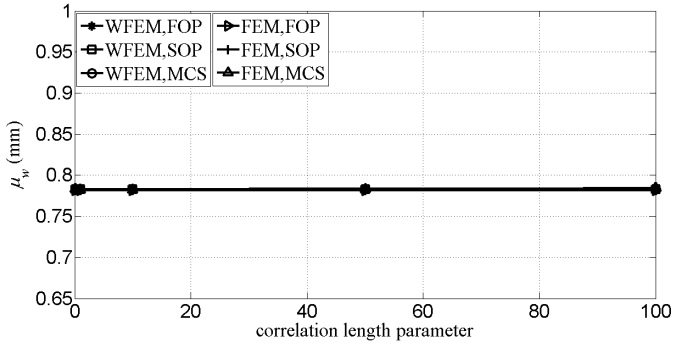

Figure 4.42: Variation of mean value of deflection at $x = 50$mm for the EBT based simply supported beam against correlation length parameter, when quadratic BSWI WFEM and FEM based shape functions are used for random field modelling

The results obtained from the current study (for both cantilever and simply supported boundary conditions) in which the effects of variation of correlation length parameter is studied, show a significant deviation between the values of standard deviation obtained from SFEM and WFEM at smaller correlation length parameters. The deviation could be because of the improper mapping between FEM response mesh and random field mesh due to non-selection of appropriate mesh size for the given correlation length parameter. It is based on the fact, which is well documented in the literature [9, 95, 208, 209] that the size

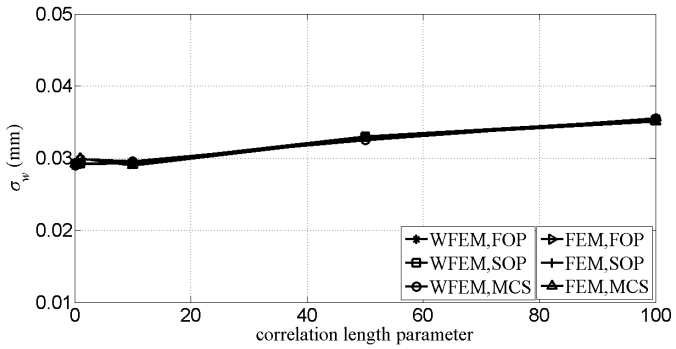

Figure 4.43: Variation of standard deviation of deflection at $x = 50$mm for the EBT based simply supported beam against correlation length parameter, when linear BSWI WFEM and FEM based shape functions are used for random field modelling

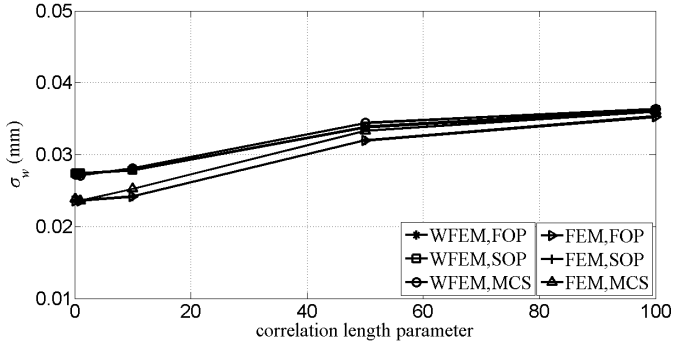

Figure 4.44: Variation of standard deviation of deflection at $x = 50$mm for the EBT based simply supported beam against correlation length parameter, when quadratic BSWI WFEM and FEM based shape functions are used for random field modelling

of the SFEM mesh should be selected in accordance with the correlation length parameter being used. Thus, it limits the selection of the random field mesh size in the case of FEM. On the contrary, no such limitations are observed when BSWI scaling functions are used and a coarse random field discretization accurately captures the results irrespective of the correlation length parameter.

4.3.2.3 Cantilever beam based on Timoshenko beam theory

In this example, the cantilever beam as shown in Figure 3.17 is considered for analysis wherein the formulation is based on TBT. The depth of the beam is considered as $h = 15$mm, shear correction coefficient $K_s = 5/6$, Poisson's ratio $\nu = 0.3$, load $q(x) = 10\mathrm{N/mm}$ and rest of the material and geometric properties are kept the same as that considered in the case of EBT based cantilever beam. The domain is modelled

using one BSWI WFEM element with C_0 continuity. The deflection field is approximated using quadratic scaling functions with $m = 3$ and resolution $j = 3$ and for random field discretization both linear and quadratic scaling functions with resolution $j = 1$ are used. A SFEM analysis of the beam is also carried out to conduct a comparative study. For FEM, 5 quadratic elements based on Lagrange shape functions are used for modelling the deflection field and 2 linear or quadratic elements based on Lagrange shape functions are used for the discretization of the random field.

The mean values of deflection field when linear and quadratic shape functions are used to model the random field at $x = 100$mm are shown in Figure 4.45 and Figure 4.46 respectively. The mean values obtained by using the perturbation approach are compared with the MCS values and the results are plotted for different values of CV, obtained by varying the standard deviation of Young's modulus $E(\mathbf{x})$. The correlation length parameter considered during the process is equal to 50. It can be observed from Figure 4.45 and Figure 4.46 that for a CV of more than 14%, FOP under-predicts the mean values in comparison with SOP and MCS. The corresponding standard deviation of deflection is shown in Figure 4.47 and Figure 4.48. It can be observed from Figure 4.47 and Figure 4.48 that at a CV of 20%, the deviation between the values obtained from perturbation approach and MCS is around 11% regardless of tools (FEM or WFEM) used. When the CV is increased to 25%, the deviation also increases to 18%.

The variation of mean values of deflection calculated at a CV of 5% for different correlation length parameters while linear and quadratic shape functions is used for random field modelling are shown in Figure 4.49 and Figure 4.50 respectively. It can be observed that the mean values of deflection evaluated using the perturbation approach, concur well with the MCS values for different correlation length parameters regardless of the tools used. Figure 4.51 and Figure 4.52 shows the variation of standard deviation of deflection at $x = 100$mm against correlation length parameter, for random field discretization using linear and quadratic shape functions respectively. When the random field is discretized using linear shape functions, it can be seen in Figure 4.51 that the standard deviation values obtained from both FEM and WFEM using perturbation and MCS approaches remain in good agreement with each other. However, for random field discretization done using quadratic shape functions as shown in Figure 4.52, a deviation of less than 5% is observed between FEM and WFEM for correlation length parameter less than 10. The deviation between the values obtained from FEM and WFEM at certain correlation length parameters can be attributed to the reasons already discussed in the context of EBT based beams.

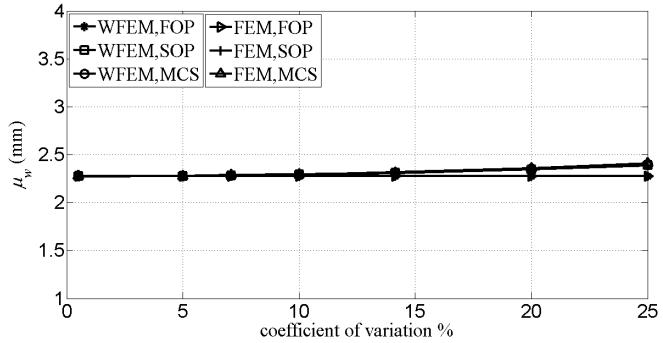

Figure 4.45: Variation of mean value of deflection at $x = 100$mm for the TBT based cantilever beam against CV, when linear BSWI WFEM and FEM based shape functions are used for random field modelling

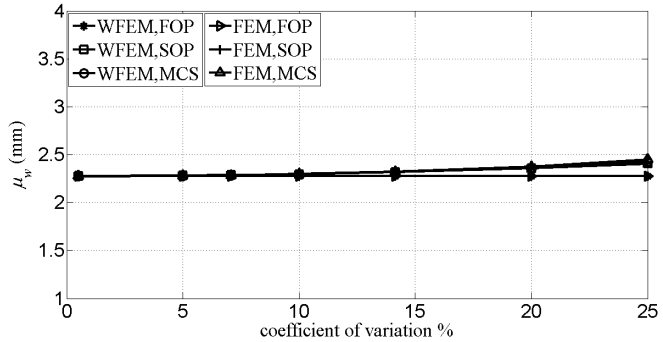

Figure 4.46: Variation of mean value of deflection at $x = 100$mm for the TBT based cantilever beam against CV, when quadratic BSWI WFEM and FEM based shape functions are used for random field modelling

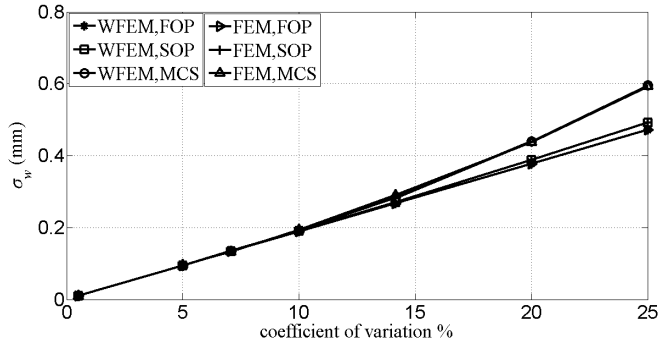

Figure 4.47: Variation of standard deviation value of deflection at $x = 100$mm for the TBT based cantilever beam against CV, when linear BSWI WFEM and FEM based shape functions are used for random field modelling

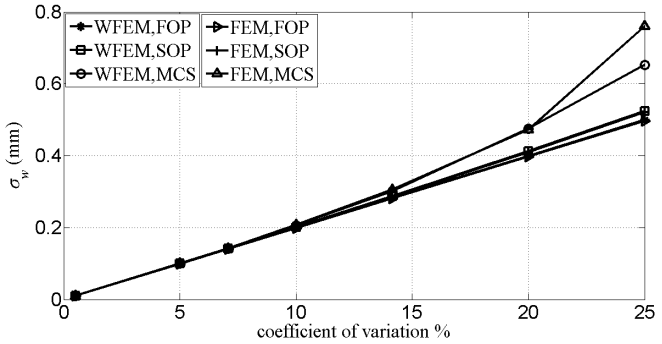

Figure 4.48: Variation of standard deviation value of deflection at $x = 100$mm for the TBT based cantilever beam against CV, when quadratic BSWI WFEM and FEM based shape functions are used for random field modelling

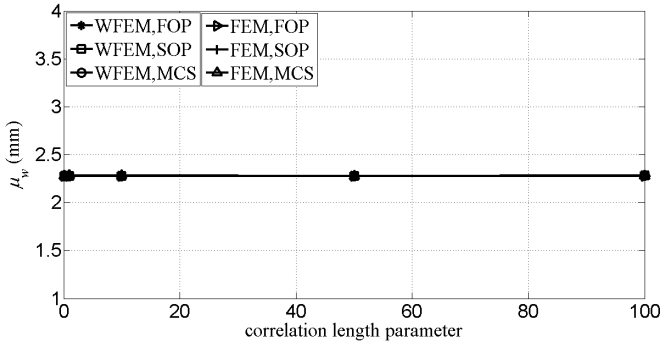

Figure 4.49: Variation of mean value of deflection at $x = 100$mm for the TBT based cantilever beam against correlation length parameter, when linear BSWI WFEM and FEM based shape functions are used for random field modelling

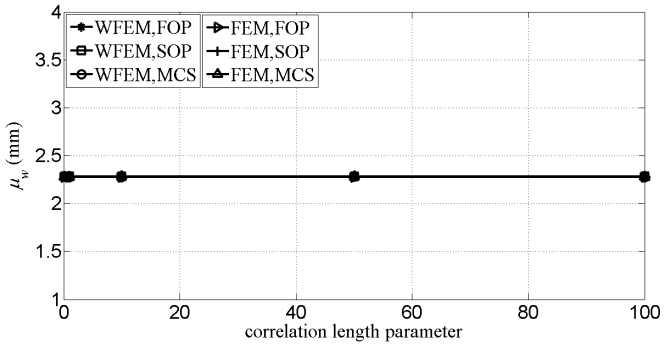

Figure 4.50: Variation of mean value of deflection at $x = 100$mm for the TBT based cantilever beam against correlation length parameter, when quadratic BSWI WFEM and FEM based shape functions are used for random field modelling

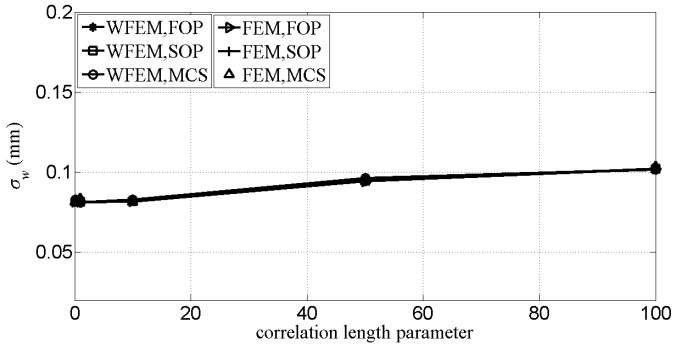

Figure 4.51: Variation of standard deviation value of deflection at $x = 100$mm for the TBT based cantilever beam against correlation length parameter, when linear BSWI WFEM and FEM based shape functions are used for random field modelling

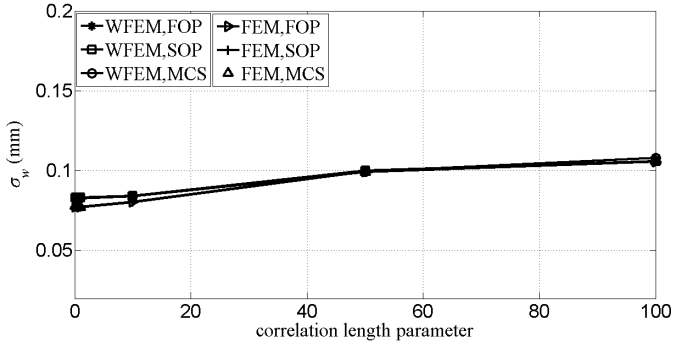

Figure 4.52: Variation of standard deviation value of deflection at $x = 100$mm for the TBT based cantilever beam against correlation length parameter, when quadratic BSWI WFEM and FEM based shape functions are used for random field modelling

4.3.2.4 Simply supported beam based on Timoshenko beam theory

In this example, a simply supported beam as shown in Figure 3.18 is considered for analysis. The material, geometric properties and discretization that were considered in the case of a TBT based cantilever beam are used in the current study as well. The mean and standard deviation values of deflection field at $x = 50$mm are shown in Figure 4.53 -Figure 4.56 in which the perturbation values are compared with the values obtained from MCS and the results are plotted for different values of CV. It can be observed from Figure 4.53 and Figure 4.54 that mean values are under-predicted by FOP in comparison with SOP and MCS results by around 5% at a CV of 20%. For values of CV higher than 20%, the deviation between FOP values and the rest also increases, similar to the observation that has been noted so far from previous examples. The values of standard deviation as seen in Figure 4.55 and Figure 4.56 show that for CV values less than 15% both perturbation

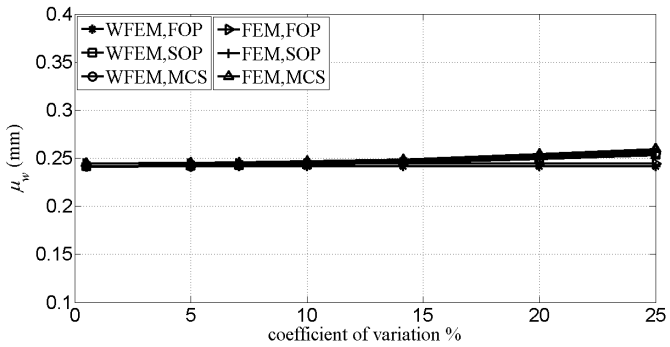

Figure 4.53: Variation of mean value of deflection at $x = 50$mm for the TBT based simply supported beam against CV, when linear BSWI WFEM and FEM based shape functions are used for random field modelling

and MCS values match well, however for CV of 20% and more, the deviation observed in the value of standard deviation obtained from the perturbation approach and MCS is between 18% - 28%. This reiterates the assumption that perturbation approach is suitable for analysis with small variances only.

Figure 4.57 and Figure 4.58 shows the variation of mean values of deflection calculated at $x = 50$mm and at a CV of 5% for different correlation length parameters by using linear and quadratic shape functions for random field modelling respectively. It can be observed that perturbation values remain in good agreement with the MCS results for different correlation length parameters. Similarly, the variation of standard deviation of deflection against correlation length parameters for random field modelling using linear and quadratic shape functions is shown in Figure 4.59 and Figure 4.60 respectively. It can be observed from Figure 4.59 that when the random field is discretized using linear shape functions, the values obtained from perturbation approach are in good agreement with the values of MCS for different correlation length parameters. However, when quadratic shape functions are used for random field discretization, it can be observed from Figure 4.60 that for correlation length parameter less than 50, the perturbation and MCS values obtained by using FEM Lagrange shape functions deviate away from the values obtained with WFEM. A maximum deviation of 12% is observed when the correlation length parameter is less than 1.

In addition to evaluating the values of mean and standard deviation of deflection for various boundary conditions, the normalized computational time required for implementing the perturbation method (FOP and SOP combined) and MCS using BSWI WFEM and FEM is also calculated for beams and shown in Tables 4.5-4.8. The configuration of CPU is

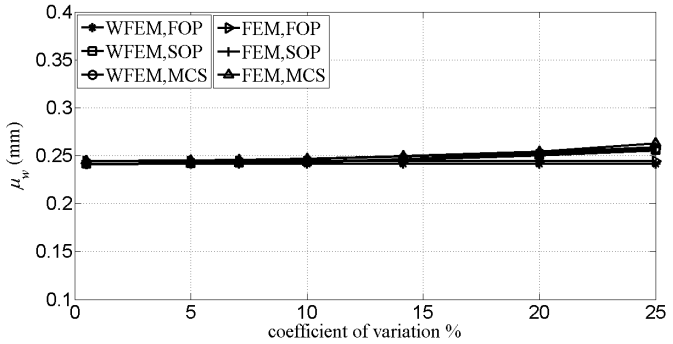

Figure 4.54: Variation of mean value of deflection at $x = 50$mm for the TBT based simply supported beam against CV, when quadratic BSWI WFEM and FEM based shape functions are used for random field modelling

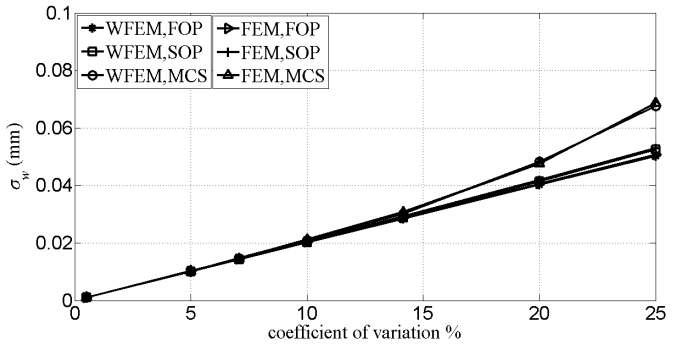

Figure 4.55: Variation of standard deviation value of deflection at $x = 50$mm for the TBT based simply supported beam against CV, when linear BSWI WFEM and FEM based shape functions are used for random field modelling

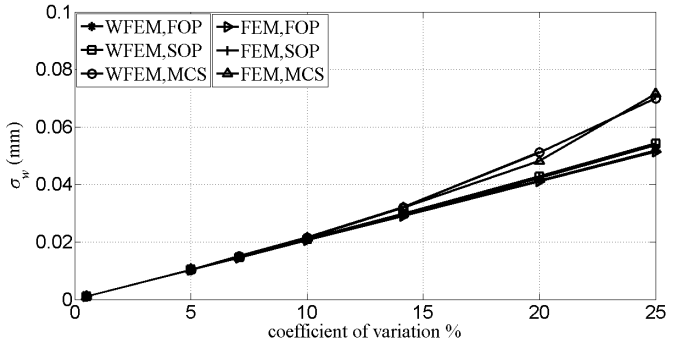

Figure 4.56: Variation of standard deviation value of deflection at $x = 50$mm for the TBT based simply supported beam against CV, when quadratic BSWI WFEM and FEM based shape functions are used for random field modelling

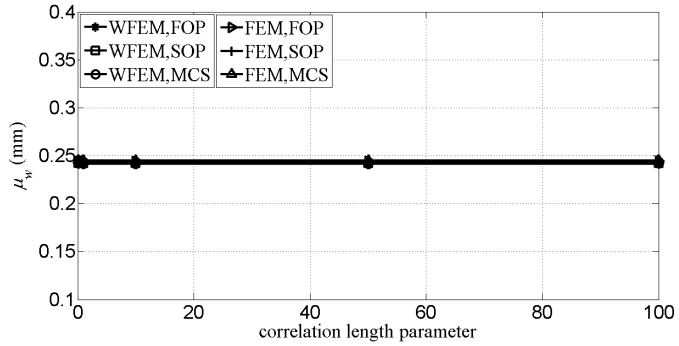

Figure 4.57: Variation of mean value of deflection at $x = 50$mm for the TBT based simply supported beam against correlation length parameter, when linear BSWI WFEM and FEM based shape functions are used for random field modelling

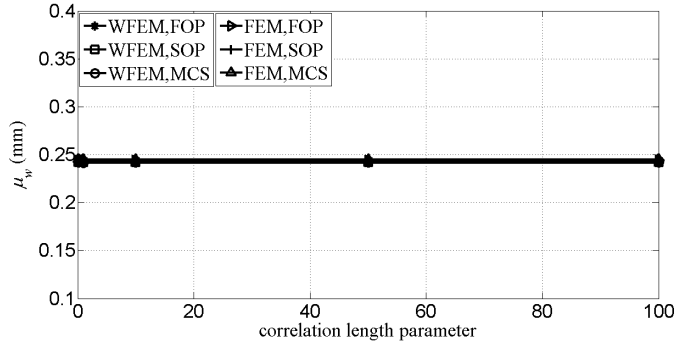

Figure 4.58: Variation of mean value of deflection at $x = 50$mm for the TBT based simply supported beam against correlation length parameter, when quadratic BSWI WFEM and FEM based shape functions are used for random field modelling

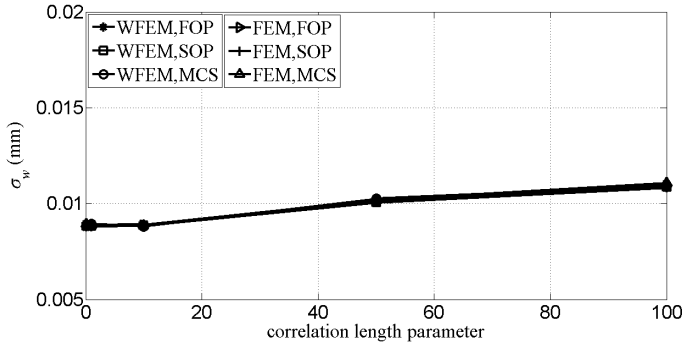

Figure 4.59: Variation of standard deviation value of deflection at $x = 50$mm for the TBT based simply supported beam against correlation length parameter, when linear BSWI WFEM and FEM based shape functions are used for random field modelling

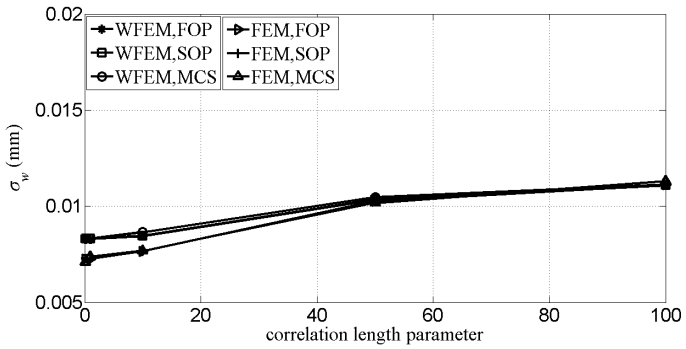

Figure 4.60: Variation of standard deviation value of deflection at $x = 50$mm for the TBT based simply supported beam against correlation length parameter, when quadratic BSWI WFEM and FEM based shape functions are used for random field modelling

kept the same throughout the computational process. While evaluating the computational time, the correlation length parameter is kept equal to 50 and CV of 5% is assumed. The sample size used for MCS is equal to 5000. It can be observed from Table 4.5 and Table 4.6 that for beams based on EBT formulation, the perturbation approach (FOP and SOP combined) takes less computational time when compared with MCS in the case of both WFEM and FEM. However, it is also noted that FEM based perturbation approach takes less time when compared with WFEM. The higher computational times needed by WFEM could be attributed to the reasons already discussed in the context of stochastic 1D bar element. However, for the benefit of the reader it is once again emphasized here.

The underlying cardinal B-splines which form the scaling functions of WFEM are piecewise polynomials and its explicit expression are obtained at Gauss points during the evaluation of system of equations. Hence, as the number of Gauss points increases, the number of function calls for obtaining the explicit expression of cardinal B-splines and thereby evaluating the scaling functions also increases. This increases the computational overhead resulting in a higher computational time. On the contrary, FEM shape functions are not piecewise polynomials due to which, this issue is not encountered. By way of better programming practices and optimized implementation of algorithms, the issue of higher computational overhead as encountered in the case of WFEM can be possibly addressed and the computational times can be further reduced. It is also noted from Tables 4.5-4.6 that MCS times obtained from FEM are higher when compared with WFEM because the total DOF used by EBT based BSWI WFEM element is less when compared with the total DOF used by multiple FEM elements. The normalized computational times based on TBT formulation are given in Tables 4.7-4.8. For the perturbation case, a similar conclusion

Table 4.5: Normalized computational times of WFEM based perturbation method (for both FOP and SOP) and MCS using linear and quadratic shape functions for random field modelling for EBT based cantilever beam

Cantilever (EBT)	**Perturbation**		**MCS**	
	$m_r = 2$	$m_r = 3$	$m_r = 2$	$m_r = 3$
WFEM	5.47	6.92	27.56	30.63
FEM	1	1.92	44.53	52.44

Table 4.6: Normalized computational times of WFEM based perturbation method (for both FOP and SOP) and MCS using linear and quadratic shape functions for random field modelling for EBT based simply supported beam

Simply supported (EBT)	**Perturbation**		**MCS**	
	$m_r = 2$	$m_r = 3$	$m_r = 2$	$m_r = 3$
WFEM	5.07	5.95	26.79	30.86
FEM	1	1.96	43.93	50.24

can be drawn that is observed in the case of EBT based formulation. The DOF in the case of WFEM and FEM are same for the TBT based formulation, and hence the difference between their MCS computational times is reduced. Nonetheless, the more computational time taken by WFEM can be attributed to the reasons discussed earlier. However, it is important to note that if randomness associated with geometric parameters are involved, re-meshing and convergence studies needs to be done; in which case WFEM due to its inherent properties like MRA could become more attractive with respect to computational time too. Further, the effect of small correlation length on convergence associated with FEM discretization also needs to be accounted for in the overall computational time.

The numerical examples on beams considered so far show that the random field with a

Table 4.7: Normalized computational times of WFEM based perturbation method (for both FOP and SOP) and MCS using linear and quadratic shape functions for random field modelling for TBT based cantilever beam

Cantilever (TBT)	**Perturbation**		**MCS**	
	$m_r = 2$	$m_r = 3$	$m_r = 2$	$m_r = 3$
WFEM	6.74	7.80	50.25	54.68
FEM	1	1.98	44.01	51.27

Table 4.8: Normalized computational times of WFEM based perturbation method (for both FOP and SOP) and MCS using linear and quadratic shape functions for random field modelling for TBT based simply supported beam

Simply supported (TBT)	Perturbation		MCS	
	$m_r = 2$	$m_r = 3$	$m_r = 2$	$m_r = 3$
WFEM	5.45	6.81	44.89	48.49
FEM	1	1.73	36.63	44.20

Gaussian distribution can be accurately modelled using BSWI WFEM scaling functions. To demonstrate that the proposed method is effective for non-Gaussian distributions as well, a random field with a lognormal distribution is considered in the next numerical example.

4.3.2.5 Modelling of random field with a non-Gaussian distribution

In this example, a cantilever beam as shown in Figure 3.17 is considered for analysis wherein, the modulus of elasticity is modelled as a homogeneous random field with a lognormal distribution, as given by Equation 4.4. Exponential auto-covariance function is considered during the study. The formulations based on both EBT and TBT are used in the analysis. The dimensions and loading for the cantilever beam are kept the same as considered in the previous examples. The displacement field is modelled using $m = 4, j = 3$ for the EBT based formulation and $m = 3, j = 3$ for the TBT based formulation. The random field is modelled using $m = 3, j = 1$ in both the cases and correlation length parameter used is equal to 50. Tables 4.9 and 4.10 show the variation of mean and standard deviation values against CV for the EBT based formulation and Tables 4.11 and 4.12 show the variation of mean and standard deviation values against CV for the TBT based formulation.

It can be observed from Table 4.9 for EBT based formulation that at a CV of 20% the deviation in mean values between SOP and MCS is around 2% using both WFEM and FEM. However, the variation for standard deviation, as observed from Table 4.10 is around 4% using WFEM and 7.45% using FEM. For TBT based formulations, Table 4.11 shows that the variation in mean values is around 1.8-2% at 20% CV. In the case of standard deviation values, the variation as observed from Table 4.12 is around 4-5% for both WFEM and FEM. Further, it is observed from all the Tables 4.9 - 4.12 that the variation in mean and standard deviation values reduces to around 1% when the CV value is less than 15%.

Table 4.9: Variation of mean value of deflection at $x = 100$mm for the EBT based cantilever beam against CV, when quadratic BSWI WFEM and FEM based shape functions are used for modelling lognormal random field

CV%	WFEM			FEM		
	FOP	SOP	MCS	FOP	SOP	MCS
5.00	7.500	7.508	7.518	7.500	7.508	7.519
10.00	7.500	7.534	7.562	7.500	7.533	7.573
14.14	7.500	7.567	7.638	7.500	7.566	7.644
20.00	7.500	7.629	7.800	7.500	7.627	7.773
25.00	7.500	7.693	7.937	7.500	7.690	7.924

Table 4.10: Variation of standard deviation value of deflection at $x = 100$mm for the EBT based cantilever beam against CV, when quadratic BSWI WFEM and FEM based shape functions are used for modelling lognormal random field

CV%	WFEM			FEM		
	FOP	SOP	MCS	FOP	SOP	MCS
5.00	0.329	0.329	0.325	0.316	0.316	0.321
10.00	0.655	0.656	0.659	0.629	0.631	0.656
14.14	0.920	0.923	0.940	0.884	0.887	0.929
20.00	1.282	1.292	1.351	1.232	1.241	1.341
25.00	1.577	1.594	1.756	1.515	1.531	1.701

Table 4.11: Variation of mean value of deflection at $x = 100$mm for the TBT based cantilever beam against CV, when quadratic BSWI WFEM and FEM based shape functions are used for modelling lognormal random field

CV%	WFEM			FEM		
	FOP	SOP	MCS	FOP	SOP	MCS
5.00	2.274	2.277	2.279	2.274	2.276	2.279
10.00	2.274	2.284	2.294	2.274	2.284	2.296
14.14	2.274	2.294	2.314	2.274	2.294	2.318
20.00	2.274	2.313	2.368	2.274	2.313	2.357
25.00	2.274	2.333	2.402	2.274	2.332	2.401

Table 4.12: Variation of standard deviation value of deflection at $x = 100$mm for the TBT based cantilever beam against CV, when quadratic BSWI WFEM and FEM based shape functions are used for modelling lognormal random field

CV%	WFEM			FEM		
	FOP	SOP	MCS	FOP	SOP	MCS
5.00	0.099	0.099	0.098	0.099	0.099	0.097
10.00	0.198	0.198	0.199	0.197	0.197	0.198
14.14	0.278	0.279	0.284	0.276	0.277	0.281
20.00	0.387	0.390	0.407	0.385	0.388	0.406
25.00	0.476	0.482	0.531	0.474	0.479	0.515

4.3.3 Numerical examples for stochastic buckling of columns

Two numerical examples are solved with the proposed stochastic BSWI WFEM formulation for elastic buckling of columns. As numerical examples, columns with pinned-pinned (p-p) and fixed-pinned (f-p) boundary conditions under axial compressive loading as shown in Figure 4.61 are considered. Column of length $L = 100$mm, cross-sectional dimensions $b = 1$mm and $h = 1$mm is considered for the study. Young's modulus is taken as a homogeneous lognormal random field with a mean $\mu_{E_l} = 2 \times 10^5$MPa. The response statistics for buckling loads and mode shapes are calculated via perturbation approach and the results are compared with the statistics obtained from MCS. In order to fix the number of random variables which is to be used in the modelling of Young's modulus as defined by Equation 4.4, the random field is discretized using different number of random variables and the variation of mean values and standard deviation of Young's modulus is evaluated using MCS on the same lines as shown in Figures 4.3 and 4.4 respectively. A resolution of $j = 2$ with linear scaling functions resulting in 5 nodes captures the mean and standard deviation values of Young's modulus accurately and is therefore considered for the analysis. From a convergence study, based on the calculation of relative percentage error in L^2 norm of mean and standard deviation values of Young's modulus for various MCS sample size; it is noted that an error of less than 1% is obtained when the MCS sample size is 5000. Hence, for the current study MCS sample size of 5000 is considered. The entire domain of the column is modelled using one BSWI C_1 type continuity element. The deflection field is approximated using cubic ($m = 4$) BSWI scaling functions with a resolution of ($j = 4$) and the random field is approximated with linear ($m = 2$) BSWI scaling functions with a coarse resolution of ($j = 2$).

The mean values of the buckling loads (first, second and third) for a p-p and f-p column

obtained by using the perturbation approach are shown in Figure 4.62. These values are compared with the values obtained from MCS and the results are plotted for different values of CV, obtained by varying the standard deviation of Young's modulus. The correlation length parameter considered is 50. It can be observed from Figure 4.62 that for a p-p column, at a CV of 20% the results obtained from perturbation approach are in good agreement with MCS for all the buckling loads. However, at a CV of 25%, a deviation of 3% is observed between the perturbation and MCS results in the case of third buckling load. However, for an f-p column, at a CV of 25% there is a deviation of around 5% between the results obtained from perturbation approach and MCS for the third buckling load. The variation of standard deviation values of buckling loads against CV are shown in Figure 4.63. It can be observed that for both p-p and f-p columns, even at a CV of 25%, the values obtained from perturbation approach concur well with the MCS values for all the buckling loads. The variation of mean and standard deviation values of buckling loads for a p-p column and f-p column, obtained by using the perturbation approach against varying correlation length parameter is shown in Figure 4.64 and Figure 4.65 respectively. A value of 5% is considered for CV during the process. Figure 4.64 and Figure 4.65 shows that even at a small correlation length parameter the values obtained from WFEM based perturbation approach remain in good agreement with the MCS values for both the cases. This shows that a coarse discretization of random field using BSWI WFEM is able to accurately capture the results even at extreme correlation length parameters unlike SFEM, wherein the dependency of correlation length parameter on random field mesh would require a higher number of random variables to be used for accurate results.

Besides the buckling loads, the first three mode shapes are also plotted for the p-p column and f-p column as shown in Figure 4.66 and Figure 4.67 respectively. It can be seen that WFEM based perturbation approach accurately captures the first three mode shapes when compared with MCS results. Furthermore, the first three mode shapes reinstates the accuracy of the WFEM based perturbation approach. In addition to evaluating the mean and standard deviation values of the buckling loads, the normalized computational times required by the perturbation approach (FOP and SOP combined) and MCS (5000 simulations) is also calculated. It is noted that in the case of a p-p column, the execution time of MCS is 39.63 times more in comparison with WFEM based perturbation approach. Similarly, for a f-p column, the execution time of MCS is 38.28 times more than the perturbation method. Hence, the proposed BSWI WFEM based perturbation approach is not only accurate but also computationally more efficient in comparison with the MCS based approach.

Based on the analysis from the preceding 1D and 2D examples in the current chapter, conclusions are drawn and discussed in the following section.

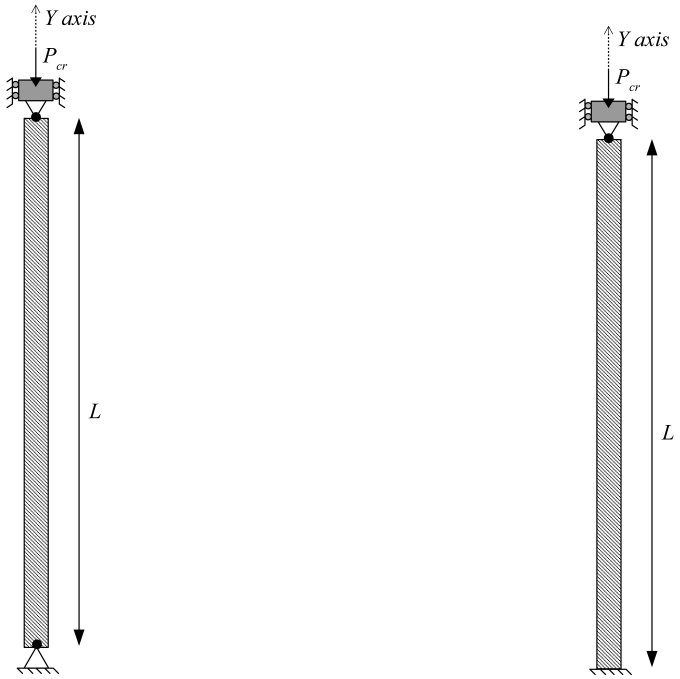

(a) Pinned-Pinned

(b) Pinned-Fixed

Figure 4.61: Columns with various boundary conditions under axial compressive loading

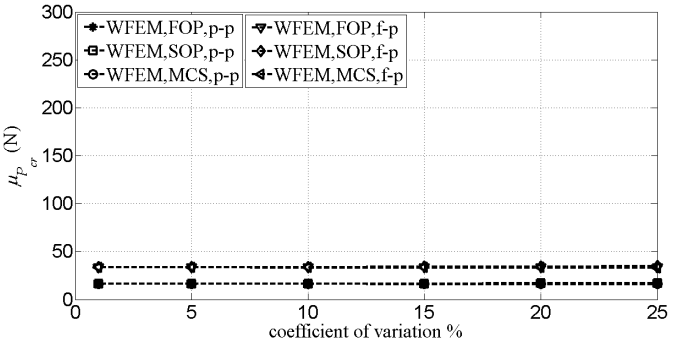

(a) First buckling load

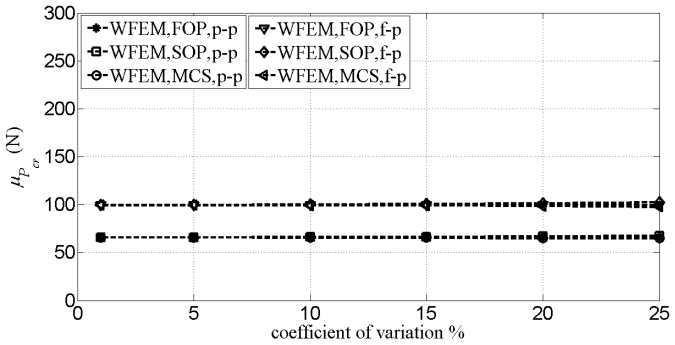

(b) Second buckling load

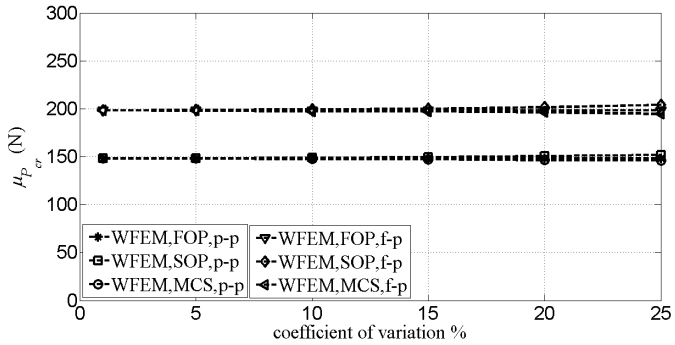

(c) Third buckling load

Figure 4.62: Variation of mean values of buckling loads for columns with different boundary conditions against CV

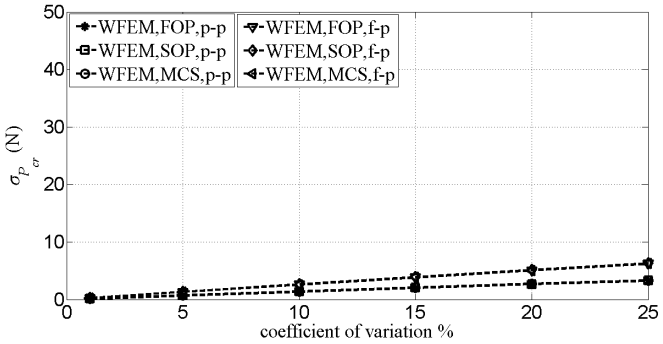

(a) First buckling load

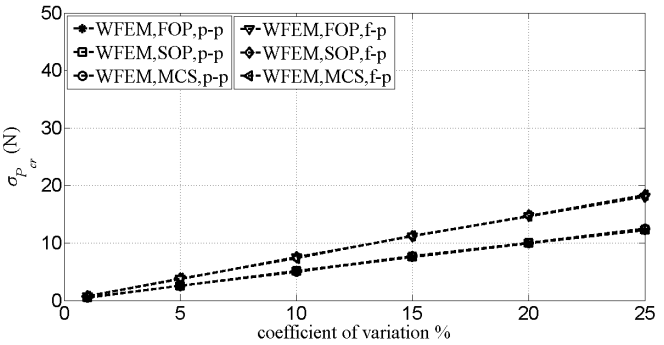

(b) Second buckling load

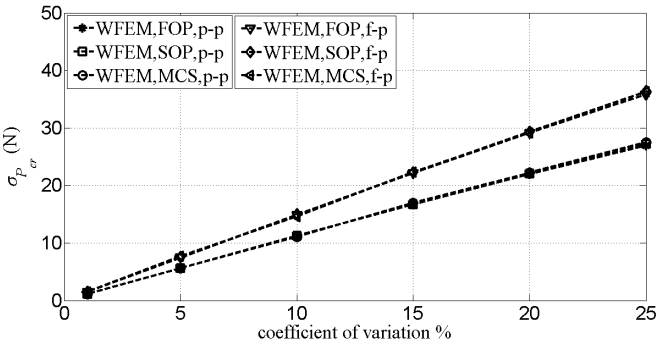

(c) Third buckling load

Figure 4.63: Variation of standard deviation values of buckling loads for columns with different boundary conditions against CV

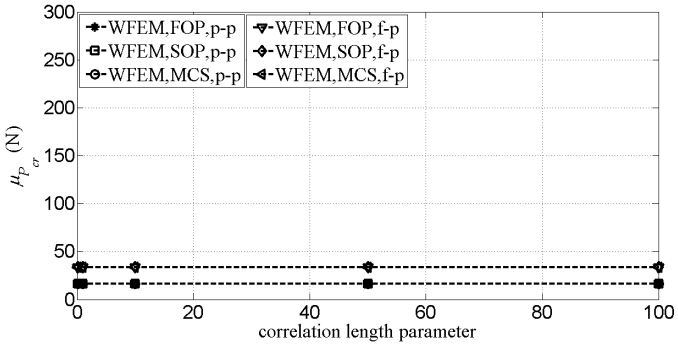

(a) First buckling load

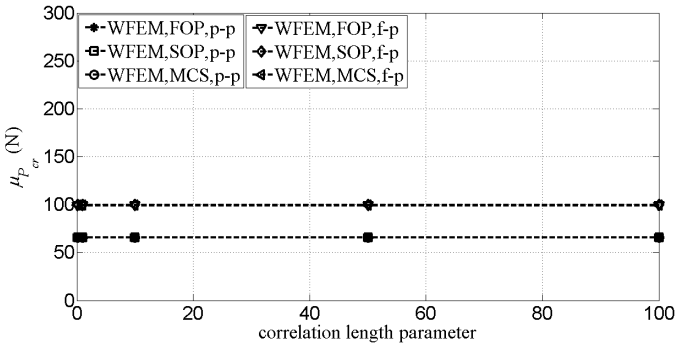

(b) Second buckling load

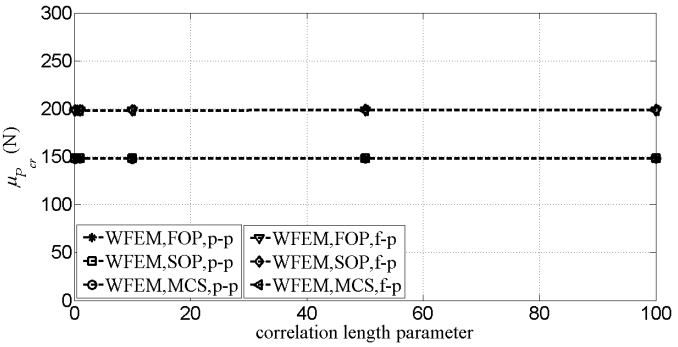

(c) Third buckling load

Figure 4.64: Variation of mean values of buckling loads for columns with different boundary conditions against correlation length parameter

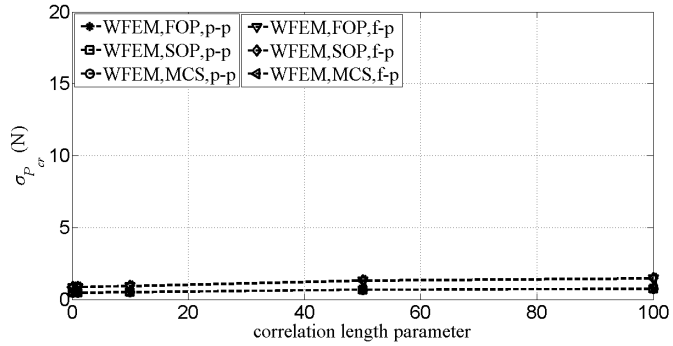

(a) First buckling load

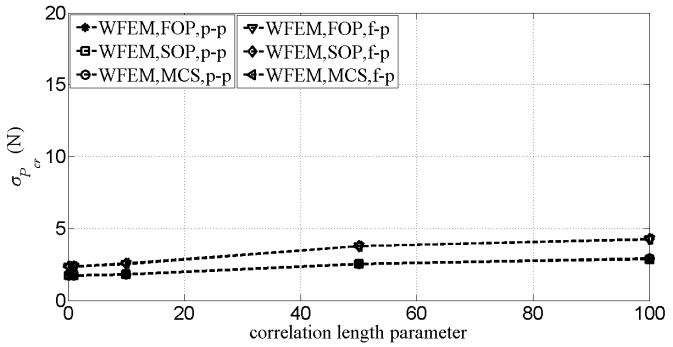

(b) Second buckling load

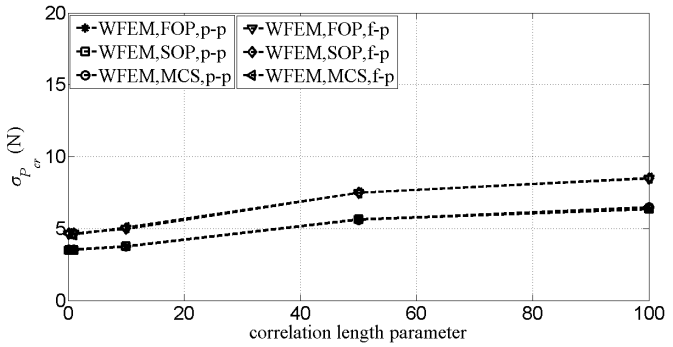

(c) Third buckling load

Figure 4.65: Variation of standard deviation values of buckling loads for columns with different boundary conditions against correlation length parameter

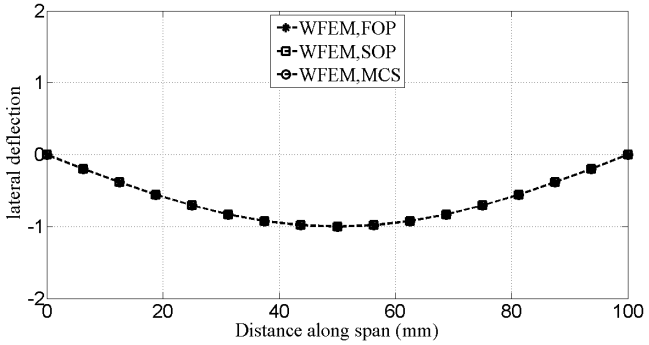

(a) First mode shape

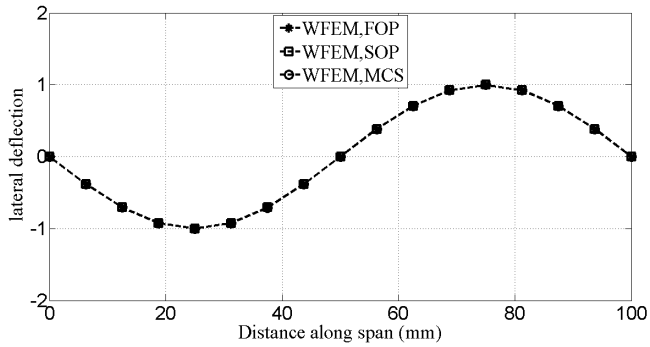

(b) Second mode shape

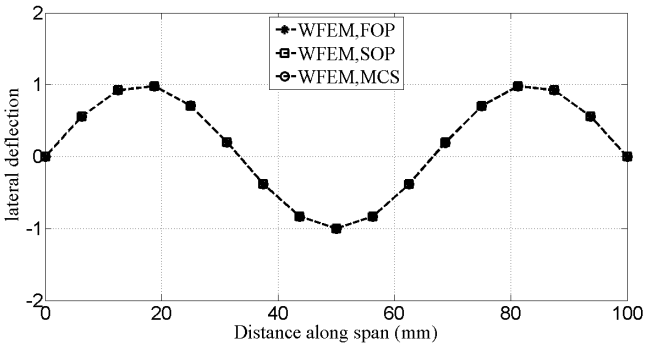

(c) Third mode shape

Figure 4.66: Mode shapes for a pinned-pinned column

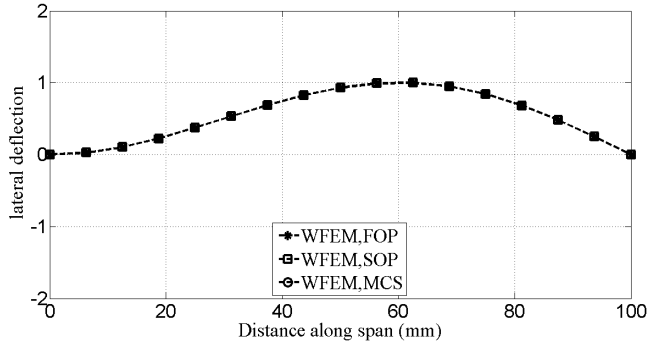

(a) First mode shape

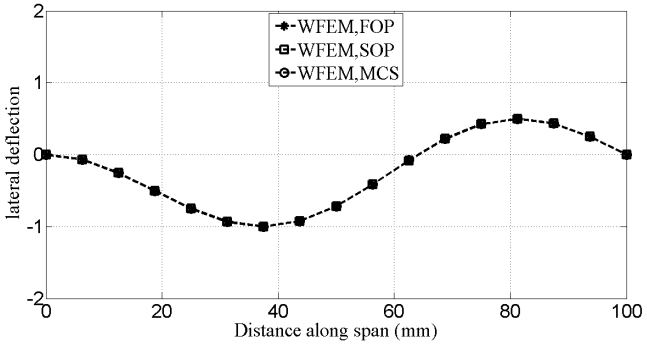

(b) Second mode shape

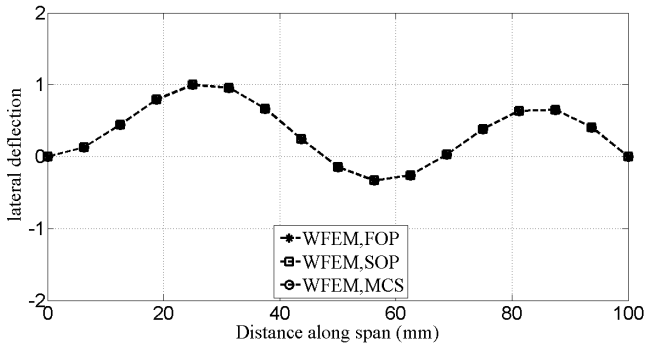

(c) Third mode shape

Figure 4.67: Mode shapes for a fixed-pinned column

4.4 Conclusion

In the current chapter, the formulation of stochastic BSWI WFEM for 1D and 2D problems in elasto-statics is proposed in which the spatial variation of modulus of elasticity is modelled as a homogeneous random field. The present work suggests using BSWI scaling functions to discretize random field. Two scale relation and MRA properties of BSWI wavelets help the physical problem to be discretized using less number of elements; say 1 or 2, as witnessed in the numerical examples and thus can reduce the computational cost required for mesh assembly when compared to FEM.

The response statistics of mean and standard deviation are calculated using the perturbation approach. Numerical examples based on 1D bar, 2D plane stress problems, beams based on EBT and TBT and stochastic buckling of columns are solved. The results obtained from WFEM based perturbation approach are compared with the results of MCS. Further, in order to validate the proposed methodology perturbation and MCS results based on FEM Lagrange shape functions for 1D problem (bar and beams) are also obtained and a comparative study between the results of WFEM and FEM is done. A single BSWI WFEM element with coarse nodal distribution for random field modelling, perform well by accurately capturing the standard deviations even at extremely small or large correlation length parameters as observed in 1D problem. On the other hand, FEM demands an appropriate response and random field mesh size in accordance with the correlation length of the input field, which otherwise would result in an erroneous result. Normalized computational times are also shown for 1D problems, from which it can be concluded that FEM based perturbation times are less in comparison with WFEM. However, it is to be noted that those computational times are estimated without accounting for the time associated with re-meshing and convergence studies. The 2D plane stress problems demonstrate that high accuracy can be maintained even when the random field is modelled with wavelet scaling functions of lower order and lower resolution, thereby reducing the computational effort needed.

It can be concluded from the results of 1D and 2D numerical examples for problems in elasto-statics that the proposed BSWI WFEM based perturbation approach (both FOP and SOP) accurately captures the response statistics of the displacement field for CV values of up to 15-20% . For problems in beams, accurate results are obtained when the values of CV is less than or equal to 15% and in the case of stochastic buckling of columns, WFEM based perturbation approach can be used to accurately capture the response statistics of the buckling load for values of CV up to 25%. In the next chapter, deterministic and stochastic

BSWI WFEM formulation for beam analysis incorporating von Kármán nonlinear strains is shown and discussed in detail.

Chapter 5

BSWI WFEM formulation for beams incorporating von Kármán nonlinear strains

Generally, thin metallic beams and plates can undergo large deflection in transverse directions with small strains (without generating plastic strains and hence linear constitutive relations) and moderate rotations. However, this can introduce nonlinearity into the set of equations due to the presence of in-plane forces which are related to the rotations. The von Kármán nonlinear strains based WFEM formulation introduced in this chapter is applicable for such class of beam problems undergoing large transverse deflection with small strains, resulting in stretching of the neutral axis leading to nonlinear strain displacement behaviour [210, 211]. Thus, the strain displacement relation is modified to incorporate nonlinear coupling terms (ignoring large strain terms) that account for axial displacement even when there are no applied axial forces. Further, it is found that the construction of beam elements incorporating von Kármán nonlinear strains with BSWI WFEM does not exist in the literature.

Hence, the current chapter proposes the deterministic and stochastic formulation of beam elements using BSWI based WFEM by incorporating von Kármán nonlinear strains. Formulation is used for both EBT and TBT. The background cell based Gauss quadrature is used for numerical integration. For the deterministic case, numerical examples are solved for transverse deflections and stresses in axial direction and are compared with the existing converged results from FEM. The issues of membrane and shear locking for the proposed elements are examined and solution techniques are also suggested to overcome the issues. Following the deterministic formulation, a stochastic BSWI WFEM formulation is shown for beams incorporating von Kármán nonlinear strains wherein, the spatial variation of

modulus of elasticity is modelled as a homogeneous random field. A set of three nonlinear of equations are derived based on perturbation approach for evaluating derivatives of field variable with respect to random variables. Numerical examples based on the stochastic formulation are analyzed for response statistics, on similar lines as discussed in the previous chapter 4.

5.1 Deterministic BSWI WFEM formulation for beams incorporating von Kármán nonlinear strains

The proposed wavelet finite element formulation by incorporating von Kármán strains for both Euler-Bernoulli BSWI beam element and Timoshenko BSWI beam element are given in this section.

5.1.1 Euler-Bernoulli beam element with von Kármán nonlinear strains

In the present formulation, the deformation of a continuous body is analytically described using the Total Lagrangian (TL) approach, in which the motion of the body is referred to an undeformed reference configuration and the variation of field variable over the body is described in relation to the material co-ordinates. The general measure of deformation is described in terms of Green-Lagrange strain tensor E_{IJ}, which gives the nonlinear strain-displacement relation as,

$$E_{IJ} = \frac{1}{2}\left(\frac{\partial u_I}{\partial X_J} + \frac{\partial u_J}{\partial X_I}\right) + \frac{1}{2}\left(\frac{\partial u_K}{\partial X_I}\frac{\partial u_K}{\partial X_J}\right) \tag{5.1}$$

However, for beams with moderately large rotations and small strains, the displacement field considered is as follows [210],

$$\left.\begin{aligned} u = u_0(x) - z\frac{dw_0}{dx} \\ v = 0 \\ w = w_0(x) \end{aligned}\right\} \tag{5.2}$$

where, (u, v, w) are total displacements along the co-ordinate directions (x, y, z), u_0 and w_0 denote the axial and transverse displacements. Hence, von Kármán strains for beams which omits large strain but includes moderately large rotations and small strains can be

written as,

$$E_{XX} = \left(\frac{du_0}{dX} + \frac{1}{2} \left(\frac{dw_0}{dX} \right)^2 \right) - z \left(\frac{d^2 w_0}{dX^2} \right) \tag{5.3}$$

Since, the geometry of the deformed configuration is unknown; the equilibrium equations are also expressed in terms of known reference configuration. The second Piola-Kirchhoff stress tensor S_{IJ}, which gives the transformed current force per unit undeformed area, is used in the TL formulation for geometrically nonlinear analysis. Additionally, the incremental stress-strain constitutive relationship for nonlinear analysis of solid continua in TL formulation is given as,

$$S_{IJ} = C_{IJKL} E_{KL} \tag{5.4}$$

where, C_{IJKL} is the material elasticity tensor. The stress and strain measures that have been discussed for the TL formulation are substituted in the weak form obtained from the principal of virtual work, for the development of BSWI WFEM. The analytical form for the principle of virtual work for Ω_i is given as,

$$\delta W^i = \delta (W_I^i - W_E^i) = 0 \tag{5.5}$$

where, δW_I^i is the virtual strain energy stored in the sub-domain due to Cauchy stresses σ_{ij} in moving through the virtual strains $\delta \epsilon_{ij}$, and δW_E^i is the work done in moving through their respective virtual displacements by the externally applied loads. It is assumed that the strains are small and hence no distinction is made between σ_{ij} and S_{IJ}. Since, the virtual quantities in Equation 5.5 are considered as the variations of real quantities, it can be re-written in the domain of an Euler-Bernoulli BSWI beam element by substituting von Kármán nonlinear strains and second Piola-Kirchhoff stress tensor into the virtual work

equation and expressing it in terms of displacement as,

$$\left.\begin{aligned} \delta\left(W_I^i - W_E^i\right) = 0 \\ \delta\left(\int_{V^i} \frac{1}{2} S_{XX} E_{XX} dV - \int_{x_a}^{x_b} q w_0 dx - \int_{x_a}^{x_b} f u_0 dx - \sum_{i=1}^{n_d} Q_i \Delta_i\right) = 0 \\ \delta\left(\int_{V^i} \frac{1}{2} E \left\{\frac{du_0}{dX} + \frac{1}{2}\left(\frac{dw_0}{dX}\right)^2 - z\left(\frac{d^2 w_0}{dX^2}\right)\right\}^2 dV - \int_{x_a}^{x_b} q w_0 dx - \right. \\ \left. \int_{x_a}^{x_b} f u_0 dx - \sum_{i=1}^{n_e} Q_i \Delta_i\right) = 0 \end{aligned}\right\} \tag{5.6}$$

Here, $q(x)$ is the distributed transverse load per unit length, $f(x)$ is the distributed axial load per unit length, Q_i are the generalized nodal forces, n_e is the total number of nodes in the element and Δ_i are the generalized nodal displacements.

In the present formulation, the incorporation of von Kármán strain leads to membrane strain terms and that necessitates the modelling/incorporation of axial DOF along with transverse and rotational DOF. This is done by superimposing an existing beam element and a bar (axial) element. Hence, the beam element based on von Kármán strains and BSWI WFEM is constructed by superposition of axial rod BSWI element with $m = 2$ and Euler-Bernoulli BSWI beam element with $m = 4$, following the method proposed for plane bar elements by Xiang et al. [111]. The preceding orders for bar and beam elements are ergo selected, to maintain equal number of nodes in both the bar and beam elements and facilitate superposition. The plane beam element is shown in Figure 5.1, in which each end node is having 3 DOF u_i, w_i, θ_i $(i = 1, ..., 2^j + 1)$ and each inner node is having 2 DOF u_i, w_i $(i = 2, ..., 2^j)$.

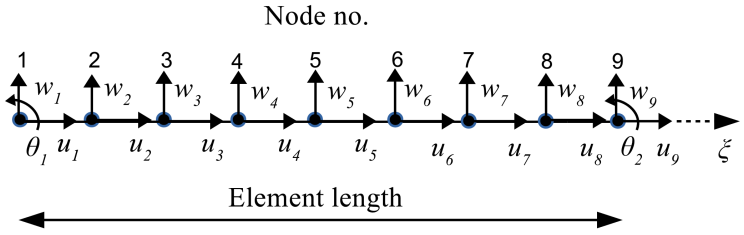

Figure 5.1: Distribution of nodes and DOF in a plane beam element for $j = 3$

The unknown axial displacement field function of a rod element in the element solving domain ξ is approximated in terms of linear wavelet scaling functions in the same way as given in Equation 3.5 and the unknown transverse displacement field function of Euler-Bernoulli beam element is approximated in terms of cubic wavelet scaling functions as given in Equation 3.11. The C_0 and C_1 type transformation matrices are obtained in the same way as given in Equations 3.6,3.7 and 3.12,3.13 respectively. The approximations of axial and transverse displacement fields are substituted into the virtual work equations of Equations 5.6. Then using the principle of minimum potential energy and mapping it onto the standard element solving domain, the algebraic form of it can be written as,

$$\left.\begin{aligned}\int_0^1 \Bigg\{ A_1 \frac{1}{l_{ex}} \frac{d(\boldsymbol{\varphi_1 T_1^e})}{d\xi} \left(\frac{1}{l_{ex}} \frac{d(\boldsymbol{\varphi_1 T_1^e u^e})}{d\xi} + \frac{1}{2} \frac{1}{l_{ex}^2} \left(\frac{d(\boldsymbol{\varphi_2 T_2^e w^e})}{d\xi} \right)^2 \right) - \\ A_2 \frac{1}{l_{ex}} \frac{d(\boldsymbol{\varphi_1 T_1^e})}{d\xi} \left(\frac{1}{l_{ex}^2} \frac{d^2(\boldsymbol{\varphi_2 T_2^e w^e})}{d\xi^2} \right) \Bigg\} l_{ex} d\xi - \\ l_{ex} \int_0^1 f(\xi) \left(\boldsymbol{\varphi_1 T_1^e} \right) d\xi - \sum_{i=1}^{n_e} Q_i^a \left(\boldsymbol{\varphi_1 T_1^e} \right) (\xi_i) = 0 \end{aligned}\right\} \tag{5.7}$$

$$\left.\begin{aligned}\int_0^1 \Bigg\{ A_1 \frac{1}{l_{ex}} \frac{d(\boldsymbol{\varphi_2 T_2^e})}{d\xi} \frac{1}{l_{ex}} \frac{d(\boldsymbol{\varphi_2 T_2^e w^e})}{d\xi} \left(\frac{1}{l_{ex}} \frac{d(\boldsymbol{\varphi_1 T_1^e u^e})}{d\xi} + \right. \\ \left. \frac{1}{2} \frac{1}{l_{ex}^2} \left(\frac{d(\boldsymbol{\varphi_2 T_2^e w^e})}{d\xi} \right)^2 \right) + A_3 \frac{1}{l_{ex}^4} \frac{d^2(\boldsymbol{\varphi_2 T_2^e})}{d\xi^2} \frac{d^2(\boldsymbol{\varphi_2 T_2^e w^e})}{d\xi^2} - \\ A_2 \frac{1}{l_{ex}} \frac{d(\boldsymbol{\varphi_1 T_1^e u^e})}{d\xi} \left(\frac{1}{l_{ex}^2} \frac{d^2(\boldsymbol{\varphi_2 T_2^e})}{d\xi^2} \right) - \\ \frac{A_2}{2} \left(\frac{1}{l_{ex}} \frac{d(\boldsymbol{\varphi_2 T_2^e w^e})}{d\xi} \right)^2 \frac{1}{l_{ex}^2} \frac{d^2(\boldsymbol{\varphi_2 T_2^e})}{d\xi^2} - \\ A_2 \frac{1}{l_{ex}^4} \frac{d^2(\boldsymbol{\varphi_2 T_2^e w_e})}{d\xi^2} \frac{d(\boldsymbol{\varphi_2 T_2^e w_e})}{d\xi} \frac{d(\boldsymbol{\varphi_2 T_2^e})}{d\xi} \Bigg\} l_{ex} d\xi - \\ l_{ex} \int_0^1 q(\xi) \left(\boldsymbol{\varphi_2 T_2^e} \right) d\xi - \sum_{i=1}^{n_e} Q_i^t \left(\boldsymbol{\varphi_2 T_2^e} \right) (\xi_i) - Q_1^r \delta\theta(0) - Q_1^r \delta\theta(1) = 0 \end{aligned}\right\} \tag{5.8}$$

Here, $\boldsymbol{\varphi_1}, \boldsymbol{T_1^e}$ with subscript 1 are associated with $u_0(\xi)$ and $\boldsymbol{\varphi_2}, \boldsymbol{T_2^e}$ with subscript 2 are associated with $w_0(\xi)$. Also, n_e is the total number of nodes per BSWI WFEM based Euler-Bernoulli beam element and $Q_i^a, Q_i^t, (Q_1^r \text{and } Q_2^r)$ are the generalized nodal forces associated with axial, transverse and rotational DOF respectively. $A_1 = \int_{A^e} E^e dA$ is the

extensional stiffness of the beam element, $A_2 = \int_{A^e} E^e z dA$ is the extensional-bending stiffness of the beam element and $A_3 = \int_{A^e} E^e z^2 dA$ is the bending stiffness of the beam element. For isotropic materials, $A_2 = 0$ when x axis coincides with geometric centroidal axis. Upon simplification, the algebraic form of system of nonlinear equations for BSWI WFEM based Euler-Bernoulli beam element which takes care of the von Kármán strains is obtained in the element solving domain $\xi \in [0, 1]$ as,

$$\boldsymbol{K^e}(\boldsymbol{U^e})\boldsymbol{U^e} = \boldsymbol{F^e} \tag{5.9}$$

where,

$$\left.\begin{aligned} \boldsymbol{K^e}(\boldsymbol{U^e}) &= \begin{bmatrix} \boldsymbol{K_1^e} \boldsymbol{K_2^e} \\ \boldsymbol{K_3^e} \boldsymbol{K_4^e} \end{bmatrix} \\ \boldsymbol{U^e} = \begin{Bmatrix} \boldsymbol{u^e} \\ \boldsymbol{w^e} \end{Bmatrix}, \boldsymbol{F^e} &= \begin{Bmatrix} \boldsymbol{F_a}^e \\ \boldsymbol{F_b}^e \end{Bmatrix} \end{aligned}\right\} \tag{5.10}$$

such that,

$$\left.\begin{aligned} \boldsymbol{K_1^e} &= \int_0^1 \frac{A_1}{l_{ex}} \left(\boldsymbol{T_1^e}\right)^T \left(\frac{d\boldsymbol{\varphi_1}}{d\xi}\right)^T \left(\frac{d\boldsymbol{\varphi_1}}{d\xi}\right) \left(\boldsymbol{T_1^e}\right) d\xi \\ \boldsymbol{K_2^e} &= \frac{1}{2} \int_0^1 \frac{A_1}{l_{ex}^2} \left\{ \left(\frac{d\boldsymbol{\varphi_2}}{d\xi}\right) \left(\boldsymbol{T_2^e}\right) \boldsymbol{w^e} \right\} \left(\boldsymbol{T_1^e}\right)^T \left(\frac{d\boldsymbol{\varphi_1}}{d\xi}\right)^T \left(\frac{d\boldsymbol{\varphi_2}}{d\xi}\right)^T \left(\boldsymbol{T_2^e}\right) d\xi \\ \boldsymbol{K_3^e} &= 2\left(\boldsymbol{K_2^e}\right)^T \\ \boldsymbol{K_4^e} &= \int_0^1 \frac{1}{l_{ex}^3} \left\{ \frac{1}{2} A_1 \left\{ \left(\frac{d\boldsymbol{\varphi_2}}{d\xi}\right) \left(\boldsymbol{T_2^e}\right) \boldsymbol{w^e} \right\} \left\{ \left(\frac{d\boldsymbol{\varphi_2}}{d\xi}\right) \left(\boldsymbol{T_2^e}\right) \boldsymbol{w^e} \right\}^T \right. \\ &\quad \left\{ \left(\boldsymbol{T_2^e}\right)^T \left(\frac{d\boldsymbol{\varphi_2}}{d\xi}\right)^T \left(\frac{d\boldsymbol{\varphi_2}}{d\xi}\right) \left(\boldsymbol{T_2^e}\right) \right\} + \\ &\quad \left. A_3 \left\{ \left(\boldsymbol{T_2^e}\right)^T \left(\frac{d^2\boldsymbol{\varphi_2}}{d\xi^2}\right)^T \left(\frac{d^2\boldsymbol{\varphi_2}}{d\xi^2}\right) \left(\boldsymbol{T_2^e}\right) \right\} \right\} d\xi \end{aligned}\right\} \tag{5.11}$$

and

$$\left.\begin{aligned} \boldsymbol{F_a^e} &= \int_0^1 l_{ex} f \left(\boldsymbol{T_1^e}\right)^T \left(\boldsymbol{\varphi_1}\right)^T d\xi + \sum_{i=1}^{n_e} Q_i^a \\ \boldsymbol{F_b^e} &= \int_0^1 l_{ex} q \left(\boldsymbol{T_2^e}\right)^T \left(\boldsymbol{\varphi_2}\right)^T d\xi + \sum_{i=1}^{n_e} Q_i^t + Q_1^r + Q_2^r \end{aligned}\right\} \tag{5.12}$$

After assembling the element equations to a global form as given in 5.13.

$$\boldsymbol{K}(\boldsymbol{U})\boldsymbol{U} = \boldsymbol{F} \tag{5.13}$$

Here, Equation 5.13 is nonlinear in nature as the stiffness matrix is a function of displacement DOF. The essential boundary conditions can be implemented by setting the corresponding DOF to the respective value, without any additional boundary treatment as BSWI is used. The formulation for the BSWI WFEM based Timoshenko beam element with von Kármán nonlinear strains is presented in the next subsection.

5.1.2 Timoshenko beam element with von Kármán nonlinear strains

The displacement field for TBT beams with large deflections, moderate rotations and small strains is considered is as follows [210],

$$\left.\begin{aligned} u &= u_0(x) + z\theta_x(x) \\ v &= 0 \\ w &= w_0(x) \end{aligned}\right\} \tag{5.14}$$

where, (u, v, w) are total displacements along the co-ordinate directions (x, y, z), u_0 and w_0 denote the axial and transverse displacements on the mid-plane of undeformed beam and $\theta_x(x)$ is the rotation about y axis of a transverse straight line. The von Kármán strains are given as,

$$\left.\begin{aligned} E_{XX} &= \left(\frac{du_0}{dX} + \frac{1}{2}\left(\frac{dw_0}{dX}\right)^2\right) + z\left(\frac{d\theta_x}{dX}\right) \\ \gamma_{XZ} &= \theta_x + \left(\frac{dw_0}{dX}\right) \end{aligned}\right\} \tag{5.15}$$

Analogous to Euler-Bernoulli beam element, von Kármán nonlinear strains and second Piola-Kirchhoff stress tensor are substituted into the virtual work equation and expressed in terms of displacement as,

$$\left.\begin{aligned} \delta\left(W_I^i - W_E^i\right) &= 0 \\ \delta\left(\int_{V^i} \frac{1}{2} S_{XX} E_{XX} dV + \int_{V^i} \frac{1}{2} S_{XZ}\gamma_{XZ} dV - \right. & \\ \left. \int_{x_a}^{x_b} q w_0 dx - \int_{x_a}^{x_b} f u_0 dx - \sum_{i=1}^{n_d} Q_i \Delta_i\right) &= 0 \end{aligned}\right\} \tag{5.16}$$

$$\delta\left(\begin{array}{l}\displaystyle\int_{V^i}\frac{1}{2}E\left\{\frac{du_0}{dX}+\frac{1}{2}\left(\frac{dw_0}{dX}\right)^2+z\left(\frac{d\theta_x}{dX}\right)\right\}^2 dV+\\ \displaystyle\int_{V^i}\frac{1}{2}G\left\{\frac{dw_0}{dX}+\theta_x\right\}^2 dV-\int_{x_a}^{x_b}qw_0dx-\\ \displaystyle\int_{x_a}^{x_b}fu_0dx-\sum_{i=1}^{n_d}Q_i\Delta_i\Bigg)=0\end{array}\right\} \tag{5.17}$$

The unknown axial, transverse and rotational displacement field functions are approximated using either linear or quadratic BSWI scaling functions analogous to the Equations given in 3.5 and 3.17. During this approximation C_0 continuity is maintained and the element solving domain ξ is divided into $n = 2^j + m - 1$ nodes. The TBT element incorporating von Kármán nonlinear strains is shown in Figure 5.2, in which each node is having 3 DOF u_i, w_i, θ_i $(i = 1, ..., 2^j + m - 1)$.

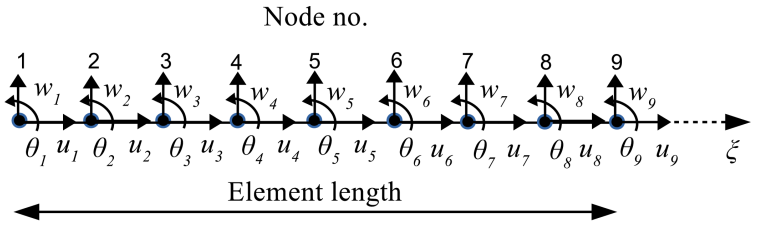

Figure 5.2: Distribution of nodes and DOF in a TBT beam element with von Kármán nonlinear strains for $m = 2, j = 3$

The C_0 type transformation matrix is obtained in the same way as given in Equations 3.6,3.7 and 3.18,3.19. The approximations of u_0, w_0 and $\theta_x(x)$ are substituted into the virtual work equations of Equations 5.16 and 5.17. Then using the principle of minimum potential energy and mapping it onto the standard element solving domain, the algebraic form of it

can be written as,

$$\int_0^1 \left\{ A_1 \frac{1}{l_{ex}} \frac{d(\boldsymbol{\varphi T^e})}{d\xi} \left(\frac{1}{l_{ex}} \frac{d(\boldsymbol{\varphi T^e u^e})}{d\xi} + \frac{1}{2} \left(\frac{1}{l_{ex}} \frac{d(\boldsymbol{\varphi T^e w^e})}{d\xi} \right)^2 \right) - A_2 \left(\frac{1}{l_{ex}^2} \frac{d(\boldsymbol{\varphi T^e \theta^e})}{d\xi} \frac{d(\boldsymbol{\varphi T^e})}{d\xi} \right) - f\left(\boldsymbol{\varphi T^e}\right) \right\} l_{ex} d\xi - \sum_{i=1}^{n_f} Q_i^a \left(\boldsymbol{\varphi T^e}\right)(\xi_i) = 0 \tag{5.18}$$

$$\int_0^1 \left\{ A_1 \frac{1}{l_{ex}} \frac{d(\boldsymbol{\varphi T^e})}{d\xi} \left(\frac{1}{l_{ex}^2} \frac{d(\boldsymbol{\varphi T^e u^e})}{d\xi} \frac{d(\boldsymbol{\varphi T^e w^e})}{d\xi} + \frac{1}{2} \left(\frac{1}{l_{ex}} \frac{d(\boldsymbol{\varphi T^e w^e})}{d\xi} \right)^3 \right) - A_2 \left(\frac{1}{l_{ex}^3} \frac{d(\boldsymbol{\varphi T^e \theta^e})}{d\xi} \frac{d(\boldsymbol{\varphi T^e w^e})}{d\xi} \frac{d(\boldsymbol{\varphi T^e})}{d\xi} \right) + A_4 \frac{1}{l_{ex}} \frac{d(\boldsymbol{\varphi T^e})}{d\xi} \left((\boldsymbol{\varphi T^e \theta^e}) + \frac{1}{l_{ex}} \frac{d(\boldsymbol{\varphi T^e w^e})}{d\xi} \right) - q\left(\boldsymbol{\varphi T^e}\right) \right\} l_{ex} d\xi - \sum_{i=1}^{n_f} Q_i^t \left(\boldsymbol{\varphi T^e}\right)(\xi_i) = 0 \tag{5.19}$$

$$\int_0^1 \left\{ A_2 \frac{-1}{l_{ex}} \frac{d(\boldsymbol{\varphi T^e})}{d\xi} \left(\frac{1}{l_{ex}} \frac{d(\boldsymbol{\varphi T^e u^e})}{d\xi} + \frac{1}{2} \left(\frac{1}{l_{ex}} \frac{d(\boldsymbol{\varphi T^e w^e})}{d\xi} \right)^2 \right) + A_3 \left(\frac{1}{l_{ex}^2} \frac{d(\boldsymbol{\varphi T^e \theta^e})}{d\xi} \frac{d(\boldsymbol{\varphi T^e})}{d\xi} \right) + A_4 \left(\boldsymbol{\varphi T^e}\right) \left((\boldsymbol{\varphi T^e \theta^e}) + \frac{1}{l_{ex}} \frac{d(\boldsymbol{\varphi T^e w^e})}{d\xi} \right) \right\} l_{ex} d\xi - \sum_{i=1}^{n_f} Q_i^r \left(\boldsymbol{\varphi T^e}\right)(\xi_i) = 0 \tag{5.20}$$

Here, $A_4 = K_s \int_{A^e} G dA$ is the shear stiffness, n_f is the total number of nodes per BSWI WFEM based Timoshenko beam element and K_s is the shear correction coefficient. Rest of the variables that are discussed in the context of Euler-Bernoulli beam element are applicable for Timoshenko beam element as well. Upon simplification, the algebraic system of nonlinear equations in element solving domain $\xi \in [0, 1]$ of BSWI WFEM Timoshenko beam element can be derived as,

$$\boldsymbol{K^e}(\boldsymbol{U^e})\boldsymbol{U^e} = \boldsymbol{F^e} \tag{5.21}$$

where,

$$\left.\begin{aligned} \boldsymbol{K}^{\boldsymbol{e}}(\boldsymbol{U}^{\boldsymbol{e}}) &= \begin{bmatrix} \boldsymbol{K}_{\mathbf{1}}^{\boldsymbol{e}} \boldsymbol{K}_{\mathbf{2}}^{\boldsymbol{e}} \boldsymbol{K}_{\mathbf{3}}^{\boldsymbol{e}} \\ \boldsymbol{K}_{\mathbf{4}}^{\boldsymbol{e}} \boldsymbol{K}_{\mathbf{5}}^{\boldsymbol{e}} \boldsymbol{K}_{\mathbf{6}}^{\boldsymbol{e}} \\ \boldsymbol{K}_{\mathbf{7}}^{\boldsymbol{e}} \boldsymbol{K}_{\mathbf{8}}^{\boldsymbol{e}} \boldsymbol{K}_{\mathbf{9}}^{\boldsymbol{e}} \end{bmatrix} \\ \boldsymbol{U}^{\boldsymbol{e}} = \begin{Bmatrix} \boldsymbol{u}^{\boldsymbol{e}} \\ \boldsymbol{w}^{\boldsymbol{e}} \\ \boldsymbol{\theta}^{\boldsymbol{e}} \end{Bmatrix}, \boldsymbol{F}^{\boldsymbol{e}} &= \begin{Bmatrix} \boldsymbol{F_a}^{\boldsymbol{e}} \\ \boldsymbol{F_b}^{\boldsymbol{e}} \\ \boldsymbol{F_c}^{\boldsymbol{e}} \end{Bmatrix} \end{aligned}\right\} \tag{5.22}$$

such that,

$$\left.\begin{aligned} \boldsymbol{K}_{\mathbf{1}}^{\boldsymbol{e}} &= \int_0^1 \frac{A_1}{l_{ex}} (\boldsymbol{T}^{\boldsymbol{e}})^T \left(\frac{d\boldsymbol{\varphi}}{d\xi}\right)^T \left(\frac{d\boldsymbol{\varphi}}{d\xi}\right) (\boldsymbol{T}^{\boldsymbol{e}})\, d\xi \\ \boldsymbol{K}_{\mathbf{2}}^{\boldsymbol{e}} = \frac{1}{2} \int_0^1 \frac{A_1}{l_{ex}^2} \left\{ \left(\frac{d\boldsymbol{\varphi}}{d\xi}\right) (\boldsymbol{T}^{\boldsymbol{e}})\, \boldsymbol{w}^{\boldsymbol{e}} \right\} &\left\{ (\boldsymbol{T}^{\boldsymbol{e}})^T \left(\frac{d\boldsymbol{\varphi}}{d\xi}\right)^T \left(\frac{d\boldsymbol{\varphi}}{d\xi}\right) (\boldsymbol{T}^{\boldsymbol{e}}) \right\} d\xi \\ &\boldsymbol{K}_{\mathbf{3}}^{\boldsymbol{e}} = 0,\ \boldsymbol{K}_{\mathbf{7}}^{\boldsymbol{e}} = 0 \end{aligned}\right\} \tag{5.23}$$

$$\left.\begin{aligned} \boldsymbol{K}_{\mathbf{4}}^{\boldsymbol{e}} &= \int_0^1 \frac{A_1}{l_{ex}^2} \left\{ \left(\frac{d\boldsymbol{\varphi}}{d\xi}\right) (\boldsymbol{T}^{\boldsymbol{e}})\, \boldsymbol{w}^{\boldsymbol{e}} \right\} \left\{ (\boldsymbol{T}^{\boldsymbol{e}})^T \left(\frac{d\boldsymbol{\varphi}}{d\xi}\right)^T \left(\frac{d\boldsymbol{\varphi}}{d\xi}\right) (\boldsymbol{T}^{\boldsymbol{e}}) \right\} d\xi \\ \boldsymbol{K}_{\mathbf{5}}^{\boldsymbol{e}} &= \int_0^1 \frac{1}{2} \frac{A_1}{l_{ex}^3} \left\{ \left(\frac{d\boldsymbol{\varphi}}{d\xi}\right) (\boldsymbol{T}^{\boldsymbol{e}})\, \boldsymbol{w}^{\boldsymbol{e}} \right\} \left\{ \left(\frac{d\boldsymbol{\varphi}}{d\xi}\right) (\boldsymbol{T}^{\boldsymbol{e}})\, \boldsymbol{w}^{\boldsymbol{e}} \right\}^T \\ &\quad \left\{ (\boldsymbol{T}^{\boldsymbol{e}})^T \left(\frac{d\boldsymbol{\varphi}}{d\xi}\right)^T \left(\frac{d\boldsymbol{\varphi}}{d\xi}\right) (\boldsymbol{T}^{\boldsymbol{e}})\, d\xi \right\} + \\ &\quad \frac{A_4}{l_{ex}} \left\{ (\boldsymbol{T}^{\boldsymbol{e}})^T \left(\frac{d\boldsymbol{\varphi}}{d\xi}\right)^T \left(\frac{d\boldsymbol{\varphi}}{d\xi}\right) (\boldsymbol{T}^{\boldsymbol{e}}) \right\} d\xi \\ \boldsymbol{K}_{\mathbf{6}}^{\boldsymbol{e}} &= \int_0^1 A_4 \left\{ (\boldsymbol{T}^{\boldsymbol{e}})^T \left(\frac{d\boldsymbol{\varphi}}{d\xi}\right)^T (\boldsymbol{\varphi}) (\boldsymbol{T}^{\boldsymbol{e}}) \right\} d\xi \end{aligned}\right\} \tag{5.24}$$

$$\left.\begin{aligned}
\boldsymbol{K_8^e} &= \left(\boldsymbol{K_6^e}\right)^T \\
\boldsymbol{K_9^e} &= \int_0^1 \frac{A_3}{l_{ex}} \left\{ \left(\boldsymbol{T^e}\right)^T \left(\frac{d\boldsymbol{\varphi}}{d\xi}\right)^T \left(\frac{d\boldsymbol{\varphi}}{d\xi}\right) \left(\boldsymbol{T^e}\right) \right\} + \\
&\qquad l_{ex} A_4 \left\{ \left(\boldsymbol{T^e}\right)^T \left(\boldsymbol{\varphi}\right)^T \left(\boldsymbol{\varphi}\right) \left(\boldsymbol{T^e}\right) \right\} d\xi \\
\boldsymbol{F_a^e} &= \int_0^1 l_{ex} f \left(\boldsymbol{T^e}\right)^T \left(\boldsymbol{\varphi}\right)^T d\xi + \sum_{i=1}^{n_f} Q_i^a \left(\boldsymbol{\varphi T^e}\left(\xi_i\right)\right) \\
\boldsymbol{F_b^e} &= \int_0^1 l_{ex} q \left(\boldsymbol{T^e}\right)^T \left(\boldsymbol{\varphi}\right)^T d\xi + \sum_{i=1}^{n_f} Q_i^t \left(\boldsymbol{\varphi T^e}\left(\xi_i\right)\right) \\
\boldsymbol{F_c^e} &= \sum_{i=1}^{n_f} Q_i^r \left(\boldsymbol{\varphi T^e}\left(\xi_i\right)\right)
\end{aligned}\right\} \tag{5.25}$$

The essential boundary conditions can be applied as in FEM after assembling the element equations to obtain a global form on the same lines as given in 5.13, if more than one element is used for modelling. The solution procedure that is used for solving the nonlinear matrix equations given in Equation 5.13 is discussed in the coming subsection.

5.1.3 Solution procedure for nonlinear equations

The matrix equations in Equation 5.13 are nonlinear in nature. Therefore, Newton-Raphson method is used for the solution process. The residual ($\boldsymbol{R}_s$) is calculated from the nonlinear matrix equation as,

$$\boldsymbol{R}_s \equiv \boldsymbol{K}(\boldsymbol{U})^{q-1}\boldsymbol{U}^q - \boldsymbol{F} \tag{5.26}$$

where, $\boldsymbol{K}(\boldsymbol{U})$ is the global stiffness matrix, $\boldsymbol{U}$ is the displacement column vector and $\boldsymbol{F}$ is the force column vector; $q \in [1, ...\text{total iterations}(N_n)]$. The residual vector is expanded using Taylor series about the known solution at $(q-1)^{st}$ iteration as,

$$\boldsymbol{R}_s(\boldsymbol{U}) = \boldsymbol{R}_s(\boldsymbol{U}^{q-1}) + \left(\frac{\partial \boldsymbol{R}_s}{\partial \boldsymbol{U}}\right)^{q-1} \delta\boldsymbol{U} + ... \tag{5.27}$$

Omitting the higher order terms, Equation 5.27 becomes,

$$\boldsymbol{T}_s(\boldsymbol{U}^{q-1})\delta\boldsymbol{U} = -\boldsymbol{R}_s(\boldsymbol{U}^{q-1}) \tag{5.28}$$

where,

$$\boldsymbol{T}_s(\boldsymbol{U}^{q-1}) = \left(\frac{\partial \boldsymbol{R}_s}{\partial \boldsymbol{U}}\right)^{q-1} \tag{5.29}$$

is the tangent stiffness matrix. Thus, solution at the q^{th} iteration is calculated as,

$$\boldsymbol{U}^q = \boldsymbol{U}^{q-1} + \delta \boldsymbol{U} \tag{5.30}$$

The coefficients for the tangent stiffness matrix at the element level are derived explicitly from Equation 5.29. The tangent stiffness matrix for Euler-Bernoulli BSWI WFEM beam element is,

$$\boldsymbol{T}_{\boldsymbol{s}}^{\boldsymbol{e}} = \begin{bmatrix} \boldsymbol{T}_{\boldsymbol{s1}}^{\boldsymbol{e}} \boldsymbol{T}_{\boldsymbol{s2}}^{\boldsymbol{e}} \\ \boldsymbol{T}_{\boldsymbol{s3}}^{\boldsymbol{e}} \boldsymbol{T}_{\boldsymbol{s4}}^{\boldsymbol{e}} \end{bmatrix} \tag{5.31}$$

where,

$$\left.\begin{aligned} \boldsymbol{T}_{\boldsymbol{s1}}^{\boldsymbol{e}} &= \boldsymbol{K}_{\boldsymbol{1}}^{\boldsymbol{e}} \\ \boldsymbol{T}_{\boldsymbol{s2}}^{\boldsymbol{e}} &= 2\boldsymbol{K}_{\boldsymbol{2}}^{\boldsymbol{e}} \\ \boldsymbol{T}_{\boldsymbol{s3}}^{\boldsymbol{e}} &= \boldsymbol{K}_{\boldsymbol{3}}^{\boldsymbol{e}} \\ \boldsymbol{T}_{\boldsymbol{s4}}^{\boldsymbol{e}} &= \boldsymbol{K}_{\boldsymbol{4}}^{\boldsymbol{e}} + \int_0^1 \left\{ \frac{A_1}{l_{ex}^2} \left\{ \left(\frac{d\boldsymbol{\varphi_1}}{d\xi}\right) \left(\boldsymbol{T}_{\boldsymbol{1}}^{\boldsymbol{e}}\right) \boldsymbol{u}^{\boldsymbol{e}} \right\} \right. \\ &\quad \left. \left\{ \left(\boldsymbol{T}_{\boldsymbol{2}}^{\boldsymbol{e}}\right)^T \left(\frac{d\boldsymbol{\varphi_2}}{d\xi}\right)^T \left(\frac{d\boldsymbol{\varphi_2}}{d\xi}\right) \left(\boldsymbol{T}_{\boldsymbol{2}}^{\boldsymbol{e}}\right) \right\} + \right. \\ &\quad \left. \frac{A_1}{l_{ex}^3} \left\{ \left(\frac{d\boldsymbol{\varphi_2}}{d\xi}\right) \left(\boldsymbol{T}_{\boldsymbol{2}}^{\boldsymbol{e}}\right) \boldsymbol{w}^{\boldsymbol{e}} \right\} \left\{ \left(\frac{d\boldsymbol{\varphi_2}}{d\xi}\right) \left(\boldsymbol{T}_{\boldsymbol{2}}^{\boldsymbol{e}}\right) \boldsymbol{w}^{\boldsymbol{e}} \right\}^T \right. \\ &\quad \left. \left\{ \left(\boldsymbol{T}_{\boldsymbol{2}}^{\boldsymbol{e}}\right)^T \left(\frac{d\boldsymbol{\varphi_2}}{d\xi}\right)^T \left(\frac{d\boldsymbol{\varphi_2}}{d\xi}\right) \left(\boldsymbol{T}_{\boldsymbol{2}}^{\boldsymbol{e}}\right) \right\} d\xi \right\} \end{aligned}\right\} \tag{5.32}$$

Here, $\boldsymbol{K}_{\boldsymbol{1}}^{\boldsymbol{e}}$, $\boldsymbol{K}_{\boldsymbol{2}}^{\boldsymbol{e}}$, $\boldsymbol{K}_{\boldsymbol{3}}^{\boldsymbol{e}}$ and $\boldsymbol{K}_{\boldsymbol{4}}^{\boldsymbol{e}}$ are the coefficients of the stiffness matrix obtained from Equation 5.10. The tangent stiffness matrix for Timoshenko BSWI WFEM beam element can be calculated from,

$$\boldsymbol{T}_{\boldsymbol{s}}^{\boldsymbol{e}} = \begin{bmatrix} \boldsymbol{T}_{\boldsymbol{s1}}^{\boldsymbol{e}} \boldsymbol{T}_{\boldsymbol{s2}}^{\boldsymbol{e}} \boldsymbol{T}_{\boldsymbol{s3}}^{\boldsymbol{e}} \\ \boldsymbol{T}_{\boldsymbol{s4}}^{\boldsymbol{e}} \boldsymbol{T}_{\boldsymbol{s5}}^{\boldsymbol{e}} \boldsymbol{T}_{\boldsymbol{s6}}^{\boldsymbol{e}} \\ \boldsymbol{T}_{\boldsymbol{s7}}^{\boldsymbol{e}} \boldsymbol{T}_{\boldsymbol{s8}}^{\boldsymbol{e}} \boldsymbol{T}_{\boldsymbol{s9}}^{\boldsymbol{e}} \end{bmatrix} \tag{5.33}$$

where,

$$\left.\begin{aligned}
\boldsymbol{T}^{e}_{\boldsymbol{s1}} = \boldsymbol{K}^{e}_{\boldsymbol{1}}, \boldsymbol{T}^{e}_{\boldsymbol{s2}} = 2\boldsymbol{K}^{e}_{\boldsymbol{2}} \\
\boldsymbol{T}^{e}_{\boldsymbol{s3}} = \boldsymbol{K}^{e}_{\boldsymbol{3}}, \boldsymbol{T}^{e}_{\boldsymbol{s4}} = \boldsymbol{K}^{e}_{\boldsymbol{4}} \\
\boldsymbol{T}^{e}_{\boldsymbol{s6}} = \boldsymbol{K}^{e}_{\boldsymbol{6}}, \boldsymbol{T}^{e}_{\boldsymbol{s7}} = \boldsymbol{K}^{e}_{\boldsymbol{7}} \\
\boldsymbol{T}^{e}_{\boldsymbol{s8}} = \boldsymbol{K}^{e}_{\boldsymbol{8}}, \boldsymbol{T}^{e}_{\boldsymbol{s9}} = \boldsymbol{K}^{e}_{\boldsymbol{9}} \\
\boldsymbol{T}^{e}_{\boldsymbol{s5}} = \boldsymbol{K}^{e}_{\boldsymbol{5}} + \int_0^1 \left\{ \frac{A_1}{l_{ex}^2} \left\{ \left(\frac{d\boldsymbol{\varphi_1}}{d\xi} \right) \left(\boldsymbol{T}^{e}_{\boldsymbol{1}} \right) \boldsymbol{u}^{e} \right\} \right. \\
\left\{ \left(\boldsymbol{T}^{e}_{\boldsymbol{1}} \right)^{T} \left(\frac{d\boldsymbol{\varphi_1}}{d\xi} \right)^{T} \left(\frac{d\boldsymbol{\varphi_1}}{d\xi} \right) \left(\boldsymbol{T}^{e}_{\boldsymbol{1}} \right) \right\} + \\
\frac{A_1}{l_{ex}^3} \left\{ \left(\frac{d\boldsymbol{\varphi_1}}{d\xi} \right) \left(\boldsymbol{T}^{e}_{\boldsymbol{1}} \right) \boldsymbol{w}^{e} \right\} \left\{ \left(\frac{d\boldsymbol{\varphi_1}}{d\xi} \right) \left(\boldsymbol{T}^{e}_{\boldsymbol{1}} \right) \boldsymbol{w}^{e} \right\}^{T} \\
\left. \left\{ \left(\boldsymbol{T}^{e}_{\boldsymbol{1}} \right)^{T} \left(\frac{d\boldsymbol{\varphi_1}}{d\xi} \right)^{T} \left(\frac{d\boldsymbol{\varphi_1}}{d\xi} \right) \left(\boldsymbol{T}^{e}_{\boldsymbol{1}} \right) \right\} d\xi \right\}
\end{aligned}\right\} \tag{5.34}$$

Here, $\boldsymbol{K}^{e}_{\boldsymbol{1}}$, $\boldsymbol{K}^{e}_{\boldsymbol{2}}$, $\boldsymbol{K}^{e}_{\boldsymbol{3}}$, $\boldsymbol{K}^{e}_{\boldsymbol{4}}$, $\boldsymbol{K}^{e}_{\boldsymbol{5}}$, $\boldsymbol{K}^{e}_{\boldsymbol{6}}$, $\boldsymbol{K}^{e}_{\boldsymbol{7}}$, $\boldsymbol{K}^{e}_{\boldsymbol{8}}$ and $\boldsymbol{K}^{e}_{\boldsymbol{9}}$ are the coefficients of the stiffness matrix obtained from Equation 5.22.

When large load increments are used, convergence can be an issue due to the nonlinear nature of the matrix equations. Hence, the load is applied in small increments $\delta \boldsymbol{F}_i$ such that,

$$\boldsymbol{F} = \sum_{i=1}^{N} \delta \boldsymbol{F}_i \tag{5.35}$$

where, N is the total number of load increments.

In the next section, stochastic BSWI WFEM formulations for beams incorporating von Kármán nonlinear strains are shown wherein, Young's modulus is considered as a spatially varying homogeneous random field.

5.2 Stochastic BSWI WFEM formulation for beams incorporating von Kármán nonlinear strains

The proposed stochastic BSWI wavelet finite element formulation by incorporating von Kármán strains for both Euler-Bernoulli BSWI beam element and Timoshenko BSWI beam element are given in this section.

5.2.1 Stochastic BSWI WFEM formulation for EBT beams incorporating von Kármán nonlinear strains

In the formulation of stochastic BSWI WFEM beam element incorporating von Kármán nonlinear strains, $E(\mathbf{x})$ is modelled as homogeneous random field. When the formulation is based on EBT, $u_0(\xi)$ and $\alpha(\xi)$ are expressed in terms of C_0 type element transformation matrix and $w_0(\xi)$ is expressed in terms of C_1 type element transformation matrix. On similar lines, as the approximation of deflection field in chapter 3 and 4, the unknown random field can be approximated in the element solving domain in terms of BSWI wavelet scaling functions and expressed in terms of elemental transformation matrix. The element stiffness coefficients and hence the element deflections will become functions of random variables $\boldsymbol{\alpha_R}$ and Equation 5.9 which is based on EBT formulation can be written as,

$$\boldsymbol{K}^e(\boldsymbol{U}^e(\boldsymbol{\alpha}_{\boldsymbol{R}}^e), \boldsymbol{\alpha}_{\boldsymbol{R}}^e)\boldsymbol{U}^e(\boldsymbol{\alpha}_{\boldsymbol{R}}^e) = \boldsymbol{F}^e \tag{5.36}$$

It has been shown in the numerical examples of bar and beam in chapter 4 that BSWI WFEM results are comparable in different aspects to FEM, for both Gaussian and non-Gaussian input fields. Hence, in the current study of beams with geometric nonlinearity, only Gaussian input field is considered. When $E(\mathbf{x})$ is modelled as homogeneous Gaussian field as given in Equation 4.1, the components of

$\boldsymbol{K}^e(\boldsymbol{U}^e(\boldsymbol{\alpha}_{\boldsymbol{R}}^{\boldsymbol{e}}), \boldsymbol{\alpha}_{\boldsymbol{R}}^{\boldsymbol{e}})$ can be written as,

$$\left.\begin{aligned}
\boldsymbol{K}_{\boldsymbol{1}}^{\boldsymbol{e}} = \int_0^1 \frac{A_1}{l_{ex}} \left(\boldsymbol{T}_{\boldsymbol{1}}^{\boldsymbol{e}}\right)^T \left(\frac{d\boldsymbol{\varphi_1}}{d\xi}\right)^T \left(\frac{d\boldsymbol{\varphi_1}}{d\xi}\right) \left(\boldsymbol{T}_{\boldsymbol{1}}^{\boldsymbol{e}}\right) d\xi + \\
\int_0^1 \frac{A_1}{l_{ex}} \left(\boldsymbol{\varphi_R} \boldsymbol{T}_{\boldsymbol{R}}^{\boldsymbol{e}} \boldsymbol{\alpha}_{\boldsymbol{R}}^{\boldsymbol{e}}\right) \left(\boldsymbol{T}_{\boldsymbol{1}}^{\boldsymbol{e}}\right)^T \left(\frac{d\boldsymbol{\varphi_1}}{d\xi}\right)^T \left(\frac{d\boldsymbol{\varphi_1}}{d\xi}\right) \left(\boldsymbol{T}_{\boldsymbol{1}}^{\boldsymbol{e}}\right) d\xi \\
\boldsymbol{K}_{\boldsymbol{2}}^{\boldsymbol{e}} = \frac{1}{2} \int_0^1 \frac{A_1}{l_{ex}^2} \left\{ \left(\frac{d\boldsymbol{\varphi_2}}{d\xi}\right) \left(\boldsymbol{T}_{\boldsymbol{2}}^{\boldsymbol{e}}\right) \boldsymbol{w}^{\boldsymbol{e}} \right\} \left(\boldsymbol{T}_{\boldsymbol{1}}^{\boldsymbol{e}}\right)^T \left(\frac{d\boldsymbol{\varphi_1}}{d\xi}\right)^T \left(\frac{d\boldsymbol{\varphi_2}}{d\xi}\right) \left(\boldsymbol{T}_{\boldsymbol{2}}^{\boldsymbol{e}}\right) d\xi + \\
\frac{1}{2} \int_0^1 \frac{A_1}{l_{ex}^2} \left(\boldsymbol{\varphi_R} \boldsymbol{T}_{\boldsymbol{R}}^{\boldsymbol{e}} \boldsymbol{\alpha}_{\boldsymbol{R}}^{\boldsymbol{e}}\right) \left\{ \left(\frac{d\boldsymbol{\varphi_2}}{d\xi}\right) \left(\boldsymbol{T}_{\boldsymbol{2}}^{\boldsymbol{e}}\right) \boldsymbol{w}^{\boldsymbol{e}} \right\} \left(\boldsymbol{T}_{\boldsymbol{1}}^{\boldsymbol{e}}\right)^T \left(\frac{d\boldsymbol{\varphi_1}}{d\xi}\right)^T \left(\frac{d\boldsymbol{\varphi_2}}{d\xi}\right) \left(\boldsymbol{T}_{\boldsymbol{2}}^{\boldsymbol{e}}\right) d\xi \\
\boldsymbol{K}_{\boldsymbol{3}}^{\boldsymbol{e}} = 2 \left(\boldsymbol{K}_{\boldsymbol{2}}^{\boldsymbol{e}}\right)^T \\
\boldsymbol{K}_{\boldsymbol{4}}^{\boldsymbol{e}} = \int_0^1 \frac{1}{l_{ex}^3} \left\{ \frac{1}{2} A_1 \left\{ \left(\frac{d\boldsymbol{\varphi_2}}{d\xi}\right) \left(\boldsymbol{T}_{\boldsymbol{2}}^{\boldsymbol{e}}\right) \boldsymbol{w}^{\boldsymbol{e}} \right\} \left\{ \left(\frac{d\boldsymbol{\varphi_2}}{d\xi}\right) \left(\boldsymbol{T}_{\boldsymbol{2}}^{\boldsymbol{e}}\right) \boldsymbol{w}^{\boldsymbol{e}} \right\}^T \right. \\
\left\{ \left(\boldsymbol{T}_{\boldsymbol{2}}^{\boldsymbol{e}}\right)^T \left(\frac{d\boldsymbol{\varphi_2}}{d\xi}\right)^T \left(\frac{d\boldsymbol{\varphi_2}}{d\xi}\right) \left(\boldsymbol{T}_{\boldsymbol{2}}^{\boldsymbol{e}}\right) \right\} + \\
\left. A_3 \left\{ \left(\boldsymbol{T}_{\boldsymbol{2}}^{\boldsymbol{e}}\right)^T \left(\frac{d^2\boldsymbol{\varphi_2}}{d\xi^2}\right)^T \left(\frac{d^2\boldsymbol{\varphi_2}}{d\xi^2}\right) \left(\boldsymbol{T}_{\boldsymbol{2}}^{\boldsymbol{e}}\right) \right\} \right\} d\xi + \\
\int_0^1 \frac{1}{l_{ex}^3} \left\{ \frac{1}{2} A_1 \left(\boldsymbol{\varphi_R} \boldsymbol{T}_{\boldsymbol{R}}^{\boldsymbol{e}} \boldsymbol{\alpha}_{\boldsymbol{R}}^{\boldsymbol{e}}\right) \left\{ \left(\frac{d\boldsymbol{\varphi_2}}{d\xi}\right) \left(\boldsymbol{T}_{\boldsymbol{2}}^{\boldsymbol{e}}\right) \boldsymbol{w}^{\boldsymbol{e}} \right\} \left\{ \left(\frac{d\boldsymbol{\varphi_2}}{d\xi}\right) \left(\boldsymbol{T}_{\boldsymbol{2}}^{\boldsymbol{e}}\right) \boldsymbol{w}^{\boldsymbol{e}} \right\}^T \right. \\
\left\{ \left(\boldsymbol{T}_{\boldsymbol{2}}^{\boldsymbol{e}}\right)^T \left(\frac{d\boldsymbol{\varphi_2}}{d\xi}\right)^T \left(\frac{d\boldsymbol{\varphi_2}}{d\xi}\right) \left(\boldsymbol{T}_{\boldsymbol{2}}^{\boldsymbol{e}}\right) \right\} + \\
\left. A_3 \left(\boldsymbol{\varphi_R} \boldsymbol{T}_{\boldsymbol{R}}^{\boldsymbol{e}} \boldsymbol{\alpha}_{\boldsymbol{R}}^{\boldsymbol{e}}\right) \left\{ \left(\boldsymbol{T}_{\boldsymbol{2}}^{\boldsymbol{e}}\right)^T \left(\frac{d^2\boldsymbol{\varphi_2}}{d\xi^2}\right)^T \left(\frac{d^2\boldsymbol{\varphi_2}}{d\xi^2}\right) \left(\boldsymbol{T}_{\boldsymbol{2}}^{\boldsymbol{e}}\right) \right\} \right\} d\xi
\end{aligned}\right\} \tag{5.37}$$

The element stochastic stiffness matrices as given in Equations 5.36 for all the sub-domains can be assembled to form the algebraic set of respective global stochastic equilibrium equations as,

$$\boldsymbol{K}(\boldsymbol{U}(\boldsymbol{\alpha}_{\boldsymbol{R}}), \boldsymbol{\alpha}_{\boldsymbol{R}}) \boldsymbol{U}(\boldsymbol{\alpha}_{\boldsymbol{R}}) = \boldsymbol{F} \tag{5.38}$$

5.2.2 Stochastic BSWI WFEM formulation for TBT beams incorporating von Kármán nonlinear strains

When the formulation is based on TBT, $u_0(\xi)$, $w_0(\xi)$, $\theta_x(\xi)$ and $\alpha(\xi)$ are all expressed in terms of C_0 type element transformation matrix. When $E(\mathbf{x})$ is modelled as homogeneous Gaussian field as given in Equation 4.1, Equation 5.21 can be written as,

$$\boldsymbol{K}_{\boldsymbol{t}}^{\boldsymbol{e}}(\boldsymbol{U}_{\boldsymbol{t}}^{\boldsymbol{e}}(\boldsymbol{\alpha}_{\boldsymbol{R}}^{\boldsymbol{e}}), \boldsymbol{\alpha}_{\boldsymbol{R}}^{\boldsymbol{e}})\boldsymbol{U}_{\boldsymbol{t}}^{\boldsymbol{e}}(\boldsymbol{\alpha}_{\boldsymbol{R}}^{\boldsymbol{e}}) = \boldsymbol{F}_{\boldsymbol{t}}^{\boldsymbol{e}} \tag{5.39}$$

The components of $\boldsymbol{K}_{\boldsymbol{t}}^{\boldsymbol{e}}(\boldsymbol{U}_{\boldsymbol{t}}^{\boldsymbol{e}}(\boldsymbol{\alpha}_{\boldsymbol{R}}^{\boldsymbol{e}}), \boldsymbol{\alpha}_{\boldsymbol{R}}^{\boldsymbol{e}})$ can be written as,

$$\left.\begin{aligned}
\boldsymbol{K}_{\mathbf{1}}^{\boldsymbol{e}} = \int_0^1 \frac{A_1}{l_{ex}} (\boldsymbol{T}^{\boldsymbol{e}})^T \left(\frac{d\boldsymbol{\varphi}}{d\xi}\right)^T \left(\frac{d\boldsymbol{\varphi}}{d\xi}\right) (\boldsymbol{T}^{\boldsymbol{e}})\, d\xi + \\
\int_0^1 \frac{A_1}{l_{ex}} \left(\boldsymbol{\varphi}_{\boldsymbol{R}} \boldsymbol{T}_{\boldsymbol{R}}^{\boldsymbol{e}} \boldsymbol{\alpha}_{\boldsymbol{R}}^{\boldsymbol{e}}\right) (\boldsymbol{T}^{\boldsymbol{e}})^T \left(\frac{d\boldsymbol{\varphi}}{d\xi}\right)^T \left(\frac{d\boldsymbol{\varphi}}{d\xi}\right) (\boldsymbol{T}^{\boldsymbol{e}})\, d\xi \\
\boldsymbol{K}_{\mathbf{2}}^{\boldsymbol{e}} = \frac{1}{2} \int_0^1 \frac{A_1}{l_{ex}^2} \left\{ \left(\frac{d\boldsymbol{\varphi}}{d\xi}\right) (\boldsymbol{T}^{\boldsymbol{e}})\, \boldsymbol{w}^{\boldsymbol{e}} \right\} \left\{ (\boldsymbol{T}^{\boldsymbol{e}})^T \left(\frac{d\boldsymbol{\varphi}}{d\xi}\right)^T \left(\frac{d\boldsymbol{\varphi}}{d\xi}\right) (\boldsymbol{T}^{\boldsymbol{e}}) \right\} d\xi + \\
\frac{1}{2} \int_0^1 \frac{A_1}{l_{ex}^2} \left(\boldsymbol{\varphi}_{\boldsymbol{R}} \boldsymbol{T}_{\boldsymbol{R}}^{\boldsymbol{e}} \boldsymbol{\alpha}_{\boldsymbol{R}}^{\boldsymbol{e}}\right) \left\{ \left(\frac{d\boldsymbol{\varphi}}{d\xi}\right) (\boldsymbol{T}^{\boldsymbol{e}})\, \boldsymbol{w}^{\boldsymbol{e}} \right\} \left\{ (\boldsymbol{T}^{\boldsymbol{e}})^T \left(\frac{d\boldsymbol{\varphi}}{d\xi}\right)^T \left(\frac{d\boldsymbol{\varphi}}{d\xi}\right) (\boldsymbol{T}^{\boldsymbol{e}}) \right\} d\xi \\
\boldsymbol{K}_{\mathbf{3}}^{\boldsymbol{e}} = 0,\ \boldsymbol{K}_{\mathbf{7}}^{\boldsymbol{e}} = 0 \\
\boldsymbol{K}_{\mathbf{4}}^{\boldsymbol{e}} = \int_0^1 \frac{A_1}{l_{ex}^2} \left\{ \left(\frac{d\boldsymbol{\varphi}}{d\xi}\right) (\boldsymbol{T}^{\boldsymbol{e}})\, \boldsymbol{w}^{\boldsymbol{e}} \right\} \left\{ (\boldsymbol{T}^{\boldsymbol{e}})^T \left(\frac{d\boldsymbol{\varphi}}{d\xi}\right)^T \left(\frac{d\boldsymbol{\varphi}}{d\xi}\right) (\boldsymbol{T}^{\boldsymbol{e}}) \right\} d\xi + \\
\frac{A_1}{l_{ex}^2} \left(\boldsymbol{\varphi}_{\boldsymbol{R}} \boldsymbol{T}_{\boldsymbol{R}}^{\boldsymbol{e}} \boldsymbol{\alpha}_{\boldsymbol{R}}^{\boldsymbol{e}}\right) \left\{ \left(\frac{d\boldsymbol{\varphi}}{d\xi}\right) (\boldsymbol{T}^{\boldsymbol{e}})\, \boldsymbol{w}^{\boldsymbol{e}} \right\} \left\{ (\boldsymbol{T}^{\boldsymbol{e}})^T \left(\frac{d\boldsymbol{\varphi}}{d\xi}\right)^T \left(\frac{d\boldsymbol{\varphi}}{d\xi}\right) (\boldsymbol{T}^{\boldsymbol{e}}) \right\} d\xi
\end{aligned}\right\} \tag{5.40}$$

$$
\left.
\begin{aligned}
\boldsymbol{K_5^e} = \int_0^1 \frac{1}{2}\frac{A_1}{l_{ex}^3} \left\{ \left(\frac{d\boldsymbol{\varphi}}{d\xi} \right) (\boldsymbol{T^e})\, \boldsymbol{w^e} \right\} \left\{ \left(\frac{d\boldsymbol{\varphi}}{d\xi} \right) (\boldsymbol{T^e})\, \boldsymbol{w^e} \right\}^T \\
\left\{ (\boldsymbol{T^e})^T \left(\frac{d\boldsymbol{\varphi}}{d\xi} \right)^T \left(\frac{d\boldsymbol{\varphi}}{d\xi} \right) (\boldsymbol{T^e})\, d\xi \right\} + \\
\frac{A_4}{l_{ex}} \left\{ (\boldsymbol{T^e})^T \left(\frac{d\boldsymbol{\varphi}}{d\xi} \right)^T \left(\frac{d\boldsymbol{\varphi}}{d\xi} \right) (\boldsymbol{T^e}) \right\} d\xi + \\
\int_0^1 \frac{1}{2}\frac{A_1}{l_{ex}^3} \left(\boldsymbol{\varphi_R} \boldsymbol{T_R^e} \boldsymbol{\alpha_R^e} \right) \left\{ \left(\frac{d\boldsymbol{\varphi}}{d\xi} \right) (\boldsymbol{T^e})\, \boldsymbol{w^e} \right\} \left\{ \left(\frac{d\boldsymbol{\varphi}}{d\xi} \right) (\boldsymbol{T^e})\, \boldsymbol{w^e} \right\}^T \\
\left\{ (\boldsymbol{T^e})^T \left(\frac{d\boldsymbol{\varphi}}{d\xi} \right)^T \left(\frac{d\boldsymbol{\varphi}}{d\xi} \right) (\boldsymbol{T^e})\, d\xi \right\} + \\
\frac{A_4}{l_{ex}} \left(\boldsymbol{\varphi_R} \boldsymbol{T_R^e} \boldsymbol{\alpha_R^e} \right) \left\{ (\boldsymbol{T^e})^T \left(\frac{d\boldsymbol{\varphi}}{d\xi} \right)^T \left(\frac{d\boldsymbol{\varphi}}{d\xi} \right) (\boldsymbol{T^e}) \right\} d\xi \\
\boldsymbol{K_6^e} = \int_0^1 A_4 \left\{ (\boldsymbol{T^e})^T \left(\frac{d\boldsymbol{\varphi}}{d\xi} \right)^T (\boldsymbol{\varphi})\, (\boldsymbol{T^e}) \right\} d\xi + \\
\int_0^1 A_4 \left(\boldsymbol{\varphi_R} \boldsymbol{T_R^e} \boldsymbol{\alpha_R^e} \right) \left\{ (\boldsymbol{T^e})^T \left(\frac{d\boldsymbol{\varphi}}{d\xi} \right)^T (\boldsymbol{\varphi})\, (\boldsymbol{T^e}) \right\} d\xi
\end{aligned}
\right\} \tag{5.41}
$$

$$
\left.
\begin{aligned}
\boldsymbol{K_8^e} = \left(\boldsymbol{K_6^e} \right)^T \\
\boldsymbol{K_9^e} = \int_0^1 \frac{A_3}{l_{ex}} \left\{ (\boldsymbol{T^e})^T \left(\frac{d\boldsymbol{\varphi}}{d\xi} \right)^T \left(\frac{d\boldsymbol{\varphi}}{d\xi} \right) (\boldsymbol{T^e}) \right\} + \\
l_{ex} A_4 \left\{ (\boldsymbol{T^e})^T (\boldsymbol{\varphi})^T (\boldsymbol{\varphi})\, (\boldsymbol{T^e}) \right\} d\xi + \\
\int_0^1 \frac{A_3}{l_{ex}} \left(\boldsymbol{\varphi_R} \boldsymbol{T_R^e} \boldsymbol{\alpha_R^e} \right) \left\{ (\boldsymbol{T^e})^T \left(\frac{d\boldsymbol{\varphi}}{d\xi} \right)^T \left(\frac{d\boldsymbol{\varphi}}{d\xi} \right) (\boldsymbol{T^e}) \right\} + \\
l_{ex} A_4 \left(\boldsymbol{\varphi_R} \boldsymbol{T_R^e} \boldsymbol{\alpha_R^e} \right) \left\{ (\boldsymbol{T^e})^T (\boldsymbol{\varphi})^T (\boldsymbol{\varphi})\, (\boldsymbol{T^e}) \right\} d\xi
\end{aligned}
\right\} \tag{5.42}
$$

The element stiffness matrices as given in Equations 5.39 can be assembled for all the sub-domains to obtain global stiffness matrix on the same lines as given in Equation 5.38.

5.2.3 Proposed perturbation approximation for stochastic formulation with geometric nonlinearity

The global stiffness matrix $\boldsymbol{K}$ used in the perturbation method 4.2 as discussed in chapter 4 is a function of random variables $\{\alpha_i\}_{i=1}^N$, where N is number of random variables.

However, with incorporation of von Kármán nonlinear strains, the global stiffness matrix $\boldsymbol{K}(\boldsymbol{U}(\alpha_i), \alpha_i)$ becomes a function of both displacement DOF $\boldsymbol{U}(\alpha_i)$ and random variables α_i. Therefore, the partial derivatives of $\boldsymbol{K}$ with respect to α (dropping the subscript i from α_i) can be written as,

$$\frac{\partial \boldsymbol{K}}{\partial \alpha} = \frac{\partial \boldsymbol{K}}{\partial \hat{\boldsymbol{U}}} \frac{\partial \boldsymbol{U}}{\partial \alpha} + \frac{\partial \boldsymbol{K}}{\partial \hat{\alpha}} \tag{5.43}$$

$$\frac{\partial^2 \boldsymbol{K}}{\partial \alpha^2} = \frac{\partial^2 \boldsymbol{K}}{\partial \hat{\boldsymbol{U}}^2} \left(\frac{\partial \boldsymbol{U}}{\partial \alpha} \right)^2 + \frac{\partial \boldsymbol{K}}{\partial \hat{\boldsymbol{U}} \partial \hat{\alpha}} \frac{\partial \boldsymbol{U}}{\partial \alpha} + \frac{\partial \boldsymbol{K}}{\partial \hat{\boldsymbol{U}}} \frac{\partial^2 \boldsymbol{U}}{\partial \alpha^2} + \frac{\partial \boldsymbol{K}}{\partial \hat{\alpha} \partial \hat{\boldsymbol{U}}} \frac{\partial \boldsymbol{U}}{\partial \alpha} + \frac{\partial^2 \boldsymbol{K}}{\partial \hat{\alpha}^2} \tag{5.44}$$

where, $\boldsymbol{K}(\boldsymbol{U}(\alpha), \alpha) = \boldsymbol{K} \circ \hat{\boldsymbol{K}}(\alpha)$ with $\hat{\boldsymbol{K}}(\alpha) = (\boldsymbol{U}(\alpha), \alpha)$. Here, $\hat{\alpha}, \hat{\boldsymbol{U}}$ lie in the domain of $\boldsymbol{K}(\boldsymbol{U}(\alpha), \alpha)$ and α lies in the domain of $\hat{\boldsymbol{K}}(\alpha)$.

Equation 5.43 and 5.44 can be substituted into the Taylor series expansion of Equation 5.38 and upon further substitution into equilibrium equations, terms with the same order are equated and the following equations are obtained,

$$\boldsymbol{K_0 U_0} = \boldsymbol{F_0} \tag{5.45}$$

$$\boldsymbol{K_0 U_i^I} + \frac{\partial \boldsymbol{K}}{\partial \boldsymbol{U}} \boldsymbol{U_i^I U_0} + \boldsymbol{K_i^I U_0} = 0 \tag{5.46}$$

$$\left.\begin{aligned} \boldsymbol{K_0 U_{ij}^{II}} + \frac{\partial \boldsymbol{K}}{\partial \boldsymbol{U}} \boldsymbol{U_i^I U_j^I} + \frac{\partial \boldsymbol{K}}{\partial \boldsymbol{U}} \boldsymbol{U_j^I U_i^I} + \boldsymbol{K_i^I U_j^I} + \boldsymbol{K_j^I U_i^I} + \\ \frac{\partial^2 \boldsymbol{K}}{\partial \boldsymbol{U}^2} \boldsymbol{U_i^I U_j^I U_0} + \frac{\partial \boldsymbol{K}_i^I}{\partial \boldsymbol{U}} \boldsymbol{U_j^I U_0} + \frac{\partial \boldsymbol{K}_j^I}{\partial \boldsymbol{U}} \boldsymbol{U_i^I U_0} + \frac{\partial \boldsymbol{K}}{\partial \boldsymbol{U}} \boldsymbol{U_{ij}^{II} U_0} + \boldsymbol{K_{ij}^{II} U_0} = 0 \end{aligned}\right\} \tag{5.47}$$

where, $\boldsymbol{K_0}$, $\boldsymbol{U_0}$ and $\boldsymbol{F_0}$ are evaluated at $\boldsymbol{K}(0)$, $\boldsymbol{U}(0)$ and $\boldsymbol{F}(0)$ respectively; and $(.)_i^I = \left.\frac{\partial (.)}{\partial \alpha_i}\right|_{\boldsymbol{\Lambda}=0}$ and $(.)_{ij}^{II} = \left.\frac{\partial^2 (.)}{\partial \alpha_i \partial \alpha_j}\right|_{\boldsymbol{\Lambda}=0}$ as given in section 4.2. It is to be noted here that Equation 5.45, 5.46 and 5.47 are nonlinear in nature and for the present work, Newton-Raphson method is proposed for solving these equations to obtain $\boldsymbol{U_0}$, $\boldsymbol{U_i^I}$ and $\boldsymbol{U_{ij}^{II}}$.

Once the derivatives are found, by applying expectation and variance operators on truncated Taylor series expansion of response functions, the first order or second order approximations of statistical moments of these quantities can be found as in Equation 4.34 and 4.35. Based on the preceding deterministic and stochastic BSWI WFEM formulations for beams incorporating von Kármán nonlinear strains; in the next section, a few numerical

examples are solved.

5.3 Numerical examples

5.3.1 Based on deterministic BSWI WFEM formulation for beams incorporating von Kármán nonlinear strains

A beam under different boundary conditions is considered to demonstrate the performance of BSWI WFEM beam elements based on von Kármán strains. The main numerical issue that a von Kármán beam element may produce is membrane locking when axial deformations are unconstrained (roller supports). Hence, a beam with a uniformly distributed non-follower load under different boundary conditions (having roller, pinned and clamped support at both ends) is considered. Moreover, shear locking issues can be expected when Timoshenko BSWI WFEM beam elements are used for thin beams. Hence a study has been performed on thin beams with pinned ends and fixed ends, where membrane locking does not exist whereas shear locking exists.

Three separate cases, each consisting of a beam with different boundary conditions viz., both ends roller, both ends pinned and both ends clamped as shown in Figure 5.3 are solved using EBT and TBT to show the performance of BSWI WFEM beam elements based on von Kármán strains. The material of the beam is considered to be isotropic with Young's modulus $E = 2 \times 10^5$MPa. For all the examples beam is taken to have a span of $L = 100$mm. For the beam with both ends roller support, it is considered to be carrying a uniformly distributed load of $q = 0.1$N/mm over the entire span, and for the rest of the boundary conditions a uniformly distributed load of $q = 10$N/mm over the entire span is considered during the analysis. The boundary conditions for various cases are as follows: a) Beam with roller ends, $w_0 = 0$ at $x = 0$ and $x = L$, b) Beam with pinned ends, $u_0 = w_0 = 0$ at $x = 0$ and $x = L$, c) Beam with clamped ends: $u_0 = w_0 = \frac{dw_0}{dx} = 0$ at $x = 0$ and $x = L$. For all the cases, due to symmetry, only one-half domain with span $L/2 = 50$mm is considered for analysis by applying boundary condition $u_0 = \frac{dw_0}{dx} = 0$ at $x = L/2$. Only one BSWI WFEM element is used for modelling the domain in all the cases and thus the storage of element connectivity data and cumbersome element assembly procedure can be eliminated. The variation of deflections obtained using BSWI WFEM Euler-Bernoulli beam elements are compared with those available in the FEM examples solved by Reddy [210] for all boundary conditions. Numerical examples solved by Reddy [210] uses cubic Hermite interpolation functions and linear Lagrange

interpolation functions to model transverse deflection and axial displacement field variables for beams based on EBT. Whereas, for beams based on TBT, linear or quadratic Lagrange interpolation functions are used to model the axial, transverse and rotational field variables independently.

Additionally, for pinned-pinned boundary conditions, analytical solutions using approximate methods based on Galerkin approaches are found in Sathyamoorthy [211] and Nishawala [212]. Hence a comparison with the same is done for TBT beam elements for this particular boundary condition. Roller boundary condition, does not constrain the axial displacements and the relationship becomes linear and hence the results for this case can be compared with linear analytical solution. For BSWI WFEM Timoshenko beam element, commercial FEM package ABAQUS is used for the comparison study. In addition, the variation of stresses in axial direction from BSWI WFEM beam elements are compared with the stresses in axial direction obtained using commercial FEM package ABAQUS. Beams based on EBT is modelled using ABAQUS with a 2 node cubic beam element B23 and beams based on TBT is modelled using 2 node linear B21 and 3 node quadratic B22 elements. All of three elements B21, B22 and B23 have 3 DOF at each node $(u_0, w_0, \frac{dw_0}{dx})$. While modelling geometric nonlinearity with large displacements in ABAQUS, the NLGEOM is selected along with full Newton scheme for solving the nonlinear system of equations [213].

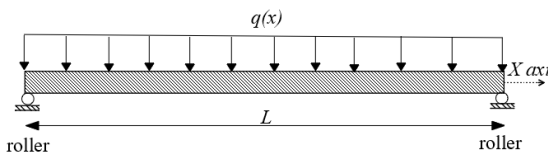

(a) With roller ends

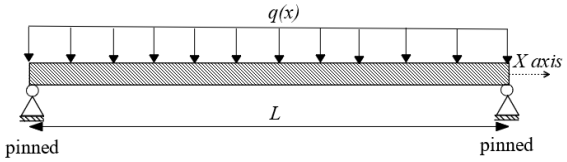

(b) With pinned ends

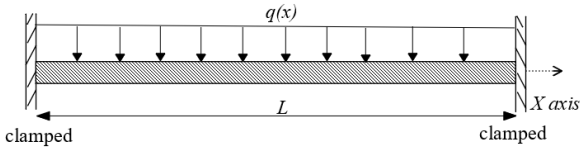

(c) With clamped ends

Figure 5.3: A beam under uniformly distributed load $q(x)$

5.3.1.1 Beam with roller ends

In this example, a beam having rollers at both ends as shown in Figure 5.3a is considered for analysis using EBT and TBT. For the analysis based on EBT, a combination of linear (order $m = 2$) and cubic (order $m = 4$) scaling functions are used in the approximation of axial displacement u_0 and bending deflection w_0 respectively. However, the roller beam has no axial strain, since it slides on rollers under transverse deflection and hence,

$$E^0_{XX} = \frac{du_0}{dX} + \frac{1}{2}\left(\frac{dw_0}{dX}\right)^2 = 0 \tag{5.48}$$

Moreover, the aforementioned combination of scaling functions when used for approximating u_0 and w_0 do not satisfy Equation 5.48 and results in a phenomena known as membrane locking. Generally in FEM, a reduced one-point integration scheme is suggested for the evaluation of nonlinear stiffness matrix coefficients to overcome the issue of membrane locking. In the current study which uses WFEM, both one-point integration and two-point integration schemes as discussed in chapter 3 are used to examine the presence of membrane locking. Variation of deflection at $x = L/2$ with load for different resolutions $j = \{1, 2, 3\}$ is shown in Figure 5.4. The deflection calculated using one-point and two-point integration schemes are compared with the analytical solution, which is linear in the present case due to the absence of axial strains, and FEM results using reduced integration scheme (one-point integration). It is observed that the deflections obtained from BSWI WFEM for all values of j are in good agreement with the analytical solution and FEM results when one-point integration is used. However, two-point integration leads to a lower deflection even for higher resolutions, proving the presence of membrane locking and hence the study recommends lower integration for nonlinear terms in stiffness matrix to get rid of the membrane locking.

A beam with same boundary conditions and span, but having different cross-section area $1 \times 15\mathrm{mm}^2$ to treat it as a deep beam is considered for analysis based on TBT. For the analysis of the beam based on TBT, the domain is modelled using one BSWI element with C_0 continuity. The current numerical example is modelled using TBT based beam element, where the unknown field variables u_0, w_0, θ_x are equally interpolated with either linear scaling functions or by quadratic scaling functions. The membrane locking phenomena, which is discussed in the context of Euler-Bernoulli beam element is applicable for a beam element based on TBT as well. Hence, proper numerical integration scheme for all the nonlinear terms of the stiffness matrix, which can prevent the effects of membrane locking, needs to be examined for TBT beam elements too. Variation of deflections at $x = L/2$,

obtained using linear and quadratic scaling functions with resolutions $j = \{1, 2, 3\}$ is plotted using BSWI WFEM and compared with linear analytical deflection (incorporating transverse shear effects for thick beams) as given by Wang et al. [214] and results obtained from FEM using ABAQUS with linear and quadratic shape functions as shown in Figure 5.5 and 5.6 respectively. It is observed from Figure 5.5 that at lower resolution for both one-point and two-point integration, linear scaling functions produce less accurate results. However, the results converge as the resolution is increased. On the other hand, quadratic scaling functions produce converged results (for both one-point and two-point integration) even at lower resolutions as observed in Figure 5.6.

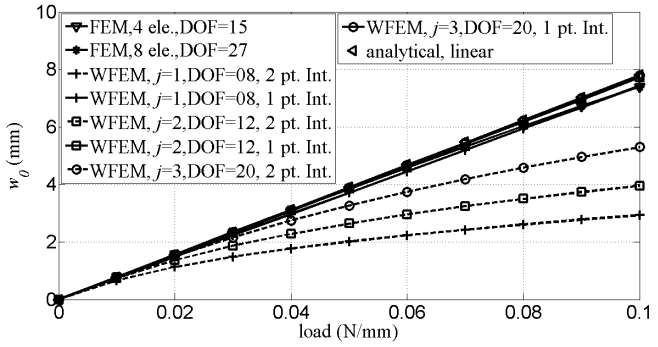

Figure 5.4: Variation of deflection at $x = L/2$ with load for the EBT beam with roller ends having $b, h = 1$mm, when BSWI WFEM and FEM elements are used for modelling

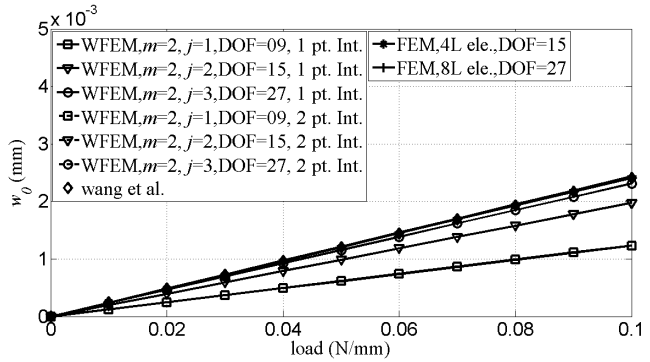

Figure 5.5: Variation of deflection at $x = L/2$ with load for the TBT beam with roller ends having $b, h = (1, 15)$mm, when linear BSWI WFEM and FEM elements are used for modelling

Besides deflection, the variation of stresses in axial direction along $y = -h/2$ was also studied using BSWI WFEM beam elements based on EBT and TBT for $m = 2, j = 3$. Variation of σ_{xx} at $y = -h/2$ obtained using BSWI WFEM and FEM elements, based

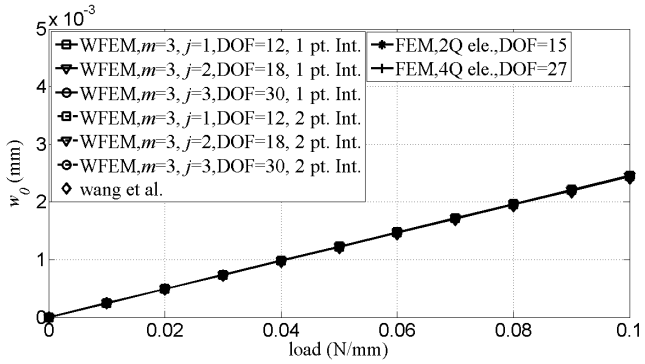

Figure 5.6: Variation of deflection at $x = L/2$ with load for the TBT beam with roller ends having $b, h = (1, 15)$mm, when quadratic BSWI WFEM and FEM elements are used for modelling

on EBT for $b, h = 1$mm is plotted in Figure 5.7. It is noticed from Figure 5.7 that for $b, h = 1$mm stresses produced by BSWI WFEM concur well with the results obtained from FEM. The values of b, h are then varied and normalized σ_{xx} values are plotted to investigate the variation between BSWI and FEM results at different b, h values at $y = -h/2$ in Figure 5.8. It is observed that for all b, h values both WFEM and FEM results are in good agreement. Variation of σ_{xx} along $y = -h/2$ based on TBT which takes transverse shear effects into account for thick beams with $b, h = (1, 15)$mm is shown in Figure 5.9, wherein $m = 2, j = 3$ is used for WFEM and linear shape functions for FEM analysis. It is observed that results of both BSWI WFEM and FEM are in good agreement with each other.

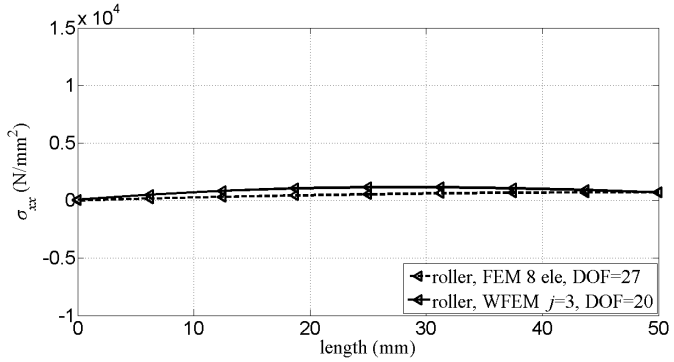

Figure 5.7: Variation of $\sigma_{xx}\,(\mathrm{N/mm^2})$ at $y = -h/2$ along the span of EBT beam with roller ends for $b, h = 1$mm, when BSWI WFEM and FEM elements are used for modelling

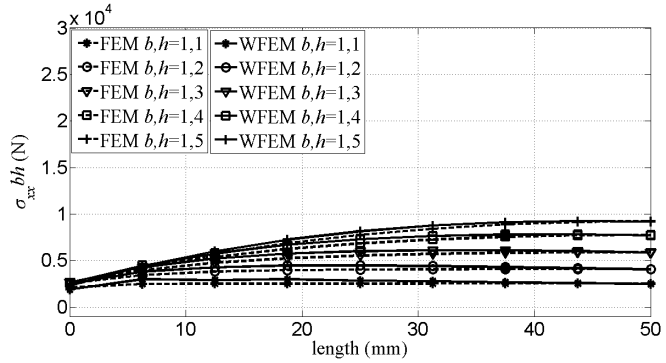

Figure 5.8: Variation of $\sigma_{xx}bh$ at $y = -h/2$ along the span of EBT beam with roller ends for various b, h values, when BSWI WFEM and FEM elements are used for modelling

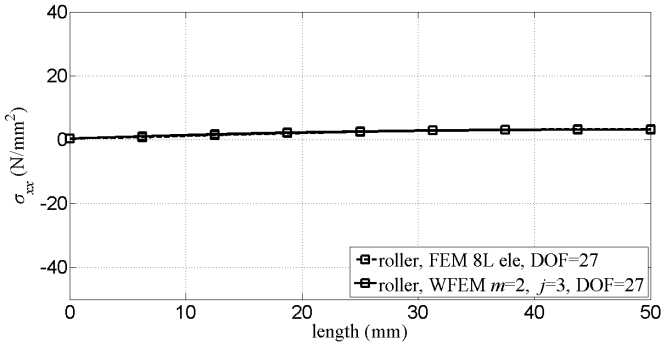

Figure 5.9: Variation of σ_{xx} $(\mathrm{N/mm^2})$ at $y = -h/2$ along the span of TBT beam with roller ends for $b, h = (1, 15)$mm, when linear BSWI WFEM and FEM elements are used for modelling

5.3.1.2 Beam with pinned ends

In this example, a beam having pinned support at both ends as shown in Figure 5.3b is considered for analysis using EBT and TBT. The linear (order $m = 2$) and cubic (order $m = 4$) scaling functions which are used in the approximation of axial displacement u_0 and bending deflection w_0 need not satisfy axial strain of Equation 5.48 for pinned boundary conditions, thereby eliminating the chances of membrane locking. Hence for this numerical example where EBT is used, only two-point integration scheme is employed to evaluate the stiffness coefficients. The variation of deflection at $x = L/2$, with load, obtained using BSWI WFEM for different resolutions $j = \{1, 2, 3\}$ are compared with the results obtained from Sathyamoorthy [211] and FEM as shown in Figure 5.10. A good compliance is observed between the results of BSWI WFEM, Sathyamoorthy [211] and FEM.

For a thick beam based on TBT $1 \times 15\mathrm{mm}^2$ the variation of deflections at $x = L/2$, obtained using BSWI WFEM is compared with deflection obtained using FEM for linear

and quadratic scaling functions with resolutions $j = \{1, 2, 3\}$ in Figure 5.11 and Figure 5.12, respectively. When two-point integration is used for TBT, the deflections obtained from WFEM using linear scaling functions are underestimated when compared with converged FEM results at lower resolutions. However, this issue is resolved when either one-point or two-point integration scheme at a higher resolution is used. Also, it can be observed that at a higher order (for both one-point and two-point integration), there is a good agreement between BSWI WFEM and FEM results even when lower resolutions are used. Additionally, σ_{xx} plot along $y = -h/2$ based on EBT $b, h = 1$mm is shown in Figure 5.13 and that for based on TBT $b, h = (1, 15)$mm is shown in Figure 5.14. For evaluation of these results one-point integration scheme is used. In all the cases, it is observed that results from BSWI WFEM concur well with the results obtained from FEM.

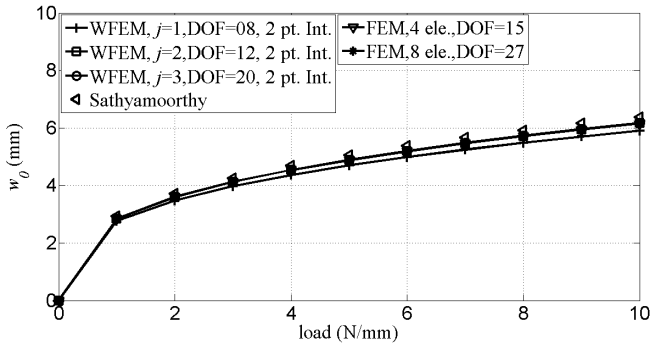

Figure 5.10: Variation of deflection at $x = L/2$ with load for the EBT beam with pinned ends having $b, h = 1$mm, when BSWI WFEM and FEM elements are used for modelling

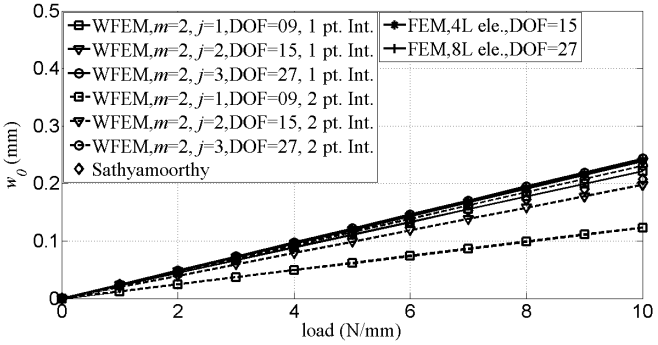

Figure 5.11: Variation of deflection at $x = L/2$ with load for the TBT beam with pinned ends having $b, h = (1, 15)$mm, when linear BSWI WFEM and FEM elements are used for modelling

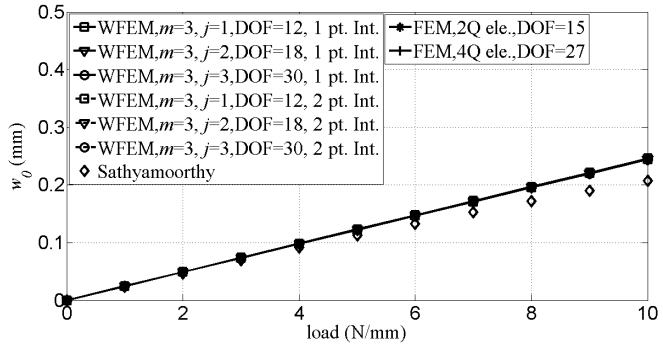

Figure 5.12: Variation of deflection at $x = L/2$ with load for the TBT beam with pinned ends having $b, h = (1, 15)$mm, when quadratic BSWI WFEM and FEM elements are used for modelling

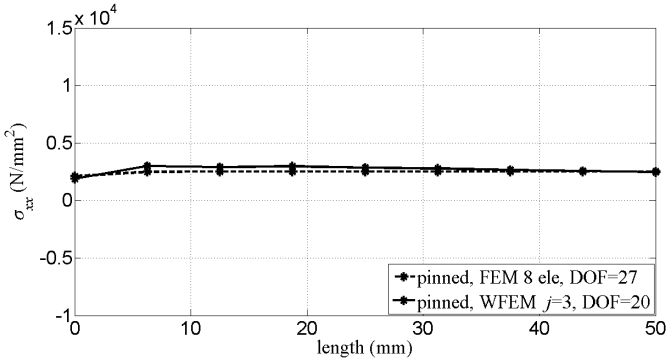

Figure 5.13: Variation of $\sigma_{xx}\,(\mathrm{N/mm^2})$ at $y = -h/2$ along the span of EBT beam with pinned ends for $b, h = 1$mm, when BSWI WFEM and FEM elements are used for modelling

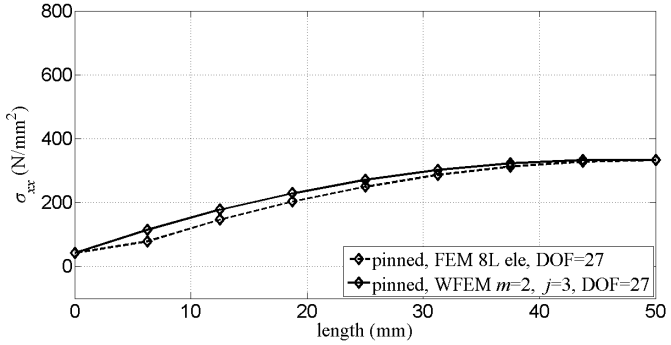

Figure 5.14: Variation of $\sigma_{xx}\,(\mathrm{N/mm^2})$ at $y = -h/2$ along the span of TBT beam with pinned ends for $b, h = (1, 15)$mm, when linear BSWI WFEM and FEM elements are used for modelling

5.3.1.3 Beam with clamped ends

In this example, a beam having clamped support at both ends as shown in Figure 5.3c is considered for analysis based on EBT $b, h = 1$mm and TBT $b, h = (1, 15)$mm. The issue of membrane locking does not exist for EBT based beam element in this example for the reasons already discussed in the earlier cases. Hence, the deflections are calculated using EBT based BSWI FEM beam elements by employing two-point integration scheme to evaluate the stiffness coefficients and is plotted in Figure 5.15. It can be observed that the results obtained from WFEM converge to those obtained from FEM when the resolution is increased. The variation of deflections for TBT based beam element for thick beam is shown in Figure 5.16 and 5.17 for linear and quadratic scaling functions respectively. It is observed that results obtained from BSWI WFEM based on TBT converge with that of corresponding FEM results with one-point integration as the resolution is increased. When two-point integration is used for beams based on TBT, either a quadratic order scaling function (with all the resolutions) or a linear order scaling function with a higher resolution is needed, to obtain accurate results. Analogous to previous cases, the variation of σ_{xx} based on EBT for $b, h = 1$mm along $y = -h/2$ is plotted as shown in Figure 5.18 which shows a good agreement between WFEM and FEM results. The variation of σ_{xx} based on TBT is shown in Figure 5.19 for $b, h = (1, 15)$mm which confirms the effectiveness of WFEM in capturing the converged results.

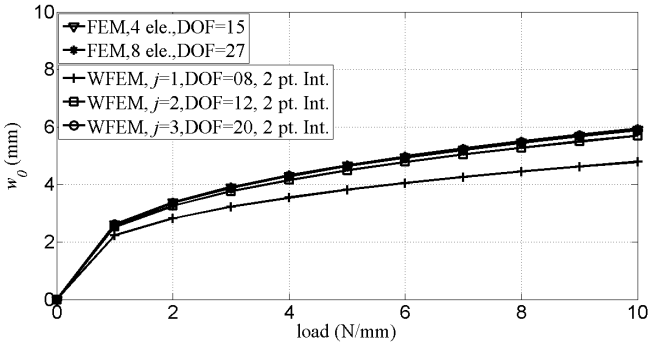

Figure 5.15: Variation of deflection at $x = L/2$ with load for the EBT beam with clamped ends having $b, h = 1$mm, when BSWI WFEM and FEM elements are used for modelling

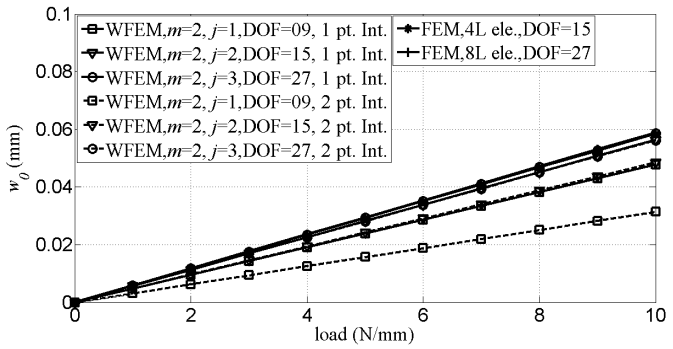

Figure 5.16: Variation of deflection at $x = L/2$ with load for the TBT beam with clamped ends having $b, h = (1, 15)$mm, when linear BSWI WFEM and FEM elements are used for modelling

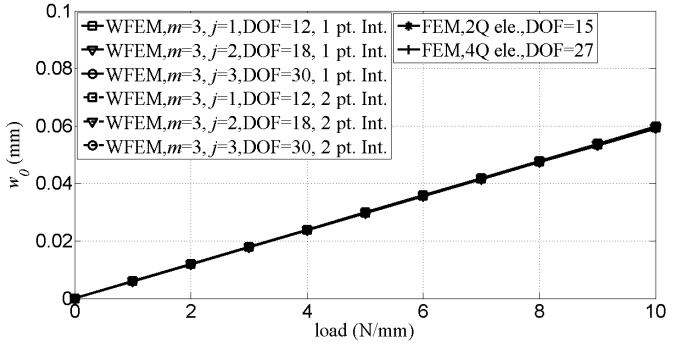

Figure 5.17: Variation of deflection at $x = L/2$ with load for the TBT beam with clamped ends having $b, h = (1, 15)$mm, when quadratic BSWI WFEM and FEM elements are used for modelling

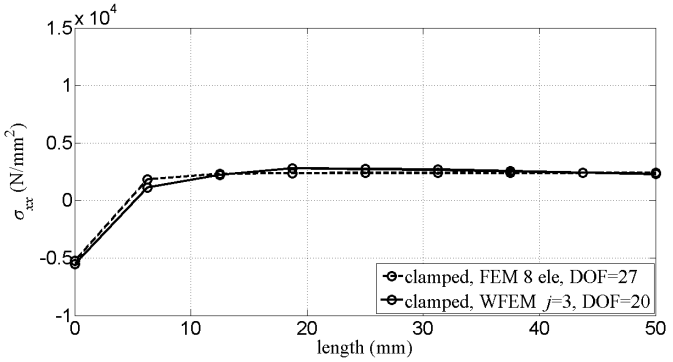

Figure 5.18: Variation of $\sigma_{xx}\,(\mathrm{N/mm^2})$ at $y = -h/2$ along the span of EBT beam with clamped ends for $b, h = 1$mm, when BSWI WFEM and FEM elements are used for modelling

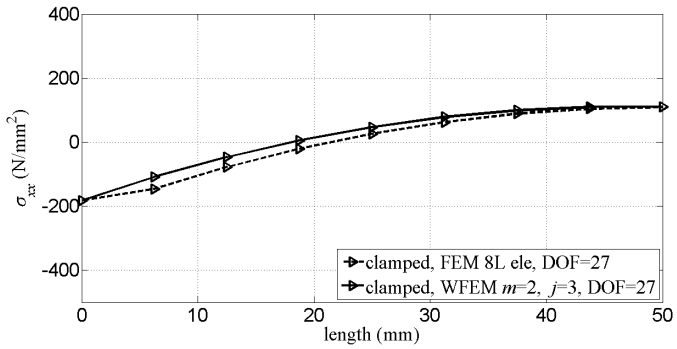

Figure 5.19: Variation of $\sigma_{xx}\,(\mathrm{N/mm^2})$ at $y = -h/2$ along the span of TBT beam with clamped ends for $b, h = (1, 15)$mm, when linear BSWI WFEM and FEM elements are used for modelling

5.3.1.4 Discussion on effects of numerical locking

When the issue of membrane locking do not exist, a two-point Gauss quadrature scheme is used in between each of the internal nodes of BSWI EBT beam element for the evaluation of linear and nonlinear terms of the stiffness matrix. However, when a membrane locking exists, a one-point integration scheme is suggested to evaluate all the nonlinear terms of the stiffness matrix. On the other hand, a thick beam modelled by TBT under predicts the deflection for the linear order of scaling functions, when two-point integration scheme is used. It is to be noted that a single WFEM BSWI element consists of more than one background integration cell depending on the resolution of the displacement approximation and hence, more integration points. This will lead to over rigid stiffness coefficients for TBT element due to the presence of nonlinear terms including additional shear terms, when compared to EBT element and that can be the reason for under predicting the deflection. Moreover, there can be shear locking as in FEM when TBT based WFEM beam elements are used for thin beams. In general, the reduced integration (i.e. here the one-point integration) should give a better result. To examine the same, a beam within the thin beam limit $b, h = 1$mm is modelled using TBT beam element and solved. Beam with roller ends is not considered for the study to keep away the effects of membrane locking.

In the one-point integration scheme used here, shear stiffness coefficients are integrated such that the cell between each of the internal nodes of the BSWI element consists of one Gauss point. Deflections at $x = L/2$ of the beam $b, h = 1$mm in cases (both ends pinned, both ends clamped) are solved using WFEM TBT beam elements with linear and quadratic scaling functions using both one-point and two-point Gauss quadrature scheme and are shown in Figures 5.20,5.21,5.22,5.23. For comparison, results obtained using FEM

is also shown. It can be clearly observed that when linear elements are used for modelling, two-point integration of shear terms lead to a large variation in deflection as compared to the converged FEM results. However, one-point integration produces matching results with that of FEM. When quadratic elements are used for modelling, the results obtained from both one-point and two-point integration remain in good agreement with converged FEM results. Thus, it can be observed that for BSWI TBT element one-point integration of shear terms is necessary for linear elements and this can get rid of any kind of locking issue.

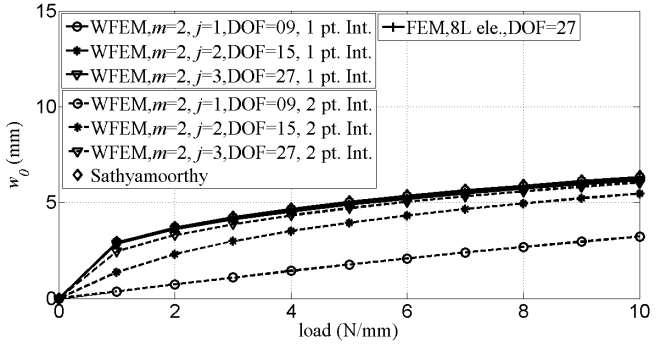

Figure 5.20: Variation of deflection at $x = L/2$ with load for the TBT beam with pinned ends having $b, h = 1$mm, when linear BSWI WFEM and FEM elements are used for modelling

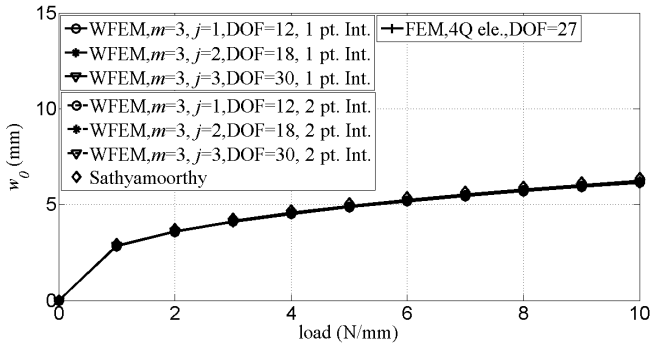

Figure 5.21: Variation of deflection at $x = L/2$ with load for the TBT beam with pinned ends having $b, h = 1$mm, when quadratic BSWI WFEM and FEM elements are used for modelling

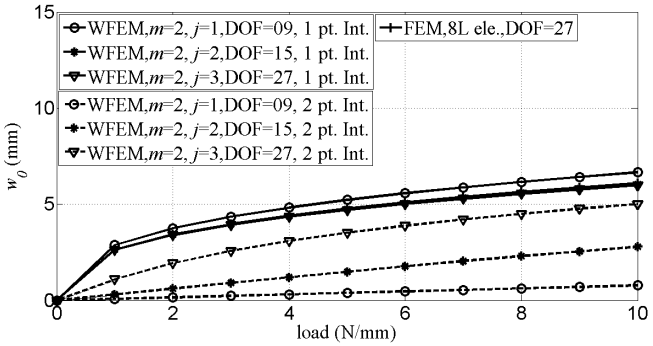

Figure 5.22: Variation of deflection at $x = L/2$ with load for the TBT beam with clamped ends having $b, h = 1$mm, when linear BSWI WFEM and FEM elements are used for modelling

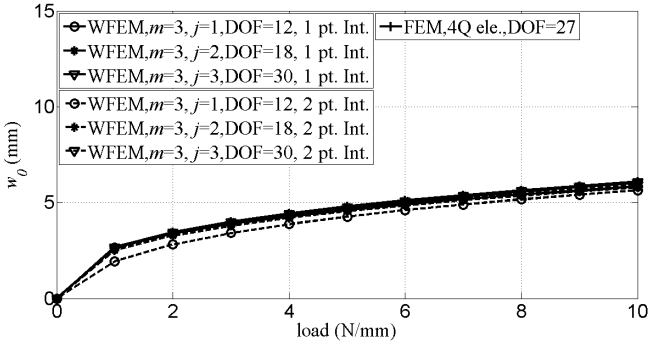

Figure 5.23: Variation of deflection at $x = L/2$ with load for the TBT beam with clamped ends having $b, h = 1$mm, when quadratic BSWI WFEM and FEM elements are used for modelling

Following the analysis of numerical examples based on deterministic BSWI WFEM formulation for beams with geometric nonlinearity; in the next subsection numerical examples based on stochastic BSWI WFEM formulation for beams with geometric nonlinearity is discussed.

5.3.2 Based on stochastic BSWI WFEM formulation for beams incorporating von Kármán nonlinear strains

The numerical examples that were discussed in the previous subsection 5.3.1 (both ends roller, both ends pinned, both ends clamped) are considered for analysis in the stochastic framework as well. The modulus of elasticity is modelled as a homogeneous random field with a Gaussian distribution, as given by Equation 4.1. The results from stochastic WFEM wherein both the input random field and response are discretized using BSWI scaling

functions are compared with those obtained from stochastic FEM wherein both random field and response are discretized using Lagrange shape functions. The response statistics are calculated via perturbation method and the results are compared with the statistics obtained from MCS (for both WFEM and FEM). The mean value of Young's modulus is taken as $\mu_E = 2 \times 10^5$MPa and rest of the material and geometric properties are kept the same that were considered in the deterministic case. For the formulation based on EBT, the axial and transverse deflection fields are approximated using $m = 2$ and $m = 4$ respectively for the reasons already discussed in the deterministic case. For the formulation based on TBT, $m = 3$ is used for the approximation of the deflection field. A converged resolution of $j = 3$ is used for both the cases. The difference in the results when the random field is discretized using linear or quadratic scaling functions, as shown in chapter 4 is observed to be small. Hence, in the current study only linear scaling functions $m = 2$ are used for the discretization of random fields with a lower resolution $j = 1$.

The mean and standard deviation values of transverse deflection field for the beam based on EBT with both ends pinned, at $x = 50$mm obtained by using the perturbation approach are shown in Figure 5.24 and Figure 5.25 respectively. The perturbation values are compared with the values obtained from MCS and the results are plotted for different values of CV, obtained by varying the standard deviation of Young's modulus $E(\mathbf{x})$. The correlation length parameter considered is 25. It can be observed from Figure 5.24 that the variation observed in mean values between perturbation and MCS results is less than 1% for all the CV values. However, the variation in standard deviation values increases to 5-7% at 20% CV as seen in Figure 5.25. The mean and standard deviation values calculated for the beam based on TBT with both ends pinned, at $x = 50$mm obtained for different CV values are shown in Figure 5.26 and Figure 5.27 respectively. It can be observed that mean values obtained from perturbation approach and MCS remain in good agreement for different values of CV. The standard deviation of response obtained from FOP and SOP matches well with the MCS values till a CV of 15% and a variation of 9-10% is observed when CV of input field is increased to 20%.

The variation of mean and standard deviation values for the EBT and TBT based beams with pinned ends against correlation length parameter at a CV of 10% are shown in Figure 5.28-5.31. It can be observed that even at extreme correlation length parameters, the results obtained from perturbation approach and MCS concur well for both WFEM and FEM. Further, the variation of mean and standard deviation values for beams based on EBT and TBT with clamped and roller ends boundary conditions, evaluated at a CV of 10% and a correlation length parameter of 25 are shown in Table 5.1,5.2,5.3,5.4. The results show

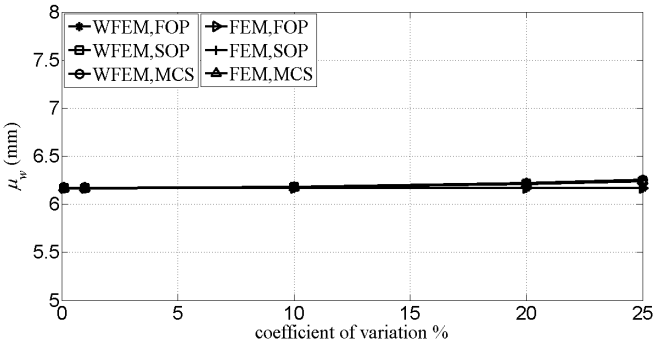

Figure 5.24: Variation of mean value of deflection at $x = 50$mm for the EBT beam with pinned ends having $b, h = 1$mm against CV

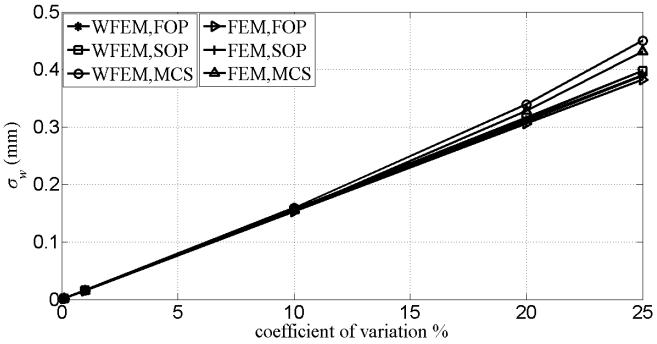

Figure 5.25: Variation of standard deviation of deflection at $x = 50$mm for the EBT beam with pinned ends having $b, h = 1$mm against CV

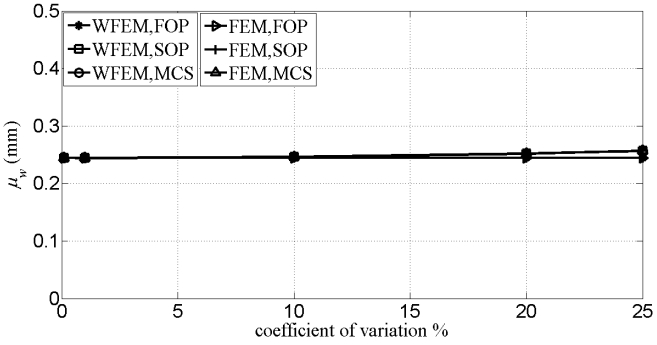

Figure 5.26: Variation of mean value of deflection at $x = 50$mm for the TBT beam with pinned ends having $b, h = (1, 15)$mm against CV

that perturbation approach (SOP) based on WFEM performs accurately in comparison with MCS.

Analogous to the case of 1D problems in chapter 4, the normalized computational time required for implementing the perturbation method and MCS (5000 samples) based on

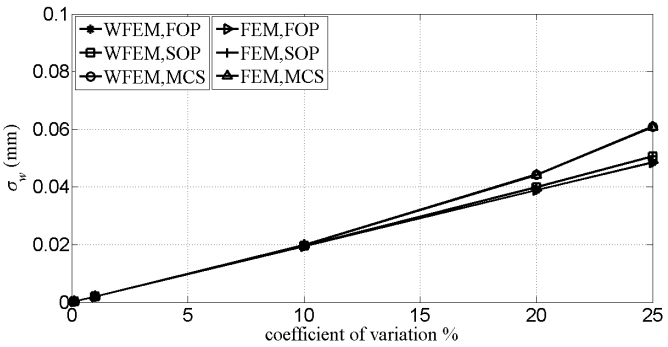

Figure 5.27: Variation of standard deviation of deflection at $x = 50$mm for the TBT beam with pinned ends having $b, h = (1, 15)$mm against CV

WFEM and FEM shape functions is also calculated for the current study and shown in Table 5.5 and 5.6 for beams based on EBT and TBT respectively. A CV of 10% and a correlation length parameter of 25 is considered for the study. Similar to the observations made in chapter 4, FEM based perturbation method takes the least amount of computational time when compared with other methods due to the reasons that have been discussed in chapter 4. Further, the results reiterate that perturbation approach is computationally more efficient in comparison with MCS.

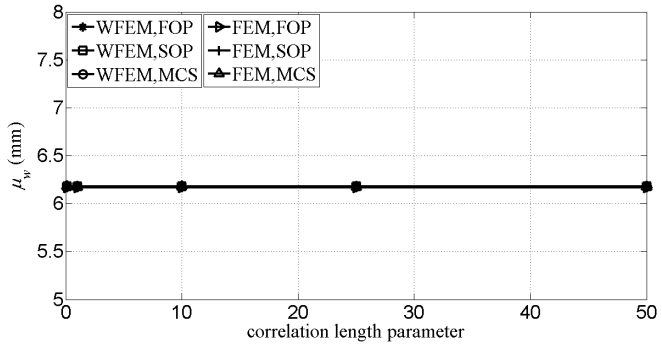

Figure 5.28: Variation of mean value of deflection at $x = 50$mm for the EBT beam with pinned ends having $b, h = 1$mm against correlation length parameter

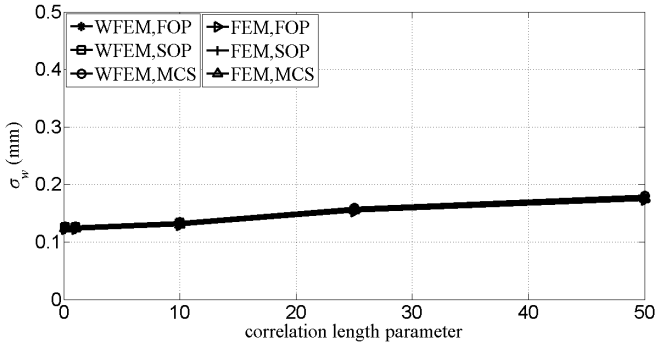

Figure 5.29: Variation of standard deviation of deflection at $x = 50$mm for the EBT beam with pinned ends having $b, h = 1$mm against correlation length parameter

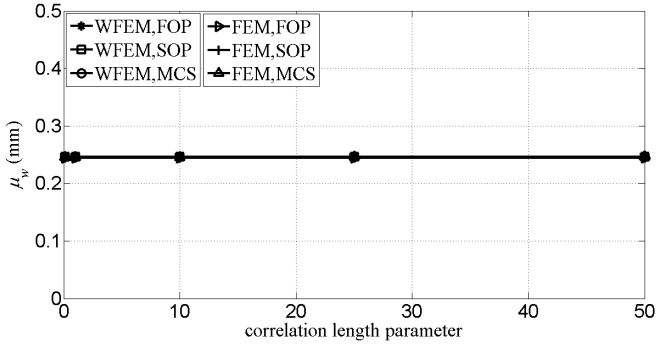

Figure 5.30: Variation of mean value of deflection at $x = 50$mm for the TBT beam with pinned ends having $b, h = (1, 15)$mm against correlation length parameter

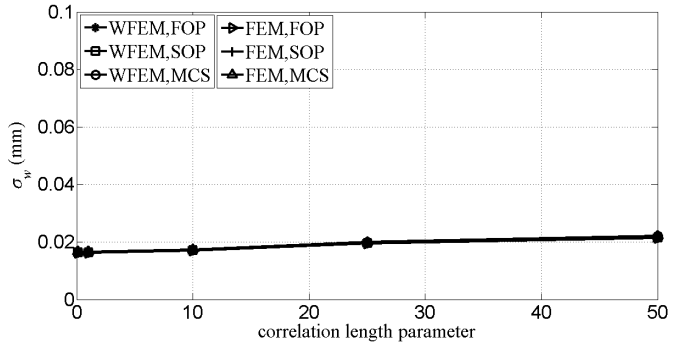

Figure 5.31: Variation of standard deviation of deflection at $x = 50$mm for the TBT beam with pinned ends having $b, h = (1, 15)$mm against correlation length parameter

Table 5.1: Mean values of deflection at $x = 50$mm for the EBT beam under different boundary conditions

Boundary conditions	WFEM			FEM		
	FOP	SOP	MCS	FOP	SOP	MCS
clamped-clamped	5.889	5.900	5.894	5.902	5.914	5.910
roller-roller	7.788	7.849	7.834	7.812	7.874	7.860

Table 5.2: Mean values of deflection at $x = 50$mm for the TBT beam under different boundary conditions

Boundary conditions	WFEM			FEM		
	FOP	SOP	MCS	FOP	SOP	MCS
clamped-clamped	0.0593	0.0597	0.0596	0.0593	0.0597	0.0595
roller-roller	0.00244	0.00246	0.00245	0.00244	0.00246	0.00245

Table 5.3: Standard deviation of deflection at $x = 50$mm for the EBT beam under different boundary conditions

Boundary conditions	WFEM			FEM		
	FOP	SOP	MCS	FOP	SOP	MCS
clamped-clamped	0.151	0.152	0.152	0.149	0.150	0.150
roller-roller	0.627	0.631	0.643	0.636	0.640	0.652

Table 5.4: Standard deviation of deflection at $x = 50$mm for the TBT beam under different boundary conditions

Boundary conditions	WFEM			FEM		
	FOP	SOP	MCS	FOP	SOP	MCS
clamped-clamped	0.00434	0.00437	0.00445	0.00434	0.00436	0.00444
roller-roller	0.000194	0.000196	0.000199	0.000194	0.000195	0.000198

Table 5.5: Normalized computational times for perturbation method and MCS for EBT based beam with clamped-clamped boundary conditions

Boundary conditions	WFEM		FEM	
	Perturbation	MCS	Perturbation	MCS
clamped-clamped	1.94	450.433	1	558.00

Table 5.6: Normalized computational times for perturbation method and MCS for TBT based beam with clamped-clamped boundary conditions

Boundary conditions	WFEM		FEM	
	Perturbation	MCS	Perturbation	MCS
clamped-clamped	2.8055	561.706	1	683.416

5.4 Conclusion

The current chapter presents the formulation of deterministic and stochastic BSWI WFEM based beam elements by incorporating von Kármán nonlinear strains. Formulation is proposed for both EBT and TBT. The elements are constructed by incorporating axial DOF to take care of the membrane strains over the bending DOF. The nonlinear system of matrix equations is solved by Newton-Raphson method. Though only one element is necessary to capture accurate results, the total number of Gauss points depends on the resolution and quadrature rule employed.

For the deterministic case, numerical examples with different boundary conditions are studied for maximum transverse deflection and stress in axial direction using BSWI WFEM. The results obtained are compared with the existing converged FEM results. The proposed method produces matching results with that of FEM. Only one element is sufficient to model the problem domain in BSWI WFEM. For all the numerical examples convergence is achieved by increasing the resolution of the wavelet scaling function without altering the number of elements. This alleviates storage requirement of a large element connectivity data and element assembly procedure when compared to FEM. As a result, BSWI WFEM saves memory and reduces the burden in programming. Moreover, the deterministic study addresses the issues of membrane and shear locking in beam analysis. It is observed that for beams based on EBT where membrane locking exists, a one-point integration of nonlinear terms can produce accurate results rather than a two-point integration which is used otherwise. However, for TBT based beam analysis, regardless of order of scaling functions a one-point integration of nonlinear terms produces accurate results. This also takes care of shear locking, when TBT based BSWI WFEM beam element is used for modelling thin beams.

For the stochastic case, the spatial variation of modulus of elasticity is modelled as a homogeneous random field and the response statistics of mean and standard deviation are calculated using the perturbation approach and compared with MCS (for both WFEM and

FEM). Results indicate that with the proposed BSWI WFEM based perturbation approach (both FOP and SOP), accurate results are obtained for CV values of up to 15%. Further, normalized computational times are also shown for the beam with clamped-clamped boundary conditions and, since the current study does not account for re-meshing/mesh sensitive problems, FEM based perturbation times are found to be less in comparison with WFEM.

Based on the proposed formulations, numerical analysis and conclusions that have been drawn so far, a summary to the current thesis is presented in the next chapter.

Chapter 6

Conclusion

6.1 Conclusion

Due to the growing complexity in system design, development of accurate and efficient stochastic based numerical methods has become quintessential. Based on the motivation and an extensive literature review presented in chapters 1 and 2 respectively, the primary objective of this study is identified as to develop a stochastic wavelet finite element method using BSWI for the analysis of problems in elasto-statics, wherein the material properties are modelled as random fields.

In the process of developing a stochastic based BSWI WFEM, it is observed that the existing literature does not discuss about the salient aspects of numerical integrations involved and hence in chapter 3, a background cell-based Gauss point integration approach for BSWI WFEM is proposed in which, background cells are placed over the BSWI WFEM element solving domain and Gauss points are positioned inside each background cell. The study suggests having sufficient number of Gauss points in the support domain of scaling functions for constructing a well-conditioned stiffness matrix and shows that the accuracy of the solution for the given order and resolution of BSWI scaling function is improved when the size of the background cells is decreased and more number of Gauss points, as encountered in two-point integration approach are used. Further, only one element is sufficient to model the problem domain in BSWI WFEM. Convergence can be achieved by increasing the resolution of the wavelet scaling function without altering the number of elements. This alleviates storage requirement of a large element connectivity data and element assembly procedure when compared to FEM. As a result, BSWI WFEM saves memory and reduces the burden in programming.

Chapter 4 proposes the formulation of stochastic BSWI WFEM for 1D and 2D problems in elasto-statics and beams (EBT and TBT). Here, the spatial variation of modulus

of elasticity is modelled as a homogeneous random field. BSWI scaling functions are used for the discretization of both displacement and random fields. The response statistics of mean and standard deviation are calculated using the perturbation approach and the results are compared with MCS. The methodology is further validated via a comparative study between the results of WFEM and FEM for 1D problem. It can be concluded from the results of 1D and 2D numerical examples for problems in elasto-statics that the proposed BSWI WFEM based perturbation approach (both FOP and SOP) accurately captures the response statistics of the displacement field for CV values of up to 15-20% . For problems in beams, accurate results are obtained when the values of CV is less than or equal to 15%. Additionally, for stochastic buckling of columns, WFEM based perturbation approach can be used to accurately capture the response statistics of the buckling load for values of CV up to 25%.

The proposed formulation of deterministic and stochastic BSWI WFEM based beam elements (EBT and TBT) by incorporating von Kármán strains is presented in chapter 5. The elements are constructed by incorporating axial DOF to take care of the membrane strains over the bending DOF. The nonlinear system of matrix equations is solved by Newton-Raphson method. For the deterministic case, it is observed that for beams based on EBT where membrane locking exists, a one-point integration of nonlinear terms can produce accurate results rather than a two-point integration which is used otherwise. However, for TBT based beam analysis, it is observed that results obtained from BSWI WFEM converge with that of corresponding FEM results with one-point integration as the resolution is increased. When two-point integration is used for beams based on TBT, either a quadratic order scaling function (with all the resolutions) or a linear order scaling function with a higher resolution is needed, to obtain accurate results. This also takes care of shear locking, when TBT based BSWI WFEM beam element is used for modelling thin beams. A perturbation approach for the analysis of beams incorporating von Kármán strains is also proposed in chapter 5. A set of three nonlinear equations are derived with the help of Taylor series expansion to find the partial derivatives of response quantities. It is observed that accurate results from WFEM based perturbation approach are obtained for CV values of up to 15%.

Besides varying the standard deviation, a parametric study by varying correlation length parameters is also done for all the 1D problems. Results show that a single BSWI WFEM element with a coarse nodal distribution for random field modelling, perform well by accurately capturing the standard deviations even at extremely small or large correlation length parameters as observed in 1D problem. On the other hand, FEM requires an

appropriate response and random field mesh size in accordance with the correlation length of the input field, which otherwise would result in an erroneous result. Two scale relation and MRA properties of BSWI wavelets help the physical problem to be discretized using less number of elements and thus can reduce the computational cost required for mesh assembly when compared to FEM.

However, normalized computational times, calculated for 1D problems show that FEM based perturbation approach takes less time in comparison with BSWI WFEM. In this context, it is to be noted that those computational times are estimated without accounting for the time associated with re-meshing and convergence studies. The 2D plane stress problems demonstrate that high accuracy can be maintained even when the random field is modelled with wavelet scaling functions of lower order and lower resolution, thereby reducing the computational effort needed.

Hence, based on the results that are presented in the current thesis, it can be concluded that BSWI WFEM is an accurate and efficient numerical tool which can be used for the estimation of response statistics of problems in structural mechanics, wherein material properties are considered as random fields.

6.2 Major contribution

- Guidelines for numerical integration using Gauss quadrature for BSWI WFEM is proposed via a background cell approach
- Formulations of stochastic BSWI WFEM for 1D and 2D problems in elasto-statics and beams (EBT and TBT) is shown. The study also recommends the use of wavelet shape functions for random field modelling.
- Deterministic BSWI WFEM formulation for analysis of beams (EBT and TBT) incorporating von Kármán nonlinear strains is shown
- Finally this research puts forward a stochastic BSWI WFEM formulation based on perturbation approach for beams incorporating von Kármán nonlinear strains. An algorithm for evaluating the derivatives of response quantities from nonlinear equilibrium equations is derived.

6.3 Future work

Based on the vast potential that is offered by wavelets and BSWI WFEM in particular, the following recommendations for future work are made to further exploit its capabilities,

- In the current thesis, response statistics are calculated using the conventional perturbation approach which is based on Taylor series expansion. However, as seen from the results, to capture accurate results this approach puts a limit on the CV to be used. Hence, algorithms can be developed using BSWI WFEM to calculate response statistics for large CV.

- A background cell based numerical integration scheme is proposed in the current thesis. However, for 2D problems with increase in number of background cells, the number of Gauss points used for integration also increase and this escalates the computational effort. Hence, to make BSWI WFEM algorithms even more efficient, new techniques/integration schemes can be suggested for evaluating the integrals and algorithms can be implemented in an optimized manner.

- The current thesis does not discuss about the hourglass effects (which arise due to reduced integration in FEM) in the context of BSWI WFEM. Hence, a detailed study on it can be carried out.

- A stochastic BSWI WFEM formulation for problems in elasto-statics, beams and beams with geometric nonlinearity is shown. The proposed approach can be extended to problems with material and contact nonlinearity, plate bending and composites modelling as well.

- The current thesis uses BSWI scaling functions for different formulations. In future, the application of BSWI wavelet functions can be explored for problems where adaptive analysis is necessary.

- In the current thesis a uni-variate modelling approach is considered wherein, the spatial variation of modulus of elasticity is modelled as a homogeneous random field using the proposed stochastic BSWI WFEM. However, the uni-variate modelling approach restricts the design of a stochastic system. Therefore, a multivariate modelling approach incorporating randomness in other geometric quantities (cross-section area, thickness, etc.) as well could be considered which could lead to a more comprehensive design of the stochastic part.

- The proposed BSWI WFEM algorithm cannot be immediately used in its present form for commercial applications. However, with further additions to its element library, parallel implementation of its loops to make it work faster (to reduce computational times further), implementation of wavelet functions (for adaptive analysis) and development of a GUI would be beneficial to seeing BSWI WFEM used as a full-fledged in-house algorithm for various design applications.

- The current thesis demonstrates the capability of the proposed BSWI WFEM algorithm for various class of problems by considering several benchmark problems and validating the results wherever possible. However, a realistic example of an engineering structure could be modelled in the future.

Bibliography

[1] S.-K. Choi, R. V. Grandhi, and R. A. Canfield, *Reliability-based Structural Design*. Springer London, 2007.

[2] A. Haldar and S. Mahadevan, *Probability, Reliability, and Statistical Methods in Engineering Design*. John Wiley & Sons, 1999.

[3] G. Stefanou, "The stochastic finite element method: Past, present and future," *Computer Methods in Applied Mechanics and Engineering*, vol. 198, no. 9-12, pp. 1031–1051, feb 2009.

[4] K. J. Bathe, *Finite element procedures*. PHI learning private limited, New Delhi, 2010.

[5] E. Vanmarcke and M. Grigoriu, "Stochastic Finite Element Analysis of Simple Beams," *Journal of Engineering Mechanics*, vol. 109, no. 5, pp. 1203–1214, oct 1983.

[6] F. Yamazaki, M. Shinozuka, and G. Dasgupta, "Neumann Expansion for Stochastic Finite Element Analysis," *Journal of Engineering Mechanics*, vol. 114, no. 8, pp. 1335–1354, aug 1988.

[7] F. Yamazaki and M. Shinozuka, "Safety analysis of stochastic finite element systems by monte carlo simulation." *Doboku Gakkai Ronbunshu*, no. 398, pp. 109–119, 1988.

[8] W. K. Liu, T. Belytschko, and A. Mani, "Random field finite elements," *International Journal for Numerical Methods in Engineering*, vol. 23, no. 10, pp. 1831–1845, oct 1986.

[9] B. A. Zeldin and P. D. Spanos, "On Random Field Discretization in Stochastic Finite Elements," *Journal of Applied Mechanics*, vol. 65, no. 2, pp. 320–327, jun 1998.

[10] P. D. Spanos and R. Ghanem, "Stochastic Finite Element Expansion for Random Media," *Journal of Engineering Mechanics*, vol. 115, no. 5, pp. 1035–1053, may 1989.

[11] T. Takada, "Weighted integral method in stochastic finite element analysis," *Probabilistic Engineering Mechanics*, vol. 5, no. 3, pp. 146–156, sep 1990.

[12] T. Takada, "Weighted integral method in multi-dimensional stochastic finite element analysis," *Probabilistic Engineering Mechanics*, vol. 5, no. 4, pp. 158–166, dec 1990.

[13] G. Blatman and B. Sudret, "An adaptive algorithm to build up sparse polynomial chaos expansions for stochastic finite element analysis," *Probabilistic Engineering Mechanics*, vol. 25, no. 2, pp. 183–197, apr 2010.

[14] M. Manjuprasad and C. S. Manohar, "Adaptive Random Field Mesh Refinements in Stochastic Finite Element Reliability Analysis of Structures," *Computer Modeling in Engineering and Sciences*, vol. 19, no. 1, pp. 23–54, 2007.

[15] G. Deodatis, "Weighted Integral Method. I: Stochastic Stiffness Matrix," *Journal of Engineering Mechanics*, vol. 117, no. 8, pp. 1851–1864, aug 1991.

[16] G. Deodatis and M. Shinozuka, "Weighted Integral Method. II: Response Variability and Reliability," *Journal of Engineering Mechanics*, vol. 117, no. 8, pp. 1865–1877, aug 1991.

[17] I. Babuška and B. Guo, "The h, p and h-p version of the finite element method; basis theory and applications," *Advances in Engineering Software*, vol. 15, no. 3-4, pp. 159–174, jan 1992.

[18] J. Dolbow and T. Belytschko, "An introduction to programming the meshless Element Free Galerkin method," *Archives of Computational Methods in Engineering*, vol. 5, no. 3, pp. 207–241, sep 1998.

[19] G. Liu and Y. Gu, *An Introduction to Meshfree Methods and Their Programming*. Berlin/Heidelberg: Springer-Verlag, 2005.

[20] S. Rahman and B. N. Rao, "A perturbation method for stochastic meshless analysis in elastostatics," *International Journal for Numerical Methods in Engineering*, vol. 50, no. 8, pp. 1969–1991, mar 2001.

[21] S. Rahman and H. Xu, "A Meshless Method for Computational Stochastic Mechanics," *International Journal for Computational Methods in Engineering Science and Mechanics*, vol. 6, no. 1, pp. 41–58, jan 2005.

[22] B. Li and X. Chen, "Wavelet-based numerical analysis: A review and classification," *Finite Elements in Analysis and Design*, vol. 81, pp. 14–31, apr 2014.

[23] I. Daubechies, "Orthonormal bases of compactly supported wavelets," *Communications on Pure and Applied Mathematics*, vol. 41, no. 7, pp. 909–996, oct 1988.

[24] C. K. Chui, *An Introduction to Wavelets - Wavelet Analysis and its applications*. Academic press, 1992.

[25] I. Daubechies, *Ten Lectures on Wavelets*. Society for Industrial and Applied Mathematics, jan 1992, vol. 61.

[26] K. Amaratunga, J. R. Williams, S. Qian, and J. Weiss, "Wavelet-Galerkin solutions for one-dimensional partial differential equations," *International Journal for Numerical Methods in Engineering*, vol. 37, no. 16, pp. 2703–2716, aug 1994.

[27] C. K. Chui and E. Quak, "Wavelets on a Bounded Interval," in *Numerical Methods in Approximation Theory, Vol. 9*. Basel: Birkhäuser Basel, 1992, pp. 53–75.

[28] G. Strang, "Wavelets and Dilation Equations: A Brief Introduction," *SIAM Review*, vol. 31, no. 4, pp. 614–627, dec 1989.

[29] S. Mallat, "A theory for multiresolution signal decomposition: the wavelet representation," *IEEE Transactions on Pattern Analysis and Machine Intelligence*, vol. 11, no. 7, pp. 674–693, jul 1989.

[30] S. Mallat, *A wavelet tour of signal processing - The sparse way*. Academic Press, 2009.

[31] J. Morlet, "Sampling Theory and Wave Propagation," in *Issues in Acoustic Signal - Image Processing and Recognition*, C. H. Chen, Ed. Berlin, Heidelberg: Springer Berlin Heidelberg, 1983, vol. F1, pp. 233–261.

[32] J. Morlet, G. Arens, E. Fourgeau, and D. Glard, "Wave propagation and sampling theory - Part I: Complex signal and scattering in multilayered media," *GEOPHYSICS*, vol. 47, no. 2, pp. 203–221, feb 1982.

[33] J. Morlet, G. Arens, E. Fourgeau, and D. Giard, "Wave propagation and sampling theory - Part II: Sampling theory and complex waves," *GEOPHYSICS*, vol. 47, no. 2, pp. 222–236, feb 1982.

[34] Y. Meyer, *Wavelets and Operators: Volume 1 (Cambridge Studies in Advanced Mathematics), ; Translated by Salinger*. Cambridge University Press, 1992.

[35] K. Amaratunga and J. R. Williams, "Wavelet-Galerkin solution of boundary value problems," *Archives of Computational Methods in Engineering*, vol. 4, no. 3, pp. 243–285, sep 1997.

[36] A. Graps, "An introduction to wavelets," *IEEE Computational Science and Engineering*, vol. 2, no. 2, pp. 50–61, 1995.

[37] J. Goswami, A. Chan, and C. Chui, "On solving first-kind integral equations using wavelets on a bounded interval," *IEEE Transactions on Antennas and Propagation*, vol. 43, no. 6, pp. 614–622, jun 1995.

[38] K. Gurley and A. Kareem, "Applications of wavelet transforms in earthquake, wind and ocean engineering," *Engineering Structures*, vol. 21, no. 2, pp. 149–167, feb 1999.

[39] L. Debnath and F. A. Shah, *Wavelet Transforms and Their Applications*. Boston, MA: Birkhäuser Boston, 2015.

[40] R. T. Ogden, *Essential Wavelets for Statistical Applications and Data Analysis*. Boston, MA: Birkhäuser Boston, 1997.

[41] G. P. Nason, *Wavelet Methods in Statistics with R*, G. P. Nason, Ed. New York, NY: Springer New York, 2008.

[42] H. L. Resnikoff and R. O. Wells, *Wavelet Analysis*. New York, NY: Springer New York, 1998.

[43] D. F. Walnut, *An Introduction to Wavelet Analysis*, ser. Applied and Numerical Harmonic Analysis. Boston, MA: Birkhäuser Boston, 2004.

[44] D. Lu, T. Ohyoshi, and K. Miura, "Treatment of Boundary Conditions in One-Dimensional Wavelet-Galerkin Method." *JSME International Journal Series A*, vol. 40, no. 4, pp. 382–388, 1997.

[45] D. Lu, T. Ohyoshi, and L. Zhu, "Treatment of Boundary Conditions in the Application of Wavelet-Galerkin Method to an SH Wave Problem." *International Journal of the Society of Materials Engineering for Resources*, vol. 5, no. 1, pp. 15–25, 1997.

[46] S. Bertoluzza, G. Naldi, and J. C. Ravel, "Wavelet Methods for the Numerical Solution of Boundary Value Problems on the Interval," in *Wavelets: Theory, Algorithms, and Applications*, C. K. Chui and Others, Eds., 1994, pp. 425–448.

[47] L. Andersson, N. Hall, B. Jawerth, and G. Peters, "Wavelets on closed subsets of the real line," in *Topics in the Theory and Applications of Wavelets*, L. L. Schumaker and G. Webb, Eds., 1993.

[48] P. Monasse and V. Perrier, "Orthonormal Wavelet Bases Adapted for Partial Differential Equations with Boundary Conditions," *SIAM Journal on Mathematical Analysis*, vol. 29, no. 4, pp. 1040–1065, jul 1998.

[49] A. Cohen and R. Masson, "Wavelet Methods for Second-Order Elliptic Problems, Preconditioning, and Adaptivity," *SIAM Journal on Scientific Computing*, vol. 21, no. 3, pp. 1006–1026, jan 1999.

[50] G.-W. Jang, J. E. Kim, and Y. Y. Kim, "Multiscale Galerkin method using interpolation wavelets for two-dimensional elliptic problems in general domains," *International Journal for Numerical Methods in Engineering*, vol. 59, no. 2, pp. 225–253, jan 2004.

[51] W. Proskurowski and O. Widlund, "On the numerical solution of Helmholtz's equation by the capacitance matrix method," *Mathematics of Computation*, vol. 30, no. 135, pp. 433–433, sep 1976.

[52] S. Qian and J. Weiss, "Wavelets and the numerical solution of boundary value problems," *Applied Mathematics Letters*, vol. 6, no. 1, pp. 47–52, jan 1993.

[53] J.-C. Xu and W.-C. Shann, "Galerkin-wavelet methods for two-point boundary value problems," *Numerische Mathematik*, vol. 63, no. 1, pp. 123–144, dec 1992.

[54] A. R. Diaz, "A wavelet-Galerkin scheme for analysis of large-scale problems on simple domains," *International Journal for Numerical Methods in Engineering*, vol. 44, no. 11, pp. 1599–1616, apr 1999.

[55] G. C. A. DeRose Jr. and A. R. Díaz, "Solving three-dimensional layout optimization problems using fixed scale wavelets," *Computational Mechanics*, vol. 25, no. 2-3, pp. 274–285, mar 2000.

[56] R. Glowinski, A. Rieder, R. O. Wells, and Xiaodong Zhou, "A wavelet multigrid preconditioner for Dirichlet boundary value problems in general domains," *ESAIM: Mathematical Modelling and Numerical Analysis*, vol. 30, no. 6, pp. 711–729, may 1996.

[57] R. Glowinski, T. Pan, R. O. Wells Jr., and X. Zhou, "Wavelet and Finite Element Solutions for the Neumann Problem Using Fictitious Domains," *Journal of Computational Physics*, vol. 126, no. 1, pp. 40–51, jun 1996.

[58] R. O. Wells, Jr. and X. Zhou, "Wavelet solutions for the Dirichlet problem," *Numerische Mathematik*, vol. 70, no. 3, pp. 379–396, apr 1995.

[59] G. C. A. DeRose Jr., "Solving topology optimization problems using wavelet-Galerkin techniques," Ph.D. dissertation, Michigan State University, 1998.

[60] Y. Liu, Y. Liu, and Z. Cen, "A meshless method based on Daubechies wavelet for 2-D elastoplaticity problems," in *International conference on computational & experimental engineering and sciences*, vol. 3, 2007, pp. 139–144.

[61] Y. Liu, F. Qin, Y. Liu, and Z. Cen, "A Daubechies wavelet-based method for elastic problems," *Engineering Analysis with Boundary Elements*, vol. 34, no. 2, pp. 114–121, feb 2010.

[62] Y. Liu, Y. Liu, and Z. Cen, "Multi-scale Daubechies wavelet-based method for 2-D elastic problems," *Finite Elements in Analysis and Design*, vol. 47, no. 4, pp. 334–341, apr 2011.

[63] Y. Liu, L. Sun, F. Xu, Y. Liu, and Z. Cen, "B spline-based method for 2-D large deformation analysis," *Engineering Analysis with Boundary Elements*, vol. 35, no. 5, pp. 761–767, may 2011.

[64] V. Vampa, M. T. Martín, and E. Serrano, "A new refinement wavelet-Galerkin method in a spline local multiresolution analysis scheme for boundary value problems," *International Journal of Wavelets, Multiresolution and Information Processing*, vol. 11, no. 02, p. 1350015, mar 2013.

[65] M. A. Unser, "Ten good reasons for using spline wavelets," in *Proceedings of SPIE*, A. Aldroubi, A. F. Laine, and M. A. Unser, Eds., vol. 3169, oct 1997, pp. 422–431.

[66] S. Tanaka and H. Okada, "An Adaptive Wavelet Finite Element Method with High-Order B-Spline Basis Functions," *Key Engineering Materials*, vol. 345-346, pp. 877–880, aug 2007.

[67] S. Tanaka and H. Okada, "B-Spline Wavelet Galerkin Method for the Problems of Elastostatics," in *International Conference on Computational & Experimental Engineering and Sciences*, vol. 3, no. 4, 2007, pp. 217–223.

[68] S. Tanaka, H. Okada, and S. Okazawa, "A wavelet Galerkin method employing B-spline bases for solid mechanics problems without the use of a fictitious domain," *Computational Mechanics*, vol. 50, no. 1, pp. 35–48, jul 2012.

[69] M. Hori, *Introduction to Computational Earthquake Engineering*. Imperial College Press, feb 2006.

[70] S. J. Hollister and N. Kikuchi, "Homogenization theory and digital imaging: A basis for studying the mechanics and design principles of bone tissue," *Biotechnology and Bioengineering*, vol. 43, no. 7, pp. 586–596, mar 1994.

[71] K. Watanabe, Y. Iijima, K. Kawano, and H. Igarashi, "Voxel Based Finite Element Method Using Homogenization," *IEEE Transactions on Magnetics*, vol. 48, no. 2, pp. 543–546, feb 2012.

[72] S. Tanaka, H. Suzuki, S. Ueda, and S. Sannomaru, "An extended wavelet Galerkin method with a high-order B-spline for 2D crack problems," *Acta Mechanica*, vol. 226, no. 7, pp. 2159–2175, jul 2015.

[73] S. Tanaka, S. Sannomaru, M. Imachi, S. Hagihara, S. Okazawa, and H. Okada, "Analysis of dynamic stress concentration problems employing spline-based wavelet Galerkin method," *Engineering Analysis with Boundary Elements*, vol. 58, pp. 129–139, sep 2015.

[74] P. Venini and P. Morana, "An adaptive wavelet-Galerkin method for an elastic-plastic-damage constitutive model: 1D problem," *Computer Methods in Applied Mechanics and Engineering*, vol. 190, no. 42, pp. 5619–5638, aug 2001.

[75] H. A. Navarro, M. K. Kaibara, J. B. Rubert, A. N. Montagnoli, L. Cabezas-Gómez, and R. C. da Silva, "Wavelet-Galerkin method for one-dimensional elastoplasticity and damage problems: Constitutive modeling and computational aspects," *Applied Mathematics and Computation*, vol. 198, no. 2, pp. 904–915, may 2008.

[76] O. Goubet, "Nonlinear galerkin methods using hierarchical almost-orthogonal finite elements bases," *Nonlinear Analysis: Theory, Methods & Applications*, vol. 20, no. 3, pp. 223–247, feb 1993.

[77] J. E. Kim, G.-W. Jang, and Y. Y. Kim, "Adaptive multiscale wavelet-Galerkin analysis for plane elasticity problems and its applications to multiscale topology design optimization," *International Journal of Solids and Structures*, vol. 40, no. 23, pp. 6473–6496, nov 2003.

[78] G.-W. Jang, Y. Y. Kim, and K. K. Choi, "Remesh-free shape optimization using the wavelet-Galerkin method," *International Journal of Solids and Structures*, vol. 41, no. 22-23, pp. 6465–6483, nov 2004.

[79] Y. Y. Kim and G.-W. Jang, "Hat interpolation wavelet-based multi-scale Galerkin method for thin-walled box beam analysis," *International Journal for Numerical Methods in Engineering*, vol. 53, no. 7, pp. 1575–1592, mar 2002.

[80] S. Yang, G. Ni, J. Cardoso, S. Ho, and J. Machado, "A combined wavelet-element free galerkin method for numerical calculations of electromagnetic fields," *IEEE Transactions on Magnetics*, vol. 39, no. 3, pp. 1413–1416, may 2003.

[81] M. R. Yousefi, R. Jafari, and H. A. Moghaddam, "A Combined Wavelet-Based Mesh-Free Method for Solving the Forward Problem in Electrical Impedance Tomography," *IEEE Transactions on Instrumentation and Measurement*, vol. 62, no. 10, pp. 2629–2638, 2013.

[82] D. Li and Z. Lin, "h-Adaptive Analysis Based on Meshless Local Petrov-Galerkin Method with B Spline Wavelet for Plates and Shells," *Acta Mechanica Solida Sinica*, vol. 22, no. 4, pp. 337–346, aug 2009.

[83] A. Afsari and M. Movahhedi, "Proposing a wavelet based meshless method for simulation of conducting materials," *Progress In Electromagnetics Research M*, vol. 31, pp. 159–169, 2013.

[84] M. H. Xia and W. H. Ren, "Element-free Galerkin method with wavelet basis and its application in electromagnetic field," *Applied Mathematics*, vol. 38, pp. 4082–4085, 2011.

[85] T. Xu, P. Zou, T. Xu, and C. Jiye, "Study on Weight Function of Meshless Method Based on B-spline Wavelet Function," in *Third International Joint Conference on Computational Science and Optimization*, vol. 1. IEEE, 2010, pp. 36–40.

[86] J. Chen, W. Tang, P. Huang, and L. Xu, "A mesh-free analysis method of structural elements of engineering structures based on B-spline wavelet basis function," *Structural Engineering and Mechanics*, vol. 57, no. 2, pp. 281–294, jan 2016.

[87] Y. Liu and K. Din, "A Numerical Method Based on Daubechies Wavelet Basis and B-Spline Patches for Elasticity Problems," *Mathematical Problems in Engineering*, vol. 2016, pp. 1–11, 2016.

[88] M. Kamiński, "Interface defects in unidirectional composites by multiresolutional finite element analysis," *Computers & Structures*, vol. 84, no. 19-20, pp. 1190–1199, jul 2006.

[89] G. W. Wornell, "A Karhunen-Loève like expansion for 1/f processes via wavelets," *IEEE Transactions on Information Theory*, vol. 36, no. 4, pp. 859–861, jul 1990.

[90] B. A. Zeldin and P. D. Spanos, "Random Field Representation and Synthesis Using Wavelet Bases," *Journal of Applied Mechanics*, vol. 63, no. 4, pp. 946–952, dec 1996.

[91] K. Phoon, S. Huang, and S. Quek, "Implementation of Karhunen-Loève expansion for simulation using a wavelet-Galerkin scheme," *Probabilistic Engineering Mechanics*, vol. 17, no. 3, pp. 293–303, jul 2002.

[92] C. Proppe, "Reliability Analysis with Stochastic Finite Elements and Wavelet Approximations," in *8th. World Congress on Computational Mechanics (WCCM8)*, Venice, Italy, 2008.

[93] C. Proppe, "Multiresolution Analysis for Stochastic Finite Element Problems with Wavelet-Based Karhunen-Loève Expansion," *Mathematical Problems in Engineering*, vol. 2012, pp. 1–15, 2012.

[94] K. Phoon, H. Huang, and S. Quek, "Comparison between Karhunen-Loève and wavelet expansions for simulation of Gaussian processes," *Computers & Structures*, vol. 82, no. 13-14, pp. 985–991, may 2004.

[95] B. Sudret and A. D. Kiureghian, "Stochastic Finite Element Methods and Reliability: A State-of-the-Art Report," University of California, Berkeley, Tech. Rep., 2000.

[96] J. M. Angulo and M. D. Ruiz-Medina, "Multi-Resolution Approximation to the Stochastic Inverse Problem," *Advances in Applied Probability*, vol. 31, no. 4, pp. 1039–1057, 1999.

[97] O. Le Maître, O. Knio, H. Najm, and R. Ghanem, "Uncertainty propagation using Wiener-Haar expansions," *Journal of Computational Physics*, vol. 197, no. 1, pp. 28–57, jun 2004.

[98] M. Kamiński, "Stochastic perturbation approach to the wavelet-based analysis," *Numerical Linear Algebra with Applications*, vol. 11, no. 4, pp. 355–370, may 2004.

[99] P. D. Spanos, J. Tezcan, and P. Tratskas, "Stochastic processes evolutionary spectrum estimation via harmonic wavelets," *Computer Methods in Applied Mechanics and Engineering*, vol. 194, no. 12-16, pp. 1367–1383, apr 2005.

[100] R. Andreev, "Implementation of Sparse Wavelet-Galerkin FEM for Stochastic PDEs," ETH Zurich, Tech. Rep., 2009.

[101] C. Romine and B. Peyton, "Computing connection coefficients of compactly supported wavelets on bounded intervals," Oak Ridge National Laboratory (ORNL), Oak Ridge, TN, Tech. Rep., apr 1997.

[102] A. Latto, H. Resnikoff, and E. Tenenbaum, "The evaluation of connection coefficients of compactly supported wavelets," in *Proceedings French-USA workshop on Wavelets and Turbulence, Princeton University (1991)*. Springer-Verlag, 1991, pp. 76–89.

[103] G. Beylkin, "On the Representation of Operators in Bases of Compactly Supported Wavelets," *SIAM Journal on Numerical Analysis*, vol. 29, no. 6, pp. 1716–1740, dec 1992.

[104] M.-Q. Chen, C. Hwang, and Y.-P. Shih, "The computation of wavelet-Galerkin approximation on a bounded interval," *International Journal for Numerical Methods in Engineering*, vol. 39, no. 17, pp. 2921–2944, sep 1996.

[105] X. Zhou and W. Zhang, “The evaluation of connection coefficients on an interval,” *Communications in Nonlinear Science and Numerical Simulation*, vol. 3, no. 4, pp. 252–255, dec 1998.

[106] E. Lin and X. Zhou, “Connection coefficients on an interval and wavelet solutions of Burgers equation,” *Journal of Computational and Applied Mathematics*, vol. 135, no. 1, pp. 63–78, oct 2001.

[107] T. Zhang, Y.-C. Tian, M. O. Tadé, and J. Utomo, “Comments on ’The computation of wavelet-Galerkin approximation on a bounded interval’,” *International Journal for Numerical Methods in Engineering*, vol. 72, no. 2, pp. 244–251, oct 2007.

[108] X. Chen, Z. He, J. Xiang, and B. Li, “A dynamic multiscale lifting computation method using Daubechies wavelet,” *Journal of Computational and Applied Mathematics*, vol. 188, no. 2, pp. 228–245, apr 2006.

[109] S. Jones, T. Zhang, and M. Legrand, “The Computation of Wavelet-Galerkin Three-Term Connection Coefficients on a Bounded Domain,” *Progress in Applied Mathematics*, vol. 7, no. 1, pp. 1–8, 2014.

[110] F. Bulut, “An alternative approach to compute wavelet connection coefficients,” *Applied Mathematics Letters*, vol. 53, pp. 1–9, mar 2016.

[111] J. W. Xiang, X. F. Chen, Z. J. He, and H. B. Dong, “The construction of 1D wavelet finite elements for structural analysis,” *Computational Mechanics*, vol. 40, no. 2, pp. 325–339, apr 2007.

[112] W. H. Chen and C. W. Wu, “A spline wavelets element method for frame structures vibration,” *Computational Mechanics*, vol. 16, no. 1, pp. 11–21, apr 1995.

[113] C. W. Wu and W. H. Chen, “Extension of spline wavelets element method to membrane vibration analysis,” *Computational Mechanics*, vol. 18, no. 1, pp. 46–54, may 1996.

[114] J. Xiang, X. Chen, Y. He, and Z. He, “The construction of plane elastomechanics and Mindlin plate elements of B-spline wavelet on the interval,” *Finite Elements in Analysis and Design*, vol. 42, no. 14-15, pp. 1269–1280, oct 2006.

[115] J. Ko, J. Kurdila, and M. S. Pilant, “A class of finite element methods based on orthonormal, compactly supported wavelets,” *Computational Mechanics*, vol. 16, no. 4, pp. 235–244, jul 1995.

[116] Z. Youhe, W. Jizeng, and Z. Xiaojing, "Applications of wavelet galerkin fem to bending of beam and plate structures," *Applied Mathematics and Mechanics*, vol. 19, no. 8, pp. 745–755, aug 1998.

[117] S. Ho, S. Yang, and H. Wong, "Weak formulation of finite element method using wavelet basis functions," *IEEE Transactions on Magnetics*, vol. 37, no. 5, pp. 3203–3207, 2001.

[118] J. Ma, J. Xue, S. Yang, and Z. He, "A study of the construction and application of a Daubechies wavelet-based beam element," *Finite Elements in Analysis and Design*, vol. 39, no. 10, pp. 965–975, jul 2003.

[119] X. Chen, S. Yang, J. Ma, and Z. He, "The construction of wavelet finite element and its application," *Finite Elements in Analysis and Design*, vol. 40, no. 5-6, pp. 541–554, mar 2004.

[120] M. T. Martin and V. Vampa, "A Daubechies Wavelet Mindlin-Reissner plate element," *Mecánica Computacional*, vol. XXVII, pp. 2253–2263, 2008.

[121] L. A. Díaz, M. T. Martín, and V. Vampa, "Daubechies wavelet beam and plate finite elements," *Finite Elements in Analysis and Design*, vol. 45, no. 3, pp. 200–209, feb 2009.

[122] M. Mitra and S. Gopalakrishnan, "Spectrally formulated wavelet finite element for wave propagation and impact force identification in connected 1-D waveguides," *International Journal of Solids and Structures*, vol. 42, no. 16-17, pp. 4695–4721, aug 2005.

[123] M. Mitra and S. Gopalakrishnan, "Extraction of wave characteristics from wavelet-based spectral finite element formulation," *Mechanical Systems and Signal Processing*, vol. 20, no. 8, pp. 2046–2079, nov 2006.

[124] M. Mitra and S. Gopalakrishnan, "Wavelet based spectral finite element for analysis of coupled wave propagation in higher order composite beams," *Composite Structures*, vol. 73, no. 3, pp. 263–277, jun 2006.

[125] M. Mitra and S. Gopalakrishnan, "Wavelet Based 2-D Spectral Finite Element Formulation for Wave Propagation Analysis in Isotropic Plates," *Computer Modeling in Engineering & Sciences*, vol. 15, no. 1, pp. 49–67, 2006.

[126] M. Mitra and S. Gopalakrishnan, "Wavelet based spectral finite element modelling and detection of de-lamination in composite beams," *Proceedings of the Royal Society A: Mathematical, Physical and Engineering Sciences*, vol. 462, no. 2070, pp. 1721–1740, jun 2006.

[127] L. Pahlavan, C. Kassapoglou, and Z. Gürdal, "Spectral formulation of finite element methods using Daubechies compactly-supported wavelets for elastic wave propagation simulation," *Wave Motion*, vol. 50, no. 3, pp. 558–578, apr 2013.

[128] E. Quak, "Trigonometric Wavelets for Hermite Interpolation," *Mathematics of Computation*, vol. 65, no. 214, pp. 683–722, 1996.

[129] W.-Y. He and W.-X. Ren, "Finite element analysis of beam structures based on trigonometric wavelet," *Finite Elements in Analysis and Design*, vol. 51, pp. 59–66, apr 2012.

[130] W.-Y. He and W.-X. Ren, "Trigonometric wavelet-based method for elastic thin plate analysis," *Applied Mathematical Modelling*, vol. 37, no. 4, pp. 1607–1617, feb 2013.

[131] Z. Shan and Q. Du, "Trigonometric wavelet method for some elliptic boundary value problems," *Journal of Mathematical Analysis and Applications*, vol. 344, no. 2, pp. 1105–1119, aug 2008.

[132] J. Gao and Y.-L. Jiang, "Trigonometric Hermite wavelet approximation for the integral equations of second kind with weakly singular kernel," *Journal of Computational and Applied Mathematics*, vol. 215, no. 1, pp. 242–259, may 2008.

[133] R.-Q. Jia and S.-T. Liu, "Wavelet bases of Hermite cubic splines on the interval," *Advances in Computational Mathematics*, vol. 25, no. 1-3, pp. 23–39, jul 2006.

[134] J. W. Xiang, J. Q. Long, and Z. S. Jiang, "A numerical study using Hermitian cubic spline wavelets for the analysis of shafts," *Proceedings of the Institution of Mechanical Engineers, Part C: Journal of Mechanical Engineering Science*, vol. 224, no. 9, pp. 1843–1851, sep 2010.

[135] P. Shen, Y. M. He, Z. S. Duan, Z. B. Wei, and P. Gao, "Wavelet Finite Element Method Analysis of Bending Plate Based on Hermite Interpolation," *Applied Mechanics and Materials*, vol. 389, pp. 267–272, aug 2013.

[136] X. Xue, X. Chen, X. Zhang, and B. Qiao, "Hermitian plane wavelet finite element method: Wave propagation and load identification," *Computers & Mathematics with Applications*, vol. 72, no. 12, pp. 2920–2942, dec 2016.

[137] X. Xue, X. Chen, X. Zhang, B. Qiao, and J. Geng, "Hermitian Mindlin Plate Wavelet Finite Element Method for Load Identification," *Shock and Vibration*, vol. 2016, pp. 1–24, Article ID 8618202.

[138] X. Xue, X. Zhang, B. Li, B. Qiao, and X. Chen, "Modified Hermitian cubic spline wavelet on interval finite element for wave propagation and load identification," *Finite Elements in Analysis and Design*, vol. 91, pp. 48–58, nov 2014.

[139] S. Zhu, W.-Y. He, and W.-X. Ren, "Adaptive-scale damage detection for frame structures using beam-type wavelet finite element: experimental validation," *Journal of Earthquake and Tsunami*, vol. 07, no. 03, p. 1350024, sep 2013.

[140] W.-Y. He, S. Zhu, and W.-X. Ren, "A wavelet finite element-based adaptive-scale damage detection strategy," *Smart Structures and Systems*, vol. 14, no. 3, pp. 285–305, sep 2014.

[141] W.-Y. He and S. Zhu, "Adaptive-scale damage detection strategy for plate structures based on wavelet finite element model," *Structural Engineering and Mechanics*, vol. 54, no. 2, pp. 239–256, apr 2015.

[142] W. Sweldens, "The Lifting Scheme: A Construction of Second Generation Wavelets," *SIAM Journal on Mathematical Analysis*, vol. 29, no. 2, pp. 511–546, mar 1998.

[143] S. D'Heedene, K. Amaratunga, and J. Castrillón-Candás, "Generalized hierarchical bases: a Wavelet-Ritz-Galerkin framework for Lagrangian FEM," *Engineering Computations*, vol. 22, no. 1, pp. 15–37, jan 2005.

[144] Y. Wang, X. Chen, and Z. He, "A second-generation wavelet-based finite element method for the solution of partial differential equations," *Applied Mathematics Letters*, vol. 25, no. 11, pp. 1608–1613, nov 2012.

[145] K. Amaratunga and R. Sudarshan, "Multiresolution modeling with operator-customized wavelets derived from finite elements," *Computer Methods in Applied Mechanics and Engineering*, vol. 195, no. 19-22, pp. 2509–2532, apr 2006.

[146] R. Sudarshan, K. Amaratunga, and T. Grätsch, "A combined approach for goal-oriented error estimation and adaptivity using operator-customized finite element wavelets," *International Journal for Numerical Methods in Engineering*, vol. 66, no. 6, pp. 1002–1035, may 2006.

[147] J.-G. Han, W.-X. Ren, and Y. Huang, "A spline wavelet finite-element method in structural mechanics," *International Journal for Numerical Methods in Engineering*, vol. 66, no. 1, pp. 166–190, apr 2006.

[148] J.-G. Han, W.-X. Ren, and Y. Huang, "A spline wavelet finite element formulation of thin plate bending," *Engineering with Computers*, vol. 25, no. 4, pp. 319–326, nov 2009.

[149] C. K. Chui and J.-Z. Wang, "On compactly supported spline wavelets and a duality principle," *Transactions of the American Mathematical Society*, vol. 330, no. 2, pp. 903–915, feb 1992.

[150] C. K. Chui and J.-Z. Wang, "A cardinal spline approach to wavelets," *Proceedings of the American Mathematical Society*, vol. 113, no. 3, pp. 785–785, mar 1991.

[151] C. Chui and J. Wang, "An Analysis of Cardinal Spline-Wavelets," *Journal of Approximation Theory*, vol. 72, no. 1, pp. 54–68, jan 1993.

[152] E. Quak and N. Weyrich, "Decomposition and Reconstruction Algorithms for Spline Wavelets on a Bounded Interval," *Applied and Computational Harmonic Analysis*, vol. 1, no. 3, pp. 217–231, jun 1994.

[153] M. G. Cox, "The Numerical Evaluation of B -Splines," *IMA Journal of Applied Mathematics*, vol. 10, no. 2, pp. 134–149, 1972.

[154] C. de Boor, "On calculating with B-splines," *Journal of Approximation Theory*, vol. 6, no. 1, pp. 50–62, jul 1972.

[155] J. Xiang, Z. He, and X. Chen, "The construction of wavelet-based truncated conical shell element using B-spline wavelet on the interval," *Acta Mechanica Solida Sinica*, vol. 19, no. 4, pp. 316–326, dec 2006.

[156] X. Jiawei, C. Xuefeng, H. Zhengjia, and Z. Yinghong, "A new wavelet-based thin plate element using B-spline wavelet on the interval," *Computational Mechanics*, vol. 41, no. 2, pp. 243–255, oct 2007.

[157] J. Xiang, X. Chen, L. Yang, and Z. He, "A class of wavelet-based flat shell elements using B-spline wavelet on the interval and its applications," *CMES - Computer Modeling in Engineering and Sciences*, vol. 23, no. 1, pp. 1–12, 2008.

[158] X. Chen, J. Xiang, B. Li, and Z. He, "A study of multiscale wavelet-based elements for adaptive finite element analysis," *Advances in Engineering Software*, vol. 41, no. 2, pp. 196–205, feb 2010.

[159] Y. Zhong and J. Xiang, "Construction of wavelet-based elements for static and stability analysis of elastic problems," *Acta Mechanica Solida Sinica*, vol. 24, no. 4, pp. 355–364, aug 2011.

[160] Q. Xu, J.-Y. Chen, J. Li, G. Xu, and H.-Y. Yue, "Study on spline wavelet finite-element method in multi-scale analysis for foundation," *Acta Mechanica Sinica*, vol. 29, no. 5, pp. 699–708, oct 2013.

[161] Z. Yang, X. Chen, Y. He, Z. He, and J. Zhang, "The Analysis of Curved Beam Using B-Spline Wavelet on Interval Finite Element Method," *Shock and Vibration*, vol. 2014, pp. 1–9, Article ID 738162.

[162] J. Xiang, Z. Jiang, and X. Chen, "A class of wavelet based Rayleigh-Euler beam element for analyzing rotating shafts," *Shock and Vibration*, vol. 18, no. 3, pp. 447–458, 2009.

[163] Z. Yang, X. Chen, B. Li, Z. He, and H. Miao, "Vibration analysis of curved shell using B-spline Wavelet on the interval (BSWI) finite elements method and general shell theory," *CMES - Computer Modeling in Engineering and Sciences*, vol. 85, no. 2, pp. 129–155, 2012.

[164] L. Shen, Z. Liu, and J. H. Wu, "B-spline finite element method based on node moving adaptive refinement strategy," *Finite Elements in Analysis and Design*, vol. 91, pp. 84–94, nov 2014.

[165] Z. Yang, X. Chen, X. Zhang, and Z. He, "Free vibration and buckling analysis of plates using B-spline wavelet on the interval Mindlin element," *Applied Mathematical Modelling*, vol. 37, no. 5, pp. 3449–3466, mar 2013.

[166] J. Geng, X. Zhang, X. Chen, and X. Xue, "High-frequency vibration analysis of thin plate based on wavelet-based FEM using B-spline wavelet on interval," *Science China Technological Sciences*, vol. 60, no. 5, pp. 792–806, may 2017.

[167] W. A. Oke and Y. A. Khulief, "B-Spline Wavelet-Based Finite Element Vibration Analysis of Composite Pipes with Internal Surface Defects of Different Geometries," *International Journal of Structural Stability and Dynamics*, vol. 17, no. 04, p. 1750051, may 2017.

[168] H. Zuo, Z. B. Yang, X. F. Chen, Y. Xie, X. W. Zhang, and Y. Liu, "Static, free vibration and buckling analysis of functionally graded beam via B-spline wavelet on the interval and Timoshenko beam theory," *CMES - Computer Modeling in Engineering and Sciences*, vol. 100, no. 6, pp. 477–506, 2014.

[169] H. Zuo, Z. Yang, X. Chen, Y. Xie, and X. Zhang, "Bending, Free Vibration and Buckling Analysis of Functionally Graded Plates via Wavelet Finite Element Method," *CMC: Computers, Materials & Continua*, vol. 44, no. 3, pp. 167–204, 2014.

[170] X. Zhang, X. Chen, Z. He, and H. Cao, "The multivariable finite elements based on B-spline wavelet on the interval for 1D structural mechanics," *Journal of Vibroengineering*, vol. 14, no. 1, pp. 363–380, 2012.

[171] P. C. Shen and H. B. Kan, "Multivariable spline element analysis for plate bending problems," *Computers & Structures*, vol. 40, no. 6, pp. 1343–1349, jan 1991.

[172] P. Shen, P. He, and G. Su, "Stability analysis for plates using the multivariable spline element method," *Computers & Structures*, vol. 45, no. 5-6, pp. 1073–1077, dec 1992.

[173] P. Shen and H. Peixiang, "Bending analysis of plates and spherical shells by multivariable spline element method based on generalized variational principle," *Computers & Structures*, vol. 55, no. 1, pp. 151–157, apr 1995.

[174] P. Shen and H. Peixiang, "Analysis of bending, vibration and stability for thin plate on elastic foundation by the multivariable spline element method," *Applied Mathematics and Mechanics*, vol. 18, no. 8, pp. 779–787, aug 1997.

[175] X. Zhang, X. Chen, X. Wang, and Z. He, "Multivariable finite elements based on B-spline wavelet on the interval for thin plate static and vibration analysis," *Finite Elements in Analysis and Design*, vol. 46, no. 5, pp. 416–427, may 2010.

[176] X. Zhang, X. Chen, and Z. He, "The construction of multivariable Reissner-Mindlin plate elements based on B-spline wavelet on the interval," *Structural Engineering and Mechanics*, vol. 38, no. 6, pp. 733–751, jun 2011.

[177] X. Zhang, X. Chen, Z. He, and Z. Yang, "The analysis of shallow shells based on multivariable wavelet finite element method," *Acta Mechanica Solida Sinica*, vol. 24, no. 5, pp. 450–460, oct 2011.

[178] X. Zhang, X. Chen, Z. Yang, and Z. Shen, "Multivariable wavelet finite element for flexible skew thin plate analysis," *Science China Technological Sciences*, vol. 57, no. 8, pp. 1532–1540, aug 2014.

[179] X. Zhang, H. Zuo, J. Liu, X. Chen, and Z. Yang, "Analysis of shallow hyperbolic shell by different kinds of wavelet elements based on B-spline wavelet on the interval," *Applied Mathematical Modelling*, vol. 40, no. 3, pp. 1914–1928, feb 2016.

[180] J.-G. Han, W.-X. Ren, and Y. Huang, "A multivariable wavelet-based finite element method and its application to thick plates," *Finite Elements in Analysis and Design*, vol. 41, no. 9-10, pp. 821–833, may 2005.

[181] C. Canuto, A. Tabacco, and K. Urban, "The Wavelet Element Method," *Applied and Computational Harmonic Analysis*, vol. 6, no. 1, pp. 1–52, jan 1999.

[182] C. Canuto, A. Tabacco, and K. Urban, "The Wavelet Element Method Part II. Realization and Additional Features in 2D and 3D," *Applied and Computational Harmonic Analysis*, vol. 8, no. 2, pp. 123–165, mar 2000.

[183] J. Xiang, X. Chen, B. Li, Y. He, and Z. He, "Identification of a crack in a beam based on the finite element method of a B-spline wavelet on the interval," *Journal of Sound and Vibration*, vol. 296, no. 4-5, pp. 1046–1052, oct 2006.

[184] J. Xiang, Y. Zhong, X. Chen, and Z. He, "Crack detection in a shaft by combination of wavelet-based elements and genetic algorithm," *International Journal of Solids and Structures*, vol. 45, no. 17, pp. 4782–4795, aug 2008.

[185] G. G. Amiri, M. Jalalinia, A. Z. Hosseinzadeh, and A. Nasrollahi, "Multiple crack identification in Euler beams by means of B-spline wavelet," *Archive of Applied Mechanics*, vol. 85, no. 4, pp. 503–515, apr 2015.

[186] J. Xiang, X. Chen, Q. Mo, and Z. He, "Identification of crack in a rotor system based on wavelet finite element method," *Finite Elements in Analysis and Design*, vol. 43, no. 14, pp. 1068–1081, oct 2007.

[187] J.-W. Xiang, M. Liang, and Y.-T. Zhong, "Computation of Stress Intensity Factors Using Wavelet-Based Element," *Journal of Mechanics*, vol. 32, no. 3, pp. N1–N6, jun 2016.

[188] H. Zuo, Z. Yang, X. Chen, Y. Xie, and H. Miao, "Analysis of laminated composite plates using wavelet finite element method and higher-order plate theory," *Composite Structures*, vol. 131, pp. 248–258, nov 2015.

[189] X. Zhang, R. X. Gao, R. Yan, X. Chen, C. Sun, and Z. Yang, "Analysis of Laminated Plates and Shells Using B-Spline Wavelet on Interval Finite Element," *International Journal of Structural Stability and Dynamics*, vol. 17, no. 04, pp. 1 750 062 (1–18), aug 2017.

[190] X. Chen, Z. Yang, X. Zhang, and Z. He, "Modeling of wave propagation in one-dimension structures using B-spline wavelet on interval finite element," *Finite Elements in Analysis and Design*, vol. 51, pp. 1–9, apr 2012.

[191] Z.-B. Yang, X.-F. Chen, Y. Xie, H. Zuo, H.-H. Miao, and X.-W. Zhang, "Wave motion analysis and modeling of membrane structures using the wavelet finite element method," *Applied Mathematical Modelling*, vol. 40, no. 3, pp. 2407–2420, feb 2016.

[192] Z. Yang, X. Chen, X. Li, Y. Jiang, H. Miao, and Z. He, "Wave motion analysis in arch structures via wavelet finite element method," *Journal of Sound and Vibration*, vol. 333, no. 2, pp. 446–469, jan 2014.

[193] M. Liu, J. Xiang, and Y. Zhong, "Band Structures Analysis Method of Two-Dimensional Phononic Crystals Using Wavelet-Based Elements," *Crystals*, vol. 7, no. 11, p. 328, oct 2017.

[194] J.-G. Han, W.-X. Ren, and Y. Huang, "A wavelet-based stochastic finite element method of thin plate bending," *Applied Mathematical Modelling*, vol. 31, no. 2, pp. 181–193, feb 2007.

[195] X. Zhang, X. Chen, Z. Yang, B. Li, and Z. He, "A Stochastic Wavelet Finite Element Method for 1D and 2D Structures Analysis," *Shock and Vibration*, vol. 2014, pp. 1–15, Article ID 104347.

[196] S. Timoshenko, *Strength of Materials : Part I*, 2nd ed. D.Van Nostrand company, Inc., 1940.

[197] E. Oñate, *Structural Analysis with the Finite Element Method Linear Statics - Vol. 2 - Beams, Plates and Shells*, 1st ed. Barcelona: Springer, 2013.

[198] M. H. Sadd, *Elasicity - Theory, Applications, and Numerics*. Elsevier Academic Press, 2005.

[199] H. Xu and S. Rahman, "Decomposition methods for structural reliability analysis," *Probabilistic Engineering Mechanics*, vol. 20, no. 3, pp. 239–250, jul 2005.

[200] P.-L. Liu and A. Der Kiureghian, "Multivariate distribution models with prescribed marginals and covariances," *Probabilistic Engineering Mechanics*, vol. 1, no. 2, pp. 105–112, jun 1986.

[201] E. Vanmarcke, M. Shinozuka, S. Nakagiri, G. Schuëller, and M. Grigoriu, "Random fields and stochastic finite elements," *Structural Safety*, vol. 3, no. 3-4, pp. 143–166, aug 1986.

[202] S. Mahadevan and A. Haldar, "Practical random field discretization in stochastic finite element analysis," *Structural Safety*, vol. 9, no. 4, pp. 283–304, jun 1991.

[203] M. Kamiński, *The Stochastic Perturbation Method for Computational Mechanics*. Chichester, UK: John Wiley & Sons, Ltd, jan 2013.

[204] G. Falsone and N. Impollonia, "A new approach for the stochastic analysis of finite element modelled structures with uncertain parameters," *Computer Methods in Applied Mechanics and Engineering*, vol. 191, no. 44, pp. 5067–5085, oct 2002.

[205] G. Falsone and N. Impollonia, "Erratum to 'A new approach for the stochastic analysis of finite element modelled structures with uncertain parameters' in Comput. Methods Appl. Mech. Engrg. 191 (2002) 5067-5085," *Computer Methods in Applied Mechanics and Engineering*, vol. 192, no. 16-18, pp. 2187–2188, apr 2003.

[206] C. Arun, B. Rao, and S. Srinivasan, "Stochastic meshfree method for elasto-plastic damage analysis," *Computer Methods in Applied Mechanics and Engineering*, vol. 199, no. 37-40, pp. 2590–2606, aug 2010.

[207] S. Rahman and B. Rao, "An element-free Galerkin method for probabilistic mechanics and reliability," *International Journal of Solids and Structures*, vol. 38, no. 50-51, pp. 9313–9330, dec 2001.

[208] A. Der Kiureghian and J.-B. Ke, "The stochastic finite element method in structural reliability," *Probabilistic Engineering Mechanics*, vol. 3, no. 2, pp. 83–91, jun 1988.

[209] C. Li and A. Der Kiureghian, "Optimal Discretization of Random Fields," *Journal of Engineering Mechanics*, vol. 119, no. 6, pp. 1136–1154, jun 1993.

[210] J. N. Reddy, *An Introduction to Nonlinear Finite Element Analysis*. Oxford University Press, mar 2004.

[211] M. Sathyamoorthy, *Nonlinear Analysis of Structures*, 1st ed. CRC Press, 1997.

[212] V. V. Nishawala, "A study of large deflection of beams and plates," Master thesis, Rutgers, The State University of New Jersey, 2011.

[213] D. S. SIMULIA, "Abaqus 6.13 Documentation."

[214] K. H. Wang, C. M.; Reddy, J. N.; Lee, *Shear Deformable Beams and Plates: Relationships with Classical Solutions*, 1st ed. Elsevier Academic Press, 2000.

List of publications

Refereed Journals

1. S. Vadlamani, Arun C.O., A background cell based numerical integration for B-spline wavelet on the interval finite element method, *Engineering Computations*, 36(2), (2019), 569-598

2. S. Vadlamani, Arun C.O., Construction of beam elements considering von Kármán nonlinear strains using B-spline wavelet on the interval, *Applied Mathematical Modelling*, 68, (2019), 675-695

3. S. Vadlamani, Arun C.O., A stochastic B-spline wavelet on the interval finite element method for problems in Elasto-statics, *Probabilistic Engineering Mechanics*, 58, (2019), 102996

4. S. Vadlamani, Arun C.O., A stochastic B-spline wavelet on the interval finite element method for beams, *Computers and Structures*, (under review)

5. S. Vadlamani, Arun C.O., A stochastic B-spline wavelet on the interval finite element method for beams considering von Kármán nonlinear strains (under preparation)

6. S. Vadlamani, Arun C.O., A review on wavelet based numerical methods (under preparation)

Refereed Conferences

1. S. Vadlamani, Arun C.O., A stochastic B-spline wavelet on the interval finite element method for elastic buckling of columns, 10^{th} *International Conference on Computational Methods 2019*, Singapore

2. S. Vadlamani, Arun C.O., B-spline wavelet finite element method for static analysis of 1D problems with material nonhomogeneity, *International Conference*

on Composite Materials and Structures 2017, IIT Hyderabad

3. S. Vadlamani, Arun C.O., B-spline wavelet finite element method and its application to elastic bi-material models, *Sixth International Congress on Computational Mechanics and Simulation 2016*, IIT Bombay

Doctoral committee members

1. Dr. Manoj T. Nair (Chairman)
   Associate Professor & Head of the Department
   Department of Aerospace Engineering
   Indian Institute of Space Science and Technology, Trivandrum, Kerala

2. Dr. Arun C.O. (Research supervisor)
   Assistant Professor, Department of Aerospace Engineering
   Indian Institute of Space Science and Technology, Trivandrum, Kerala

3. Dr. Rajib Chowdhury (External member)
   Associate Professor, Department of Civil Engineering
   Indian Institute of Technology, Roorkee, Uttarakhand

4. Dr. Mira Mitra (External member)
   Associate Professor, Department of Aerospace Engineering
   Indian Institute of Technology, Kharagpur, West Bengal

5. Dr. Praveen Krishna (Internal member)
   Associate Professor, Department of Aerospace Engineering
   Indian Institute of Space Science and Technology, Trivandrum, Kerala

6. Dr. Bijudas C.R. (Internal member)
   Assistant Professor, Department of Aerospace Engineering
   Indian Institute of Space Science and Technology, Trivandrum, Kerala

7. Dr. Deepak T.G. (Internal member)
   Associate Professor, Department of Mathematics
   Indian Institute of Space Science and Technology, Trivandrum, Kerala